Physical aspects of hydrogen storage in subsurface porous media

Flow mechanisms, hysteresis and storage efficiency

Maksim Lysyy

Thesis for the degree of Philosophiae Doctor (PhD)
University of Bergen, Norway
2024

UNIVERSITY OF BERGEN

Physical aspects of hydrogen storage in subsurface porous media
Flow mechanisms, hysteresis and storage efficiency

Maksim Lysyy

Thesis for the degree of Philosophiae Doctor (PhD)
at the University of Bergen

Date of defense: 28.06.2024

Acknowledgements

I would like to acknowledge my supervisors Professor Geir Ersland and Professor Martin Fernø for their guidance throughout this PhD journey. The Department of Physics and Technology is acknowledged for facilitating my work as a PhD Research Fellow. The Reservoir Physics group created a productive working environment with memorable lunch times.

The following projects from the Research Council of Norway are acknowledged for sponsoring various scientific events: "Hydrogen Storage in Subsurface Porous Media—Enabling Transition to Net-Zero Society" and the "Centre for Sustainable Subsurface Resources". For my research stay in Trondheim, I would like to thank the Petroleum Research School of Norway for the financial support and the SINTEF Industry for providing the excess to laboratory facilities.

And of course, I would like to express my greatest gratitude to my family for their support.

Abstract

Hydrogen (H_2) is experiencing an unparalleled level of business and political support, with numerous projects and policies being launched worldwide. A broader implementation of H_2 in sectors like transport, heating and power generation will require sufficient storage capacity and functionality to meet peak demand. Current storage technologies are mostly suitable for small-scale applications, and underground H_2 storage (UHS) in porous media has been therefore proposed as a suitable solution for large-scale and long-term storage. The technical concept is based on the experience gained from natural gas storage in aquifers and depleted hydrocarbon reservoirs. Gas injection and withdrawal follow a seasonal cycle in response to changes in demand.

The injection of H_2 into porous media can result in undesired outcomes due to its low viscosity and low density coupled with pronounced bio-geochemical activity. UHS has received a great attention in the scientific community over the last couple of years, focusing on bio-geochemical interactions, wettability and reservoir storage performance. This dissertation aims at advancing the understanding of H_2 flow physics across the length scales using microfluidics, core scale measurements and reservoir simulations.

This dissertation presents the integrated nature of the work published in six journal publications. Papers 1-3 examine the pore scale H_2 flow mechanisms in an aquifer storage setting using microfluidics. Paper 4 reports a full cycle of H_2-water relative permeability measurements in a sandstone based on a steady state technique. Papers 5-6 are based on reservoir simulations to study the effect of reservoir type, cushion gas and hysteresis on the storage efficiency. A brief summary of papers is provided below.

Paper 1 studies the impact of gas type and injection rate on pore scale flow patterns, gas saturation and its connectivity during drainage experiments. The dominant flow regime is identified, shown to be independent of the gas type and injection rate. Conversely, the injection rate controls the gas saturation and its connectivity. The optimal injection rate is proposed to yield a maximum gas saturation with minimal amount of disconnected gas.

Paper 2 identifies the dominant displacement and trapping mechanisms during one cycle of drainage and imbibition experiments. The kinetics of H_2 dissolution in water is controlled by a non-equilibrium regime, and the observed dynamic contact angles show hysteresis. Paper 3 studies multiple cycles of drainage and imbibition, extending the work from paper 2. The evolution of H_2 saturation over the injection cycles is quantified, demonstrating reproducibility of residual H_2 saturations after imbibition. Approximately half of the residual H_2 reconnects in the next drainage injection, where reconnection is favoured in the vicinity of large pore-size clusters.

Paper 4 reports drainage and imbibition H_2-water relative permeability measurements in a sandstone, demonstrating strong hysteresis. The drainage experiment is repeated with nitrogen (N_2), questioning its applicability as a laboratory substitute for H_2. The experimental results are extrapolated with numerical history matching to include the entire mobile saturation range, making the resulting relative permeabilities suitable input for reservoir simulations.

Paper 5 highlights reservoir simulations of H_2 storage in a depleted oil and gas field using the Eclipse black-oil simulator. The storage efficiency is compared between three scenarios: pure H_2 injection into 1) gas, 2) oil or 3) water zones of a vertical injector. The gas zone is a recommended target for H_2 storage with a final recovery factor of 87%. The use of formation gas as cushion gas increases the H_2 recovery factor, albeit with reduced H_2 concentration in the withdrawn gas stream. In paper 6, the relative permeabilities from paper 4 are implemented in an aquifer reservoir model to examine the hysteresis effects. The results show that relative permeability hysteresis cannot be neglected as it significantly affects the storage efficiency.

Sammendrag

Hydrogen (H_2) som energibærer er i dag et prioritert satsningsområde med en rekke prosjekter som lanseres over hele verden. En bred implementering av H_2 i sektorer som transport, oppvarming og kraftproduksjon vil kreve stor lagringskapasitet med funksjonalitet og fleksibilitet til å møte etterspørselen. Nåværende lagringsteknologier er mest egnet for småskalaapplikasjoner, og det trengs derfor ny teknologi for å møte fremtidig etterspørsel. Hydrogenlagring i undergrunnen (*Underground Hydrogen Storage*, UHS) har derfor blitt foreslått som en mulighet for storskala lagring. Det tekniske konseptet er basert på erfaringene fra lagring av naturgass i undergrunnen, som f.k.s vannreservoar eller ferdigproduserte petroleumsreservoarer. Gassinjeksjon for lagring og senere uttak følger typisk en sesongsyklus som følge av større etterspørsel gjennom vinterhalvåret. Injeksjon av H_2 i porøse medier kan imidlertid resultere i uønskede utfall på grunn av dens lave viskositet, lave tetthet og høye bio-geokjemisk aktivitet. UHS har fått stor oppmerksomhet i vitenskapelige miljøer de siste par årene, med søkelys på bio-geokjemiske interaksjoner, fuktpreferanse og reservoareffektivitet. Denne avhandlingen tar sikte på å fremme forståelsen av strømningsfysikk for H_2 i porøse medier på tvers av lengdeskalaene ved bruk av mikrofluidikk, kjerneflømming og reservoarsimuleringer.

Det vitenskapelige arbeidet er publisert i seks tidsskriftpublikasjoner. Artikler 1-3 undersøker H_2-vann strømningsmekanismer på porenivå ved bruk av poreskalaeksperimenter, relevant for lagring i et vannreservoar (akviferer). Artikkel 4 rapporterer en full syklus av H_2-vann relative permeabilitetsmålinger i en sandstein basert på en steady state-teknikk. Artikler 5-6 er basert på resultater fra reservoarsimuleringer for å studere effekten av reservoartype, basegass og hysterese på lagringseffektiviteten. Et kort sammendrag av artiklene er gitt nedenfor.

Artikkel 1 studerer effekten av gasstype og injeksjonshastighet på strømningsmønstre, gassmetning og gassens kontinuitet på poreskala under dreneringseksperimenter. Det dominerende strømningsregimet er identifisert, og er uavhengig av gasstype og injeksjonshastighet. Injeksjonshastigheten er imidlertid styrende for gassmetningen og

dens kontinuitet. En gunstig injeksjonshastighet er foreslått for å gi maksimal gassmetning og minimal mengde diskontinuerlig gass.

Artikkel 2 identifiserer de dominerende fortrengnings- og fangemekanismene i løpet av en syklus med drenerings- og imbibisjonseksperimenter. Kinetikken til H_2-oppløsning i vann kontrolleres av et ikke-likevektsregime, og de observerte dynamiske kontaktvinklene viser hysterese. Artikkel 3 studerer flere sykluser med drenering og imbibisjon, og utvider arbeidet fra artikkel 2. Utviklingen av H_2-metning over injeksjonssyklusene er kvantifisert, noe som viser reproduserbarhet av restmetninger av H_2-gass etter imbibisjon. Omtrent halvparten av den resterende H_2 gass kobles sammen igjen i neste dreneringsinjeksjon, hvor gjenkobling favoriseres i nærheten av store porestørrelser.

Artikkel 4 rapporterer relativ permeabilitet for H_2-vann systemet under drenering og imbibisjon i en sandstein, som viser sterk hysterese. Dreneringseksperimentet gjentas med nitrogen (N_2), og diskuterer nitrogengass som analog for H_2 i slike laboratorieeksperimenter. De eksperimentelle resultatene er ekstrapolert med numerisk historietilpasning for å inkludere hele det mobile metningsområdet, noe som gjør de resulterende relative permeabilitetsdataene til verdifull input for reservoarsimuleringer.

Artikkel 5 beskriver resultat fra reservoarsimuleringer av H_2-lagring i et trykkavlastet olje- og gassfelt ved bruk av Eclipse simulator. Lagringseffektiviteten sammenlignes mellom tre scenarier: ren H_2-injeksjon i en vertikal injektor med tre soner: 1) gass, 2) olje eller 3) vann. Gassonen er et anbefalt mål for H_2-lagring med en utvinningsgrad på 87 %. Bruk av formasjonsgass som basegass øker H_2-utvinningsfaktoren, men med redusert H_2-konsentrasjon i den produserte gasstrømmen. Artikkel 6 bruker data fra relativ permeabilitetsmålinger fra artikkel 4 i en reservoarmodell for å undersøke hystereseeffektene på feltskala. Resultatene viser at hysterese ikke kan neglisjeres da den påvirker lagringseffektiviteten betydelig.

List of Publications

1. **Lysyy, M.**, N. Liu, D. Landa-Marbán, G. Ersland, and M. Fernø, *Impact of gas type on microfluidic drainage experiments and pore network modeling relevant for underground hydrogen storage*. Journal of Energy Storage, 2024. Under review.

2. **Lysyy, M.**, G. Ersland, and M. Fernø, *Pore-scale dynamics for underground porous media hydrogen storage.* Advances in Water Resources, 2022. **163**.

3. **Lysyy, M.**, N. Liu, C. M. Solstad, M. A. Fernø, and G. Ersland, *Microfluidic hydrogen storage capacity and residual trapping during cyclic injections: Implications for underground storage.* International Journal of Hydrogen Energy, 2023. **48**(80): p. 31294-31304.

4. **Lysyy, M.**, T. Føyen, E. B. Johannesen, M. Fernø, and G. Ersland, *Hydrogen Relative Permeability Hysteresis in Underground Storage.* Geophysical Research Letters, 2022. **49**(17).

5. **Lysyy, M.**, M. Fernø, and G. Ersland, *Seasonal hydrogen storage in a depleted oil and gas field.* International Journal of Hydrogen Energy, 2021. **46**(49): p. 25160-25174.

6. **Lysyy, M.**, M.A. Fernø, and G. Ersland, *Effect of relative permeability hysteresis on reservoir simulation of underground hydrogen storage in an offshore aquifer.* Journal of Energy Storage, 2023. **64**.

Additional contributions

Below is a list of scientific work not included in the dissertation.

Almenningen, S., **M. Lysyy**, and G. Ersland, *Quantification of CH$_4$ Hydrate Film Growth Rates in Micromodel Pores.* Crystal Growth & Design, 2021. **21**(7): p. 4090-4099.

Medina, O.E., J. F. Gallego, I. Moncayo-Riascos, **M. Lysyy**, P. N. Benjumea, F. B. Cortés, and C. A. Franco, *Salinity influence on underground hydrogen storage: Insights from molecular dynamics and pore-scale analysis.* International Journal of Hydrogen Energy, 2024. **60**: p. 959-975.

Viveros. F.E., O.E. Medina, I. Moncayo-Riascos, **M. Lysyy**, P. N. Benjumea, F. B. Cortés, and C. A. Franco, *Hydrogen Storage in Depleted Gas Reservoirs using Methane Cushion Gas: An Interfacial Tension and Pore Scale Study*, 2024. Manuscript in preparation.

Presentations at international conferences

Lysyy, M., N. Liu, C. M. Solstad, M. A. Fernø, and G. Ersland, *Microfluidic hydrogen storage capacity and residual trapping during cyclic injections.* Oral presentation, 15th InterPore Annual Meeting, Edinburgh, UK, 22-25 May 2023.

Lysyy, M., P.H.K. van der Hart, G. Ersland, and M. Fernø, *Microfluidic hydrogen injection for porous media storage*. Poster presentation, Energy Norway Conference, Stavanger, Norway, 25-26 April 2022.

Lysyy, M., P.H.K. van der Hart, G. Ersland, and M. Fernø, *Pore-scale displacement and trapping mechanisms for underground hydrogen storage*. Poster presentation, 14th InterPore Annual Meeting, Abu Dhabi, UAE, 30 May-2 June 2022.

Datasets

Lysyy, M., T. Føyen, *Steady state core flood data for hydrogen- and nitrogen-water systems*. Mendeley Data, 2022. V1, http://dx.doi.org/10.17632/rfhf7wjydn.1

Lysyy, M., *Dataset from reservoir simulation of underground hydrogen storage in the Johansen formation*. Mendeley Data, 2023. V1, http://dx.doi.org/10.17632/xdydw7j3xf.1

Lysyy, M., *Dataset from seasonal hydrogen storage in the modified Norne model using Eclipse 100 Solvent simulator*. Mendeley Data, 2023. V1, http://dx.doi.org/10.17632/yxycfh8ydg.1

Contents

Introduction

Future energy systems must rely on clean and affordable energy to achieve Sustainable Development Goal 7 set by the United Nations. Hydrogen (H_2) is an energy carrier with no carbon dioxide emissions (CO_2) upon combustion, and its demand is predicted to increase by ~60% in 2030 [1]. The IEA Net Zero Emissions scenario highlights H_2 as one of the key elements in reducing CO_2 emissions, especially when electricity is not a feasible replacement for fossil fuels. H_2 is not abundantly present in the Earth, requiring large-scale production. Current production technologies are not sustainable, based on fossil fuels with associated CO_2 emissions (grey H_2), and are designed to meet H_2 demand in petroleum refining and chemical industries. To become an integral part of the global energy mix, it is imperative to upscale the use of green H_2 in transport, power generation and heating [2]. A broader integration of H_2 in the global energy markets may be facilitated in two ways. First, an oversupply of renewable electricity can be converted into H_2 through water electrolysis, which can be temporarily stored or transported directly to customers. Second, H_2 may partially or fully replace natural gas in the existing energy sectors.

The widespread scale-up of H_2 will require numerous storage alternatives to balance seasonal fluctuations in supply and demand. However, current storage technologies and volumes are insufficient to meet the growing demand for H_2. The storage of an equivalent amount of energy using H_2 scales up to four times the volume of natural gas. Surface tanks have limited storage capacity and pose safety concerns, whereas subsurface salt caverns are not widely accessible and come with high operation costs [3]. Subsurface porous formations like depleted hydrocarbon fields and aquifers have been identified as the most economically feasible media for large-scale H_2 storage. Many potential storage sites are located on land, but offshore storage in the North Sea is an appealing alternative due to the presence of existing petroleum infrastructure and the growing offshore wind industry [4]. Green H_2 can be produced onsite using excess wind power and then injected into the subsurface for temporary storage.

Subsurface H_2 storage leans on decades with experience in natural gas storage, which involves multiple cycles of gas injection and withdrawal reflecting seasonal variation

in demand. Despite operational similarities, direct knowledge transfer from natural gas storage is hampered due to low H_2 density, low viscosity and high bio-geochemical activity. H_2 storage in porous media can lead to undesired outcomes such as gravity override, viscous fingering, chemical reactions with rock minerals, and consumption by bacteria [5-7]. Moreover, hysteresis effects and various loss mechanisms can significantly impact storage efficiency [8-10]. Cyclic injections may induce strong relative permeability hysteresis [11, 12], caused by residual trapping [13] and contact angle hysteresis [14]. Residual trapping results in disconnected H_2 ganglia, one of the primary mechanisms for H_2 loss [5, 15]. However, trapped ganglia may later reconnect during subsequent H_2 injections, making it a complex process that requires scientific investigations.

Despite an exponentially growing number of scientific publications, subsurface H_2 storage in porous reservoirs is still in its infancy. The current research is mainly related to the biogeochemical reactions, the induced physical effects, and storage efficiency criteria at a particular length scale [16]. Further investigations are required to advance the understanding of H_2 interactions with other fluids and porous rocks across different length scales. This dissertation examines the physical aspects of H_2 behavior in porous media at multiple scales. Specifically, it investigates flow mechanisms, hysteresis and storage efficiency through multiscale experimental work and reservoir modeling. The findings will contribute to the development of effective H_2 storage systems, crucial for the low-carbon energy transitions.

This dissertation includes, in addition to the six scientific papers listed, four chapters structured as follows: Chapter 1 introduces the general concept of underground H_2 storage and briefly describes physical phenomena of H_2 flow in porous media. Chapter 2 summarizes the methodological approaches of this work. Chapter 3 highlights and connect the main results of the papers. Chapter 4 concludes the key findings and suggests future research directions in the field.

1 Underground hydrogen storage

Underground H_2 storage (UHS) in porous media is proposed as a technically feasible solution to meet seasonal variations in global energy systems [5]. Produced from renewable electricity, H_2 can be temporarily injected into aquifers and depleted hydrocarbon fields for later consumption (Fig. 1). At peak demand, H_2 is withdrawn back from a storage reservoir and distributed to end-customers in sectors like transport, heating and power generation. This chapter describes a general concept of gas storage in subsurface reservoirs and highlights the main factors influencing H_2 flow in porous media.
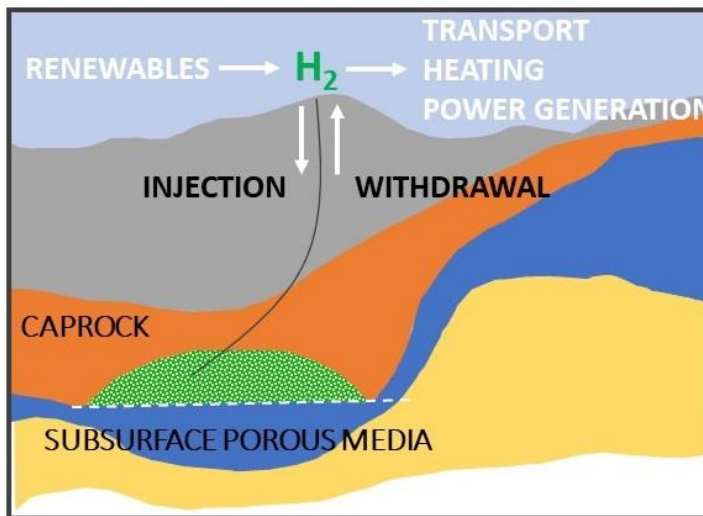
Fig. 1. Conceptual drawing of underground H_2 storage (UHS) in porous media. H_2, produced from low-carbon energy sources, is temporarily stored in porous reservoirs to meet peak demand in different industries. Modified from paper 2.

1.1 General concept

The concept of UHS is based on experience using natural gas storage sites as buffers for seasonal variation in demand. A storage reservoir is initially filled with so-called cushion gas, which serves as pressure support during cyclic gas loading. The type of cushion gas can be the same in composition as the stored gas, so-called working gas,

or be different from it, depending on gas availability, cost and storage needs. Around 50-80% of the overall injected gas must remain in a reservoir as cushion gas [17], which can be partially recovered upon storage termination. Several cushion gases have been suggested for UHS, including nitrogen (N_2), methane (CH_4), CO_2 or H_2 itself [18-20]. The use of an inappropriate cushion gas may result in undesirable outcomes, such as inadequate pressure support and extensive mixing between cushion and working gases.

Following cushion gas injection, storage facilities are typically operated on a single annual cycle, involving one injection period during summer and one withdrawal period during winter peak demand. The reservoir pressure must be sufficiently high to maintain gas deliverability, but at the same time cannot exceed its fracturing pressure. The injection and withdrawal rates are not strictly fixed and may vary depending on several parameters such as reservoir pressure, reservoir gas volume, surface facility requirements, market needs, etc. The storage efficiency can be reduced by various physical, chemical and operational losses [5].

There are about 700 underground natural gas storage sites worldwide, both in porous reservoirs and artificial nonporous salt caverns [3]. For comparison, only three storage facilities are currently in operation for UHS, utilizing salt caverns in the UK and USA. The industrial experience with UHS in porous formations is even more scarce, limited to historical records of town gas storage in aquifers [21, 22] and two recent pilot tests in depleted gas fields in Argentina [23] and Austria [24]. The pilot results demonstrated feasibility of H_2 storage, with H_2 recovery factor of up to 82% and no negative impact on infrastructure. The operating companies prefer depleted hydrocarbon fields over aquifers for UHS due to the established infrastructure and pre-existing knowledge about their structure.

Despite promising pilot results and well-established technology of natural gas storage, direct knowledge transfer to UHS is not straightforward. H_2 behavior in porous media may differ from that of CH_4 due to low density and low viscosity of H_2, coupled with its high flammability and high bio-geochemical activity [6, 7]. H_2 is nine times less dense and four times less viscous than CH_4 at 100 bar and 50 °C [25]. Microbial activity

is a significant contributor to H_2 loss in subsurface porous media [26, 27], as these environments usually accommodate a variety of microorganisms that can covert H_2 to CH_4, or to hydrogen sulfide (H_2S). Another important difference between gases is that H_2 has lower energy density per unit volume than CH_4, requiring larger storage space. Overall, the unique properties of H_2 emphasize the importance of understanding H_2 interactions in porous media, essential for establishing feasible storage technologies. This dissertation focuses on physical characteristics of H_2 in the subsurface, whereas its bio-geochemical activity is outside the scope of this work.

1.2 Physical factors influencing H_2 flow in porous media

This chapter outlines the dominant physical phenomena, which are expected to affect storage efficiency (Fig. 2). Storage reservoirs cannot use 100% of their pore space to accommodate H_2 due to critical saturations of native fluids such as water, oil and/or formation gas. Injection and withdrawal of H_2 in porous reservoirs will induce a variety of complex physical processes including trapping mechanisms, unstable displacement, gravitational effects, gas mixing and hysteresis. Microscopic trapping will occur through residual and dissolution trapping mechanisms, making H_2 physically unrecoverable. Low viscosity and low density of H_2 can promote viscous fingering and gravity override, which represents a risk of migration and leakage. The intermittent nature of H_2 injection and withdrawal can cause hysteresis effects, leading to less predictable storage cycles. Mixing between cushion and working gases can reduce the purity of withdrawn gas stream. The aforementioned factors are described in detail below.
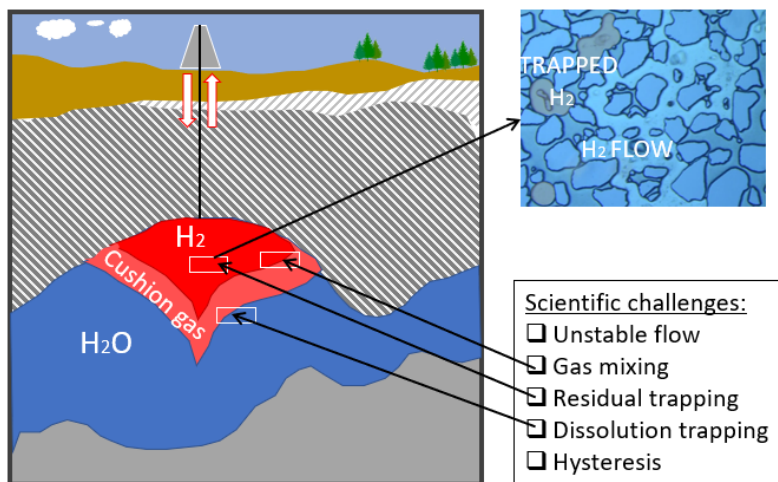
Fig. 2. Overview of scientific challenges related to physical aspects of UHS. Modified from paper 3.

1.2.1 Microscopic factors

Pore scale drainage mechanisms

Prior to H_2 injection, i.e. non-wetting phase drainage, a storage media is saturated with native fluids such as water and formation gas, which must be displaced by H_2. The concept of drainage displacement at the pore level was described by Lenormand et al., based on the interplay between capillary and viscous forces in the absence of gravitational forces [28]. When capillary forces dominate in the two-phase displacement, pore-filling direction is controlled by capillary pressure, defined as the difference between the non-wetting and wetting phase pressures. For the non-wetting phase to invade a pore, the capillary pressure must exceed the threshold pressure of the pore throats, which is inversely proportional to their radius. With a uniform pressure distribution between two fluids, the non-wetting phase invades first the pore bodies with the largest throats, following the direction of the lowest capillary resistance. The non-uniform pressure distribution emerges with the increasing influence of viscous forces, allowing the non-wetting fluid to enter smaller pore throats.

Flow regimes

The interplay between capillary and viscous forces is quantified through two dimensionless formulations: the viscosity ratio (M), i.e. ratio between viscosities of the displacing and the displaced phases, and the microscopic capillary number (N_{Ca}), defined as:

$$N_{Ca} = \frac{\text{viscous forces}}{\text{capillary forces}} = \frac{U \cdot \mu}{\sigma} \qquad (1)$$

where U is the injection velocity [m/s], μ is the viscosity of the invading phase [Pa·s] and σ is the interfacial tension between the invading and the invaded phase [N/m].

A flow diagram, based on a logarithmic plot of N_{Ca} vs M (Fig. 3), was proposed to distinguish between different pore scale flow regimes with unique flow patterns: capillary fingering, viscous fingering or stable displacement [29]. At low capillary number, the capillary fingering prevails, characterized by flow patterns propagating in all directions independent of the main flow. At high capillary number, the viscous forces become dominant, creating the narrow fingers propagating in the direction of the main flow. In a stable displacement, the flow pattern develops a flat front with some minor irregularities. The crossover zone defines a transition from capillary to viscous fingering where both forces are suppressed. The boundaries between flow regimes depend on the specific system. The extended diagram boundaries were proposed based on the displacement experiments in a homogenous hydrophilic micromodel [30].
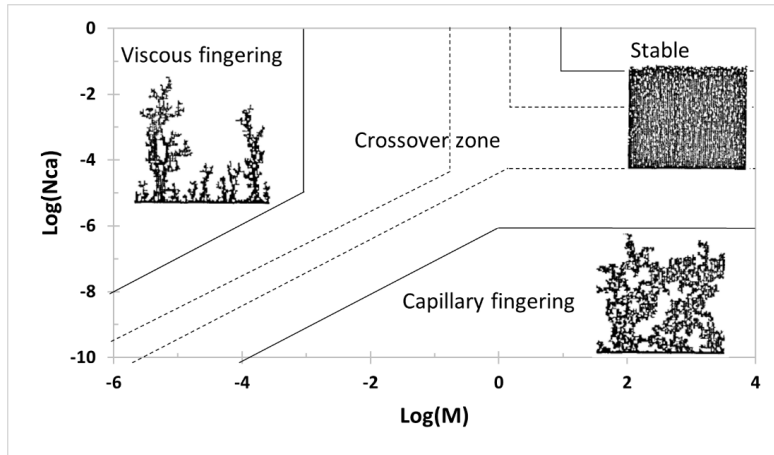
Fig. 3. A flow diagram based on a logarithmic plot of capillary number (N_{Ca}) vs viscosity ratio (M), defining different flow regimes. The solid lines define the flow boundaries and patterns, proposed by Lenormand et al. [29]. The dashed lines denote a renewed view on the flow diagram with the extended boundaries from Zhang et al. [30].

Drainage snap-off

A non-wetting phase injection normally results in well-connected flow patterns across the pore space. Under certain conditions, the displacing phase may, however, break into several non-connected ganglia (Fig. 4), caused by Roof snap-off [31]. This mechanism is triggered by destabilization of the front interface when the displacing phase enters the adjacent pore clusters. The front destabilization results from the thickening of the displaced phase in the pore throat, required to maintain capillary equilibrium. As a result, the displacing phase disconnects, leading to the formation of the trapped ganglia. In the seminal work of Roof, the conditions for snap-off during drainage were related to availability and mobility of fluids: 1) The pore throat must be surrounded by a sufficient amount of the displaced fluid, 2) the displacing fluid must be able to propagate through the pore throat for a minimum distance of seven times the throat radius. More recent studies indicated that drainage snap-off can be controlled by global dynamic parameters: capillary number, viscosity ratio and compressibility [32, 33]. In the case of UHS, the formation of disconnected H_2 ganglia represents a potential loss mechanism because these ganglia may dissolve in water during H_2 withdrawal.
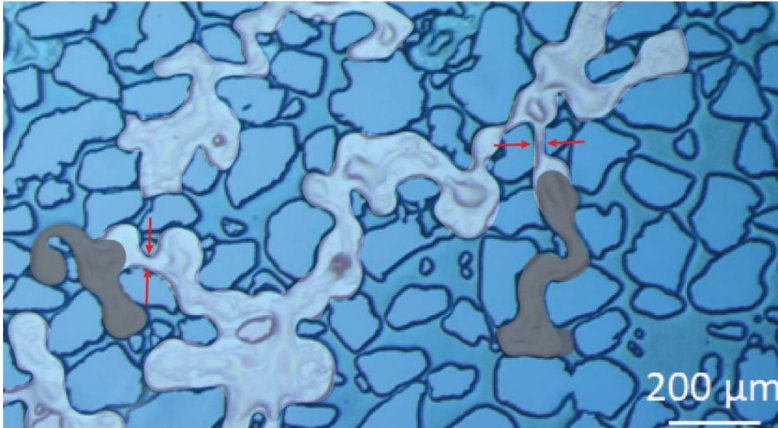
Fig. 4. Snap-off during drainage by Roof mechanism [31]. The image shows two timesteps of the Snap-off, which occurred on a millisecond scale: 1) The connected non-wetting phase (white + grey) prior to disconnection, 2) the resulting disconnected ganglia (grey) in the pore throats denoted by the red arrows. From paper 2.

Capillary desaturation theory

A traditional capillary desaturation theory states that the residual phase saturation will only be mobilized after reaching a critical capillary number. A relation between residual saturation and capillary number (Fig. 5) is described by a capillary desaturation curve (CDC), commonly used in studies of Enhanced Oil Recovery (EOR). Fig. 5 represents a theoretical CDC where constant saturation values are followed by a steeply decreasing trend after reaching a critical capillary number. Scientific studies showed that the CDC can exhibit both monotonic and non-monotonic trends [34].

The CDC concept can be adapted to UHS to estimate maximum H_2 saturation after drainage, which will represent maximum microscopic storage capacity. This will require plotting of H_2 drainage saturations (instead of apparent irreducible water saturation) as a function of capillary number. In EOR, a common measure to mobilize the residual oil is to increase capillary number by lowering the interfacial tension. This dissertation will however focus on increasing the injection velocity to achieve maximum H_2 saturation. The range of capillary number will cover typical reservoir conditions, which is expected to occur under the range of 10^{-8}-10^{-2} [35]. Caution should

be taken while using a microscopic definition of the capillary number to describe phenomena at macro scale, where the reservoir parameters such as heterogeneity, gravity and wettability become more important. Various capillary numbers have been formulated to capture macroscopic effects at the reservoir scale [34].
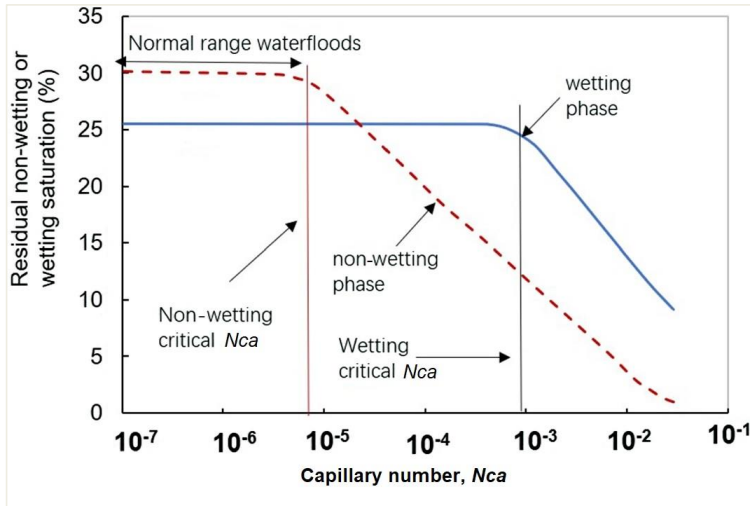
Fig. 5. Conceptual capillary desaturation curve (CDC) from Lake [36]. Image modified from Guo et al. [34].

1.2.2 Macroscopic factors
Viscous fingering

H_2 injection at the reservoir scale is prone to unstable displacement, caused by unfavourable viscosity ratio between H_2 and water. Unstable displacement, common for high injection rates, will result in the development of macroscopic viscous fingers, leading to large unswept areas. This undesired outcome can reduce storage capacity, promote H_2 dissolution in water and cause H_2 leakage if the fingers reach the reservoir outer boundaries [37]. It is suggested to mitigate viscous fingering by low injection rates while storing H_2 in steeply dipping reservoirs with high porosity and high permeability [5, 37].

Gravity override and segregation

At low injection rate, the gravitational forces control the displacement process. A large density contrast between H_2 and the displaced fluids can result in gravity override (Fig. 6), where less dense fluid accumulates preferentially at the reservoir top and denser fluid occupies the bottom. Gravity override can also influence a gas-gas displacement when using other cushion gases than H_2 due to its low density. The H_2 accumulation at the reservoir top can make it more challenging to recover from the deeper wells. On the other hand, gravity override can assist in gravitational segregation of H_2 and cushion gas, which is positive for the purity of the withdrawn gas stream. Gravity segregation is expected to emerge in the far-well area due to sufficient time for vertical separation of gases. In the absence of a shut-in period between H_2 injection and withdrawal, a dispersed gas zone can develop in the near-well area with nearly uniform vertical distribution of H_2 and cushion gas.
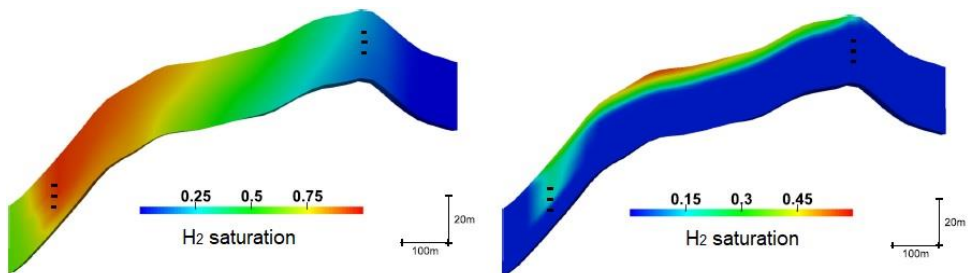
Fig. 6. Gravity override in a 2D reservoir model, occurring due to H_2 injection into a gas saturated (left) and water saturated (right) reservoir [38]. The injector is placed on the left flank of the reservoir.

Gas mixing

Gas mixing will have a vital impact on UHS in depleted gas reservoirs and/or when H_2 and cushion gas have different compositions. The mixing process will be controlled by molecular diffusion, advection and mechanical dispersion [39]. The intensity of mixing due to advection depends on the duration of injection-withdrawal cycles, where shorter cycles facilitate mixing [17]. The process of diffusive mixing occurs independently of advection and can become dominant during shut-in periods between injection and withdrawal. In mechanical dispersion, a mixing between fluids takes place when they

propagate with different velocities, caused by heterogeneities in the porous media. Mechanical dispersion is anticipated to cause a significantly greater effect on gas mixing when compared to molecular diffusion acting alone [38].

1.2.3 Pore scale loss mechanisms

Residual trapping

Various physical, bio-geochemical and operation losses can reduce storage efficiency [5]. Bio-geochemical losses are induced by chemical reactions between H_2 and rock minerals and bacterial consumption, whereas operation losses include material losses due to leakage and energy losses due to the friction in the well. This chapter highlights physical losses only, namely pore scale trapping mechanisms which are expected to occur during H_2 withdrawal, i.e. wetting phase imbibition. Residual and dissolution trapping are two main microscopic mechanisms, responsible for pore scale H_2 entrapment. When water displaces H_2, some fraction of continuous H_2 phase is disconnected, rendering H_2 immobile in the form of residually trapped ganglia. Residual trapping occurs in a reservoir where water is available and mobile, i.e. the transition zone between H_2 and water. Recent studies have quantified the residual saturation of H_2 in sandstones [40-43].

There are four displacement mechanisms that classic pore scale displacement theory identifies as dominant during imbibition [28]: piston-like, snap-off, I1 imbibition, and I2 imbibition (Fig. 7). Piston-like mechanism involves a stable displacement front between the propagating fluids in a pore channel. Snap-off is a phenomenon in which the non-wetting phase disconnects to form small droplets due to the pinching at the pore walls. The I1 and I2 imbibition mechanisms occur due to the curvature destabilization, caused by its detachment from the pore walls. Both mechanisms vary in terms of the final location of the non-wetting phase, which can be displaced either into one pore (I1) or several pores neighbouring pores (I2). The outcome of this displacement largely depends on the structure of the pore network and can result in residual trapping.
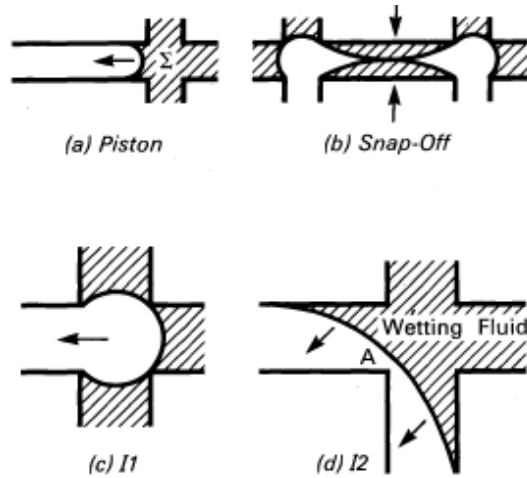
Fig. 7. Displacement mechanisms during imbibition, which can result in residual trapping of the non-wetting phase [44].

Dissolution trapping

The residually trapped H_2 ganglia can dissolve in water, governed by H_2 solubility and diffusivity. When water is mobile, dissolution is controlled by the solubility and advection, whereas diffusivity comes into play when water becomes immobile. Under storage conditions, H_2 solubility increases with increasing pressure and decrease with increasing salinity [45]. H_2 is approximately one order of magnitude more soluble in pure hydrocarbons than in brines, suggesting a more pronounced H_2 dissolution in depleted oil reservoirs than in aquifers [46]. The importance of H_2 dissolution has been reported by two previous UHS studies [41, 47].

At the pore level, the dissolution of the non-wetting phase can occur by three main mechanisms [48, 49]: dissolution from one end of the bubble, dissolution from two ends of the bubble, and dissolution while in displacement. In a one-end dissolution, the bubble dissolves from one end in the direction of the water flow; the two-end dissolution takes place at both sides of the bubble simultaneously. The displacement dissolution mechanism involves the mobilization of small bubbles which enter narrow pore throats. In porous systems, non-equilibrium dissolution can take place, that is when dissolved concentration of the non-wetting phase is less than predicted from

solubility measurements. This phenomenon was reported for CO_2 storage, attributed to small CO_2-water interface area and their non-uniform distribution [14, 50, 51]. At low injection rates and in the absence of strong heterogeneity, the dissolution will eventually approach equilibrium at the reservoir scale.

1.2.4 Hysteresis

Hysteresis can be defined as the dependence of a state of a system on its history. In porous media flow, hysteresis reflects the differences between drainage and imbibition in contact angles and flow functions, i.e. capillary pressure and relative permeability. The contact angle hysteresis originates from the differences between water receding (drainage) and water advancing (imbibition) contact angles, caused by surface roughness or chemical heterogeneities [52]. The hysteresis in flow functions arises from the differences in the flow paths due to the entrapment of the displaced phase. During drainage, the displaced wetting phase remains connected along the grain surfaces after its entrapment, facilitating the flow of the displacing non-wetting phase through the pore centre. During imbibition, the entrapment of the non-wetting phase takes place in the pore centre in the form of disconnected ganglia, acting as barrier for the flow of both wetting and non-wetting phases.

Relative permeability hysteresis is expected to play a vital role in UHS due to cyclic loading of H_2. The studies of different gas-water systems agreed that the hysteresis in the non-wetting phase is pronounced due to residual gas trapping, leading to lower imbibition relative permeability compared to drainage [13, 14, 53-55]. However, there are inconsistencies regarding the hysteresis in the wetting phase. It was shown that the relative permeability to the wetting phase was higher for imbibition, attributed to contact angle hysteresis [14, 53, 54]. Other studies did not report any hysteresis in the wetting phase relative permeability, likely because drainage and imbibition processes are reproducible in strongly hydrophilic systems [13, 55]. In the case of UHS, both H_2 and water relative permeabilities demonstrated hysteresis [11, 12], implying that this effect should be accounted for in reservoir modelling for more reliable predictions of the storage performance. Reservoir simulation studies pointed out that neglection of hysteresis will overestimate the H_2 recovery factor [8-10].

The Killough hysteresis model is one of the available formulations to describe relative permeability hysteresis [56]. This model introduces so-called scanning curves, enclosed between the drainage and imbibition curves to model the transition between them (Fig. 8). The scanning curves are reversible, meaning that they are identical for both drainage and imbibition when the injection process is reversed at any point on the curve. In addition to the actual relative permeability curves, the Land trapping model [57] is needed to calculate the scanning curves of the non-wetting phase. For the wetting phase, it is also necessary to include a free input parameter. When the actual relative permeabilities are not available, the scanning curves can be computed based on a parametric interpolation method.
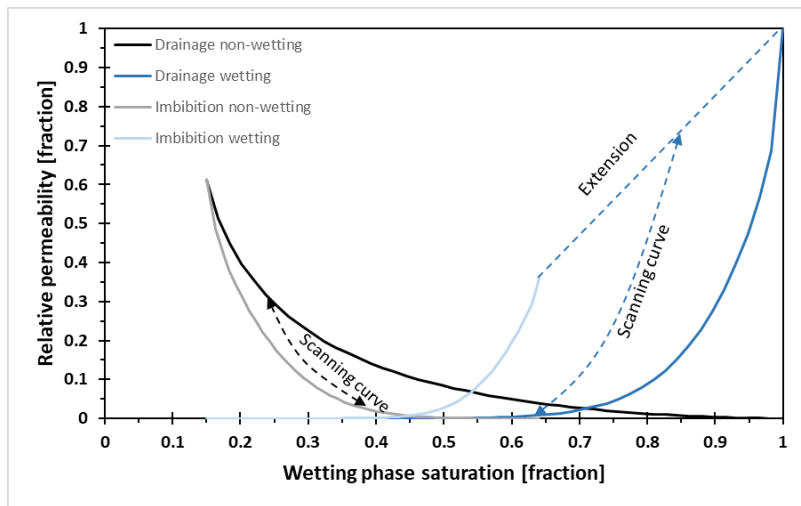

Fig. 8. Killough hysteresis model [56] of drainage and imbibition relative permeability curves. The dashed, curved arrows denote representative scanning curves at arbitrary points. Modified from paper 6.

2 Methodological summary

This dissertation represents a combined experimental and numerical approach across multiple length scales (Fig. 9). Pore scale mechanisms were examined using microfluidics (papers 1-3), which is a suitable tool to describe qualitative phenomena. The micromodel was based on 36 repetitions of the pore patterns with realistic geometry and topological features of an actual sandstone. Two experimental setups were used to observe different micromodel areas. One of the setups used the full area to gather quantitative results (paper 1), whereas the other covered about 1% of the total area (papers 2-3), referred as a field of view (FoV). The extrapolation of quantitative results to natural environments requires caution, and core scale measurements are better suited for this purpose.
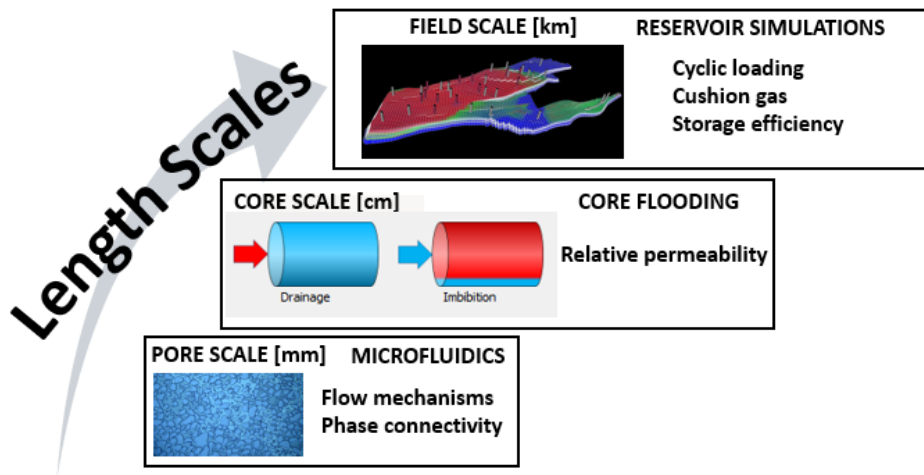
Fig. 9. Methodological approaches used in this dissertation: 1) Pore scale studies using microfluidics, 2) core flooding for relative permeability measurements and 3) reservoir simulations.

Steady state relative permeability measurements were performed in a Berea sandstone core, supported with X-ray monitoring and numerical history matching (paper 4). The resulting drainage and imbibition relative permeabilities were implemented in a reservoir model of an aquifer, using the commercial Eclipse E100 black oil simulator (paper 6). The Solvent option of this simulator, allowing to introduce H_2 as the second

gas component, was used to model the storage performance in a depleted hydrocarbon field (paper 5). Reservoir simulation is a valuable tool for predicting storage efficiency under different management strategies. The black oil models were preferred over the compositional one because of the absence of major compositional changes in the modelling process and their computational efficiency.

3   Results and discussion

This chapter summarizes key findings from a multiscale research project, based on pore scale experiments using microfluidics (papers 1-3), relative permeability measurements (paper 4) and reservoir modelling (papers 5-6). One cycle of pore scale H_2 injection and withdrawal are outlined in chapters 3.1 and 3.2, respectively, with focus on H_2 saturation, its connectivity and trapping mechanisms. To reproduce a more realistic scenario of cyclic H_2 storage, multiple cycles of H_2 injection and withdrawal are covered in chapter 3.3. Core scale H_2-H_2O relative permeability data are described in chapter 3.4, measured during drainage and imbibition and supported with numerical history matching. Chapter 3.5 discusses the impact of cushion gas and hysteresis on H_2 recovery using reservoir scale cyclic injections. Chapter 3.6 connects the separate papers by discussing their field scale implications.

3.1   Hydrogen injection

Gas injection is an initial stage of any underground gas storage project, affected by past reservoir history and interactions with native rock and reservoir fluids. The involved pore scale mechanisms are best described through visualization techniques like microfluidics, providing a direct observation of the pore space. This chapter describes microfluidic H_2 drainage experiments from paper 1, performed at 30 °C under the pressure of 30 and 100 bar. The following phenomena are covered: microscopic storage capacity (chapter 3.1.1), H_2 connectivity in the pore space (chapter 3.1.2), and comparison with other gases (chapter 3.1.3). The experimental data were extracted from the full micromodel area.

3.1.1   Microscopic storage capacity

The H_2 injection resulted in an immediate filling of the pore space, dominated by capillary fingering with forward and transverse H_2 fingers bypassing large pore clusters (Fig. 10). After H_2 break-through at the micromodel outlet, the H_2 flow propagated through the preferential displacement paths without entering the bypassed pore clusters. Capillary fingering was additionally confirmed by a fractal dimension

analysis, explained in detail in paper 1. The H_2 saturation (S_{gi}) after drainage (Fig. 11) followed a monotonically increasing trend in accordance with classic capillary desaturation curve (CDC). Moreover, the S_{gi} seemed to be independent of pressure, likely due to minor differences in viscosity (1% increase) and interfacial tension (2% decrease) from 30 to 100 bar. After reaching a critical value of capillary number (N_{Ca}) $> 7 \cdot 10^{-7}$, the S_{gi} flattened out with the values between 0.35 and 0.39, representing maximum microscopic H_2 storage capacity. The maximum S_{gi} values were comparable with the literature values of 0.36 – 0.48 derived from core flooding experiments under the N_{Ca} range of $10^{-9} – 10^{-8}$ [41, 43, 58].

$N_{Ca} = 7.1 \cdot 10^{-9}, S_{gi} = 0.08$ $N_{Ca} = 7.1 \cdot 10^{-8}, S_{gi} = 0.19$ $N_{Ca} = 3.6 \cdot 10^{-7}, S_{gi} = 0.38$

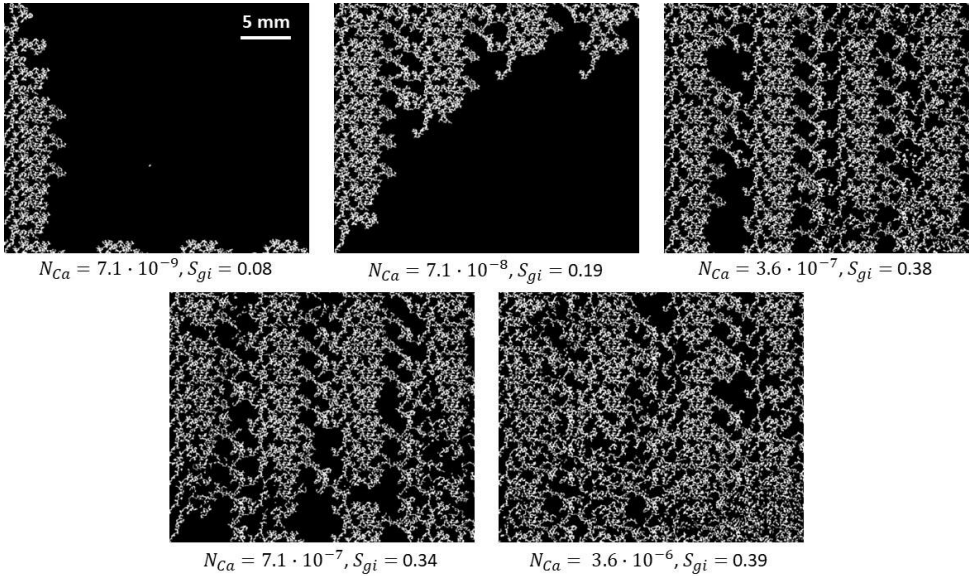$N_{Ca} = 7.1 \cdot 10^{-7}, S_{gi} = 0.34$ $N_{Ca} = 3.6 \cdot 10^{-6}, S_{gi} = 0.39$

Fig. 10. H_2 flow patterns (white) and corresponding saturation (S_{gi}) in the pore space after drainage under five capillary numbers (N_{Ca}) at 30 bar. The capillary dominated H_2 flow propagated through the preferential paths without entering the neighboring pore clusters after H_2 reached the outlet. Modified from paper 1.
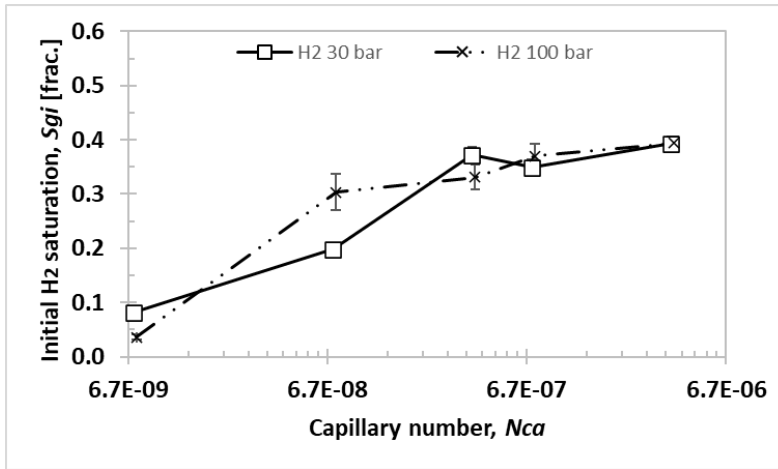
Fig. 11. Initial H_2 saturation after drainage (S_{gi}) at 30 and 100 bar. The S_{gi} increased monotonically until a critical N_{Ca} of ~ $7 \cdot 10^{-7}$, followed by a nearly flat trend. The maximum S_{gi} ranged between 0.35 and 0.39, representing maximum microscopic storage capacity of the pore space. No clear pressure impact on the S_{gi} was observed. The H_2 distribution in the pore space at 30 bar is shown in Fig. 10. Modified from paper 1.

3.1.2 Hydrogen connectivity across the pore space

The H_2 connectivity across the pore space is important for assessment of the effective storage capacity, which can be attenuated by the H_2 disconnection events. The H_2 disconnection was evident at higher N_{Ca} ($> 10^{-7}$) due to Roof snap-off [31], resulting in several disconnected H_2 ganglia (Fig. 12). The snap-off was attributed to water availability and mobility as well as N_{Ca}. The percentage of disconnected H_2 in the total saturation ranged between 12% and 25% (Fig. 14). The H_2 ganglia were larger than the average pore size and ranged between ~ 10^8 and 10^9 μm^3, consistent with the literature [41, 43, 58]. The H_2 disconnection represents a potential loss mechanism because the resulting ganglia may remain disconnected and/or dissolve during imbibition. It is therefore necessary to choose an optimal injection rate, yielding the maximum storage capacity but with the lowest risk of H_2 disconnection. Based on the microfluidic experiments, the optimal N_{Ca} was in the order of 10^{-7}, equivalent to the experimental injection velocity of ~ 70 m/day.
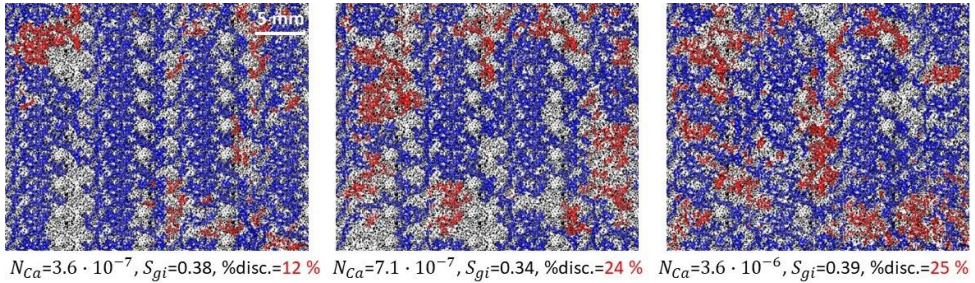
$N_{Ca}=3.6 \cdot 10^{-7}, S_{gi}=0.38, \%disc.=12\%$ $N_{Ca}=7.1 \cdot 10^{-7}, S_{gi}=0.34, \%disc.=24\%$ $N_{Ca}=3.6 \cdot 10^{-6}, S_{gi}=0.39, \%disc.=25\%$

Fig. 12. H_2 connectivity in the pore space after drainage at 30 bar: disconnected H_2 ganglia (red), connected H_2 phase (blue), water (white) and the rock grains (black). Roof snap-off occurred at higher N_{Ca} (> 10^{-7}), forming several clusters of disconnected H_2 ganglia. The percentage of disconnected H_2 ganglia ranged between 12% and 25% of the total H_2 saturation. Modified from paper 1.

3.1.3 Impact of gas type

Several decades of commercial experience with underground natural gas storage raises a question whether the knowledge transfer to UHS is technically feasible. A comparison with other gases is therefore essential for the knowledge transfer. The H_2 drainage experiments were repeated with pure CH_4, mixture of 50 mol% H_2 – 50 mol%, pure CH_4 and pure N_2. It was found that the maximum gas saturations were similar for all gases, within the range of 0.39 - 0.46 (Fig. 13). However, the gas saturations differed at lower N_{Ca} (< 10^{-7}), which increased with increasing gas viscosity as follows: pure H_2 with the lowest saturation, followed by a 50% H_2 - 50% CH_4 mixture, then pure CH_4, and finally N_2. In addition, the gas connectivity was affected by the gas type, where N_2 showed the highest amount of disconnected gas ganglia equal to 39 % - 76 % of the total gas saturation (Fig. 14). Overall, the results imply that a substitute laboratory gas for H_2 may be used at higher N_{Ca} (> 10^{-7}) only, where the gas saturations become similar. Moreover, CH_4 appears to be a more effective cushion gas due to its better connectivity compared to N_2. This will minimize cushion gas loss due to dissolution, ensuring better control of the reservoir pressure.
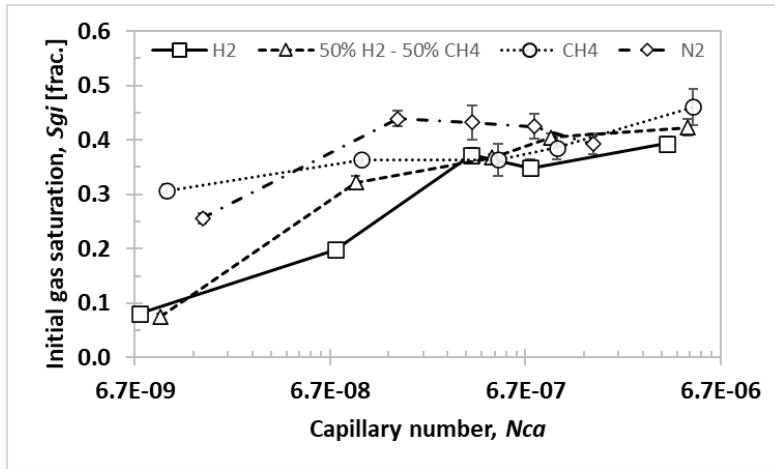
Fig. 13. Impact of gas type on the initial saturation (S_{gi}) after drainage at 30 bar. At lower N_{Ca} ($< 10^{-7}$), the S_{gi} increased with the increasing gas viscosity as follows: first H_2, followed by a 50% H_2 - 50% CH_4 mixture, then CH_4, and finally N_2. At higher N_{Ca} ($> 10^{-7}$), the difference between gases minimized yielding similar maximum S_{gi} values in the range of 0.39-0.46. Modified from paper 1.
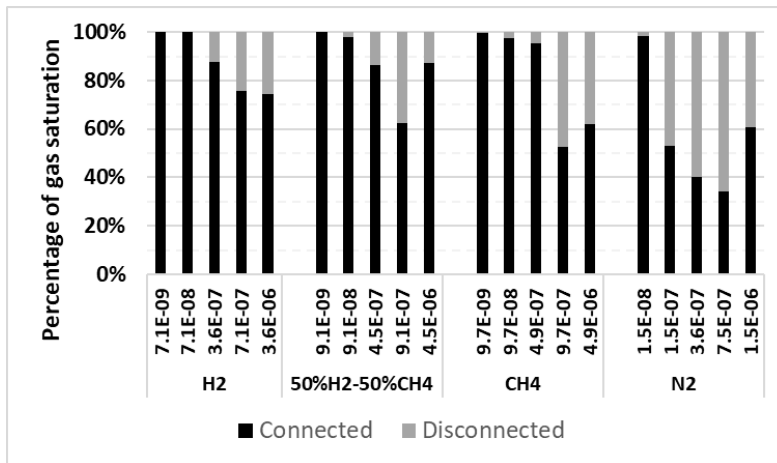
Fig. 14. Impact of gas type on the gas connectivity in the pore space after drainage at 30 bar. The H_2 connectivity was relatively high with less than 25% disconnected ganglia of the total H_2 saturation at higher N_{Ca} ($> 10^{-7}$). In contrast, the percentage of disconnected N_2 ganglia ranged between 39% and 76%. From paper 1.

3.2 Hydrogen withdrawal

The injected H_2 during drainage is withdrawn from a reservoir to meet high demand. In microfluidics this is achieved through imbibition experiments, where water is injected to displace H_2 from the pore space. During displacement some portion of H_2 is lost in the pore space due to several trapping mechanisms. This chapter describes microfluidic imbibition injections from paper 2, as part of one-cycle experiments at 5 bar and ambient temperature. The following phenomena are emphasized: the H_2 displacement and residual trapping mechanisms (chapter 3.2.1), dissolution trapping (chapter 3.2.2), and contact angle measurements (chapter 3.2.3). Contrary to paper 1 (chapter 3.1), the experimental data were extracted from a limited micromodel area equivalent to ~1% of the total area, referred as the field of view (FoV).

3.2.1 Displacement and residual trapping mechanisms

The imbibition experiments were performed under the N_{Ca} range of $7.7 \cdot 10^{-7} - 3.8 \cdot 10^{-4}$ and involved two main stages: H_2 displacement and trapping. The H_2 displacement was predominantly controlled by I1 imbibition (Fig. 15a), where H_2 was displaced from several neighbouring pores to one pore. The less common displacement mechanisms included piston-like displacement and redistribution. The piston-like displacement occurred at low N_{Ca} (= $7.7 \cdot 10^{-7}$), characterized by a stable displacement front within an individual pore channel. The H_2 redistribution was common at higher N_{Ca} ($\geq 7.7 \cdot 10^{-5}$) where H_2 was first displaced by water, followed by a reconnection with H_2 which redistributed from other pore clusters. After being displaced from the pore centre to the pore wall, H_2 was disconnected and residually trapped by I2 imbibition mechanism (Fig. 15b). In some cases ($N_{Ca} \geq 7.7 \cdot 10^{-5}$), the trapping by bypass mechanism was observed where water was not able to displace H_2 from the large pore clusters with narrow pore throats.

(a) I1 displacement   (b) Trapping by I2 displacement
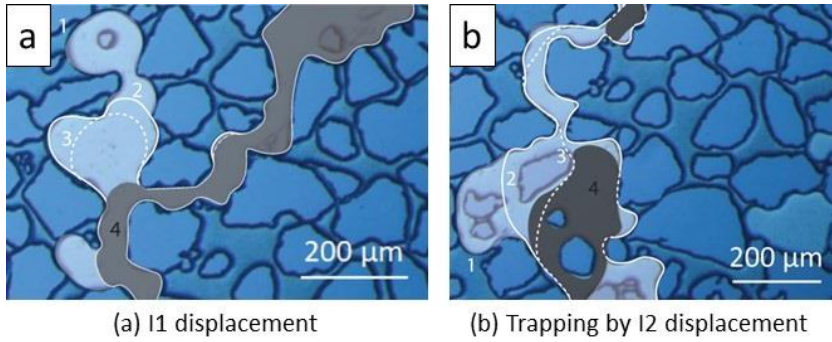
Fig. 15. Two dominant displacement and trapping mechanisms of H_2 (white and grey): I1 imbibition and I2 imbibition, respectively. Colors and outlines indicate the time intervals of displacement (1-4). (a) I1 imbibition involved H_2 displacement from several neighboring pores ($t_{1,2,3}$; white) to one pore (t_4; grey, $\Delta t_{4\text{-}1} = 1$ s). (b) I2 imbibition occurred when H_2 was displaced to the pore wall (t_3; dashed outline) where H_2 was disconnected and residually trapped (t_4; grey, $\Delta t_{4\text{-}1} = 1.3$ s). Modified from paper 2.

3.2.2 Dissolution trapping

Following the entrapment of H_2, water was continuously injected to the micromodel, promoting the dissolution of the residually trapped H_2 ganglia. Three dissolution mechanisms were identified controlled by waterfront direction and rate: one-end dissolution, two-end dissolution, and displacement dissolution (Fig. 16). The one-end dissolution was common at higher N_{Ca} ($\geq 7.7 \cdot 10^{-5}$), characterized by dissolution from one end of the ganglia in the direction of waterfront. The two-end dissolution mechanism was observed at lower N_{Ca} ($= 7.7 \cdot 10^{-6}$), where the H_2 ganglia dissolved from all sides. The displacement dissolution mechanism occurred at higher N_{Ca} ($\geq 7.7 \cdot 10^{-5}$), where smaller H_2 ganglia mobilized and entered the narrow pore throats while gradually dissolving.

(a) One-end dissolution;
$N_{Ca} = 3.8 \cdot 10^{-4}$

(b) Two-end dissolution;
$N_{Ca} = 7.7 \cdot 10^{-6}$

(c) Displacement dissolution;
$N_{Ca} = 7.7 \cdot 10^{-5}$
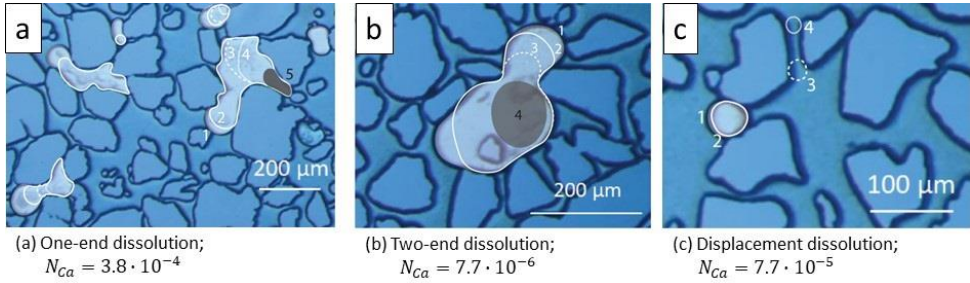
Fig. 16. H_2 (white and grey) dissolution mechanisms. Colors and outlines indicate the time intervals of dissolution (1-5). (a) One-end dissolution where H_2 dissolved from one side of the ganglia ($\Delta t_{5-1} = 22$ s). (b) In two-end dissolution, H_2 dissolved across all sides of the ganglia ($\Delta t_{4-1} = 134$ s). (c) Displacement dissolution involved dissolution of the ganglia while displacement through the pore throats ($\Delta t_{4-1} = 5$ s). Modified from paper 2.

The dissolved H_2 concentration was quantified as the average dissolved H_2 amount per the injected water mass. The dissolved H_2 amount was calculated based on the H_2 saturation decrease during dissolution, assuming that the H_2 depletion was governed by dissolution and water advection, while neglecting the diffusion. The average dissolved H_2 concentration ranged between 6.4×10^{-4} and 1.1×10^{-3} mol/kg, equivalent to 16% and 28% of the reported H_2 solubility data [45]. The fact that the dissolved H_2 concentration was lower the reported H_2 solubility (Fig. 17) indicated that dissolution occurred under the non-equilibrium regime, consistent with the studies of CO_2 dissolution [50, 51]. The non-equilibrium dissolution of H_2 was also reported for pressures of 1 and 30 bars, gathered from the same experimental setup [59].

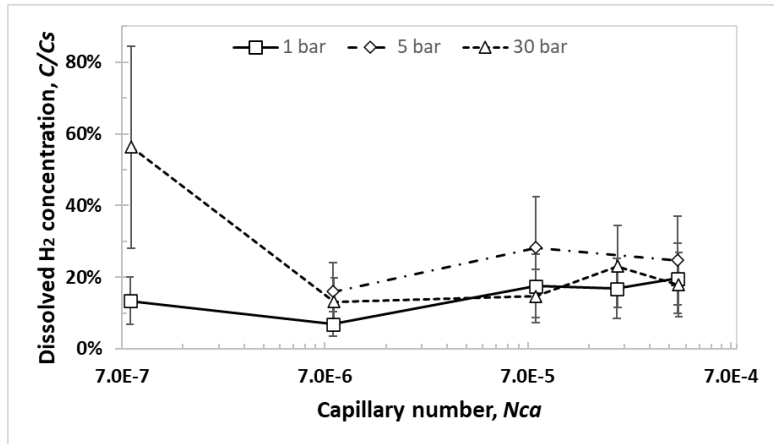**Fig. 17**. Dissolved H_2 concentration (C, mol/kg) relative to the literature H_2 solubility data (C_s, mol/kg [45]). At 5 bars, the average dissolved H_2 concentration corresponded to 16% and 28% of the reported literature solubility, indicating non-equilibrium dissolution. Similar dissolution trends were observed for the data from the same experimental setup at 1 and 30 bars [59]. Dataset from paper 2.

3.2.3 Contact angle hysteresis

The receding and advancing contact angles were measured during H_2 injection and withdrawal, respectively (Fig. 18). The receding angles ranged between 21° and 24° which were lower than the advancing angles of 39°-47°, as expected from a classic theory [60]. The measured contact angles were consistent with the literature values reported for H_2, demonstrating strong hydrophilic preference [61-64]. The difference between the receding and advancing contact angles indicated that the H_2 injection and withdrawal are hysteretic processes. The contact angles are one of the input parameters for pore scale modelling, aimed at estimating the capillary pressure and relative permeability functions [65]. The contact angle hysteresis may result in hysteretic capillary pressure and relative permeability functions, and this will be discussed in chapter 3.4. On the other hand, the observed hysteresis from one cycle of H_2 injection and withdrawal raises the question whether the hysteretic effects will intensify with the increasing number of injection-withdrawal cycles.
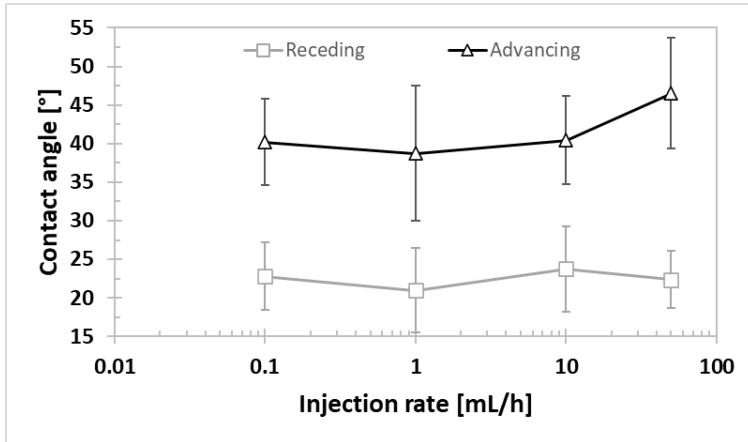
Fig. 18. Average receding and advancing contact angles, measured during H_2 drainage and imbibition, respectively. The contact angle hysteresis was evident, where the advancing contact angles (39°-47°) were higher than the receding (21-24°). Modified from paper 2.

3.3 Hydrogen reconnection and trapping during cyclic injections

The fundamental pore scale mechanisms were examined through one cycle of injection and withdrawal in chapters 3.1 and 3.2. The commercial underground storage involves numerous cycles of injection and withdrawal that may induce the hysteretic effects influencing the H_2 distribution and residual trapping. This chapter summarizes the microfluidic experiments from paper 3 examining the five cycles of H_2 injection and withdrawal at 40 bar and ambient temperature. Chapter 3.3.1 describes cyclic variations in the pore space H_2 distribution and reconnection of the residually trapped H_2. Chapter 3.3.2 quantifies the initial and residual H_2 saturations over the injection cycles. The experimental data were extracted from the micromodel field of view (FoV).

3.3.1 Reconnection mechanisms

The H_2 distribution within the pore space showed hysteresis across the injection cycles (Fig. 19). The initial H_2 distribution after drainage was mainly spread over the large, connected pore clusters (blue + purple). The residual H_2 ganglia predominantly resided in the same pores as the initial distribution (purple), with minor observations of ganglia

redistribution to the adjacent pore clusters (red). The residually trapped ganglia could either connect with the newly injected H_2 in the subsequent drainage cycle or remain disconnected, described below.

(a) Cycle 1: $S_{gi} = 0.42$ and $S_{gr} = 0.32$ (b) Cycle 2: $S_{gi} = 0.60$ and $S_{gr} = 0.31$ (c) Cycle 3: $S_{gi} = 0.67$ and $S_{gr} = 0.28$

(d) Cycle 4: $S_{gi} = 0.53$ and $S_{gr} = 0.32$ (e) Cycle 5: $S_{gi} = 0.60$ and $S_{gr} = 0.34$
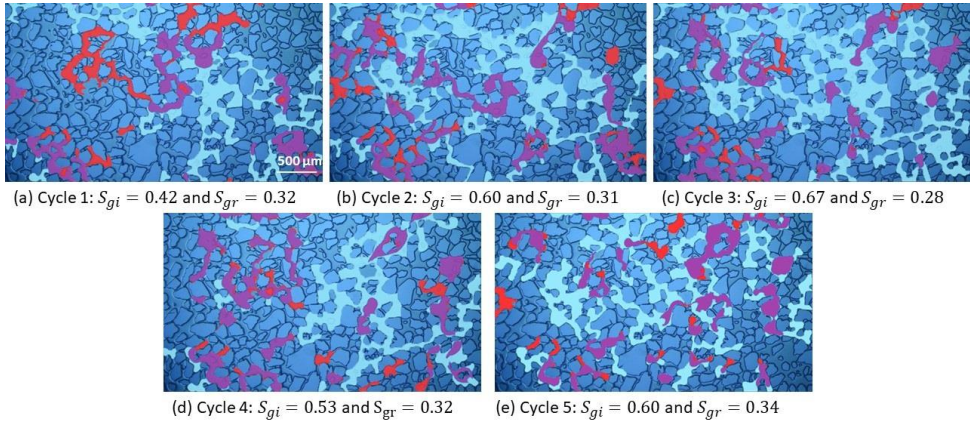
Fig. 19. Combined images of the initial, S_{gi} (blue + purple), and residual, S_{gr} (red + purple) H_2 saturations during five cycles of drainage and imbibition at 5 mL/h. The purple color highlights the intersection area of the H_2-filed pore space after drainage and after imbibition. The residual H_2 ganglia remained mainly in the same pore clusters as the initial H_2 distribution (purple), but redistribution to neighbouring pores was also observed (red). The distribution of the residual H_2 ganglia showed hysteresis over the injection cycles, characterized by changing H_2 distribution in the pore space despite similar S_{gr} values in the range of ~ 0.30. From paper 3.

The reconnection of residual H_2 ganglia seemed to be governed by the pore cluster geometry (Fig. 20). This process was favoured in the proximity to pore clusters with wide pore throats, while being hindered by narrow pore throats. The saturations of disconnected H_2 were compared between imbibition and the next drainage cycle (Fig. 21). The disconnected H_2 saturation after imbibition decreased in 9 out of 12 subsequent drainage cycles, and on average 56% of the disconnected H_2 is reconnected. A high reconnection ability is beneficial for the underground storage, minimizing the risk of H_2 loss due to residual trapping.

(a) 2.5 mL/h: Disconnected $S_{gr}(dis)$ = 0.31 and $S_{gi}(dis)$ = 0.22   (b) 5 mL/h: Disconnected $S_{gr}(dis)$ = 0.27 and $S_{gi}(dis)$ = 0.06
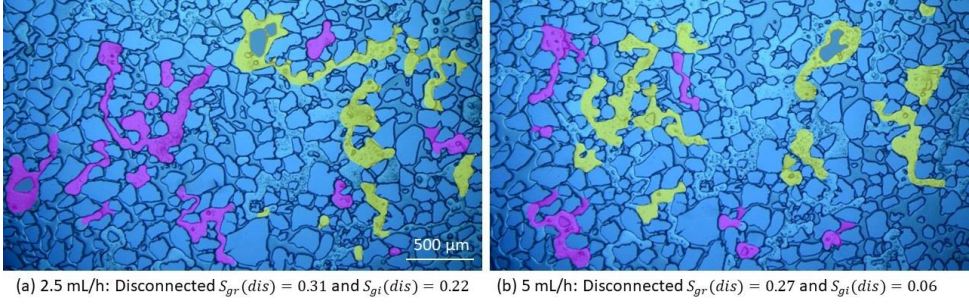
Fig. 20. Reconnection of residually trapped H_2 after imbibition, S_{gr} *(dis)* (yellow + purple) with the newly injected H_2 in a subsequent drainage cycle (light blue): (a) From cycle 3 to 4 at 2.5 mL/h, and (b) from cycle 4 to 5 at 5 mL/h. A fraction of the previously disconnected ganglia reconnected with the newly injected H_2 (yellow), whereas the remaining fraction remained disconnected, S_{gi} *(dis)* (purple). H_2 reconnection prevailed near pore clusters with wide pore throats. Quantification of the disconnected H_2 saturations is shown in Fig. 21. From paper 3.
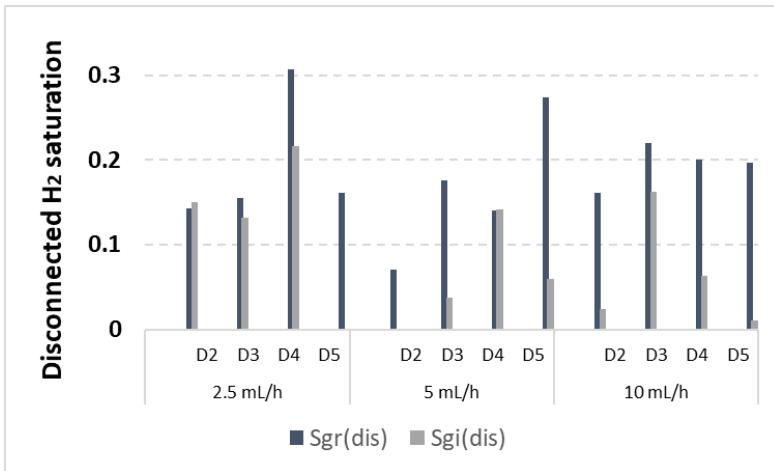
Fig. 21. Comparison between disconnected H_2 saturation after imbibition, S_{gr} *(dis)* (blue) and after subsequent drainage cycle, S_{gi} *(dis)* (gray). For all cycles in the experiments at 2.5, 5 and 10 mL/h, two disconnected saturations resulting from sequent imbibition-drainage injections are grouped on the horizontal axis. The transition from imbibition in cycle 1 to drainage in cycle 2 is defined as D2. A high reconnection ability of H_2 ganglia was observed, characterized by a decreased S_{gi} *(dis)* compared to S_{gr} *(dis)* in the previous imbibition cycle. From paper 3.

3.3.2 Residual trapping

The initial (S_{gi}) and residual (S_{gr}) H$_2$ saturations were quantified in the micromodel field of view (FoV) for all cycles in the experiments performed at four injection rates in the range of 1-10 mL/h (Fig. 22). The average S_{gi} from each experiment depended on the injection rate. The lowest injection rate (1 mL/h) resulted in the lowest S_{gi} of 0.03-0.14, with an increase to 0.27-0.73 at higher injection rates ($\geq$ 2.5 mL/h). The S_{gi} fluctuated between the cycles due to the H$_2$ redistribution from outside the FoV. Conversely, the S_{gr} values were more reproducible between the cycles, equal to $\sim$ 0.4 at 2.5 mL/h and $\sim$ 0.3 at 5-10 mL/h. This phenomenon was attributed to hydrophilic micromodel surfaces: water injection is facilitated through the wetting water films around the grain surfaces, resulting in the well-defined water injection patterns. It should be emphasized that maximum S_{gi}, observed in the micromodel FoV at high injection rates, were higher than estimated from the full micromodel area (maximum S_{gi} of 0.39 from chapter 3.1.3). This implies that the FoV saturations should not be extrapolated to the full micromodel at high injection rates (Fig. S1).
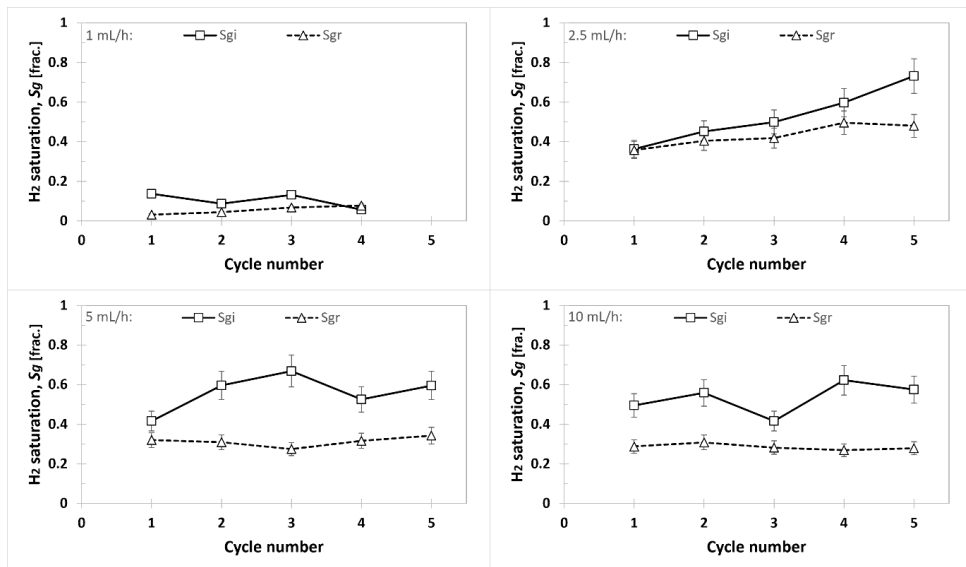

Fig. 22. Initial *(S$_{gi}$)* and residual *(S$_{gr}$)* H$_2$ saturation during cyclic injections at the experimental injection rate of: (a) 1 mL/h, (b) 2.5 mL/h, (c) 5 mL/h, and (d) 10 mL/h. The average *S$_{gi}$*, calculated for all cycles in each experiment, was the lowest (~0.10) at the injection rate of 1 mL/h. Fluctuations in the *S$_{gi}$* were

observed between the cycles, caused by H_2 redistribution from outside the FoV. In contrast, the S_{gr} demonstrated improved reproducibility, maintaining nearly constant values between the cycles. Modified from paper 3.

3.4 Hydrogen relative permeability

Data collection across different length scales is essential for enhancing the multiscale understanding of H_2 flow dynamics. Although the microfluidic experiments from chapters 3.1-3.2 provided the insight into the pore scale behaviour, the quantitative results are not directly applicable to reservoir scale models due to the influence of gravity and pore space heterogeneity. Core scale experiments are more conventional technique to acquire the quantitative data needed for input to reservoir models. In particular, relative permeability is one of the crucial functions defining the H_2 multiphase flow. This chapter reports the steady state H_2-H_2O relative permeability measurements from paper 4, performed during drainage and imbibition at 30 bar and 30 °C. Chapter 3.4.1 discusses the hysteresis between drainage and imbibition relative permeability, whereas chapter 3.4.2 compares the drainage H_2 and N_2 relative permeability curves.

3.4.1 Impact of hysteresis

The drainage experiment resulted in a high endpoint water saturation of $S_w = 0.59$, with a corresponding H_2 relative permeability of $K_{rg} = 0.04$ (Fig. 23). An irreducible water saturation (S_{wirr}) was not achieved, and porous plate capillary measurements were therefore required to find S_{wirr} (= 0.15). The next step was to measure the imbibition relative permeability, resulting in an endpoint H_2O relative permeability of $K_{rw} = 0.36$ at $S_w = 0.64$. Both drainage and imbibition experiments were history matched based on the LET correlation [66, 67] and experimental differential pressure, production and saturation data, using commercial core-scale simulator Sendra [68]. A reasonable match between the experimental and simulated data was achieved for the drainage experiment, whereas the match quality was reduced in the imbibition experiment. The experimental relative permeability assumes homogenous rock properties and zero capillary pressure, contrary to the simulated data with more realistic capillary pressure

gradients. Therefore, the simulated relative permeability better represents reservoir flow and should be used as input in numerical reservoir models.

The resulting relative permeabilities showed strong hysteresis, with lower imbibition K_{rg} and higher imbibition K_{rw}, both compared to drainage. The relative permeability hysteresis in the non-wetting phase (H_2) is attributed to residual trapping, whereas the wetting (H_2O) phase hysteresis arises from contact angle hysteresis [14, 54, 69]. It should be noted that nonhysteretic H_2O relative permeability can be found in literature, explained by reproducibility of injection cycles in hydrophilic core samples [13, 55]. The observed differences between the drainage and imbibition H_2-H_2O relative permeabilities imply that hysteresis should be included in reservoir modelling of porous media H_2 storage. This will ensure more reliable predictions of the storage efficiency and will be discussed in chapter 3.5.4. The H_2-H_2O system showed strong hydrophilic preference, reflected by a high cross-point value of $S_w = 0.71$ with the corresponding $K_{rg} = K_{rw} = 0.025$. The hysteretic and hydrophilic nature of the H_2-H_2O relative permeability corroborate the microfluidic contact angles measurements reported in chapter 3.2.3. A comparison with available H_2-H_2O relative permeability data can be found elsewhere [12].
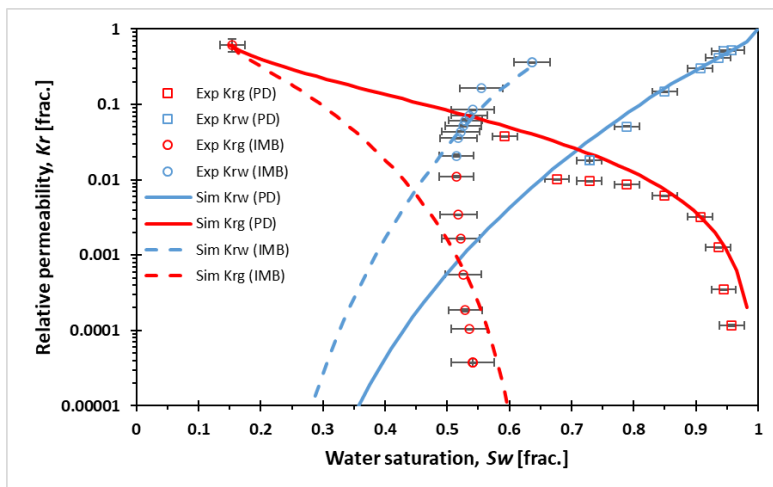

Fig. 23. Primary drainage (PD) and imbibition (IMB) H_2 (K_{rg}, red) and H_2O (K_{rw}, blue) relative permeability on semilogarithmic scale. The markers indicate experimental measurements, whereas the

solid and dashed curves denote history matched simulated data for primary drainage and imbibition, respectively. Strong hysteresis between drainage and imbibition was observed both for H_2 and H_2O. Modified from paper 4.

3.4.2 Impact of gas type

The drainage experiment was repeated with N_2 yielding a similar shape of the curve, albeit with higher K_{rg} and K_{rw} values compared to H_2-H_2O system (Fig. 24). The difference between H_2 and N_2 relative permeability curves was attributed to the increased gas-water viscosity ratio [70], where N_2 has two times higher viscosity than H_2 at experimental conditions. Note that the endpoint $K_{rg}*$ at S_{wirr} was not measured for N_2. The sensitivity analysis was therefore performed in the Sendra simulator to find the most suitable $K_{rg}*$ based on the uncertainty span from the H_2-experiment ($K_{rg}* = 0.61 \pm 0.12$). The simulation results showed that $K_{rg}*$ of 0.73 yielded a better history match of the N_2-experiment. The uncertainty in $K_{rg}*$ and other parameters in the N_2-experiment might have overestimated the actual difference between H_2 and N_2 relative permeability curves.
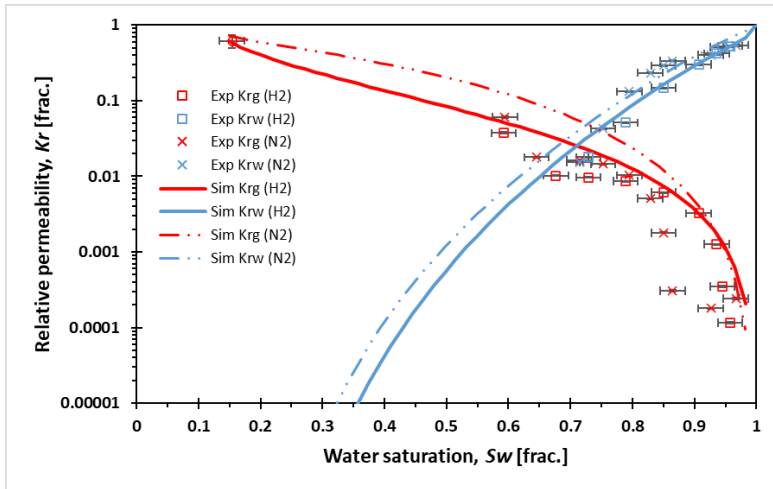
Fig. 24. Comparison between H_2- and N_2-H_2O primary drainage relative permeability on semilogarithmic scale. The markers indicate experimental H_2 (squares) and N_2 (crosses) measurements, whereas the solid and dot-dash curves denote history matched simulated data for H_2 and N_2, respectively. The N_2-H_2O relative permeability shifted upwards compared to a H_2 system, explained by a difference in the gas-water viscosity ratio. The endpoint N_2 relative permeability (0.73) was

assumed to be equal to the upper uncertainty limit of the endpoint H_2 relative permeability (0.61 ± 0.12). Modified from paper 4.

3.5 Reservoir scale cyclic injections

The knowledge about pore scale mechanisms and core scale flow functions from chapters 3.1-3.4 cannot alone serve for design of the field tests of H_2 storage in porous media. The pre-screening phase is best achieved through reservoir simulation which is a cost and time efficient tool to predict reservoir performance under various storage scenarios. This chapter summarizes key findings from reservoir simulations of H_2 storage in a depleted hydrocarbon field and in an aquifer, using a commercial black-oil reservoir simulator Eclipse 100. Chapters 3.5.1-3.5.3 are based on paper 5 which focused on the storage capacity, recovery factor and impact of cushion gas in a depleted field. Chapter 3.5.4 discusses the impact of relative permeability hysteresis on the storage performance in an aquifer reported in paper 6.

3.5.1 Macroscopic storage and working gas capacities

The middle-size oil and gas Norne field was selected to evaluate H_2 storage using one vertical well for injection and withdrawal. Three different storage schemes were implemented, examining H_2 storage in gas, oil and water storage zones separately. The results showed (Table 1) that each storage zone can accommodate ~ 3 billion Sm^3 of H_2, using the injection rate of 3 million Sm^3/day and total injection time of ~ 1000 days in the gas and oil zones and ~ 2000 days in the water zone. The injected H_2 accumulated at the uppermost regions of gas and oil zones (Fig. 25a, b) and occupied ~ 50% of the near-well pore space. The H_2 accumulation was more widespread in the water zone, eventually reaching the highest point of the oil zone due to upward movement in the far-well region (Fig. 25c).
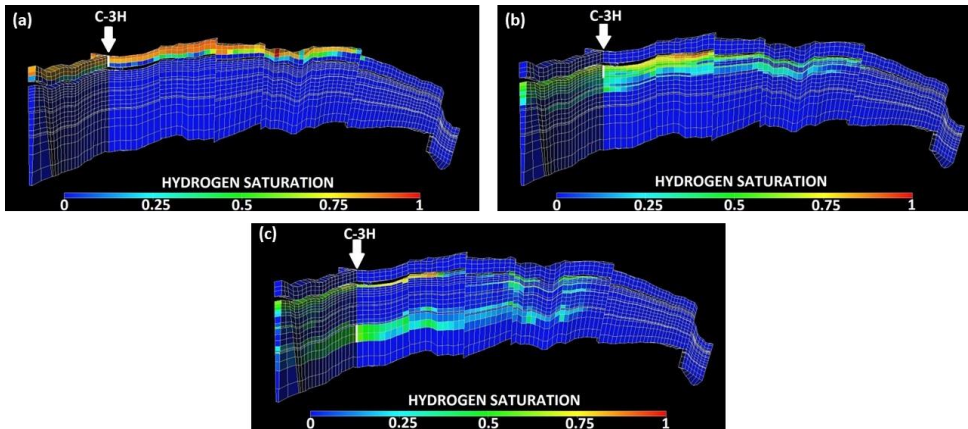
Fig. 25. Vertical xy-slice of the Norne simulation model demonstrating the H_2 distribution at the end of initial injection stage in three storage zones: (a) gas, (b) oil, and (c) water. The arrows indicate the injector location (C-3H) and the white bars show the perforation intervals. The H_2 accumulation at the reservoir top was observed in the gas and oil zones. Conversely, H_2 was more widely distributed in the water zone, reaching the uppermost regions of the oil zone. Vertical distance is 5-times exaggerated. Modified from paper 5.

After the initial injection stage, the storage cycles were repeated annually with one 5-month withdrawal and one 7-month injection periods. The withdrawal rate was constant and equal to 3 million Sm^3/day in the gas and oil zones, contrary to the water zone with the decreasing withdrawal rates (Fig. 26a). This was due to a steeper bottom-hole (BHP) decline in the water zone which reached its BHP lower limit of 180 bar (Fig. 26b). The volume of H_2 that was withdrawn from each zone after the first cycle, known as the working gas capacity, ranged between 373 and 462 million Sm^3 (Table 1). The highest working gas capacity was found in the oil zone, whereas the water zone showed the lowest capacity. It is important to note that the range of the working gas capacities in three storage zones corresponded to 12-16% of the initially injected volume. This implies that a significant amount of H_2 remained in the reservoir as cushion gas. Low working gas capacity agreed with the literature values of ~15-30% [9, 71, 72].

Table 1. Summary results of H_2 storage in the gas, oil and water zones of the Norne oil and gas field. Three cases were examined, differed in terms of gas injection during initial injection stage. Reference case (Ref): Injection of pure H_2; Case 1: Injection of pure formation gas, later replaced by pure H_2; and Case 2: Injection of a H_2-formation gas mixture (30%-70%). Modified from paper 5.

Storage zone	Case	Initial H_2 injected [Billion Sm^3]	H_2 share in initially injected gas	H_2 withdrawn 1st cycle [Billion Sm^3]	H_2 recovery factor 1st cycle	Final H_2 recovery factor
Gas	Ref	3.26	100%	0.432	13%	87%
	Case 1	0.75	20%	0.436	58%	93%
	Case 2	1.08	30%	0.137	13%	91%
Oil	Ref	2.91	100%	0.462	16%	77%
	Case 1	0.84	26%	0.436	52%	95%
	Case 2	0.97	30%	0.126	13%	82%
Water	Ref	3.05	100%	0.373	12%	49%
	Case 1	0.69	20%	0.356	52%	84%
	Case 2	0.98	30%	0.085	9%	47%

3.5.2 Recovery factor

To efficiently extract the remaining cushion gas, a prolonged withdrawal period was simulated until the withdrawal rate reached its economic limit of 1 million Sm^3/day (Fig. 26a). The prolonged withdrawal in the gas and oil zones was characterized by an initial constant rate of 3 million Sm^3/day, followed by a declining rate due to break-through of native reservoir fluids. The withdrawal lasted for 1094 and 880 days in the gas and oil zones, yielding a final recovery factor of 87% and 77%, respectively (Table 1). The water zone showed the lowest recovery factor (49%) due to shorter withdrawal period (415 days) and pronounced water production. Overall, high recovery factor makes the gas zone the most preferred target for H_2 storage in a depleted field, whereas the water zone demonstrated the lowest storage efficiency.
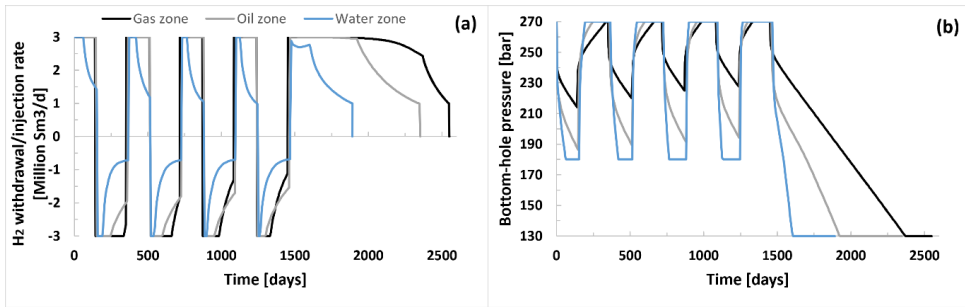
Fig. 26. Three scenarios of H_2 storage in the gas (black), oil (gray) and water (blue) zones of the Norne oil and gas field. Each storage scenario implemented four annual withdrawal-injection cycles, followed by one prolonged withdrawal period. (a) H_2 withdrawal (positive values) and injection rates (negative values). (b) Bottom-hole pressure in the injector. During the first four withdrawal cycles, constant rates prevailed in the gas and oil zones. Conversely, the water zone underwent declining withdrawal rates due to the bottom-hole pressure reaching its lower limit of 180 bar. The prolonged withdrawal period continued until the economic rate of 1 million Sm^3/day, which occurred first in the water zone, leading to the lowest H_2 recovery factor. Modified from paper 5.

3.5.3 Impact of cushion gas

When using H_2 as cushion gas, only 12-16% of the initially injected H_2 was available for cyclic withdrawal as discussed in chapter 3.5.1 (defined now as a reference case). To decrease the volume of H_2 cushion gas, two cases (Table 1) were examined focusing on the effects of cushion gas type (case 1) and its composition (case 2). In case 1, the initial injection stage started with the injection of formation gas (CH_4) until reaching the reservoir pressure of 220 bar, followed by the injection of H_2 until 250 bar. The share of H_2 in the total gas volume, injected during the initial stage, ranged between 20% and 26%. Compared to the reference case, the H_2 recovery factor after the 1st cycle increased in all storage zones: gas – 58%, oil – 52% and water – 52%. The H_2 purity in the withdrawn gas mixture was however reduced, with gradually decreasing H_2 fractions down to 81%, 82% and 70% in the gas, oil and water zones, respectively (Fig. 27a,c,e). The water zone (Fig. 27e) underwent the steepest decline in the withdrawn H_2 fraction, caused by H_2 losses due to upward migration. The final H_2 recovery factors after the prolonged withdrawal period were higher in case 1: gas – 93%, oil – 95% and water – 84%. Overall, the injection of formation gas during the initial stage increased the H_2 recovery factor (both 1st cycle and final), albeit with decreasing H_2 fractions in

the withdrawn gas mixture. The risk of impurities in the withdrawn gas mixture can be effectively reduced by injecting a minimum of 60-80% H_2 cushion gas, as shown in paper 5.

In case 2, a H_2-CH_4 gas mixture (30%-70%) was injected during the initial injection stage, yielding the H_2 recovery factors after the 1st cycle similar to the reference case: gas – 13%, oil – 13% and water – 9%. The H_2 fractions in the withdrawn gas mixture showed nonmonotonic behaviour (Fig. 27b,d,f). The initially declining H_2 fractions reversed to an increasing trend after ~50 days in the gas and oil zones (Fig. 27b,d), and ultimately stabilizing in the water zone (Fig. 27f). This behaviour was attributed to gravity segregation, which established in the far-well area only. In contrast, the near-well area represented a disperse zone with uniformly distributed H_2 and formation gas because there was no shut-in period between injection and withdrawal. During gas withdrawal, the segregated gas accumulation from the far-well area reached the well with a delay of ~50 days. This resulted in the increased H_2 fraction in the gas and oil zones due to higher H_2 mobility compared to formation gas. In the water zone, the H_2 fraction did not increase but stabilized at nearly constant values after 50 days, due to a partial H_2 loss caused by upward migration.

Another feature of case 2 was that the H_2 fraction increased with the increasing number of cycles in all storage zones, attributed to longer injection (7 months) relative to withdrawal periods (5 months). Compared to the reference case, the final H_2 recovery factors were higher in the gas and oil zones, but lower in the water zone: gas – 91%, oil – 82% and water – 47%. To summarize, the injection of a H_2-CH_4 mixture (case 2) increased the final H_2 recovery factor, but most of the initially injected H_2 (87-91%) remained in the reservoir as cushion gas similar to the reference case. Therefore, the injection of pure H_2 and formation gas instead of their mixtures (case 1) is a preferred measure to reduce the volume of H_2 cushion gas.
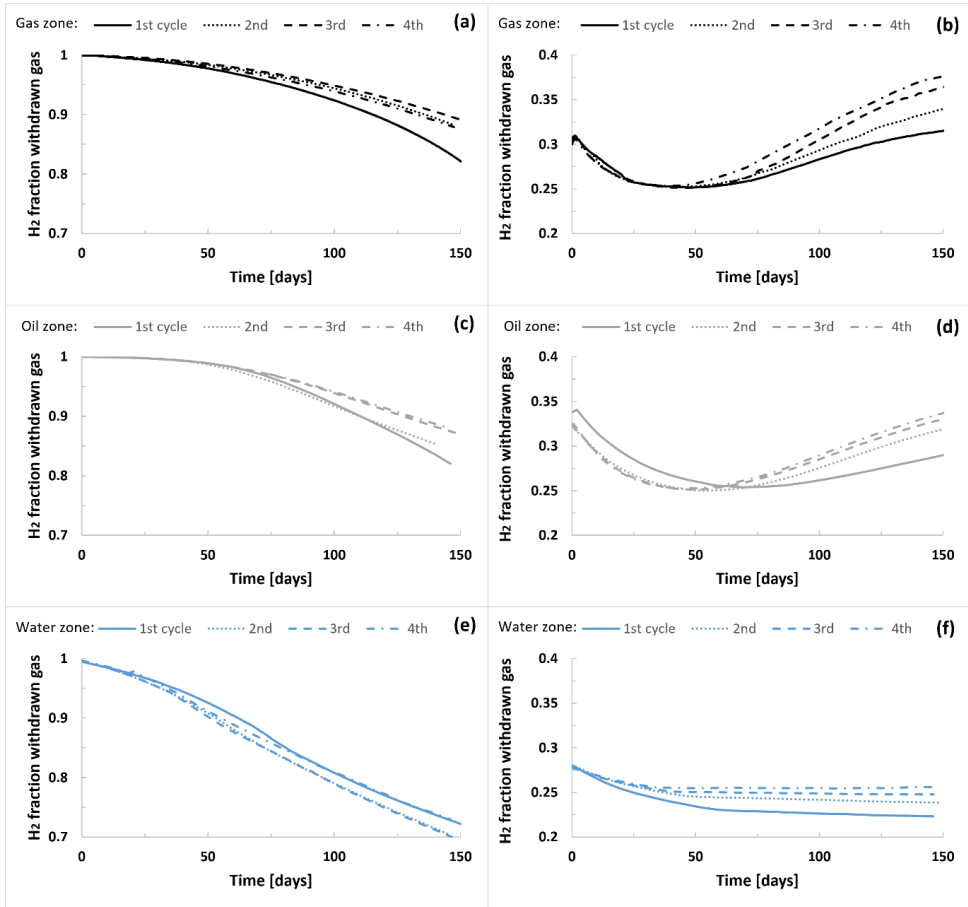
Fig. 27. H_2 fraction in the withdrawn gas mixture in the gas (black), oil (gray) and water (blue) zones during the first four withdrawal-injection cycles. Case 1 (left: a, c, e): Cushion gas injection of formation gas (CH_4) followed by H_2. The H_2 fraction reduced over time, with the most rapid decline observed in the water zone. Case 2 (right: b, d, f): Cushion gas injection of H_2-CH_4 gas mixture (30%-70%). The H_2 fraction exhibited a downward trend during the initial 50 days, followed by an upward trend in the gas and oil zones, and flattening in the water zone. The H_2 fraction increased with the number of cycles. Modified from paper 5.

3.5.4 Impact of hysteresis

The H_2-H_2O relative permeability measurements indicated a need to consider hysteresis in reservoir modelling of H_2 storage. Although hysteresis was included in the Norne model, its impact on the storage performance was not evaluated. In this chapter, the relative permeability dataset from paper 4 was implemented together with

the Killough hysteresis formulation [56] in a reservoir model of the Johansen formation aquifer to study the hysteresis effects.

The storage scheme initiated with H_2 injection at 3 million Sm^3/day for 1098 days, followed by annual cycles with equally long withdrawal and injection periods of six months. The final withdrawal period lasted until the economic limit of 1 million Sm^3/day was reached. Two different cases were simulated: without and with relative permeability hysteresis (Table 2; Fig. 28). The H_2 recovery factor after the 1st and final cycles reduced in the case with hysteresis from 16% to 14% and from 68% to 37%, respectively. This reduction was caused by BHP lower limit of 160 bar which was reached in the case with hysteresis, thus decreasing the withdrawal rate. The BHP behaviour was governed by the inflow performance equation in the Eclipse simulator: $Q_g = T_w \cdot M_g \cdot (p_{grid} - p_{BHP} - p_{head})$, where Q_g is the H_2 withdrawal rate, T_w is the grid connection transmissibility factor, M_g is the H_2 mobility, p_{grid} is the grid connection pressure, p_{BHP} is the BHP, and p_{head} is the pressure head between the grid connection and bottom hole. According to this equation, the reduced H_2 mobility in the case with hysteresis required the reduction in the BHP to maintain constant withdrawal rate of 3 million Sm^3/day. The decrease in H_2 recovery factors due to hysteresis was consistent with the literature [9, 10].

Table 2. Impact of relative permeability hysteresis on H_2 storage in the Johansen aquifer. Modified from paper 6.

Case	H_2 withdrawn [Million Sm^3]					H_2 recovery factor	
	1st cycle	2nd cycle	3rd cycle	4th cycle	5th cycle	1st cycle	Final
No hysteresis	540	540	540	540	1560	16 %	68 %
Hysteresis	451	390	388	393	391	14 %	37 %
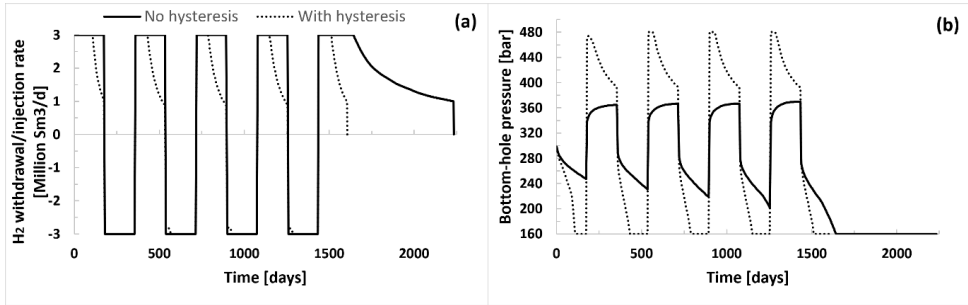
Fig. 28. Impact of relative permeability hysteresis on H_2 storage in the Johansen aquifer, examined by two cases: without (solid curves) and with hysteresis (dashed curves). (a) H_2 withdrawal (positive values) and injection rates (negative values). (b) Bottom-hole pressure in the injector. The withdrawal rate reduced in the case with hysteresis due to the bottom-hole pressure reaching its lower limit of 160 bar. Modified from paper 6.

The H_2 plume dynamics were similar for two cases, characterized by a cone-like shape and vertical contraction and expansion during withdrawal and injection, respectively (Fig. 29). No horizontal H_2 spreading was observed due to equal volumes of injected and withdrawn in each annual cycle. The control of lateral H_2 extent is needed to minimize the risk of leakage outside the reservoir boundaries. The main difference between two cases was related to the final H_2 distribution after the prolonged withdrawal period. The unextracted H_2 accumulated in the top layer in the case without hysteresis, contrary to a cone-like H_2 distribution in both top and lower layers in the case with hysteresis.
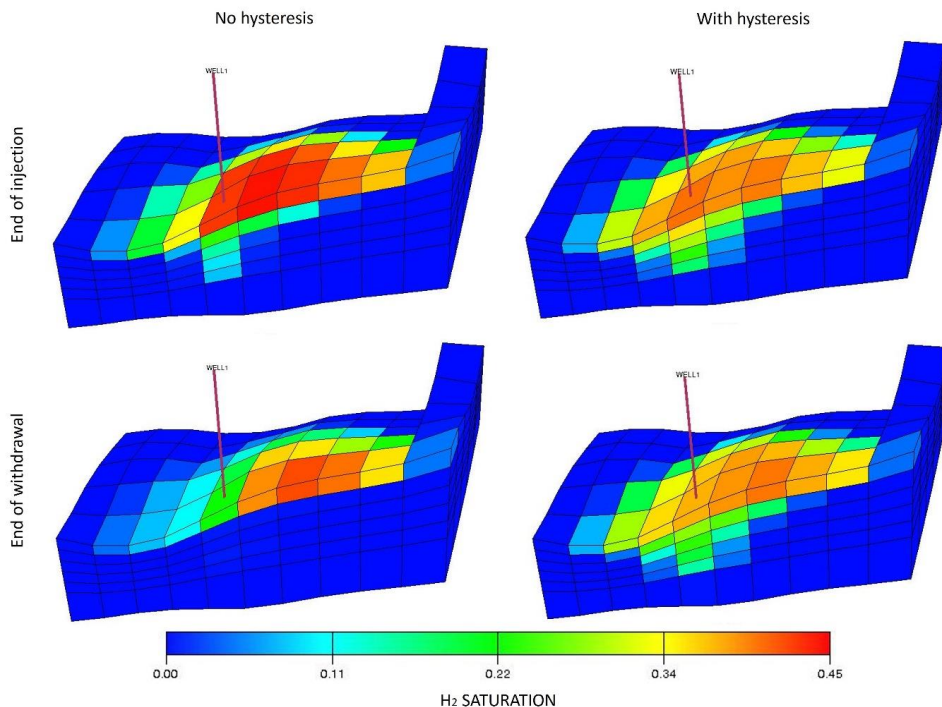
Fig. 29. Vertical slice of the Johansen aquifer simulation grid demonstrating H_2 distribution after the final injection (top) and withdrawal (bottom) periods in the cases without (left) and with hysteresis (right). Similar H_2 plume dynamics was observed, with a cone-like plume shape contracting and expanding vertically during withdrawal and injection, respectively. However, at the end of the last withdrawal period, the remaining H_2 concentrated in the uppermost layer in the nonhysteretic case, contrary to a more vertically distributed H_2 in the hysteretic case. Vertical distance is 10-times exaggerated. From paper 6.

3.6 Field scale implications

The results of this dissertation have several noteworthy implications for underground H_2 storage in porous systems. New insights are provided in optimal injection rates, trapping mechanisms, hysteresis, selection of proxy gas in laboratory tests and cushion gas in field pilots. As highlighted in chapters 3.1.1 and 3.1.2, higher injection rates resulted in the highest microscopic storage capacity, but at the same time with the highest amount of disconnected H_2 ganglia. The latter effect is undesirable because it may increase the risk of H_2 loss due to dissolution. To strike a balance between

maximizing storage capacity and minimizing the formation of disconnected H_2, an optimal N_{Ca} in the order of 10^{-7} was found. This number is equivalent to a field scale injection rate of ~50000 m^3/day, assuming an experimental injection velocity of ~ 70 m/day and an injector perforation length of 30 m.

The use of a proxy laboratory gas may be advantageous for safety reasons due to the wide H_2 flammability range. In chapter 3.1.3, it was shown that the differences in 2D drainage saturations between gases were mostly pronounced at low injection rates. This suggests that CH_4 and N_2 cannot be used as proper substitutes for H_2 in a low-rate injection mode, further confirmed by relative permeability measurements, as outlined in chapter 3.4.2. Conversely, a proxy gas may be used at high injection rates due to minor differences in the 2D saturations, yet with caution. It should be noted that microfluidic experiments are typically employed for qualitative analysis. The process of upscaling 2D saturations to underground reservoirs, where gravitational forces play a vital role, may present some limitations. However, the 2D gas saturation trends were consistent with classic capillary desaturation theory and existing 3D H_2 literature, as discussed in chapter 3.1.1. As such, the microfluidic 2D saturations may be used temporarily to supplement missing 3D data, which are important when designing field projects.

The H_2 withdrawal from a reservoir involves various trapping mechanisms, representing a potential loss risk. In chapter 3.2.2, it appeared that if sufficient imbibition times are allowed, residually trapped H_2 may be subjected to a slow non-equilibrium dissolution. The findings of this dissertation, supported by relevant literature [41, 47], suggest that dissolution seems to be a significant contributor to H_2 losses. In natural reservoirs, water upconing may intensify the dissolution process. However, the occurrence of non-equilibrium dissolution is uncertain, as dissolution could eventually approach equilibrium over longer timescales, particularly relevant for CO_2 storage [50]. In the case of H_2 storage, which involves multiple cycles of injection and withdrawal at high rates, it is reasonable to speculate that there is a higher possibility of dissolution occurring under a non-equilibrium regime. This outcome is

more favorable because less H_2 will dissolve in water compared to equilibrium dissolution.

Residually trapped H_2, if not completely dissolved in water during withdrawal, may either remain disconnected or connect with newly introduced H_2 during cyclic injections. In chapter 3.3.1, it was found that most of trapped H_2 ganglia were able to reconnect with the injected H_2 in the next drainage cycle. Moreover, the residual H_2 saturation remained nearly constant over multiple injection cycles, as highlighted in chapter 3.3.2. A high H_2 tendency to reconnect, coupled with nonincreasing residual trapping, are beneficial for minimizing the H_2 loss at field scale.

It is essential to better understand the implications of hysteresis due to cyclicity of H_2 storage. The evidence of hysteresis in contact angles (chapter 3.2.3) and relative permeability (chapter 3.5.4) proved the importance of hysteresis for H_2 storage, further confirmed by reservoir simulations (chapter 3.5.4). The relative permeability hysteresis was required in reservoir simulations to ensure more reliable predictions of storage performance, as neglecting it resulted in overestimation of the H_2 recovery factor. At the same time, the measurement uncertainties require additional sensitivity studies to reflect the range of input parameters.

The selection of appropriate cushion gas is critical for pressure support and purity of the withdrawn gas stream. In chapter 3.1.3, it appeared that N_2 and CH_4 could be preferred cushion gases compared to H_2 due to higher 2D saturations, albeit applicable at low injection rate only. The higher gas saturations imply that more cushion gas can be injected using the same injection rate. Furthermore, CH_4 can be considered as a more effective cushion gas than N_2 due to its higher connectivity in the pore space. The benefit is that the higher injected volumes and connectivity of cushion gas ensure a more controlled reservoir pressure support during withdrawal cycles.

The relative permeability measurements from chapter 3.4.2 further indicated that N_2 could be a better choice for cushion gas than H_2, especially during gas injection cycles. When displacing H_2O from a reservoir using N_2 or H_2, a higher H_2O relative permeability for a N_2-H_2O system will enhance the efficiency of water displacement

during N_2 injection compared to H_2. However, this positive outcome may be counteracted by a higher N_2 relative permeability during gas withdrawal. This will in turn lead to a faster N_2 breakthrough in the producer compared to H_2, increasing the impurities in the withdrawn gas mixture. In chapter 3.5.3, reservoir simulations showed that the use of other than H_2 cushion gases decreased the purity of the withdrawn gas stream, despite an increased H_2 recovery factor. To prevent gas impurities, it was shown that the injected gas must contain a minimum H_2 fraction in the range of 60-80%. Due to the absence of gravity segregation between H_2 and formation gas in the near-well region, it is proposed to incorporate a shut-in period between injection and withdrawal. Overall, the selection of cushion gas must be made on a case-by-case basis, with attention given to the maximum H_2 recovery and desired gas purity.

Most experimental measurements of this dissertation were performed under the pressure range of 5-40 bar in a H_2-H_2O system, relevant for H_2 storage in shallow geological formations, i.e. aquifers and a gas-water transition zone in depleted reservoirs. However, the experimental results may be applicable for deeper reservoirs too due to minor differences in H_2 properties at higher pressures, partially supported by a microfluidic experiment at 100 bar from chapter 3.1.1 and existing literature [43, 61, 73, 74].

4 Conclusions and future work

4.1 Conclusions

This dissertation presented a multiscale experimental and numerical approach, with a focus on H_2 flow physics relevant for underground storage in porous media. Pore scale mechanisms were examined using a microfluidic device with sandstone-like pore network. The injection rate of H_2 played a vital role in determining its storage capacity and connectivity in the pore space. The storage capacity increased with the increasing injection rate, resulting in a maximum H_2 saturation of $\sim 40\%$. However, an injection rate that is too high can lead to the formation of disconnected H_2 after drainage. It was therefore recommended to use an optimal injection rate equivalent to capillary number in the order of 10^{-7} to ensure maximum storage capacity with minimal amount of disconnected H_2. The maximum storage capacity appeared to be independent of gas type. Conversely, gas connectivity was significantly lower for N_2 compared to H_2, CH_4 and a mixture of 50% H_2 - 50% CH_4.

H_2 entrapment during withdrawal was governed by residual and dissolution trapping mechanisms, where the later occurred under a slow non-equilibrium regime. Cyclic injections demonstrated that most of residually trapped H_2 can reconnect in the subsequent cycles, without increasing the residual H_2 saturation. The microfluidic-based H_2 contact angles showed that the advancing angles were on average $\sim 19°$ higher than the receding one, indicating hysteresis between injection and withdrawal.

The drainage and imbibition H_2-water relative permeabilities were measured in a sandstone and extrapolated with numerical history matching to cover the full range of mobile water saturations. Strong hysteresis was evident, with higher H_2 and lower water relative permeabilities during drainage compared to imbibition. The resulting relative permeability curves were implemented in a reservoir model of the Johansen aquifer using a black-oil Eclipse 100 simulator. The effect of relative permeability hysteresis was pronounced, with significantly lower H_2 recovery factor (37%) compared to a case where the hysteresis was neglected (68%).

The effect of reservoir zone and cushion gas on the storage efficiency was examined using the reservoir model of the Norne hydrocarbon field. The H_2 storage was recommended in a thin gas zone, which showed the highest final H_2 recovery factor of 87%. In contrast, a water zone was the least preferred storage target with a much lower final recovery factor of 49%. The use of CH_4 as cushion gas instead of H_2 effectively increased the final H_2 recovery factor in all storage zones, albeit with the reduced H_2 purity in the withdrawn gas mixture. An injection of cushion gas with at least 60-80% H_2 fraction could reduce the impurities to a minimum. Conversely, the injection of a 30% H_2-70% formation gas mixture turned out to be an ineffective measure to reduce the amount of H_2 cushion gas. The cushion gas must be chosen with caution based on the preferred outcome, balancing between the maximum H_2 recovery and purity of the withdrawn gas mixture.

This dissertation contributes to an enhanced understanding of H_2 flow in porous media, relevant for subsurface storage. To improve the efficiency and safety of operations, the findings can be applied when deciding the optimal injection rate, laboratory proxy gas or reservoir cushion gas. The microfluidic results improved the comprehension of the pore scale behaviour during cyclic flow. Core scale measurements identified the importance of relative permeability hysteresis, further demonstrated by reservoir modelling.

4.2 Future work

Research in underground H_2 storage is a rapidly growing field, requiring interdisciplinary understanding to confirm its feasibility. The author's interest and unanswered research questions that remain unaddressed in this dissertation provide the basis for the following suggestions for future studies, given more time and funding. First, the use of a more realistic micromodel with non-repeatable pore patterns and heterogenous minerology would enhance the reliability of the observed pore scale H_2 flow mechanisms. Second, the microfluidic cyclic injections should be repeated with core flooding experiments, which would make it possible to extrapolate the results to natural environments. The advanced imaging techniques such as magnetic resonance

imaging (MRI) can corroborate the observed pore scale mechanisms from microfluidic experiments. Third, reservoir modelling should include H_2 dissolution and focus on the comprehensive uncertainty analysis based on the range of input relative permeabilities. Finally, H_2 is susceptible to bio-geochemical activity, and studying the microbial effects on the H_2 flow physics would be essential for advancing the understanding of coupled mechanisms.

Appendix

Extrapolation of the field-of-view (FoV) saturations to the micromodel total area

The difference between microfluidic setups in paper 1 and papers 2-3 was related to the size of the micromodel area, observed by a microscope. In paper 1, the total area of the micromodel was studied. Conversely, a limited field of view (FoV), covering ~1% of the total area, was observed in papers 2 and 3. A comparison between H_2 saturations after drainage is plotted in Fig. S1. It shows that the FoV saturations can be extrapolated to the total micromodel area at low capillary number only, where the FoV and total saturations are similar.

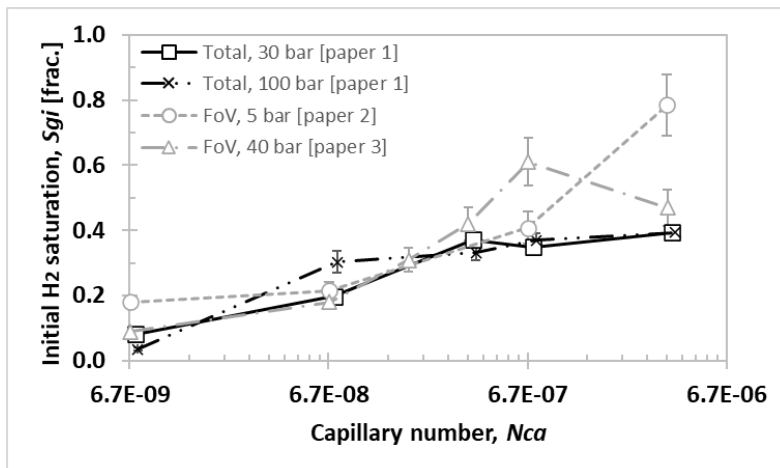**Fig. S1**. Comparison of H_2 saturations after drainage, estimated from the total micromodel area (paper 1) and from the micromodel FoV (papers 2-3). The FoV saturations at high capillary number are not representative of the total micromodel area.

Bibliography

1. IEA, *Net Zero by 2050. A roadmap for the Global Energy Sector, https://www.iea.org/reports/net-zero-by-2050*. 2021.
2. IEA, *The Future of Hydrogen, https://www.iea.org/reports/the-future-of-hydrogen*. 2019.
3. Tarkowski, R., *Underground hydrogen storage: Characteristics and prospects.* Renewable and Sustainable Energy Reviews, 2019. **105**: p. 86-94.
4. Hassanpouryouzband, A., et al., *Offshore Geological Storage of Hydrogen: Is This Our Best Option to Achieve Net-Zero?* ACS Energy Letters, 2021. **6**(6): p. 2181-2186.
5. Carden, P.O. and L. Paterson, *Physical, Chemical and Energy Aspects of Underground Hydrogen Storage.* International Journal of Hydrogen Energy, 1979. **4**(6): p. 559-569.
6. Dopffel, N., S. Jansen, and J. Gerritse, *Microbial side effects of underground hydrogen storage - Knowledge gaps, risks and opportunities for successful implementation.* International Journal of Hydrogen Energy, 2021. **46**(12): p. 8594-8606.
7. Muhammed, N.S., et al., *A review on underground hydrogen storage: Insight into geological sites, influencing factors and future outlook.* Energy Reports, 2022. **8**: p. 461-499.
8. Bo, Z., et al., *Impact of experimentally measured relative permeability hysteresis on reservoir-scale performance of underground hydrogen storage (UHS).* International Journal of Hydrogen Energy, 2023.
9. Ershadnia, R., et al., *Impact of geological and operational conditions on underground hydrogen storage.* International Journal of Hydrogen Energy, 2023. **48**(4).
10. Pan, B., et al., *Impacts of relative permeability hysteresis, wettability, and injection/withdrawal schemes on underground hydrogen storage in saline aquifers.* Fuel, 2023. **333**.
11. Boon, M. and H. Hajibeygi, *Experimental characterization of H-2/water multiphase flow in heterogeneous sandstone rock at the core scale relevant for underground hydrogen storage (UHS).* Scientific Reports, 2022. **12**(1).
12. Higgs, S., et al., *Direct measurement of hydrogen relative permeability hysteresis for underground hydrogen storage.* International Journal of Hydrogen Energy, 2024. **50**: p. 524-541.
13. Oak, M.J., L.E. Baker, and D.C. Thomas, *Three-phase relative permeability of Berea sandstone* Journal of Petroleum Technology, 1990. **42**(08): p. 1054-1061.
14. Akbarabadi, M. and M. Piri, *Relative permeability hysteresis and capillary trapping characteristics of supercritical CO2/brine systems: An experimental study at reservoir conditions.* Advances in Water Resources, 2013. **52**: p. 190-206.
15. Raza, A., et al., *A holistic overview of underground hydrogen storage: Influencing factors, current understanding, and outlook.* Fuel, 2022. **330**.

16. Sekar, L.K., et al., *Review of reservoir challenges associated with subsurface hydrogen storage and recovery in depleted oil and gas reservoirs.* Journal of Energy Storage, 2023. **72**.

17. Beckingham, L.E. and L. Winningham, *Critical Knowledge Gaps for Understanding Water-Rock-Working Phase Interactions for Compressed Energy Storage in Porous Formations.* Acs Sustainable Chemistry & Engineering, 2020. **8**(1): p. 2-11.

18. Heinemann, N., et al., *Hydrogen storage in saline aquifers: The role of cushion gas for injection and production.* International Journal of Hydrogen Energy, 2021. **46**(79): p. 39284-39296.

19. Kanaani, M., B. Sedaee, and M. Asadian-Pakfar, *Role of Cushion Gas on Underground Hydrogen Storage in Depleted Oil Reservoirs.* Journal of Energy Storage, 2022. **45**.

20. Pfeiffer, W.T., C. Beyer, and S. Bauer, *Hydrogen storage in a heterogeneous sandstone formation: dimensioning and induced hydraulic effects.* Petroleum Geoscience, 2017. **23**(3): p. 315-326.

21. Panfilov, M., *Underground and pipeline hydrogen storage. In Compendium of hydrogen energy*. 2016: Woodhead Publishing.

22. Smigan, P., et al., *Methanogenic Bacteria as a Key Factor Involved in Changes of Town Gas Stored in an Underground Reservoir.* Fems Microbiology Ecology, 1990. **73**(3): p. 221-224.

23. Pérez, A., et al., *Patagonia Wind - Hydrogen Project: Underground Storage and Methanation*, in *21st world hydrogen energy conference*. 2016: Zaragoza, Spain.

24. RAG, *RAG Austria AG - Underground Sun Storage: Final Report Public 13*. 2020.

25. Linstrom, P.J. and W.G. Mallard, *The NIST Chemistry WebBook: A chemical data resource on the internet.* Journal of Chemical and Engineering Data, 2001. **46**(5): p. 1059-1063.

26. Liu, N., et al., *Pore-scale study of microbial hydrogen consumption and wettability alteration during underground hydrogen storage.* Frontiers in Energy Research, 2023. **11**.

27. Thaysen, E.K., et al., *Estimating microbial growth and hydrogen consumption in hydrogen storage in porous media.* Renewable & Sustainable Energy Reviews, 2021. **151**.

28. Lenormand, R., C. Zarcone, and A. Sarr, *Mechanisms of the Displacement of One Fluid by Another in a Network of Capillary Ducts.* Journal of Fluid Mechanics, 1983. **135**(Oct): p. 337-353.

29. Lenormand, R., E. Touboul, and C. Zarcone, *Numerical-Models and Experiments on Immiscible Displacements in Porous-Media.* Journal of Fluid Mechanics, 1988. **189**: p. 165-187.

30. Zhang, C.Y., et al., *Influence of Viscous and Capillary Forces on Immiscible Fluid Displacement: Pore-Scale Experimental Study in a Water-Wet Micromodel Demonstrating Viscous and Capillary Fingering.* Energy & Fuels, 2011. **25**(8): p. 3493-3505.

31. Roof, J.G., *Snap-Off of Oil Droplets in Water-Wet Pores.* Society of Petroleum Engineers Journal, 1970. **10**(1): p. 85-&.

32. Deng, W., M. Balhoff, and M.B. Cardenas, *Influence of dynamic factors on nonwetting fluid snap-off in pores.* Water Resources Research, 2015. **51**(11): p. 9182-9189.

33. Herring, A.L., et al., *Observations of nonwetting phase snap-offduring drainage.* Advances in Water Resources, 2018. **121**: p. 32-43.

34. Guo, H., K.P. Song, and R. Hilfer, *A Brief Review of Capillary Number and its Use in Capillary Desaturation Curves.* Transport in Porous Media, 2022. **144**(1): p. 3-31.

35. Satter, A. and G.M. Iqbal, *Reservoir engineering: the fundamentals, simulation, and management of conventional and unconventional recoveries*. 2015: Gulf Professional Publishing.

36. Lake, L.W., *Enhanced oil recovery*. 1989: Prentice Hall, Englewood Cliffs.

37. Paterson, L., *The Implications of Fingering in Underground Hydrogen Storage.* International Journal of Hydrogen Energy, 1983. **8**(1): p. 53-59.

38. Feldmann, F., et al., *Numerical simulation of hydrodynamic and gas mixing processes in underground hydrogen storages.* Environmental Earth Sciences, 2016. **75**(16).

39. Tek, M.R., *Underground storage of natural gas: theory and practice*. 1989: Springer Science & Business Media.

40. Al-Yaseri, A., et al., *Initial and residual trapping of hydrogen and nitrogen in Fontainebleau sandstone using nuclear magnetic resonance core flooding.* International Journal of Hydrogen Energy, 2022. **47**(53): p. 22482-22494.

41. Jangda, Z., et al., *Pore-scale visualization of hydrogen storage in a sandstone at subsurface pressure and temperature conditions: Trapping, dissolution and wettability.* J Colloid Interface Sci, 2023. **629**(Pt B): p. 316-325.

42. Jha, N.K., et al., *Pore scale investigation of hydrogen injection in sandstone via X-ray micro-tomography.* International Journal of Hydrogen Energy, 2021. **46**(70): p. 34822-34829.

43. Thaysen, E.M., et al., *Pore-scale imaging of hydrogen displacement and trapping in porous media.* International Journal of Hydrogen Energy, 2023. **48**(8): p. 3091-3106.

44. Lenormand, R. and C. Zarcone. *Role of roughness and edges during imbibition in square capillaries*. in *SPE Annual Technical Conference and Exhibition?* 1984. SPE.

45. Chabab, S., et al., *Measurements and predictive models of high- pressure H-2 solubility in brine (H2O+NaCl) for underground hydrogen storage application.* International Journal of Hydrogen Energy, 2020. **45**(56): p. 32206-32220.

46. Pan, B., et al., *Underground hydrogen storage: Influencing parameters and future outlook.* Advances in Colloid and Interface Science, 2021. **294**.

47. Zhang, H.Y., et al., *Effect of cyclic hysteretic multiphase flow on underground hydrogen storage: A numerical investigation.* International Journal of Hydrogen Energy, 2024. **49**: p. 336-350.

48.   Buchgraber, M., A.R. Kovscek, and L.M. Castanier, *A Study of Microscale Gas Trapping Using Etched Silicon Micromodels.* Transport in Porous Media, 2012. **95**(3): p. 647-668.

49.   Chang, C., et al., *Pore-scale supercritical CO2 dissolution and mass transfer under imbibition conditions.* Advances in Water Resources, 2016. **92**: p. 142-158.

50.   Chang, C., et al., *Coupled supercritical CO2 dissolution and water flow in pore-scale micromodels.* Advances in Water Resources, 2019. **123**: p. 54-69.

51.   Chen, L., et al., *Pore scale study of multiphase multicomponent reactive transport during CO2 dissolution trapping.* Advances in Water Resources, 2018. **116**: p. 208-218.

52.   Gennes, P.-G., F. Brochard-Wyart, and D. Quéré, *Capillarity and wetting phenomena: drops, bubbles, pearls, waves*. 2004: Springer.

53.   Ge, J.C., X.Z. Zhang, and F. Le-Hussain, *Fines migration and mineral reactions as a mechanism for CO2 residual trapping during CO2 sequestration.* Energy, 2022. **239**.

54.   Peng, S., *Gas-water relative permeability of unconventional reservoir rocks: Hysteresis and influence on production after shut-in.* Journal of Natural Gas Science and Engineering, 2020. **82**.

55.   Ruprecht, C., et al., *Hysteretic trapping and relative permeability of CO2 in sandstone at reservoir conditions.* International Journal of Greenhouse Gas Control, 2014. **27**: p. 15-27.

56.   Killough, J.E., *Reservoir Simulation with History-Dependent Saturation Functions.* Society of Petroleum Engineers Journal, 1976. **16**(1): p. 37-48.

57.   Land, C.S., *Calculation of Imbibition Relative Permeability for Two and Three-Phase Flow from Rock Properties.* Society of Petroleum Engineers Journal, 1968. **8**(2): p. 149-&.

58.   Zhang, Y.H., et al., *Pore-Scale Observations of Hydrogen Trapping and Migration in Porous Rock: Demonstrating the Effect of Ostwald Ripening.* Geophysical Research Letters, 2023. **50**(7).

59.   van der Hart, P.H.K., *A Pore-Scale Study of Underground Hydrogen Storage in Porous Media.* 2021, The University of Bergen.

60.   Johnson, R.E. and R.H. Dettre, *Contact Angle Hysteresis .3. Study of an Idealized Heterogeneous Surface.* Journal of Physical Chemistry, 1964. **68**(7): p. 1744-&.

61.   Hashemi, L., et al., *Contact angle measurement for hydrogen/brine/sandstone system using captive-bubble method relevant for underground hydrogen storage.* Advances in Water Resources, 2021. **154**.

62.   Iglauer, S., M. Ali, and A. Keshavarz, *Hydrogen Wettability of Sandstone Reservoirs: Implications for Hydrogen Geo-Storage.* Geophysical Research Letters, 2021. **48**(3).

63.   Muhammed, N.S., B. Haq, and D.A. Al Shehri, *Hydrogen storage in depleted gas reservoirs using nitrogen cushion gas: A contact angle and surface tension study.* International Journal of Hydrogen Energy, 2023.

64. van Rooijen, W., et al., *Microfluidics-based analysis of dynamic contact angles relevant for underground hydrogen storage.* Advances in Water Resources, 2022. **164**.

65. Hashemi, L., M. Blunt, and H. Hajibeygi, *Pore-scale modelling and sensitivity analyses of hydrogen-brine multiphase flow in geological porous media.* Scientific Reports, 2021. **11**(1).

66. Lomeland, F., E. Ebeltoft, and W.H. Thomas. *A new versatile relative permeability correlation.* in *International Symposium of the Society of Core Analysts.* 2005. Toronto, Canada.

67. Lomeland, F., E. Ebeltoft, and W.H. Thomas. *A new versatile capillary pressure correlation.* in *International Symposium of the Society of Core Analysts.* 2008. Abu Dhabi, UAE.

68. Prores, *Sendra.* 2016.

69. Ge, J., et al., *Influence of capillary pressure boundary conditions and hysteresis on CO2-water relative permeability.* Fuel, 2022. **321**.

70. Jeong, G.S., et al., *Effects of viscosity ratio, interfacial tension and flow rate on hysteric relative permeability of CO2/brine systems.* Energy, 2017. **133**: p. 62-69.

71. Delshad, M., et al., *Hydrogen Storage Assessment in Depleted Oil Reservoir and Saline Aquifer.* Energies, 2022. **15**(21).

72. Sainz-Garcia, A., et al., *Assessment of feasible strategies for seasonal underground hydrogen storage in a saline aquifer.* International Journal of Hydrogen Energy, 2017. **42**(26): p. 16657-16666.

73. Hashemi, L., et al., *A comparative study for H2–CH4 mixture wettability in sandstone porous rocks relevant to underground hydrogen storage.* Advances in Water Resources, 2022. **163**.

74. Yekta, A.E., et al., *Determination of Hydrogen-Water Relative Permeability and Capillary Pressure in Sandstone: Application to Underground Hydrogen Injection in Sedimentary Formations.* Transport in Porous Media, 2018. **122**(2): p. 333-356.

Publications

Paper 1

Impact of gas type on microfluidic drainage experiments and pore network modeling relevant for underground hydrogen storage

Maksim Lysyy[1], Na Liu[1], David Landa-Marbán[2], Geir Ersland[1], Martin Fernø[1,2]

[1]Dept. of Physics and Technology, University of Bergen, Allégaten 55, Bergen 5007, Norway

[2]NORCE Norwegian Research Centre AS, Nygårdsgaten 112, Bergen 5008, Norway

Highlights

- Gas drainage in a micromodel with realistic pore patterns.
- The gas type affects its drainage saturation, but at low injection rates only.
- Nitrogen is a poor proxy for hydrogen at low injection rates.
- Maximum gas saturation equal to 39-46%, independent of the gas type.
- Large number of disconnected gas ganglia at high injection rates.

Abstract

Underground hydrogen storage (UHS) in geological reservoirs is proposed as a technically feasible solution to balance mismatch between supply and demand in emerging markets. However, unique hydrogen properties and coupled flow mechanisms require new investigations to fully understand transport and storage of hydrogen in porous media across scales. Here we use microfluidics to investigate the effect of gas type and injection rate on flow patterns, saturation and connectivity of the gas phase. We visually observe that gas flow is characterized by capillary fingering, further confirmed by fractal dimension analysis. At lower injection rates, the gas saturation after drainage appears to increase with gas viscosity, with lower hydrogen saturation compared to methane and nitrogen. The maximum gas saturations (39-46%) were achieved at higher injection rates, showing no clear correlation to gas type. However, the high-rate injections lead to undesired outcomes in terms of formation of disconnected gas ganglia, mostly pronounced for nitrogen. We identify an optimal injection rate to achieve maximum gas saturation with the least amount of disconnected gas. The experimental results are supported with pore network modeling to derive relative permeability and capillary pressure functions.

Keywords: underground hydrogen storage, microfluidics, storage capacity, gas ganglia, pore network modeling, relative permeability

1 Introduction

Hydrogen (H_2) is an energy carrier with no carbon dioxide (CO_2) emissions upon combustion and may therefore play a significant role in climate change mitigation. The H_2 demand is predicted to increase from 94 million tons (Mt) in 2021 to ~ 150 Mt in 2030 according to the IEA 2050 Net Zero Scenario, with a further increase in 2050 resulting in ~ 10 % share in the total final energy consumption [1]. An increasing H_2 demand will require storage solutions to balance seasonal fluctuations between demand and supply. Underground H_2 storage (UHS) in salt caverns and porous formations like depleted hydrocarbon fields and aquifers has been proposed as one of the solutions for large-scale storage [2,

3]. The concept of underground gas storage has been used in the petroleum industry for decades, where gas is injected at peak supply and is withdrawn at peak demand. Prior to gas injection, the storage reservoir must be filled with cushion gas to maintain constant reservoir pressure. Contrary to UHS in salt caverns, the experience with commercial storage in porous rocks is scarce, limited to two pilot tests of H_2-CH_4 gas mixture storage in depleted gas fields [4, 5] and town gas storage in aquifers [6, 7]. Compared to other gases, H_2 gas characterized by low density and low viscosity coupled with high microbial activity. We need to identify differences between H_2 and other gases from the perspective of their behavior in porous media.

Porous reservoirs cannot use 100 % of their volume to store H_2 due to the presence of reservoir fluids such as water and formation gas. The interactions between H_2 and reservoir fluids and rocks are controlled by complex pore scale mechanisms which will affect storage performance. Core flooding on miniature rocks with microCT imaging and microfluidic experiments are suitable techniques for investigation of pore- and core- scale mechanisms which control H_2 distribution, connectivity, and interplay between viscous and capillary forces. The microCT core flooding experiments reported H_2 storage capacities of 36 – 65 % [8-11]. The H_2 recovery factor was influenced by the brine type, where the H_2-equilibrated brine resulted in a 12% recovery reduction compared to the non-equilibrated brine [8]. The injection rate and pressure were other parameters influencing the H_2 recovery, which increased with increasing injection rate and decreased with increasing pressure [10]. Ostwald ripening is observed in the rearrangement of the trapped H_2, characterized by larger ganglia growing at the expense of smaller ganglia [11]. Microfluidic experiments investigated flow mechanisms, dissolution and cyclic injections [12-14]. A pore scale modeling study examined the impact of wettability on flow mechanisms [15].

Available studies did not draw consistent conclusions on the impact of gas type and pressure on UHS. A comparative study is key for the choice of cushion gas and also in laboratory applications, where a suitable proxy gas is preferred over highly flammable H_2 gas. Some studies showed that N_2 is a poor proxy for H_2, reflected by the differences in initial saturations [11, 16], residual saturations [10], and steady state relative permeability [17]. In contrast, unsteady state relative permeability measurements reported similar H_2 and N_2 values which were lower than for CH_4 [18]. Contact angle measurements did not report any meaningful difference between H_2, CH_4, H_2-CH_4 mixtures and N_2 [19, 20]. The impact of pressure was mainly examined for contact angles, showing discrepancies. The tilted plate method reported an increase in H_2 contact angles with increasing pressure [21, 22], whereas no pressure effect was observed with the captive bubble method [19, 23]. Moreover, relative permeability measurements were reported independent of pressure [24], so was the H_2 saturation after core scale drainage [10] and microfluidic experiments [13].

In this study, gas drainage experiments were performed with a range of injection rates at 30 bar and 30 °C using a silicon microfluidic device with irregular sandstone-like pore patterns. Our pore scale analysis aims at the impact of gas type and injection rate on gas flow patterns, saturation and connectivity in the pore space using pure H_2 gas, a mixture of 50 mol% H_2 – 50 mol% CH_4, pure CH_4 gas and pure N_2 gas. Furthermore, the effect of pressure on H_2 drainage was investigated at 100 bar. The experimental results were supplemented with pore network modeling to derive relative permeability and capillary pressure. To our knowledge this work is the first attempt to examine pore scale flow mechanisms using other gases than H_2 and N_2, and quantify the disconnected gas saturation under a

range of injection rates. The implications of our results are applicable for the choice of cushion gas and injection rate in field pilots and for the use of a substitute gas in the laboratory.

2 Methodology

2.1 Porous material

The gas drainage experiments were performed in a high-pressure micromodel with a silicon bottom and borosilicate glass top. The porous media was represented by a unique pore pattern from a natural sandstone which was etched on the micromodel bottom with 36 repetitions and an etching depth of 0.03 mm. The length and width of the porous media are 27 mm and 22 mm, respectively, with a total porosity of 0.61 and pore volume of 11.1 µL [25]. The micromodel permeability (2970 mD) was higher than in a representative rock sample due to the opening of the isolated pores to facilitate flow through the pore network. The manufacturing procedure [26] resulted in strongly hydrophilic grain surfaces (100% pure quartz) with a 100 nm roughness and a correct dimension of pore bodies and throats, ensuring realistic magnitude of capillary forces. The ports were created in each corner of the pore network for injection and production of fluids, and two separate open channels (100% porosity) were built between ports 1 to 2 and ports 3 to 4 (Fig. 1).
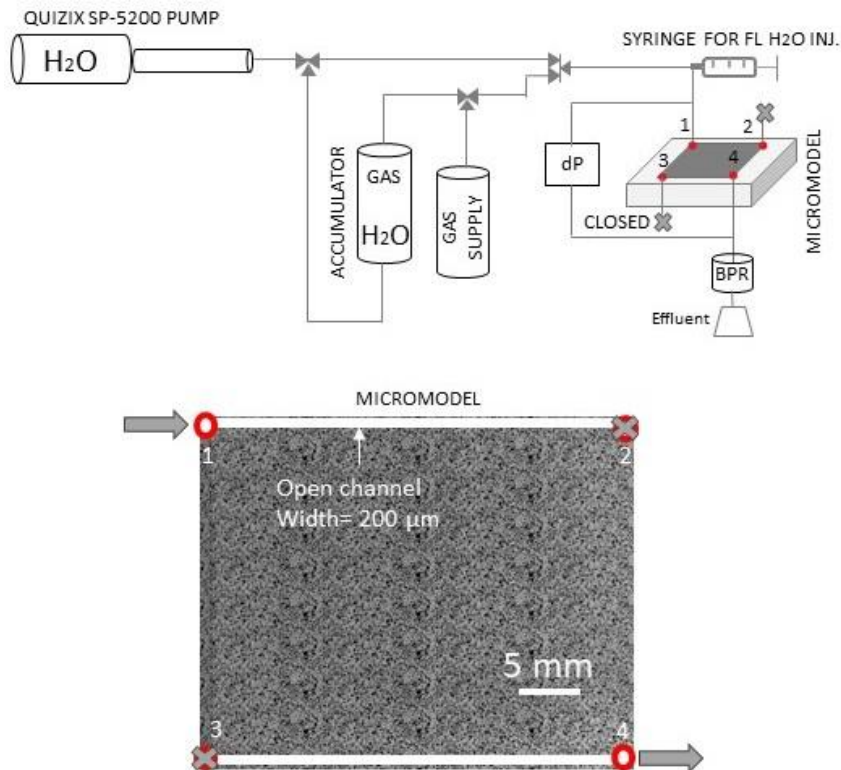
Figure 1. Top: experimental setup including the Quizix pump for H_2O injection, the gas-H_2O filled accumulator for gas injection, the syringe for dyed (FL) H_2O injection, the back pressure regulator (BPR), and the micromodel. The high-resolution microscope with a moving stage is not shown. Bottom: the micromodel with the etched irregular pore network based on a natural sandstone. The micromodel was designed with one port in each corner and two open channels (100%

porosity). The fluids were injected through port 1 and produced through port 4, keeping the remaining ports closed. The experimental setup enabled image acquisition of the entire pore network area during experiments.

2.2   Experimental setup and procedures

A syringe pump (Quizix SP-5200) controlled the injection rate of filtered and deionized H_2O and gas via an accumulator. The micromodel was mounted in a PEEK holder and placed on a moving stage (Fig. 1). Internal copper tubes ensured a constant temperature of the PEEK holder by circulating heated water. The system pressure was maintained by a back pressure regulator (EB1ZF1 Equilibar Zero Flow) connected to a pressurized 300 mL N_2 cylinder. Fluids were injected in port 1 and produced from port 4. The fluorescence-dyed (FL) H_2O was injected through a syringe in port 1, creating a color contrast between gas and H_2O on the images. The FL H_2O was prepared by mixing the distilled H_2O with fluorescein sodium salt (500 PPM $C_{20}H_{10}Na_2O_5$, F6377 Sigma-Aldrich). The experimental setup was equipped with a Zeiss microscope (Axio Zoom. V16, Zeiss), illuminated by a cold light source (CL 9000 LED). The moving stage enabled us to visualize the entire porous network area, yielding 121 unique images of different parts of the pore space with a resolution of 4.38 μm/pixel and acquisition time of 277 s. Four different gases were used in the experiments: pure H_2, 50 mol% H_2 – 50 mol% CH_4, pure CH_4 and N_2 with > 99 % purity. The gas properties are listed in Table 1.

Four different gases (Table 1) were used during gas drainage, with constant volumetric injection rates between 0.1 and 50 mL/h to establish a range of capillary numbers (Table 2). The capillary numbers (N_{Ca}) ranged between 7.1 x 10^{-9} and 4.9 x 10^{-6}, calculated according to the equation: $N_{Ca} = U$ x μ / σ, where U is the injection velocity [m/s], μ is the gas viscosity [Pa·s], and σ is the H_2-H_2O interfacial tension [N/m]. The injection velocity was calculated as follows: $U=Q / (L$ x d x $\phi)$, where Q is the injection rate [m³/s], ϕ is the micromodel porosity [faction], and L and d are the micromodel length (= 0.027 m) and depth (= 3 x 10^{-5} m), respectively. Pore pressures were kept at 30 bar and the system temperature was constant at 30 ± 1 °C, representing gas storage in shallow reservoirs. For comparison, a pilot project in Argentina tested H_2 storage in a depleted gas field at pressures down to 5-10 bar [4]. Our drainage experiments with pure H_2 were repeated at 100 bar pore pressure. A summary of experimental conditions is plotted in a Log (N_{Ca})-Log (M) flow chart (Fig. 2).

Prior to each gas drainage experiment, the porous network was cleaned with distilled H_2O, ethanol, and H_2O_2 (ACS reagent, 30 wt% solution in water) to achieve identical initial conditions. The pore network was then fully saturated with distilled H_2O and pressurized using the syringe pump and BPR to desired pore pressure. Next, 1 mL of the FL H_2O was injected into the pore network through port 1 using a syringe pump. The system was now ready for gas drainage at a constant flow rate that lasted until ~ 50 - 100 pore volumes (PVs) of gas had been injected after the gas breakthrough at the micromodel outlet. The images of the pore space were continuously taken during drainage using a high-resolution fluorescent microscope system with a movable stage. In the end, the microfluidic system was cleaned with distilled H_2O, preparing for the next experiment. Some of the experiments were repeated at the same p-T conditions to confirm reproducibility of the results.

Table 1. Fluid properties at 30 and 100 bar and 30 °C. M is defined as the viscosity ratio between gas and H_2O. The H_2-H_2O mixture viscosity (μ) was calculated assuming a 0.4% reduction of CH_4 viscosity per addition of 5 mol% H_2 [27]. The interfacial tension (σ) of H_2-CH_4 mixture was reported to be within the σ range of pure H_2 and CH_4 [28]. In our work, the $\sigma_{H2\text{-}CH4}$ was assumed to be the average of σ_{H2} and σ_{CH4} due to lack of literature data relevant for our experimental conditions.

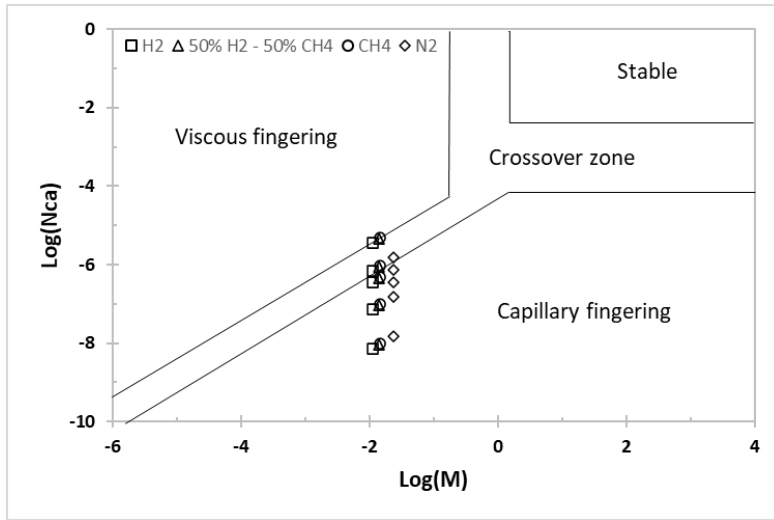| p [bar]	Gas type	μ_{gas} [Pa·s] [29]	M	$\sigma_{gas\text{-}H2O}$ [N/m] [30]
30	H_2	9.02 x 10^{-6}	1.13 x 10^{-2}	0.071
	50% H_2-50% CH_4	1.12 x 10^{-5}	1.41 x 10^{-2}	0.069
	CH_4	1.17 x 10^{-5}	1.47 x 10^{-2}	0.068
	N_2	1.85 x 10^{-5}	2.32 x 10^{-2}	0.070
100	H_2	9.12 x 10^{-6}	1.14 x 10^{-2}	0.069

Figure 2. Log (N_{Ca})-Log (M) stability diagram, where M is the viscosity ratio between gas and H_2O. The solid lines show the boundaries proposed by Zhang et al. [44], whereas the symbols locate our experiments.

2.3   Image analysis

Following the gas breakthrough in the outlet, a series of at least three images was consistently acquired, portraying the network in both fluorescence and brightfield channels. Image segmentation and subsequent analyses used an in-house coded Python algorithm [31]. The intricate pore network was divided into 288 individual units, each exhibiting a porosity ranging between 0.59 and 0.66. Within each unit, both fluorescence and brightfield channels were transformed into grayscale, thus facilitating the calculation of their corresponding grayscale histograms. The pore space was computed from the brightfield channel image using OpenCV's thresholding techniques, allowing for a precise segmentation of pore space from silicon grains. The fluorescence channel image underwent a bifurcation into two distinct classes using the Multi-Otsu algorithm from scikit-image library [32], the silicon-gas phase and the water phase highlighted by the fluorescent tracer. The quantitative evaluation of the pore network's porosity was executed by aggregating pore space pixels within each unit and subsequently dividing this by the image's size. Subsequently, gas saturation (S_g) was deduced by subtracting the quotient of water pixel count from the total pore space from 1. The determination of disconnected gas saturation (S_g^{disc}) relies on identifying gas bubbles that lack gas phase connectivity to all the four edges of the pore

network. A more detailed description of the image processing and analysis can be found elsewhere [25, 33].

For comparison, the S_g were re-calculated using a manual color thresholding method in ImageJ. The total S_g uncertainty was estimated as the squared root of the sum in quadrature of standard deviation between sequential images with equal quasi-steady-state S_g, repeated experiments (where applicable), and methodological uncertainty (code vs ImageJ). We used the ImageJ plugin FracLac [34] to calculate the fractal dimension which can be defined as the pore-filling ability of the gas.

2.4 Pore network modeling

We created a pore network model (PNM) based on the 2D image of the micromodel pore space using an open-source python-based OpenPNM package [35]. The gas-water relative permeability and capillary pressure curves were estimated by creating a 3D network, where geometric properties were assigned by an inbuilt geometry model assuming that pores are spheres and throats are cylinders. The invasion percolation algorithm was applied to generate the invasion sequence during gas drainage. Invasion percolation is a volume-controlled injection where the injected phase percolates the pore network based on the pore throat entry pressure, contrary to our rate-controlled experiments. The Stokes flow algorithm with constant pressure boundary condition was implemented to calculate relative permeability. To account for the two-phase flow, the multiphase conduit conductance model was assigned to gas and water. The input viscosities and gas-water interfacial tension were taken from Table 1. The contact angles were assumed to be identical for all gases and equal to 45 °, which is within the reported range [19, 36].

3 Results and discussion

3.1 Flow patterns

Quasi steady state gas distribution after breakthrough at the micromodel outlet are shown in Fig. 3. The resulting flow patterns can be classified into four groups, numbered according to an increasing capillary number and separated by colored boundaries in Fig. 3: 1) A single large forward (top-to-bottom) finger reaching the bottom micromodel channel, where a few minor fingers developed near the production channel because their viscous pressure exceeded the capillary pressure of the invaded pores; 2) Channelized flow with four large forward fingers distributed evenly in identical pore clusters reflecting the micromodel design with repeatable pore patterns; 3) Connection of four forward fingers through smaller transverse fingers, leaving a significant portion of pore clusters bypassed; 4) Multidirectional filling of bypassed pore space. A common observation was that the flow occurred through a preferential displacement path, developed after the gas escaped through the outlet without entering the remaining pore space. The development of the preferential flow paths was consistent with pore scale H_2 storage experiments using microfluidics [14]. Channelized flow, which was observed in our work for N_{Ca} between 9.7 x 10^{-9} and 9.1 x 10^{-8}, was also reported for microfluidic studies of CO_2 storage [37, 38].
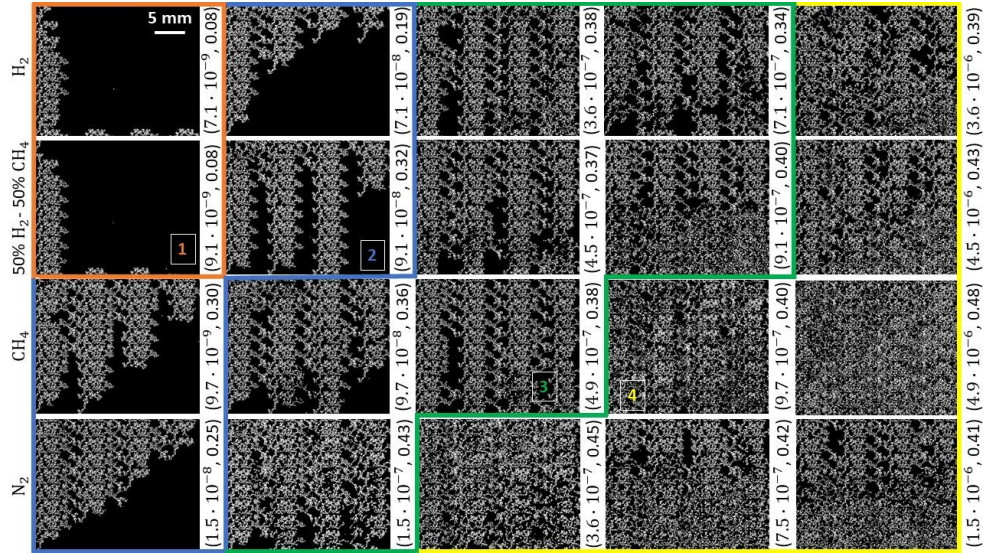
Figure 3. Gas flow patterns (white) and corresponding gas saturations (Sg) at quasi steady state after the gas breakthrough. Each row corresponds to one gas type, and the values in parentheses on the vertical right side of each image were defined as (N_{Ca}, S_g) where the N_{Ca} increases from left to right. On each image, the gas was injected from top left corner and was produced from bottom right corner, as shown in Fig. 1. The colored boundaries differentiated four different groups of flow patterns: 1) A single, large forward finger with several small fingers at the micromodel bottom; 2) Channelized flow with four large, forward fingers; 3) Connection of four forward fingers through smaller transverse fingers; 4) Multidirectional filling of bypassed pore space. The flow patterns represented typical capillary-dominated flow.

A visual inspection of flow patterns revealed that the gas drainage was dominated by capillary fingering at $N_{Ca} \leq 10^{-7}$, characterized by forward and transverse gas fingers which bypassed the large pore clusters. The characteristics of the observed capillary fingers were consistent with relevant literature [37, 39, 40]. Neither viscous fingering, with several narrow fingers and limited transverse propagation, nor crossover zone, where both capillary and viscous fingering are suppressed, were confirmed visually. Therefore, a quantitative analysis was required to determine the dominating flow regime at $N_{Ca} > 10^{-7}$. A fractal dimension (D_f) is a common parameter used to describe fluid distribution in the pore space and to identify the boundary between various flow regimes [39-42]. This parameter estimates the space-filling ability of an object by quantifying the complexity of patterns as a ratio of the change in detail to the change in scale. In this work, the D_f was calculated for the gas-invaded area, based on the box-counting method using an ImageJ FracLac plugin [34].

The D_f values (Fig. 4, Table 2) ranged between 1.65 and 1.82 with weakly increasing trend as N_{Ca} increased until $N_{Ca} > 10^{-7}$, followed by nearly constant values of $D_f \approx 1.80$. The presence of the crossover zone and viscous fingering would have been detected by the decreasing D_f. The estimated D_f range was consistent with literature [39-42], and for $N_{Ca} > 10^{-7}$ our values were close to the theoretical value (D_f = 1.82) for the capillary fingering [43]. This indicated that all our experiments were performed under the capillary-dominated flow regime, although the crossover zone was expected for $N_{Ca} > 7 \times 10^{-7}$ according to the extended *Log (N_{Ca}) - Log (M)* stability diagram in Fig. 2 [44]. Our results suggest that the boundary between capillary fingering and the crossover zone might be moved upwards in our system, but the exact boundary location could not be identified due to missing data. Note that the flow stability

diagram is sensitive to the system studied [44], and the proposed boundaries are therefore not necessarily valid for our system.

Table 2. Experimental conditions and results including injection rate (Q), capillary number (N_{Ca}), fractal dimension (D_f), gas saturation (S_g) after drainage (Fig. 5; Fig. 6), and the percentage of disconnected S_g (% S_g^{disc}) in the total S_g (Fig. 7). The following experiments were repeated confirming the reproducibility of the results: CH$_4$ (5 mL/h), N$_2$ (0.1, 5 and 10 mL/h), H$_2$ at 100 bar (5 mL/h). The provided data represents the averages derived from these experiments.

| p [bar]	Gas type	Q [mL/h]	N_{Ca}	D_f	S_g	% S_g^{disc}
30	H$_2$	0.1	7.1×10^{-9}	1.70	0.08	0 %
		1	7.1×10^{-8}	1.65	0.20	0 %
		5	3.6×10^{-7}	1.78	0.37	12 %
		10	7.1×10^{-7}	1.77	0.35	24 %
		50	3.6×10^{-6}	1.79	0.39	25 %
	50% H$_2$-50 % CH$_4$	0.1	9.1×10^{-9}	1.71	0.08	0 %
		1	9.1×10^{-8}	1.73	0.32	2 %
		5	4.5×10^{-7}	1.78	0.37	13 %
		10	9.1×10^{-7}	1.79	0.40	38 %
		50	4.5×10^{-6}	1.80	0.42	12 %
	CH$_4$	0.1	9.7×10^{-9}	1.73	0.31	0 %
		1	9.7×10^{-8}	1.76	0.36	2 %
		5	4.9×10^{-7}	1.78	0.36	5 %
		10	9.7×10^{-7}	1.79	0.39	46 %
		50	4.9×10^{-6}	1.82	0.46	36 %
	N$_2$	0.1	1.5×10^{-8}	1.72	0.26	2 %
		1	1.5×10^{-7}	1.78	0.44	46 %
		2.4	3.6×10^{-7}	1.80	0.43	60 %
		5	7.5×10^{-7}	1.80	0.43	66 %
		10	1.5×10^{-6}	1.80	0.39	39 %
100	H$_2$	0.1	7.4×10^{-9}	1.54	0.04	0 %
		1	7.4×10^{-8}	1.72	0.30	0 %
		5	3.7×10^{-7}	1.75	0.33	3 %
		10	7.4×10^{-7}	1.78	0.37	14 %
		50	3.7×10^{-6}	1.81	0.39	44 %
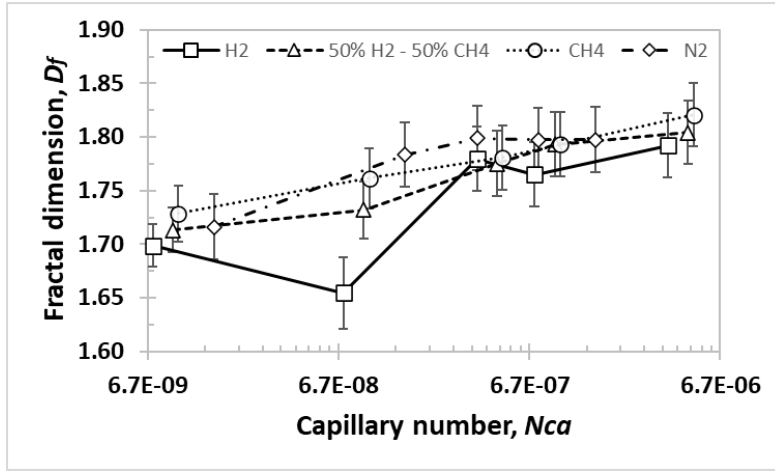
Figure 4. Fractal dimension (D_f), defined as the pore-filling ability of a gas, plotted as a function of capillary number (N_{Ca}). The D_f ranged between 1.65 and 1.82, with nearly constant values of ~ 1.80 at $N_{Ca} > 10^{-7}$ confirming the dominance of capillary-dominated flow identified in Fig. 3.

3.2   Microscopic storage capacity

Following qualitative analysis of the flow patterns in section 3.1, the 2D gas saturations (S_g) from Fig. 3 were quantified and plotted as a function of N_{Ca} to compare the microscopic storage capacities of different gases (Fig. 5, Table 2). The S_g exhibited a monotonically increasing trend until a critical N_{Ca} of ~ 7×10^{-7}, followed by a plateau region with nearly flattening S_g values. The monotonically increasing S_g values confirmed the absence of the crossover zone as concluded in section 3.1, which would otherwise have resulted in a nonmonotonic variation of S_g values [37, 41, 45]. The maximum S_g for all gases ranged between 0.39 and 0.46, representing the maximum microscopic storage capacity, i.e. available pore space for gas storage. In particular, the maximum S_g for H_2 was equal to 0.39, consistent with the literature range of 0.36 – 0.48 from core scale H_2 drainage experiments [8, 10, 11, 17, 46]. Conversely, the microfluidic H_2 and CO_2 drainage experiments reported higher maximum gas saturations: 0.50 – 0.95 [14] and 0.60 – 0.70 [37, 45], respectively.

The impact of the gas type on S_g (Fig. 5) was evident at lower N_{Ca} (< 10^{-7}). The S_g increased in a specific order, with pure H_2 gas having the lowest S_g, followed by a mixture of 50% H_2-50% CH_4, pure CH_4 gas, and finally pure N_2 gas. This increasing S_g trend reflected the increasing gas viscosity. However, the difference between the gases became less pronounced at higher N_{Ca} (> 7×10^{-7}), resulting similar S_g values. We attribute this phenomenon to a decreasing influence of viscosity when the channelized flow patterns were replaced by multidirectional filling of the bypassed, smaller pore clusters where the dominance of capillary forces increases (Fig. 3).

The saturation differences between gases have implications for using a proxy laboratory gas for H_2 and selecting a cushion gas for field pilots. Our results imply that N_2 and CH_4 are not suitable laboratory substitutes for H_2 at low injection rates (N_{Ca} < 10^{-7}). This finding correlates with existing literature that reported ~2-3 times higher N_2 drainage saturation compared to H_2 [11, 16] as well as differences in their relative permeability [17, 18]. On the other hand, N_2 and CH_4 are preferred over H_2 as cushion gas

at low injection rates due to higher drainage saturations, resulting in a larger cushion gas volume in the storage reservoir. This is beneficial for maintaining pressure support during withdrawal cycles. If a high-rate injection is technically feasible, the cushion gas volume will be unaffected by the gas type due to minimal differences in saturation between gases. Note that the micromodels are mostly suitable for qualitative analysis, implying that the 2D saturations have a limited applicability to natural reservoirs where the gravitational effects become more pronounced. Nevertheless, the monotonically increasing S_g values (Fig. 5) followed classic capillary desaturation theory [47] and were within the literature range of 3D H_2 saturations after drainage. The use of a micromodel with heterogenous pore patterns ensured that the saturations were not unrealistically overestimated, as discussed by other microfluidic studies [48, 49]. Our 2D saturations can therefore serve as a substitute for missing 3D data, covering porous media flow with different gases under a range of capillary numbers.
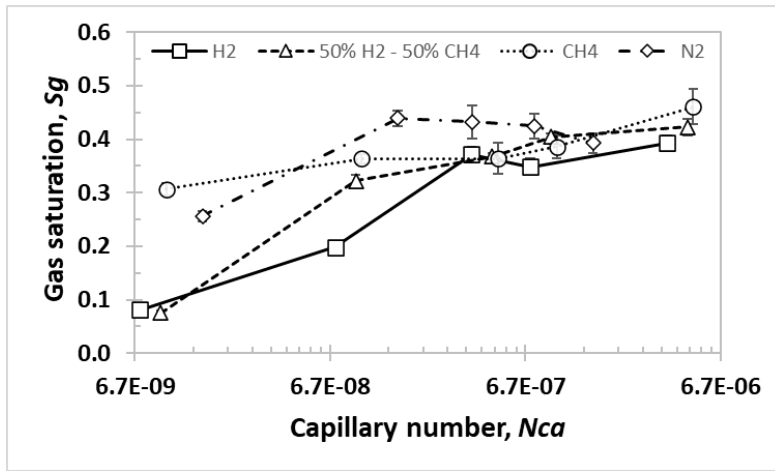

Figure 5. Gas saturations (S_g) as a function of capillary number (N_{Ca}), where maximum S_g values represent microscopic gas storage capacity of the pore space. The S_g increased with the increasing N_{Ca} and followed the order of $H_2 <$ 50% H_2–- 50% $CH_4 < CH_4 < N_2$, until a critical value of 7 x 10^{-7} was reached. In the plateau region at $N_{Ca} >$ 7 x 10^{-7}, the S_g converged to similar values for all gases with a maximum gas saturation between 39 % and 46 % of the pore space.

3.2.1 Effect of pressure

The impact of pressure on the H_2 drainage was examined at an elevated pressure of 100 bar, resulting in similar S_g (Fig. 6) and flow patterns (supplementary Fig. S1). We did not observe any significant pressure effect likely due to similar H_2 viscosity and H_2-H_2O interfacial tension at 30 and 100 bar. The H_2 viscosity increases by 1% and the interfacial tension decreases by 2% from 30 to 100 bar [50]. Insignificant pressure effect on the initial S_g was also reported for pore scale H_2 drainage [10, 13]. However, this does not necessarily imply that imbibition experiments will be unaffected by pressure. It was shown that H_2 recovery after imbibition decreased with pressure, despite similar initial S_g [10]. In addition, the difference in S_g after drainage at 30 and 100 bar can potentially be greater for N_2 and CH_4 than for H_2 due to the increasing impact of pressure on gas properties. From 30 to 100 bar, the N_2 viscosity increases by 9% and the interfacial tension decreases by 6%, whereas the corresponding properties for CH_4 change as follows: increase by 18% and decrease by 10%, respectively.
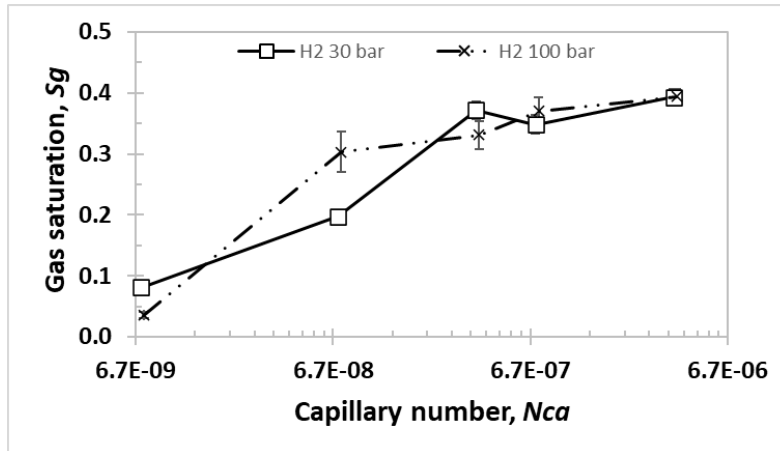
Figure 6. Effect of pressure on H$_2$ saturations (S_g) after drainage at 30 and 100 bar as a function of capillary number (N_{Ca}). No clear pressure impact was observed on the S_g. The H$_2$ flow patterns at 30 and 100 bar were similar, shown in the supplementary materials (Fig. S1).

3.3 Gas connectivity

Gas connectivity, as an indicator, controls the effectiveness of gas propagation through the pore space from the inlet to the outlet. The gas phase is considered disconnected when it is trapped in the pore space by the surrounding water without having an excess to the inlet and outlet. In sections 3.1 and 3.2, the S_g values were calculated as the total amount of connected and disconnected gas (Fig. 3; 5; 6). At lower $N_{Ca} < 10^{-7}$, the injection resulted mainly in the connected gas phase with only few small, disconnected ganglia (Fig. 7, Table 2), corroborating previous studies [8, 10, 11]. However, image analysis (Fig. 8) indicated that the gas phase underwent disconnection across the pore space at higher $N_{Ca} > 10^{-7}$ due to Roof snap-off [51], as described in detail in our previous work [12]. The percentage of disconnected gas in the total S_g was quantified (Fig. 7) showing that connectivity was relatively high for H$_2$, with less than 25% of disconnected gas. In contrast, N$_2$ connectivity was significantly reduced, with the percentage of disconnected ganglia ranging from 39% to 76%. Although the gas disconnection was promoted by high N_{Ca}, no linear relationship between the quantity of disconnected gas and N_{Ca} was observed.
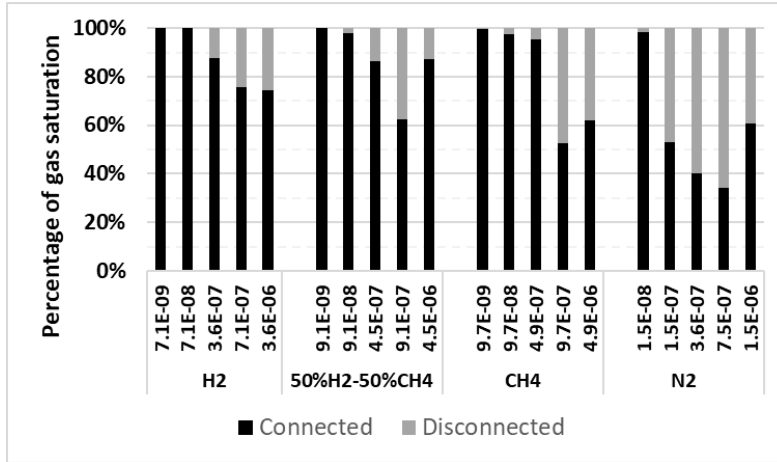
Figure 7. Percentage of the connected (black) and disconnected (grey) gas in the total gas saturation (S_g). Each column corresponds to one gas type, and the capillary number (N_{Ca}) values are printed on the horizontal axis. The gas disconnection occurred due to Roof snap-off, predominantly at higher $N_{Ca} > 10^{-7}$. The gas connectivity for H_2 was relatively high, contrary to N_2 with the percentage of disconnected gas ranging between 39% and 76%.

The disconnected gas ganglia varied in terms of size and distribution (Fig. 8). We identified small and large ganglia, which could be randomly distributed (Fig.8, bottom row) or locally concentrated (Fig. 8, top row) in the pore space. The small ganglia (Fig. 8, left column) were less than ~10^8 μm^3, being one order of magnitude smaller than the large ganglia (Fig. 8, right column). The ganglia distribution was defined based on their relative proximity to each other. The local ganglia tended to concentrate locally in well-defined, limited pore clusters and spanned over several neighboring pores (Fig. 8, top row). The random ganglia were located in the non-neighboring pore clusters in different parts of the micromodel (Fig. 8, bottom row). The ganglia size agreed with previous H_2 studies, showing that the disconnected ganglia were larger than the average pore size [8, 10, 11].

A high degree of gas disconnection at higher N_{Ca} implies that the injection rate is a crucial parameter affecting not only gas saturation but also its connectivity. When designing an optimal storage scheme, the injection rate must yield the highest possible gas saturation with the least amount of disconnected gas. In section 3.2, it was shown that the maximum gas saturation could be achieved at $N_{Ca} > 7 \times 10^{-7}$, falling within the N_{Ca} range where the gas disconnection is promoted. The presence of the disconnected H_2 ganglia represents a risk of H_2 loss because these ganglia may dissolve in water, mostly pronounced for small, randomly distributed H_2 ganglia. We therefore propose the optimal N_{Ca} of 1×10^{-7} for H_2 injection, equivalent to the field scale injection rate of ~50 thousand m^3/day assuming the experimental injection velocity and well perforation length of 30 m. Another implication is that CH_4 is preferred over N_2 as cushion gas due to better CH_4 connectivity, leading to a more controlled pressure support during H_2 withdrawal.

(CH$_4$, $4.9 \cdot 10^{-7}$, 0.38, 5 %)   (50% H$_2$-50% CH$_4$, $9.1 \cdot 10^{-7}$, 0.40, 38 %)

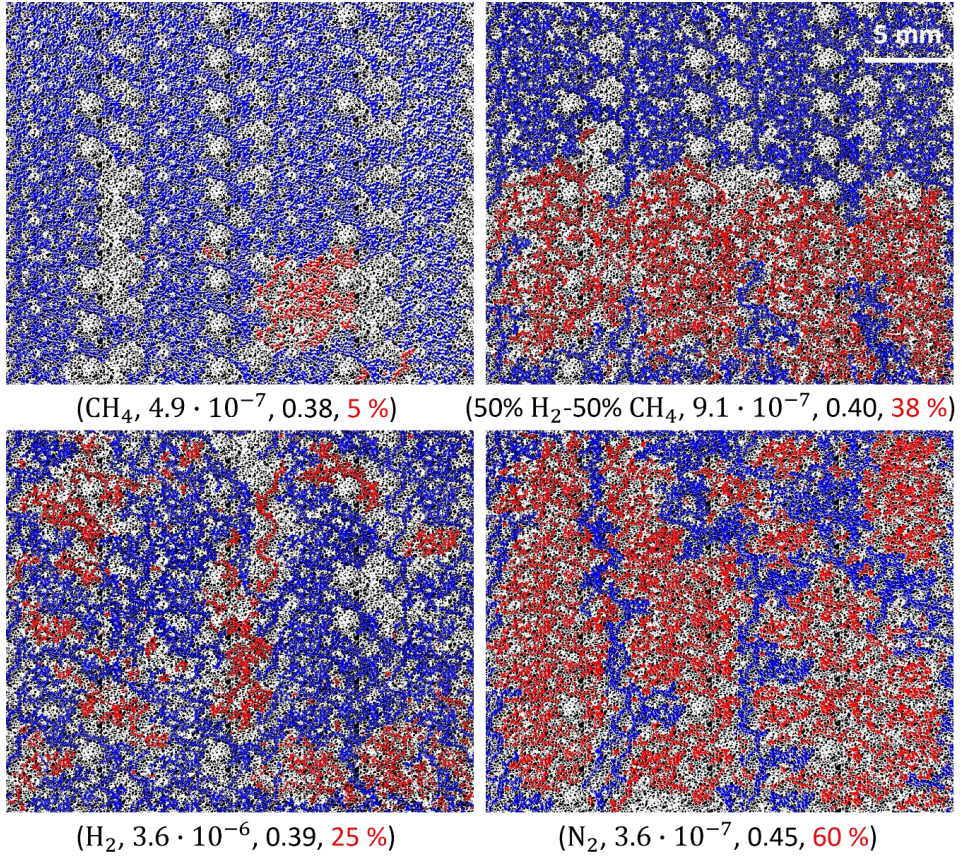(H$_2$, $3.6 \cdot 10^{-6}$, 0.39, 25 %)   (N$_2$, $3.6 \cdot 10^{-7}$, 0.45, 60 %)

Figure 8. Fluid distribution in the pore space: disconnected gas ganglia (red), connected gas phase (blue) and water (white). The rock grains are shown in black. We classified the disconnected gas ganglia in terms of size and distribution: small (left column) and large ganglia (right column), distributed locally (top row) or randomly (bottom row). The values in parentheses were defined as (gas type, N_{Ca}, S_g, percentage of the disconnected gas ganglia in the S_g).

3.4   Relative permeability and capillary pressure from pore network modeling

A pore network model (PNM) was created in OpenPNM using a 2D image of the pore network from our experiments. The absolute permeability and porosity of a 3D network were estimated to 573 mD and 20 %, respectively. This was a reduction from the original micromodel properties of 2970 mD and 61 %, respectively, because the isolated pores were removed from a 3D network to maintain the topological health of the network. The drainage H$_2$-H$_2$O relative permeability (K_r) and capillary pressure (P_c) curves (Fig. 9) were computed without trapping of the wetting phase (H$_2$O), resulting in the irreducible H$_2$O saturation (S_{wirr}) equal to zero. The inclusion of H$_2$O trapping assumes that H$_2$O remains connected through thin wetting films along the rock surfaces, that would have yielded the S_{wirr} values higher than zero. The resulting K_r and P_c curves were fitted with a LET-correlation [52, 53], and the LET parameters are provided in the supplementary materials. The K_r shape was similar to a core flooding H$_2$-H$_2$O experiment [17], characterized by low K_r values (< 0.2) in the mid-S_w region of 0.2-0.8. However, the K_r from PNM resulted in a lower crosspoint value of S_w = 0.4 (K_{rg} = K_{rw} = 0.02), indicating a less

hydrophilic system. The 2D H_2 distribution in the pore space at arbitrary saturation points is shown in Fig. 10.

In addition to H_2, the K_r and P_c curves were also estimated for CH_4, 50% H_2-CH_4 mixture and N_2, demonstrating identical results likely due to similar input viscosity, interfacial tension and contact angles. In contrast, core flooding K_r measurements showed differences between H_2, N_2 and CH_4 [17, 18]. Our PNM was generated with one set of fixed input parameters, unlike another quasi-static PNM study with focus on uncertainty quantification based on the range of fluid and rock properties [54]. I this study the authors found that the K_r and P_c curves showed hysteresis between drainage and imbibition. The magnitude of the hysteresis was shown to be affected by contact angles, rock structure and clay content. The range of flow functions from PNM enables a fine starting point for sensitivity studies to determine the most influencing parameters. However, this should be done with caution due to challenges with upscaling of pore scale phenomena to reservoir scale. Pore scale models do not properly account for reservoir scale aspects such as gravity and viscous forces. If available, the core flooding K_r must always be the first choice for input in reservoir models.
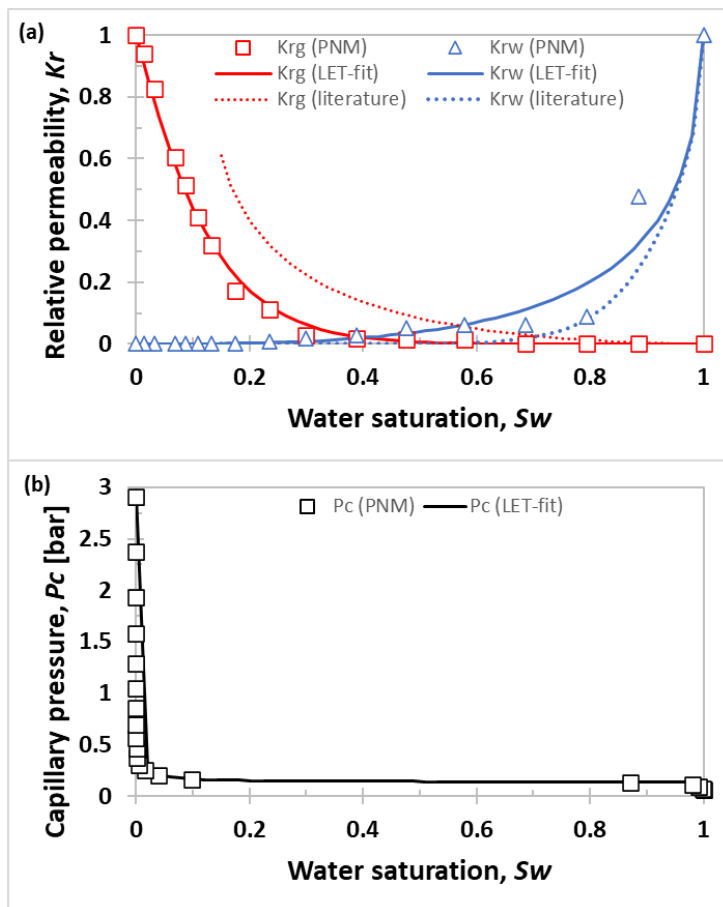

Figure 9. Drainage H_2-H_2O relative permeability (a) and capillary pressure (b) derived from pore network modeling (PNM). The model did not include trapping of the wetting phase (H_2O), implying that the irreducible H_2O saturation (S_{wirr}) reached zero. The data points from PNM (squares and triangles) were fitted with a LET-correlation (solid curves). The PNM relative

permeability was compared with the literature relative permeability (dashed curves) derived from a core flooding experiment [17].
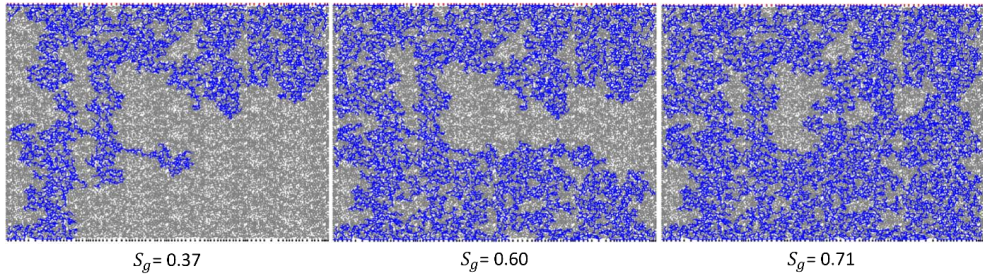

| S_g = 0.37 | S_g = 0.60 | S_g = 0.71 |

Figure 10. H_2 (blue) and H_2O (grey) distribution in the 2D pore network model at arbitrary H_2 saturation points (S_g) derived from relative permeability calculations using pore network modeling. H_2 was injected from top to bottom.

4   Conclusions

We performed a series of gas drainage experiments in a micromodel at 30 bar and 30 °C, relevant for hydrogen storage in shallow porous reservoirs. Visual and fractal dimension analysis revealed gas flow through preferred flow paths in the capillary-dominated regime. At lower injection rates, the gas saturations after drainage were higher for gases with higher viscosities. Specifically, pure H_2 gas exhibited the lowest gas saturation, followed by the mixture of 50% H_2 – 50% CH_4, then pure CH_4 gas, and finally pure N_2 gas ending at the highest saturation. As the injection rates increased, the difference in saturations between gases minimized, resulting in similar maximum gas saturations ranging from 39% to 46%. Despite being beneficial for achieving the maximum gas saturations, high-rate injections resulted in a significantly higher amount of disconnected gas ganglia. This unfavorable outcome was more pronounced for N_2, with a substantial fraction (up to 76%) of disconnected gas ganglia in the total gas saturation. When tested at an elevated pressure of 100 bar, there was no apparent pressure effect on H_2 flow patterns and saturation. The H_2-H_2O relative permeability and capillary pressure curves, derived from pore network modeling, were similar to those reported from core scale measurements. Our results imply that the use of a substitute gas for H_2 is not recommended at lower injection rates. To minimize the amount of disconnected gas yet maintaining the maximum gas saturation, the optimal field scale injection rate should correspond to the capillary number in the order of 10^{-7}. Future studies should aim at coupling our results with microbial effects and expanding the scope to include core flooding experiments.

Author contributions

Maksim Lysyy: Conceptualization, Methodology, Investigation, Formal analysis, Writing – original draft. **Na Liu**: Conceptualization, Methodology, Investigation, Software, Writing - Review & Editing. **David Landa-Marbán**: Software, Writing - Review & Editing. **Geir Ersland**: Writing - Review & Editing, Supervision, Funding acquisition. **Martin Fernø**: Writing - Review & Editing, Supervision, Funding acquisition.

Acknowledgments

References

1.   Agency, I.E., *Global Hydrogen Review 2022*. 2022: OECD Publishing.
2.   Carden, P.O. and L. Paterson, *Physical, Chemical and Energy Aspects of Underground Hydrogen Storage.* International Journal of Hydrogen Energy, 1979. **4**(6): p. 559-569.
3.   Muhammed, N.S., et al., *A review on underground hydrogen storage: Insight into geological sites, influencing factors and future outlook.* Energy Reports, 2022. **8**: p. 461-499.
4.   Pérez, A., et al., *Patagonia Wind - Hydrogen Project: Underground Storage and Methanation*, in *21st world hydrogen energy conference*. 2016: Zaragoza, Spain.
5.   RAG, *RAG Austria AG - Underground Sun Storage: Final Report Public 13*. 2020.
6.   Panfilov, M., *Underground and pipeline hydrogen storage. In Compendium of hydrogen energy*. 2016: Woodhead Publishing.
7.   Smigan, P., et al., *Methanogenic Bacteria as a Key Factor Involved in Changes of Town Gas Stored in an Underground Reservoir.* Fems Microbiology Ecology, 1990. **73**(3): p. 221-224.
8.   Jangda, Z., et al., *Pore-scale visualization of hydrogen storage in a sandstone at subsurface pressure and temperature conditions: Trapping, dissolution and wettability.* Journal of Colloid and Interface Science, 2023. **629**: p. 316-325.
9.   Jha, N.K., et al., *Pore scale investigation of hydrogen injection in sandstone via X-ray micro-tomography.* International Journal of Hydrogen Energy, 2021. **46**(70): p. 34822-34829.
10.   Thaysen, E.M., et al., *Pore-scale imaging of hydrogen displacement and trapping in porous media.* International Journal of Hydrogen Energy, 2023. **48**(8): p. 3091-3106.
11.   Zhang, Y.H., et al., *Pore-Scale Observations of Hydrogen Trapping and Migration in Porous Rock: Demonstrating the Effect of Ostwald Ripening.* Geophysical Research Letters, 2023. **50**(7).
12.   Lysyy, M., G. Ersland, and M. Ferno, *Pore-scale dynamics for underground porous media hydrogen storage.* Advances in Water Resources, 2022. **163**.
13.   Lysyy, M., et al., *Microfluidic hydrogen storage capacity and residual trapping during cyclic injections: Implications for underground storage.* International Journal of Hydrogen Energy, 2023.
14.   Song, H., et al., *Underground hydrogen storage in reservoirs: pore-scale mechanisms and optimization of storage capacity and efficiency.* Applied Energy, 2023. **337**.
15.   Wang, J.L., et al., *Pore-scale modelling on hydrogen transport in porous media: Implications for hydrogen storage in saline aquifers.* International Journal of Hydrogen Energy, 2023. **48**(37): p. 13922-13933.

16. Al-Yaseri, A., et al., *Initial and residual trapping of hydrogen and nitrogen in Fontainebleau sandstone using nuclear magnetic resonance core flooding.* International Journal of Hydrogen Energy, 2022. **47**(53): p. 22482-22494.

17. Lysyy, M., et al., *Hydrogen Relative Permeability Hysteresis in Underground Storage.* Geophysical Research Letters, 2022. **49**(17).

18. Rezaei, A., et al., *Relative Permeability of Hydrogen and Aqueous Brines in Sandstones and Carbonates at Reservoir Conditions.* Geophysical Research Letters, 2022. **49**(12).

19. Hashemi, L., et al., *A comparative study for H2–CH4 mixture wettability in sandstone porous rocks relevant to underground hydrogen storage.* Advances in Water Resources, 2022. **163**.

20. van Rooijen, W., et al., *Microfluidics-based analysis of dynamic contact angles relevant for underground hydrogen storage.* Advances in Water Resources, 2022. **164**.

21. Ali, M., et al., *Hydrogen wettability of quartz substrates exposed to organic acids; Implications for hydrogen geo-storage in sandstone reservoirs.* Journal of Petroleum Science and Engineering, 2021. **207**.

22. Iglauer, S., M. Ali, and A. Keshavarz, *Hydrogen Wettability of Sandstone Reservoirs: Implications for Hydrogen Geo-Storage.* Geophysical Research Letters, 2021. **48**(3).

23. Hashemi, L., et al., *Contact angle measurement for hydrogen/brine/sandstone system using captive-bubble method relevant for underground hydrogen storage.* Advances in Water Resources, 2021. **154**.

24. Yekta, A.E., et al., *Determination of Hydrogen-Water Relative Permeability and Capillary Pressure in Sandstone: Application to Underground Hydrogen Injection in Sedimentary Formations.* Transport in Porous Media, 2018. **122**(2): p. 333-356.

25. Benali, B., et al., *Pore-scale bubble population dynamics of CO2-foam at reservoir pressure.* International Journal of Greenhouse Gas Control, 2022. **114**.

26. Buchgraber, M., et al., *Creation of a dual-porosity micromodel for pore-level visualization of multiphase flow.* Journal of Petroleum Science and Engineering, 2012. **86-87**: p. 27-38.

27. Alkhatib, I.I.I., et al., *Accurate Predictions of the Effect of Hydrogen Composition on the Thermodynamics and Transport Properties of Natural Gas.* Industrial & Engineering Chemistry Research, 2022. **61**(18): p. 6214-6234.

28. Mirchi, V., M. Dejam, and V. Alvarado, *Interfacial tension and contact angle measurements for hydrogen-methane mixtures/brine/oil-wet rocks at reservoir conditions.* International Journal of Hydrogen Energy, 2022. **47**(82): p. 34963-34975.

29. Linstrom, P.J. and W.G. Mallard, *The NIST Chemistry WebBook: A chemical data resource on the internet.* Journal of Chemical and Engineering Data, 2001. **46**(5): p. 1059-1063.

30. Massoudi, R. and A.D. King, *Effect of Pressure on Surface-Tension of Water - Adsorption of Low-Molecular Weight Gases on Water at 25 Degrees.* Journal of Physical Chemistry, 1974. **78**(22): p. 2262-2266.

31. Benali, B., et al., *Pore-level Ostwald ripening of CO2 foams at reservoir pressure.* Transport in Porous Media, 2023.

32. Van der Walt, S., et al., *scikit-image: image processing in Python.* PeerJ, 2014. **2**: p. e453.

33. Liu, N., et al., *Pore-scale study of microbial hydrogen consumption and wettability alteration during underground hydrogen storage.* Frontiers in Energy Research, 2023. **11**.

34. Karperien, A., *FracLac for ImageJ - Fractal Dimension and Lacunarity.* https://imagej.nih.gov/ij/plugins/fraclac/fraclac.html, 2007.

35. Gostick, J., et al., *OpenPNM: A Pore Network Modeling Package.* Computing in Science & Engineering, 2016. **18**(4): p. 60-74.

36. Lysyy, M., G. Ersland, and M. Fern, *Pore-scale dynamics for underground porous media hydrogen storage.* Advances in Water Resources, 2022. **163**.

37. Chang, C., et al., *Impacts of Pore Network-Scale Wettability Heterogeneity on Immiscible Fluid Displacement: A Micromodel Study.* Water Resources Research, 2021. **57**(9).

38. Chang, C., et al., *Impacts of Mixed-Wettability on Brine Drainage and Supercritical CO2 Storage Efficiency in a 2.5-D Heterogeneous Micromodel.* Water Resources Research, 2020. **56**(7).

39. Chen, Y.F., et al., *Visualizing and quantifying the crossover from capillary fingering to viscous fingering in a rough fracture.* Water Resources Research, 2017. **53**(9): p. 7756-7772.

40. Guo, F. and S.A. Aryana, *An Experimental Investigation of Flow Regimes in Imbibition and Drainage Using a Microfluidic Platform.* Energies, 2019. **12**(7).

41. Wu, D.S., et al., *Role of Pore-Scale Disorder in Fluid Displacement: Experiments and Theoretical Model.* Water Resources Research, 2021. **57**(1).

42. Zakirov, T.R. and M.G. Khramchenkov, *Pore-scale study of the anisotropic effect on immiscible displacement in porous media under different wetting conditions and capillary numbers.* Journal of Petroleum Science and Engineering, 2022. **208**.

43. Wilkinson, D. and J.F. Willemsen, *Invasion Percolation - a New Form of Percolation Theory.* Journal of Physics a-Mathematical and General, 1983. **16**(14): p. 3365-3376.

44. Zhang, C.Y., et al., *Influence of Viscous and Capillary Forces on Immiscible Fluid Displacement: Pore-Scale Experimental Study in a Water-Wet Micromodel Demonstrating Viscous and Capillary Fingering.* Energy & Fuels, 2011. **25**(8): p. 3493-3505.

45. Song, Y.C., et al., *Pore-scale visualization study on CO2 displacement of brine in micromodels with circular and square cross sections.* International Journal of Greenhouse Gas Control, 2020. **95**.

46. Boon, M. and H. Hajibeygi, *Experimental characterization of H-2/water multiphase flow in heterogeneous sandstone rock at the core scale relevant for underground hydrogen storage (UHS).* Scientific Reports, 2022. **12**(1).

47. Guo, H., K.P. Song, and R. Hilfer, *A Brief Review of Capillary Number and its Use in Capillary Desaturation Curves.* Transport in Porous Media, 2022. **144**(1): p. 3-31.

48. Chang, C., et al., *Scaling the impacts of pore-scale characteristics on unstable supercritical CO2-water drainage using a complete capillary number.* International Journal of Greenhouse Gas Control, 2019. **86**: p. 11-21.

49. Zhang, J., et al., *Study on the effect of pore-scale heterogeneity and flow rate during repetitive two-phase fluid flow in microfluidic porous media.* Petroleum Geoscience, 2021. **27**(2).

50. Chow, Y.T.F., G.C. Maitland, and J.P.M. Trusler, *Interfacial tensions of (H2O + H2) and (H2O + CO2 + H2) systems at temperatures of (298–448) K and pressures up to 45 MPa.* Fluid Phase Equilibria, 2018. **475**: p. 37-44.

51. Roof, J.G., *Snap-Off of Oil Droplets in Water-Wet Pores.* Society of Petroleum Engineers Journal, 1970. **10**(1): p. 85-&.

52. Lomeland, F., E. Ebeltoft, and W.H. Thomas. *A new versatile relative permeability correlation.* in *International Symposium of the Society of Core Analysts*. 2005. Toronto, Canada.

53. Lomeland, F., E. Ebeltoft, and W.H. Thomas. *A new versatile capillary pressure correlation.* in *International Symposium of the Society of Core Analysts*. 2008. Abu Dhabi, UAE.

54. Hashemi, L., M. Blunt, and H. Hajibeygi, *Pore-scale modelling and sensitivity analyses of hydrogen-brine multiphase flow in geological porous media.* Scientific Reports, 2021. **11**(1).

Supplementray materials

Impact of gas type on microfluidic drainage experiments and pore network modeling relevant for underground hydrogen storage

Maksim Lysyy[*1], Na Liu[1], David Landa-Marbán[2], Geir Ersland[1], Martin Fernø[1,2]

[1]Dept. of Physics and Technology, University of Bergen, Allégaten 55, Bergen 5007, Norway

[2]NORCE Norwegian Research Centre AS, Nygårdsgaten 112, Bergen 5008, Norway

*Corresponding author:

E-mail address: Maksim.Lysyy@uib.no (M. Lysyy)

This supporting information contains the images of H_2 flow patterns at 30 and 100 bar and relative permeability and capillary pressure data, derived from pore network modeling (PNM). First, the tabulated data from PNM is presented in Tables 1 and 2. This data was then fitted to a LET correlation for relative permeability and capillary pressure [1, 2]. The LET fitting parameters for relative permeability are presented in Table 3 and the resulting data points are tabulated in Table 4. For capillary pressure, the LET fitting parameters are presented in Table 5 and the resulting data points are tabulated in Table 6.
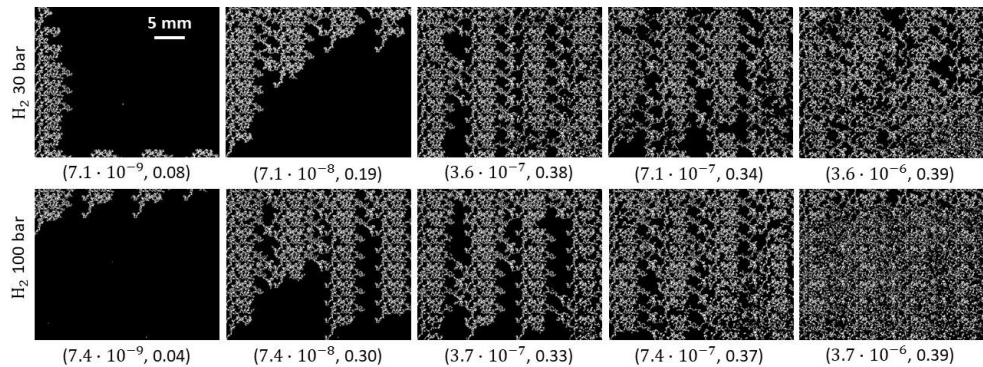

Figure S1. Comparison of H_2 flow patterns (white) at 30 bar and 100 bar, with increasing capillary number (N_{Ca}) from left to right. Each row corresponds to a particular pressure, and the gas saturation (S_g) is indicated on each image.

Table 1. Tabulated relative permeability values from pore network modeling (PNM) for H2 (Krg) and H2O (Krw).

Sw	Krg	Krw
1	0	1
0.886	1.26E-06	0.476
0.794	1.47E-06	0.090
0.687	2.80E-06	0.063
0.580	0.015	0.061
0.476	0.015	0.052
0.388	0.019	0.027
0.300	0.030	0.019
0.235	0.112	0.007
0.175	0.171	0.003
0.133	0.320	3.74E-04
0.109	0.412	9.35E-05
0.087	0.514	3.75E-05
0.069	0.606	2.00E-05
0.033	0.828	5.86E-06
0.014	0.941	2.51E-06
0	1	1.00E-06

Table 2. Tabulated capillary pressure values (Pc) from pore network modeling (PNM).

Sw	Pc [bar]
1	0.06
0.998	0.07
0.991	0.09
0.980	0.11
0.871	0.14
0.098	0.17
0.039	0.20
0.015	0.25
0.006	0.31
2.27E-03	0.38
8.03E-04	0.46
3.28E-04	0.57
8.04E-05	0.70
1.72E-05	0.86
5.15E-06	1.05
1.82E-06	1.29
3.35E-07	1.58
5.90E-08	1.94
2.90E-08	2.37
0	2.91

Table 3. LET fitting parameters for PNM relative permeability.

Lw	2.5
Ew	7
Tw	0.7
Lg	5.5
Eg	7
Tg	1

Table 4. Tabulated relative permeability values from LET correlation for H_2 (Krg) and H_2O (Krw).

Sw	Krg	Krw
0	1	0
0.020	0.862	8.62E-06
0.041	0.736	4.95E-05
0.061	0.622	1.38E-04
0.082	0.523	2.89E-04
0.102	0.436	5.12E-04
0.122	0.363	8.21E-04
0.143	0.300	1.23E-03
0.163	0.247	1.74E-03
0.184	0.203	0.002
0.204	0.166	0.003
0.224	0.136	0.004
0.245	0.111	0.005
0.265	0.090	0.006
0.286	0.073	0.008
0.306	0.059	0.009
0.327	0.047	0.011
0.347	0.038	0.013
0.367	0.030	0.016
0.388	0.024	0.019
0.408	0.019	0.021
0.429	0.015	0.025
0.449	0.012	0.028
0.469	0.009	0.033
0.490	0.007	0.037
0.510	0.005	0.042
0.531	0.004	0.047
0.551	0.003	0.053
0.571	2.36E-03	0.060
0.592	1.74E-03	0.067
0.612	1.27E-03	0.075
0.633	9.15E-04	0.084
0.653	6.47E-04	0.094
0.673	4.50E-04	0.104
0.694	3.06E-04	0.116
0.714	2.04E-04	0.129
0.735	1.32E-04	0.143
0.755	8.25E-05	0.159
0.776	4.98E-05	0.177
0.796	2.87E-05	0.197
0.816	1.57E-05	0.220
0.837	8.00E-06	0.245

0.857	3.75E-06	0.275
0.878	1.57E-06	0.310
0.898	5.62E-07	0.350
0.918	1.61E-07	0.400
0.939	3.24E-08	0.463
0.959	3.41E-09	0.547
0.980	7.38E-11	0.674
1	0	1

Table 5. LET fitting parameters for PNM capillary pressure.

Lp	1
Ep	900
Tp	1
Lt	1
Et	10
Tt	1
Pc,max	291 kPa
Pc,th	14 kPa

Table 6. Tabulated capillary pressure values from LET correlation.

Sw	Pc [kPa]
0	291
0.020	28.0253
0.041	21.0487
0.061	18.6402
0.082	17.4198
0.102	16.6822
0.122	16.1883
0.143	15.8344
0.163	15.5684
0.184	15.3612
0.204	15.1952
0.224	15.0592
0.245	14.9457
0.265	14.8497
0.286	14.7673
0.306	14.6959
0.327	14.6333
0.347	14.5781
0.367	14.529
0.388	14.4851
0.408	14.4456
0.429	14.4098
0.449	14.3772
0.469	14.3475
0.490	14.3202
0.510	14.2952
0.531	14.272
0.551	14.2506
0.571	14.2306
0.592	14.2121
0.612	14.1948

0.633	14.1786		0.837	14.06
0.653	14.1634		0.857	14.0513
0.673	14.1491		0.878	14.0429
0.694	14.1357		0.898	14.035
0.714	14.1231		0.918	14.0274
0.735	14.1111		0.939	14.0201
0.755	14.0998		0.959	14.0131
0.776	14.0891		0.980	14.0064
0.796	14.0789		1	14
0.816	14.0692			

References

1. Lomeland, F., E. Ebeltoft, and W.H. Thomas. *A new versatile relative permeability correlation*. in *International Symposium of the Society of Core Analysts*. 2005. Toronto, Canada.
2. Lomeland, F., E. Ebeltoft, and W.H. Thomas. *A new versatile capillary pressure correlation*. in *International Symposium of the Society of Core Analysts*. 2008. Abu Dhabi, UAE.

Paper 2
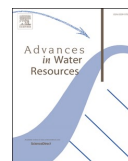
Pore-scale dynamics for underground porous media hydrogen storage

Maksim Lysyy [*], Geir Ersland, Martin Fernø

Department of Physics and Technology, University of Bergen, Allégaten 55, 5007 Bergen, Norway

ARTICLE INFO

ABSTRACT

Underground hydrogen storage (UHS) has been launched as a catalyst to the low-carbon energy transitions. The limited understanding of the subsurface processes is a major obstacle for rapid and widespread UHS implementation. We use microfluidics to experimentally describe pore-scale multiphase hydrogen flow in an aquifer storage scenario. In a series of drainage-imbibition experiments we report the effect of capillary number on hydrogen saturations, displacement/trapping mechanisms, dissolution kinetics and contact angle hysteresis. We find that the hydrogen saturation after injection (drainage) increases with increasing capillary number. During hydrogen withdrawal (imbibition) two distinct mechanisms control the displacement and residual trapping – I1 and I2 imbibition mechanisms, respectively. Local hydrogen dissolution kinetics show dependency on injection rate and hydrogen cluster size. Dissolved global hydrogen concentration corresponds up to 28% of reported hydrogen solubility, indicating pore-scale non-equilibrium dissolution. Contact angles show hysteresis and vary between 17 and 56° Our results provide key UHS experimental data to improve understanding of hydrogen multiphase flow behaviour.

1. Introduction

As a no-carbon energy carrier, hydrogen may play a significant role in the energy transition needed to reach net-zero societies. Hydrogen implementation in transport, heating and power generation will require large-scale seasonal storage, and underground hydrogen storage (UHS) in aquifers has been proposed as one option (Carden and Paterson 1979; Lord et al., 2014). Technical aspects of UHS are similar to natural gas storge (UGS), where gas is injected in the subsurface (cushion gas) and is then withdrawn at peak demand (working gas). Although knowledge transfer from UGS is possible, high hydrogen mobility and its potential biogeochemical activity (Panfilov 2010) calls for caution and revision of conventional storage practices. Experience with commercial underground storage of pure hydrogen is limited to salt caverns (Ozarslan 2012). Underground aquifers have been used for town gas storage only, with hydrogen content up to 50–60% (Smigan et al., 1990; Panfilov 2016).

Hydrogen injection and withdrawal in underground porous formations involve complex displacement and trapping mechanisms, controlled by hydrogen flow properties and interactions with reservoir fluids and rocks. The understanding of hydrogen flow physics and trapping in porous media is therefore essential to establishing reliable storage models for lab-scale tests, feasibility studies and piloting. Most

porous media research on hydrogen is mainly focused on biogeochemical interactions (Berta et al., 2018; Flesch et al., 2018; Bo et al., 2021), but there are fewer fundamental studies reporting multiphase flow data with the dominance of the numerical modelling approaches (Lubon and Tarkowski 2021; Lysyy et al., 2021; Mahdi Kanaani 2022). Most numerical studies use extrapolated flow functions not specifically measured for hydrogen; thus experimental efforts are needed to improve the hydrogen flow modelling. A single reported experimental core-scale study found that hydrogen-water relative permeability is independent of pressure and temperature conditions (Yekta et al., 2018). A major concern is that the displacement is prone to front instabilities and viscous fingering due to an unfavourable hydrogen-water mobility ratio. Microscopic viscous fingers were confirmed with laboratory models (Paterson 1983). In addition, hydrogen withdrawal will be associated with loss caused by residual and dissolution trapping. Unlike CO_2 sequestration, residual and dissolution trapping are not desirable in UHS as it leads to unrecoverable hydrogen, thus representing a permanent loss (Carden and Paterson 1979). UHS involves many injection-withdrawal cycles, and the residually trapped hydrogen may reconnect during subsequent hydrogen injections, known as hysteresis.

Microfluidic experiments are perfectly suited for visualization of porous media hydrogen flow, thereby providing direct evidence of the proposed displacement and trapping mechanisms to corroborate core-

---

* Corresponding author.
E-mail address: maksim.lysyy@uib.no (M. Lysyy).

scale measurements. Due to the 2D nature of the micromodels and their limited volume, microfluidic experiments should mainly focus on the qualitative rather than quantitative results. Extrapolation of quantitative 2D data to 3D natural environment should be done with caution, best achieved through pore-scale modelling. In particular hydrogen contact angle measurements assist the pore-scale models in estimating upscaled relative permeability and capillary pressure functions, which can be used as input for numerical studies at field scale (Hashemi et al., 2021).

Classical pore-scale displacement theory defines four displacement mechanisms which may result in residual trapping – piston-like, snap-off, I1 imbibition, and I2 imbibition (Lenormand et al., 1983). Dissolution trapping occurs when the residually trapped phase dissolves in water, controlled by the trapped phase diffusivity and solubility. Hydrogen solubility studies relevant for UHS demonstrated inconsistencies due to missing experimental support and/or different measurement approaches (De Lucia, Pilz et al. 2015; Li et al., 2018; Lopez-Lazaro et al., 2019; Chabab et al., 2020).

Contact angle measurements are commonly used in multiphase transport research to understand the effects of wettability and capillary pressure and relative permeability hysteresis on fluid systems. The hydrogen-water system is still not adequately investigated and lack consistent and systematic approaches. However, hydrogen contact angles have been derived for basalt (Al-Yaseri and Jha 2021) and measured for quartz (Iglauer et al., 2021) and sandstone (Hashemi et al., 2021) rocks, and the results showed discrepancies in terms of pressure, temperature and salinity effects.

Overall, pore-scale displacement and trapping mechanisms are well described for CO_2 sequestration (Buchgraber et al., 2012; Cao et al., 2016; Chang et al., 2016; Hu et al., 2017; Chang et al., 2020) but remains, to our knowledge, unaddressed for hydrogen. Our work examines hydrogen flow behaviour in an initially water-filled micromodel relevant for UHS in aquifers. We perform a series of injection (drainage) and withdrawal (imbibition) experiments to qualitatively describe pore-scale hydrogen displacement and trapping mechanisms. With image analysis, we quantify hydrogen dissolution kinetics and measure contact angles. This study is relevant for readers seeking to understanding of hydrogen flow physics in porous media and adds new data to experimental dataset.

2. Materials and methods

2.1. Micromodel

All drainage and imbibition experiments were conducted in a silicon-wafer micromodel based on natural sandstone pore patterns with a large variation in grain and pore sizes and shapes. Extracted from the scanning electron microscope image of a representative sandstone thin section and slightly modified to enable flow, the 2D pore network was etched into silicon wafer with deep reactive ion etching, DRIE (Hornbrook et al., 1991; Buchgraber et al., 2012). The DRIE realistically reproduces topological features such as high pore body to pore throat ratio, coordination number (4–8), sharp pore walls and surface roughness (100 nm). The exact reproduction of pore and pore throat sizes generate capillary forces at the magnitude relevant for real porous rocks. The heterogeneous mineralogy is, however, not reproduced, i.e. no clay and/or calcite minerals present. The silicon dioxide layer on the micromodel surfaces prevents hydrogen adsorption. Four ports, etched through the micromodel bottom, facilitate external access to the porous network, whereas two high-permeable fracture channels between the ports allow to easily distribute the injected fluids. The micromodel bottom (silicon wafer) and top (borosilicate glass) surfaces were connected through anodic bonding, resulting in the hydrophilic pore network. The micromodel hydrophilic nature allowed us to distinguish between the injected fluids. Under microscopic view (Fig. 2), hydrogen (light blue) develops a convex curvature towards water (blue) and the

grains.

The etched porous network has the length x width x depth dimensions of 2.8 cm x 2.2 cm x 0.0030 cm respectively and porosity of ~60%, yielding the pore volume of ~11 µL. The average pore diameter is in the order of 100 µm, with the grain size and pore throat length distributions of 100–7900 µm^2 and 10–200 µm, respectively (Alcorn et al., 2020). The pore network extraction tends to increase the total micromodel porosity compared with the representative rock, and the micromodel porosities up to 46–55% can be found in the literature (Buchgraber et al., 2012; Chang et al., 2019; Wu et al., 2021). Our pore network was based on the thin rock section, containing both small and large pore clusters. The pore network was repeated 36 (4 × 9) times and stitched together on the micromodel surface, resulting in relatively high total porosity of ~60%. Note, however, that our microscope provided the observations of the micromodel field of view (FoV) only, which is approximately 1% of the whole micromodel area. The local FoV porosity is in the order of ~30%, which is closer to the natural rocks.

2.2. Experimental set-up and procedure

The micromodel was mounted in the PEEK holder and connected to two Quizix pumps through 1/16'' PEEK and stainless-steel tubing (Fig. 1a). Quizix SP-5200 pump (cylinder C5000–10K-SS-AT) was filled with pure hydrogen (≥99.999%), whereas Quizix QX pump contained distilled water. The micromodel was illuminated by a light source (Photonic LED F1 Cold light 5500 K). A microscope (Nikon SMZ1500), connected to a camera (Nikon D7100) and computer, provided direct real-time observations of the FoV. Experimental data was acquired through live-view video recordings, with the frame rate 29.97 fps and the resolution of 0.5 pixels/µm.

Prior to every run, consisting of hydrogen and water injections, the pore-space was initially 100% saturated with distilled water. Every experiment consisted of one hydrogen injection (drainage) and one water injection (imbibition) from two opposite inlets, creating a diagonal flow through the pore network. All injections used a pore-pressure of $p = 5$ bar and room temperature. Constant pressure was maintained with a hydrogen-filled pump, whereas a water-filled pump performed water withdrawal/injection at constant flow rates. Hydrogen injections (drainage) were initiated by water withdrawal and lasted until between 50 and 500 water pore volumes (PV) were withdrawn after hydrogen invasion, enabling quasi steady-state. Subsequently, water injection (imbibition) started with the same flow rate and the injection was maintained until hydrogen was completely dissolved, thereby running a single cycle of hydrogen injection-withdrawal only. The micromodel was then cleaned with distilled water to remove any residual hydrogen and to re-saturate the pore space with 100% distilled water, making the system ready for the next experiment. Four different flow rates were applied: 0.1, 1, 10, and 50 mL/h, with corresponding capillary numbers (N_{Ca}) calculated from the equation: $N_{Ca} = U \cdot \mu/\sigma$, where U is flow velocity [m/s], μ is the wetting-phase (water) viscosity [Pa·s], and σ is the interfacial tension [N/m]. Flow velocity, U, was calculated as $U = Q/(L \cdot d \cdot \phi)$, with $Q =$ rate [m^3/s], $L =$ near-inlet length inside the micromodel [m], $d =$ porous network depth [m], $\phi =$ porosity [fraction]. Hydrogen interfacial tension, σ, at experimental pressure was calculated to 0.072 N/m based on the empirical formulation (Massoudi and King 1974). The calculated capillary numbers allowed to locate our experiments on the log(N_{Ca})-log(M) stability diagram (Fig. 1b), where M is defined as the hydrogen-water viscosity ratio.

2.3. Relevance of experimental conditions

Our experiments were run under low pressure and with distilled water. The reservoir brine salinity may affect the gas surface properties: the gas-brine interfacial tension (Duchateau and Broseta 2012) and contact angles (Jafari and Jung 2019) increase with increasing salinity. These correlations are yet to be confirmed for hydrogen-brine systems
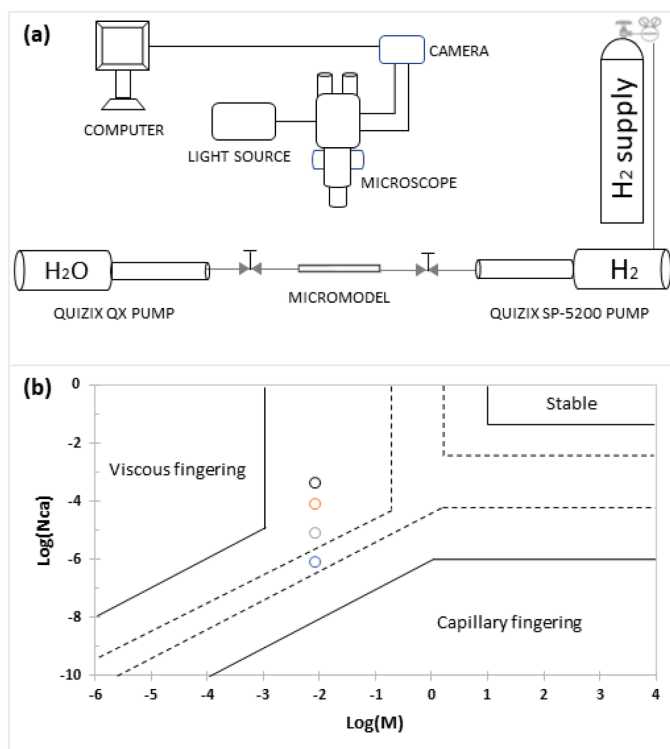
Fig. 1. *(a)* Schematic of experimental set-up with the micromodel, pumps for pressure control and fluid injection/withdrawal, the microscope, and the camera for live-view video recordings of the porous network. Hydrogen and water are injected from two opposite inlets. *(b)* Log(N_{Ca})-Log(M) stability diagram, where the solid lines represent the originally proposed boundaries (Lenormand et al., 1988), and the dashed lines denote the extended boundaries (Zhang et al., 2011). The circles locate experiments performed in this work. Reynold number (*Re*) ranges between 0.006 and 3.1, where $Re=\rho \cdot U \cdot D_{50}/\mu$ with ρ=water density [kg/m^3] and D_{50}=median grain diameter [$=1.1 \cdot 10^{-4}$ m].

and should be addressed in future studies. Low pressure was selected in our work due to the safety risks associated with hydrogen flammability and equipment compatibility under high pressure. Hydrogen properties affecting 2D porous media multiphase flow (viscosity and H_2—H_2O interfacial tension) do not vary significantly with increasing storage depths (increasing pressure and temperature), unlike many other gases like CO_2, N_2 and CH_2 (Beckingham and Winningham 2020; al. 2022). Pressure-dependant variations in hydrogen density play an important role in gravity-dominated 3D problems and thus are assumed to be insignificant in our 2D microfluidic study. Moreover, one of the hydrogen storage projects was operated at pressures down to 5–10 bars in the Argentinian depleted gas field (Pérez et al., 2016). Our low-pressure study is therefore relevant for the real storage conditions.

2.4. Image analysis

Experimental data was quantified with image analysis in the open-source ImageJ software. Hydrogen saturations were estimated based on colour thresholding, permitting to calculate local FoV porosity and distinguish hydrogen from water. Dissolution data was obtained by measuring the areal decrease of the hydrogen phase with time. Contact angles were measured using an angle tool. Static contact angles were measured when the hydrogen-water interface did not move, whereas paused videos allowed to measure dynamic contact angles when the hydrogen-water interface moved during water withdrawal/injection. Receding contact angles were measured when hydrogen displaced water (drainage). Advancing contact angles were measured when water displaced hydrogen (imbibition). Note that the image analysis is dependant on the image resolution, segmentation, and user adjustments. The image resolution was high enough to distinguish between hydrogen and water.

In some cases, the light source limitations resulting in the image gradients required pre-processing of the images, with the manual segmentation of fluids.

3. Results and discussion

3.1. Hydrogen saturation establishment during drainage

Hydrogen invaded the pores immediately after entering the FoV, indicating that non-wetting phase invasion occurred on millisecond scale independent of capillary number (N_{Ca}). This is consistent with previous micromodel studies in oil/air-water systems (Mohanty et al., 1987; Moebius and Or 2012; Armstrong and Berg 2013). Rapid hydrogen pore invasion serves as indirect evidence of hydrogen non-wetting nature (Andrew et al., 2015), which was directly confirmed by contact angle measurements (detailed in Section 3.4).

3.1.1. Initial hydrogen saturation

The FoV hydrogen saturation (Sg) after drainage increased with increasing N_{Ca} (Fig. 2), as expected from classical pore-scale displacement theory (Lenormand et al., 1983). Hydrogen invasion into neighbouring pore clusters was restricted by narrow pore throats with higher capillary entry pressures. Pores invaded by hydrogen were predominantly saturated with hydrogen, with some visible water accumulations (droplet forms) on the pore bottom due to surface roughness (white arrows in Fig. 2). Number of water droplets were largest at upper medium and high N_{Ca}, whereas they were absent at low N_{Ca} at the end of drainage. At the hydrogen breakthrough, however, water droplets formed even at low N_{Ca} (Fig. 3). With continued hydrogen injection the droplets were displaced, likely due to (1) the hydrophilic micromodel
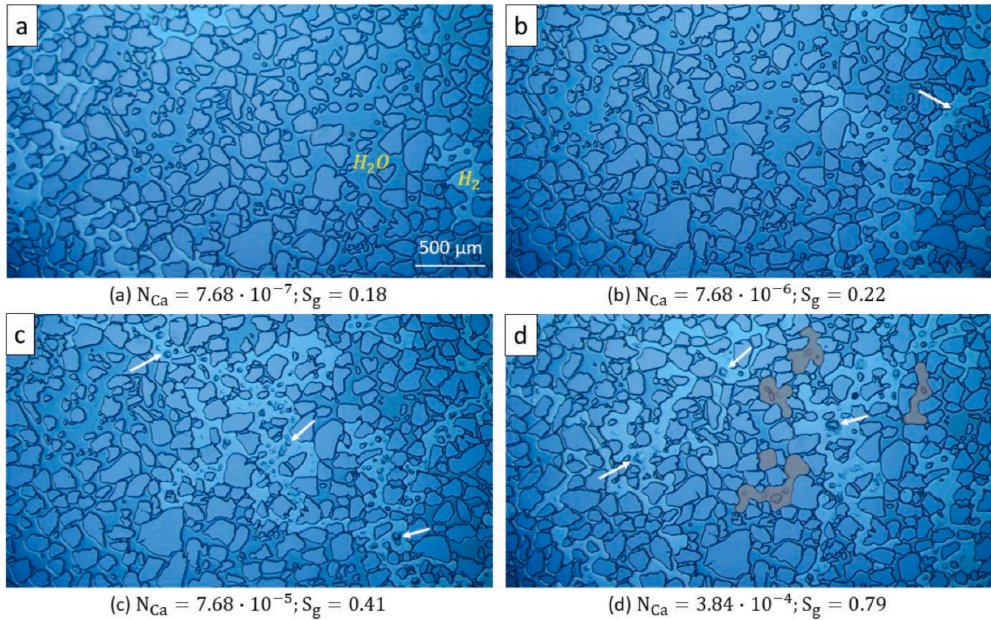
Fig. 2. FoV hydrogen (light blue) saturation (Sg) after drainage at various capillary numbers (N_{Ca}); the remaining pores were saturated with water (blue). Hydrogen was injected from the top right in every image. Sg increased with increasing N_{Ca}: *(a)* Sg=0.18 at NCa=7.68•10^{-7}, *(b)* Sg=0.22 at N_{Ca}=7.68•10^{-6}, *(c)* Sg=0.41 at N_{Ca}=7.68•10^{-5}, *(d)* Sg=0.79 at N_{Ca}=3.84•10^{-4}. The white arrows indicate water droplet accumulations in the surface roughness in the micromodel bottom. The hydrogen phase remained connected from low (image a) to upper medium (image c) N_{Ca}. At high N_{Ca} (image d) parts of the hydrogen phase became disconnected (indicated in grey). The drainage capillary desaturation curve was calculated based on Sg and N_{Ca} values and found in supplementary materials (Fig. S1).
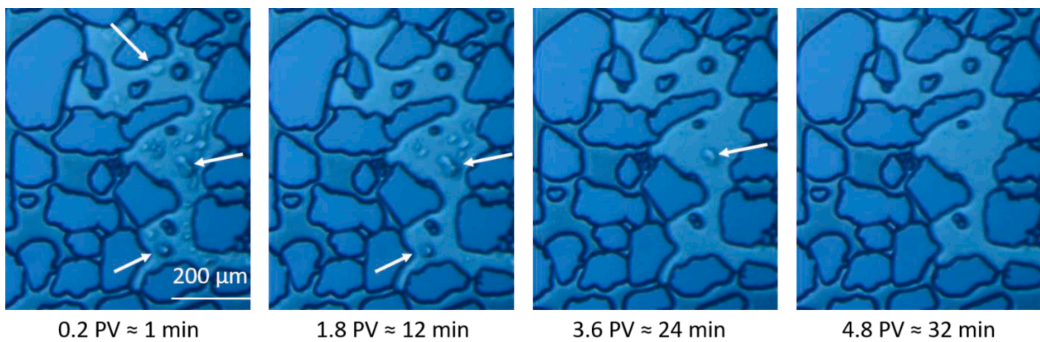
Fig. 3. Water droplets (white arrows) displacement by hydrogen during drainage at $N_{Ca}=7.68\cdot10^{-7}$. Water droplets residing below hydrogen in the surface roughness of the micromodel were gradually displaced by hydrogen. Hydrogen percolation was restricted by small pore throats.

surfaces with high water phase connectivity through connected wetting films, and/or (2) water evaporation in hydrogen. The water droplet displacement/evaporation demonstrated the pore-scale efficiency of low-N_{Ca} drainage when multiple pore-occupancies establish in hydrophilic systems. From this we could expect that hydrogen injection strategies that result in pore-occupancy by hydrogen phase only (no pore water) will decrease water-cut upon hydrogen withdrawal in aquifer storage, improving overall storage performance. Low-N_{Ca} hydrogen injection may therefore be preferred from the perspective of the pore-occupancies.

3.1.2. Hydrogen connectivity

The non-wetting phase connectivity defines if the phase is connected through the pore clusters. The hydrogen connectivity was high at low and medium N_{Ca}, with observations of several connected gas paths (Fig. 2a-c). At high N_{Ca}, both connected and disconnected hydrogen phases established (Fig. 2d), with disconnected hydrogen phase accounting for ~ 11% of the total FoV hydrogen saturation. The predominant mechanism for disconnected hydrogen was Roof snap-off (Roof 1970) due to the front interface destabilization after entering the neighbouring pore. To maintain capillary equilibrium, water thickens in the pore throat, leading to the non-wetting phase (hydrogen in our case) disconnection. For Roof snap-off to occur, high water availability is

required near the pore throat and the non-wetting phase must pass the pore throat for a distance of at least seven times the throat radius. Snap-off controlled by capillary pressure is expected in smaller pore throats. In our work, Roof snap-off occurred in small (15 μm) and large (25 μm) pore throats, without occurring in neighbouring pore throats of similar sizes (Fig. 4). This implies that Roof snap-off was a local phenomenon, likely controlled by water mobility and availability, as suggested for drainage snap-off in a CO_2-brine system (Andrew et al., 2015). The pore throat water thickening, which was believed to cause hydrogen snap-off, was not possible to confirm visually because of sub-second snap-off and insufficient microscope resolution to detect thin wetting films. Before snap-off occurred in small and large pores (Fig. 4), the distance propagated by hydrogen corresponded to ~ 35 and 15 times of the pore throat radius respectively, fulfilling the condition for Roof snap-off.

Snap-off during drainage is less common than in imbibition and is still not appropriately investigated. In the seminal work of Roof (1970), the criteria for drainage snap-off were linked to local conditions – water availability, pore throat and interface size, wettability. The drainage snap-off dependency on global dynamic conditions – viscosity ratio, compressibility, capillary number – were proposed (Deng et al., 2015; Herring et al., 2018). Our results suggest that drainage snap-off was triggered by both local and global factors. The snap-off independence on pore throat sizes (Fig. 4) showed local features of snap-off events, whereas the snap-off occurrence at high N_{Ca} only suggests that snap-off drainage was correlated to global dynamic parameter – N_{Ca}.

Snap-off during and after drainage is undesired in seasonal hydrogen storage as this may lead to permanent hydrogen entrapment. In our work, most of disconnected hydrogen bubbles (Fig. 2d) did not reconnect during imbibition, resulting in a complete hydrogen dissolution. Although the highest hydrogen saturation (Fig. 2) was achieved at high N_{Ca} (3.84$\cdot$10^{-4}), high injection rates will not necessarily yield the maximum injection efficiency in aquifer storage projects considering the possibility for snap-off.

3.1.3. Flow regime

According to the logN_{Ca}-log$M$ phase diagram (Fig. 1b), unstable viscous-dominated displacement was expected to prevail over capillary-dominated flow. The logN_{Ca}-log$M$ phase diagram boundaries are, however, system-dependant (Zhang et al., 2011), and are not necessarily applicable for our micromodel. Neither viscous nor capillary fingering were possible to observe due to the limited FoV. Nevertheless, some indirect evidence of viscous and capillary flow regimes was observed locally. The establishment of the connected hydrogen phase, stopped by narrow pore throats, may show the importance of capillary fingering at

low/medium N_{Ca}. Roof snap-off, caused by hydrogen penetration through narrow pore throats, indicate the dominance of viscous forces at high N_{Ca} (Zhang et al., 2011). Micromodel studies enabling to observe the entire micromodel at a wider N_{Ca} range will be beneficial for a direct determination of the dominating flow regime in hydrogen-water systems.

3.2. Displacement and residual trapping during imbibition

Hydrogen displacement and disconnection (residual trapping) was observed during imbibition, that started with water injection into the same fluid system which established after drainage. Imbibition proceeded in three main steps, common for all N_{Ca}: 1) displacement, 2) disconnection, 3) dissolution. An additional step (between steps 1 and 2) was observed at upper medium and high N_{Ca} – hydrogen redistribution caused by fluid displacement from outside the FoV. This section describes the first two steps, displacement and disconnection, in addition to redistribution. Dissolution will be described in Section 3.3.

3.2.1. Displacement mechanisms

Hydrogen displacement was mainly governed by I1 imbibition mechanism (Fig. 5a). Initially occupying three pores, hydrogen was forced into a single pore because of the curvature instability, resulting from the curvature detachment from the pore walls. Two other displacement mechanisms were common at specific N_{Ca}: piston-like displacement and redistribution. Piston-like displacement was observed at low N_{Ca}, where a stable displacement front moved through a single pore channel (Fig. 5b). The pore channel was surrounded by narrow pore throats, forcing water to displace hydrogen from one direction only. At upper medium and high N_{Ca}, hydrogen redistribution occurred (Fig. 5c), where the original hydrogen phase was first displaced and trapped, followed by a partial reconnection with surrounding hydrogen. This mechanism occurred because of high hydrogen saturation after upper medium/high-N_{Ca} drainage, permitting hydrogen movement through the entire micromodel during imbibition. Note that most of the hydrogen bubbles, disconnected due to Roof snap-off during drainage, remained disconnected during redistribution. Only a single hydrogen bubble in the FoV reconnected with the continuous hydrogen phase. The inability to reconnect resulted in a complete hydrogen bubble dissolution, demonstrating the disadvantages of the drainage snap-off.

3.2.2. Residual trapping

Hydrogen disconnection, leading to residual trapping, occurred mainly by I2 imbibition mechanism (Fig. 6a). Displacement from the
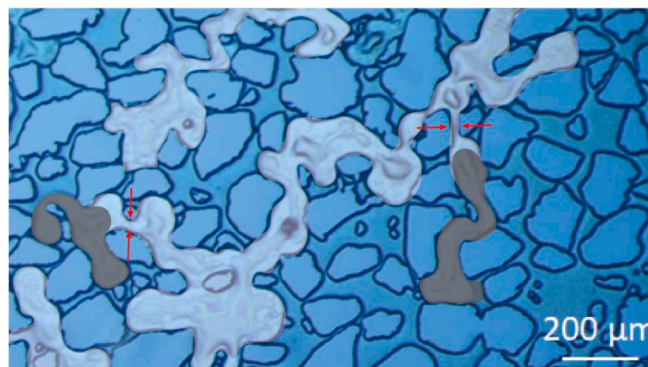

Fig. 4. Roof snap-off during drainage was observed at high N_{Ca}=3.84$\cdot$10^{-4} only. Hydrogen phase distribution after breakthrough (white) changed within less than one second due to snap-off. The red arrows locate the pore throats where snap-off occurred, resulting in disconnected hydrogen bubbles (grey).
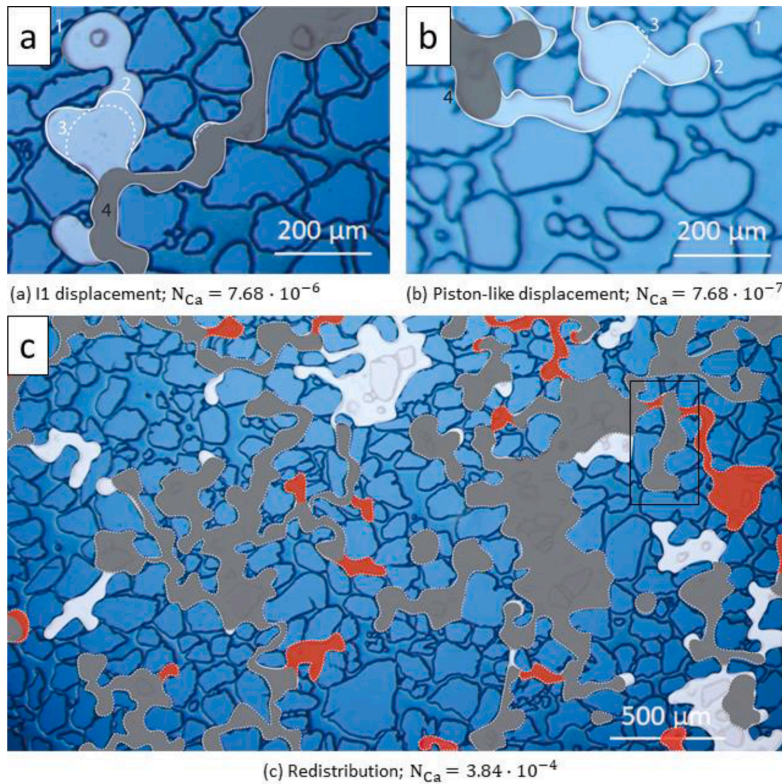
(a) I1 displacement; $N_{Ca} = 7.68 \cdot 10^{-6}$

(b) Piston-like displacement; $N_{Ca} = 7.68 \cdot 10^{-7}$

(c) Redistribution; $N_{Ca} = 3.84 \cdot 10^{-4}$

Fig. 5. Hydrogen displacement mechanisms during imbibition, where colors and outlines indicate the hydrogen phase after each time step t_i. *(a)* An example of the I1 type imbibition where hydrogen residing in several pores (t_1; white) was displaced ($t_{2,3}$; solid and dashed outlines) into a single pore (t_4; grey, $\Delta t_{4-1} = 1$ s). *(b)* Piston-like displacement was observed for low $N_{Ca}=7.68 \cdot 10^{-7}$, where initial hydrogen phase (t_1; white) was displaced ($t_{2,3}$; solid and dashed outlines) with a stable front through a single pore channel (t_4; grey, $\Delta t_{4-1} = 9$ s). *(c)* Hydrogen redistribution was observed at higher $N_{Ca} \geq 7.68 \cdot 10^{-5}$. The original hydrogen phase distribution (t_1: white + grey) was first displaced by water and then reconnected with hydrogen phase (t_2: grey + red, $\Delta t_{2-1} = 20$ s) flowing from outside the FoV. Only a single disconnected hydrogen bubble reconnected with hydrogen phase during redistribution (black square), and most of the hydrogen bubbles remained disconnected. The raw image sequence of Fig. 5 is shown in the supplementary materials (Fig. S3) together with live-time FOV videos.

pore centre towards the pore wall resulted in hydrogen disconnection when the hydrogen-water interface reached the pore wall. The disconnected hydrogen occupied two pores. Trapping by bypass was observed at upper medium and high N_{Ca} (Fig. 6b). The water flow paths did not manage to invade the large hydrogen-saturated pore clusters with narrow pore throats, resulting in a significant hydrogen fraction being bypassed. The dominance of the I2 mechanism over bypass was likely due to topological reasons (high coordination number), permitting the transverse-to-hydrogen water flow paths. Bypass is expected in large pore clusters with narrow pore throats (Chatzis et al., 1983), consistent with our observations. However, at low and lower medium N_{Ca}, hydrogen did not occupy the large pore clusters (Fig. 2a,b), where bypass was observed at upper medium and high N_{Ca}. For a more general conclusion on the relative importance of I2 and bypass mechanisms, hydrogen must occupy the same pore clusters in all experiments, which is challenging to control in the heterogeneous pore space with the micromodels used in this study. Trapping by snap-off was not identified despite high micromodel aspect ratio and roughness, likely due to experimental conditions. Snap-off is expected to dominate at $N_{Ca} < 10^{-7}$ (Hu et al., 2017), whereas our experiments were conducted at $N_{Ca} \geq 7.68 \cdot 10^{-7}$. The FoV hydrogen saturation profiles were estimated for imbibition to construct the imbibition CDC and gas trapping curves (Fig. S2 and Fig. S1 in the supplementary materials, respectively).

3.3. Dissolution

3.3.1. Dissolution mechanisms

Dissolution of disconnected and trapped hydrogen was observed during prolonged water injection. Three dissolution mechanisms were identified (Fig. 7): one-end dissolution, two-end dissolution, and displacement dissolution. The one-end dissolution (Fig. 7a) was frequently observed at upper medium and high N_{Ca}, where hydrogen bubbles dissolved from one end only, reflecting the water flow direction. The rapidly developed waterfront, propagating through the micromodel in one main direction, was not able to enter narrow pore throats countercurrently against the main flow direction. Hence, dissolution initiated only from one end of the trapped hydrogen bubble, residing in the pore corners surrounded by narrow pore throats. The one-end dissolution was also observed in supercritical CO_2 dissolution in micromodel (Chang et al., 2016). The two-end dissolution mechanism (Fig. 7b) prevailed at lower medium N_{Ca} where the hydrogen bubbles were dissolved at both sides simultaneously. This mechanism was attributed to a more stable waterfront and greater water availability, originating from lower hydrogen saturation developed after drainage. The displacement dissolution mechanism (Fig. 7c) was characterized by mobilization of smaller hydrogen bubbles that were able to penetrate narrow pore throats. This mechanism was observed at upper medium and high N_{Ca} due to faster and more directed water flow. Overall, observed dissolution mechanisms suggest that hydrogen dissolution was governed by the waterfront velocity and direction, which in turn was controlled by N_{Ca}.

Two dissolution processes were detected independent of N_{Ca} – homogeneous and heterogeneous dissolution. They differed in terms of the microbubble final state at the end of dissolution. In homogenous dissolution, microbubbles dissolved completely, whereas the residual microbubbles accumulated at the surface roughness in heterogeneous dissolution. Homogenous/heterogeneous dissolution as well as
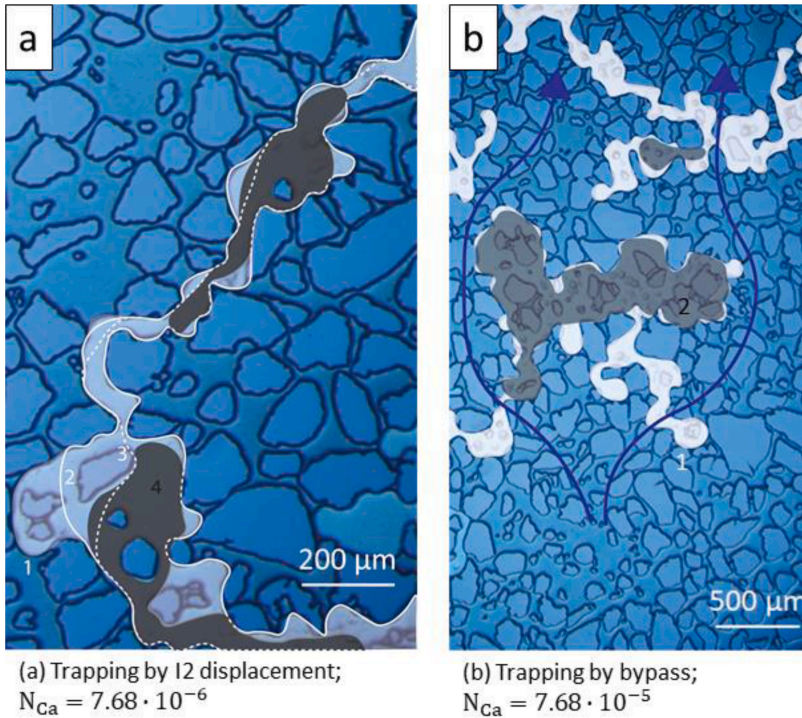
Fig. 6. Hydrogen trapping mechanisms during imbibition. Colors and outlines indicate the hydrogen phase after each time step t_i. *(a)* Trapping by I2 type imbibition resulting in residual trapping, where hydrogen originally residing in a single pore (t_1, white) was displaced towards the pore wall ($t_{2,3}$; solid and dashed outlines) until hydrogen disconnection occurred. The disconnected hydrogen occupied two pores (t_4; grey, $\Delta t_{4-1} = 1.3$ s). *(b)* Trapping by bypass was observed at $N_{Ca} \geq 7.68 \cdot 10^{-5}$. A hydrogen cluster residing in large pores surrounded by narrow pore throats (t_1, white) was bypassed by water (dark blue arrows; show the general water flow direction, but not the exact flow path through the pores) resulting in trapped hydrogen (t_2; grey, $\Delta t_{2-1} = 1$ s). The raw image sequence of Fig. 6 is shown in the supplementary materials (Fig. S4) together with live-time FOV videos.
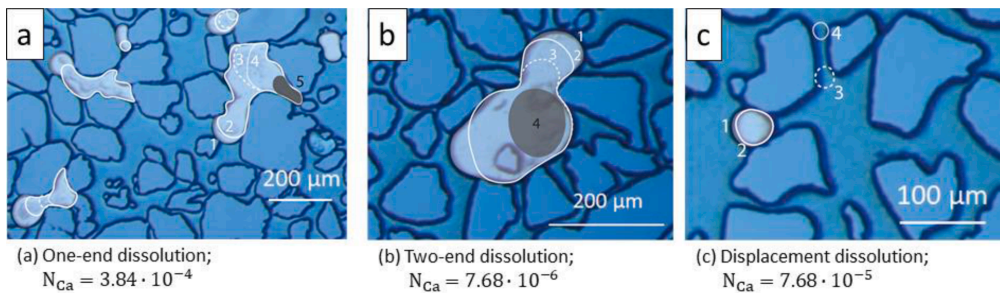
(a) Trapping by I2 displacement;
$N_{Ca} = 7.68 \cdot 10^{-6}$

(b) Trapping by bypass;
$N_{Ca} = 7.68 \cdot 10^{-5}$

(a) One-end dissolution;
$N_{Ca} = 3.84 \cdot 10^{-4}$

(b) Two-end dissolution;
$N_{Ca} = 7.68 \cdot 10^{-6}$

(c) Displacement dissolution;
$N_{Ca} = 7.68 \cdot 10^{-5}$

Fig. 7. Hydrogen dissolution mechanisms. Colors and outlines indicate the hydrogen phase after each time step t_i. *(a)* In one-end dissolution, the hydrogen bubbles (t_1, white) were dissolved from one end only ($t_{2,3,4}$; solid and dashed outlines) reflecting the water flow direction (left to right) until the hydrogen was partially (t_5, grey) or completely dissolved ($\Delta t_{5-1} = 22$ s). *(b)* In two-end dissolution, the hydrogen bubble (t_1, white) was dissolved from two ends ($t_{2,3}$; solid and dashed outlines) until partial dissolution (t_4, grey, $\Delta t_{4-1} = 134$ s). *(c)* In displacement dissolution, the hydrogen bubble (t_1, white) was displaced when its size decreased ($t_{2,3,4}$; solid and dashed outlines, $\Delta t_{4-1} = 5$ s) to below the pore throat gaps. One-end dissolution (a) and displacement dissolution (c) occurred at $N_{Ca} \geq 7.68 \cdot 10^{-5}$, whereas two-end dissolution (b) was common at $N_{Ca} = 7.68 \cdot 10^{-6}$. The one-end and two-end dissolution kinetics is quantified in Fig. 8. The raw image sequence of Fig. 7 is shown in the supplementary materials (Fig. S5) together with live-time FOV videos.

displacement dissolution (Fig. 7c) were also reported for CO_2 dissolution in micromodel (Buchgraber et al., 2012).

3.3.2. Dissolution kinetics

Local and global dissolution kinetics were estimated based on the image analysis. Local dissolution kinetics was quantified by calculating the temporal change in the individual hydrogen bubble size and the depletion rate (Fig. 8). As expected, time required for compete dissolution decreased with increasing N_{Ca} because of the faster water supply (Fig. 8a). The total dissolution time in every experiment was nearly

equal and independent of the initial bubble area, implying simultaneous dissolution in the entire FoV. The depletion rate (Fig. 8b) was calculated as the depleted hydrogen mass per time interval between two sequential images: $Q_d = (\Delta A \cdot d \cdot \rho_{H2})/\Delta t$, where ΔA = decrease in individual hydrogen bubble area between two sequential images, d = porous network depth, ρ_{H2} = hydrogen density under experimental conditions ($4.12 \cdot 10^{-4}$ g/mL), Δt = time interval between two sequential images. The depletion rate changed with time, shifting from nearly constant values to increasing or decreasing trends. Similar discrepancies in depletion rate trends were also observed in pore-scale supercritical CO_2
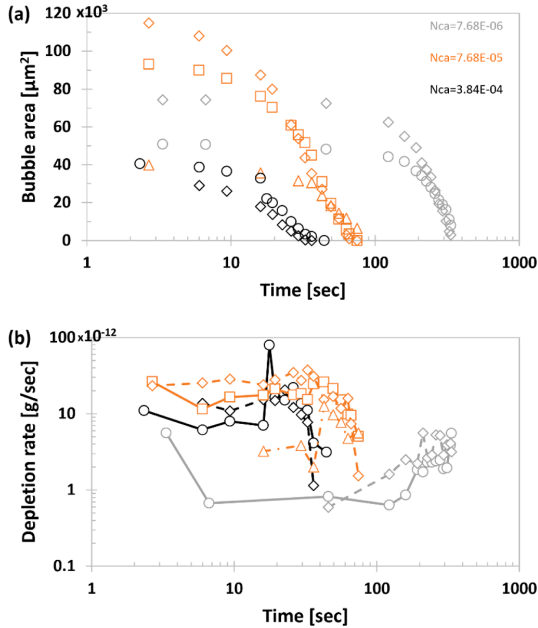
Table 1
Experimental conditions and micromodel properties.

Experimental conditions	Micromodel properties	Flow rate, Q [mL/h]	Flow velocity, U [m/s]	Capillary number, N_{Ca}	Capillary number classification
$p = 5$ bar	$L = 2.8$ cm	0.1	$5.5 \cdot 10^{-5}$	$7.68 \cdot 10^{-7}$	Low N_{Ca}
$t = 20$ °C	$d = 30$ µm	1	$5.5 \cdot 10^{-4}$	$7.68 \cdot 10^{-6}$	Lower medium N_{Ca}
	$V_p = 11$ µL	10	$5.5 \cdot 10^{-3}$	$7.68 \cdot 10^{-5}$	Upper medium N_{Ca}
	$\phi = 0.6$	50	$2.8 \cdot 10^{-2}$	$3.84 \cdot 10^{-4}$	High N_{Ca}

Table 2
Hydrogen dissolution kinetics: average hydrogen depletion rate and dissolved hydrogen concentration in injected water mass.

Capillary number, N_{Ca}	Initial bubble area, A_i [µm²]	Depletion rate, Q_d [g/sec]	Dissolved concentration, C [mol/kg]	Concentration relative to H_2 solubility, C/C_s [%]
$7.68 \cdot 10^{-6}$	$74 \cdot 10^3$	$3.3 \cdot 10^{-12}$	$5.9 \cdot 10^{-6}$	0.15
	$52 \cdot 10^3$	$2.3 \cdot 10^{-12}$	$4.2 \cdot 10^{-6}$	0.10
	Global	$3.6 \cdot 10^{-10}$	$6.4 \cdot 10^{-4}$	16.0
$7.68 \cdot 10^{-5}$	$120 \cdot 10^3$	$22 \cdot 10^{-12}$	$3.9 \cdot 10^{-6}$	0.10
	$99 \cdot 10^3$	$17 \cdot 10^{-12}$	$3.1 \cdot 10^{-6}$	0.08
	$40 \cdot 10^3$	$6.2 \cdot 10^{-12}$	$1.1 \cdot 10^{-6}$	0.03
	Global	$63 \cdot 10^{-10}$	$11 \cdot 10^{-4}$	28.3
$3.84 \cdot 10^{-4}$	$43 \cdot 10^3$	$16 \cdot 10^{-12}$	$0.6 \cdot 10^{-6}$	0.01
	$36 \cdot 10^3$	$12 \cdot 10^{-12}$	$0.4 \cdot 10^{-6}$	0.01
	Global	$277 \cdot 10^{-10}$	$9.9 \cdot 10^{-4}$	24.7

Fig. 8. Local dissolution kinetics. *(a)* Temporal change in bubble area for N_{Ca}; time required for complete dissolution decreased with increasing N_{Ca}. For the same N_{Ca}, the total dissolution time was equal, independent of initial bubble area size. *(b)* Depletion rate as a function of time was not constant. Average depletion rate was the fastest at $N_{Ca}=7.68 \cdot 10^{-5}$ and the slowest at $N_{Ca}=7.68 \cdot 10^{-6}$. The depletion rate at $N_{Ca}=7.68 \cdot 10^{-4}$ was slower than at $N_{Ca}=7.68 \cdot 10^{-5}$ due to smaller initial bubble area. Black and grey circles show the dissolution kinetics of the hydrogen bubbles presented in Fig. 7a (marked with t_{1-5}) and in Fig. 7b, respectively.

dissolution, explained by the number of water flow paths, their direction (transverse or longitudinal), and the CO_2-water interface area (Chang et al., 2016). The average hydrogen depletion rate ranged from $2.3 \cdot 10^{-12}$ to $22 \cdot 10^{-12}$ g/sec, with the lowest rate observed at lower-medium N_{Ca} (expected) and the highest rate observed at upper medium N_{Ca} (unexpected). High N_{Ca} did not yield the highest depletion rate due to the smaller initial bubble size compared with upper medium-N_{Ca} cases. When comparing bubbles of similar size, high-N_{Ca} depletion rate was higher than upper medium-N_{Ca} (Table 2).

Global dissolution kinetics was analysed based on the FoV hydrogen saturation profiles during dissolution (Fig. 9). The global depletion rate (Fig. 9b) was calculated as follows: Q_d (global) $= (\Delta S_g \cdot V_p \cdot \rho_{H2})/\Delta t$, where $\Delta S_g =$ decrease in the FoV hydrogen saturation between two sequential images, $V_p =$ micromodel pore volume, $\rho_{H2} =$ hydrogen density under experimental conditions, $\Delta t =$ time interval between two sequential images. The global depletion rate calculations assume that FoV hydrogen saturation profiles are representative for the entire micromodel. The global depletion rates showed non-constant trends, and on average varied between $3.6 \cdot 10^{-10}$ to $277 \cdot 10^{-10}$ g/sec, two orders of magnitude higher compared with local depletion rate of individual bubbles, similar to observations of CO_2 dissolution (Chang et al., 2016). The global depletion rate was the lowest at lower medium N_{Ca} and highest at high N_{Ca} (Table 2).

3.3.2.1. Dissolved hydrogen concentration and solubility. The averaged dissolved hydrogen concentration (Table 2) was calculated as the dissolved hydrogen amount per injected water mass between two
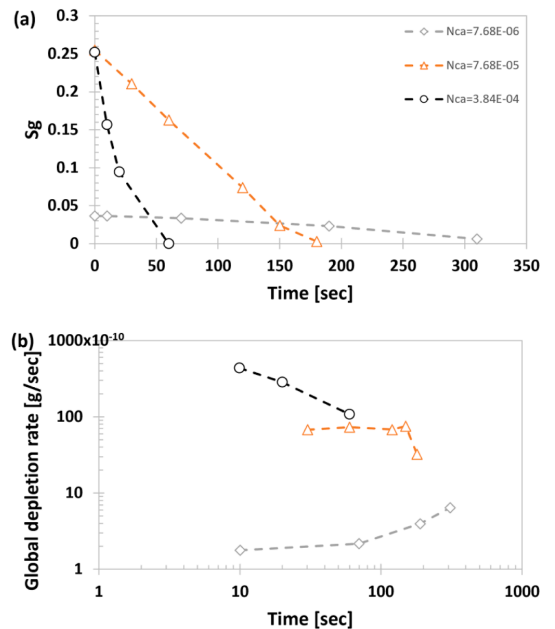

Fig. 9. Global dissolution kinetics. *(a)* Change in hydrogen saturation (Sg) as a function of time at various N_{Ca}. Sg was calculated in the FoV under the assumption to approximate the entire micromodel. *(b)* Global depletion rate as a function of time was not constant; being the fastest at $N_{Ca}=3.84 \cdot 10^{-4}$ and the slowest at $N_{Ca}=7.68 \cdot 10^{-6}$. The global depletion rate was two orders of magnitude faster than the depletion rate of individual bubbles (Fig. 8).

sequential images according to the formula: $C = Q_d/(M_{H2} \cdot Q \cdot \rho_{H2O})$, where Q_d = hydrogen depletion rate, M_{H2} = hydrogen molar mass, Q = water injection rate, ρ_{H2O} = water density. These calculations were based on the mass balance principle, assuming that hydrogen depletion is solely controlled by dissolution and water advection (Chang et al., 2016; Chang et al., 2019). Hydrogen depletion will be controlled by diffusion when the water phase is immobile, which is not the case in our work where water is continuously injected during imbibition. In local dissolution, the dissolved individual hydrogen bubble concentration ranged between $0.4 \cdot 10^{-6}$ and $5.9 \cdot 10^{-6}$ mol/kg. In global dissolution, the dissolved hydrogen concentration varied from $6.4 \cdot 10^{-4}$ to $11 \cdot 10^{-4}$ mol/kg, corresponding to 16.0% and 28.3% of the hydrogen solubility under the applied experimental conditions (Chabab et al., 2020). Lower-than-solubility hydrogen concentrations indicate non-equilibrium hydrogen dissolution in our work, conflicting with classic equilibrium dissolution theories applied in numerical modelling (Pruess and Spycher 2007).

Non-equilibrium (slow) dissolution has also been reported for CO_2, both in experimental core-scale (Akbarabadi and Piri 2013; Chang et al., 2013) and pore-scale (Chang et al., 2016; Chang et al., 2019) studies, as well as numerical studies (Chen et al., 2018). For instance, CO_2 dissolution measurements in micromodels showed that the average CO_2 concentration varied between 0.25–13% of CO_2 solubility (Chang et al., 2016; Chang et al., 2019). They explained non-equilibrium dissolution by insufficient CO_2-water interface area and non-uniform CO_2-mobile water distribution. They argued that at reservoir-scale, where dissolution occurs at slower timescales, CO_2 dissolution after the injection stop will approach equilibrium unless strong heterogeneity is present. In hydrogen aquifer storage, hydrogen is cyclically injected and withdrawn at high rates, and we therefore speculate that non-equilibrium dissolution may play an important role.

3.4. Contact angles

3.4.1. Static and dynamic contact angles

Static (θ_S) and dynamic (θ_D) contact angles were measured during drainage and imbibition. Each measurement was performed five times at the same measuring point and then averaged, with the uncertainty represented as standard deviation. The measured contact angles (Fig. 10) varied from 17 to 56°, similar to contact angles of 22–45° for hydrogen-water-sandstone systems (Yekta et al., 2018; Hashemi et al., 2021). Our results confirmed that the micromodel is hydrophilic when exposed to hydrogen. No clear relationship between contact angles and pore diameter emerged, although the contact angle range appeared to narrow with increasing pore diameter (majority of measurements

performed in pores with diameter between 50 and 125 μm).

Four contact angle types – receding (θ_R), advancing (θ_A), static in drainage ($\theta_{S,DR}$) and static in imbibition ($\theta_{S,IM}$), were averaged for each experiment (Table 3) and plotted as a function of N_{Ca} (Fig. 11a). The θ_A were significantly higher than the θ_R, consistent with classic theories (Johnson and Dettre 1964). As expected, $\theta_A > \theta_{S,IM}$, but θ_R and $\theta_{S,DR}$ were surprisingly similar, $\theta_R \approx \theta_{S,DR}$. The similarity between θ_R and $\theta_{S,DR}$ could be linked to the experimental procedure. After hydrogen breakthrough under drainage, hydrogen injection continued through the connected hydrogen phase, and the $\theta_{S,DR}$ were measured when the interface movement terminated visually. In this state, despite being motionless, the interfaces did not reach the equilibrium due to continuous hydrogen injection. The measured $\theta_{S,DR}$ approached more dynamic than static states, resulting in $\theta_R \approx \theta_{S,DR}$, and were thus believed to be underestimated and less reproducible. On the other hand, the water breakthrough under imbibition resulted in hydrogen residual trapping, with several hydrogen clusters being bypassed by water. In these regions, the interface was believed to be surrounded by immobile water, thus approaching equilibrium and yielding $\theta_A > \theta_{S,IM}$. The lower θ_S reproducibility was also reported for CO_2 contact angle measurements in micromodels using similar experimental methods (Jafari and Jung 2017). Note that θ_D are more important for hydrogen storge than less reproducible θ_S because θ_D represent dynamic hydrogen injection/withdrawal.

3.4.1.1. Equilibrium contact angles. The equilibrium contact angles (θ_E) were estimated based on the following equation (Tadmor 2004): $\theta_E = cos^{-1}(\frac{R_A \cdot cos\theta_A + R_R \cdot cos\theta_R}{R_A + R_R})$, where $R_A = \left(\frac{sin^3\theta_A}{2 - 3cos\theta_A + cos^3\theta_A}\right)^{\frac{1}{3}}$ and $R_R =$

Table 3
Average contact angles measured during drainage/imbibition and calculated equilibrium angles.

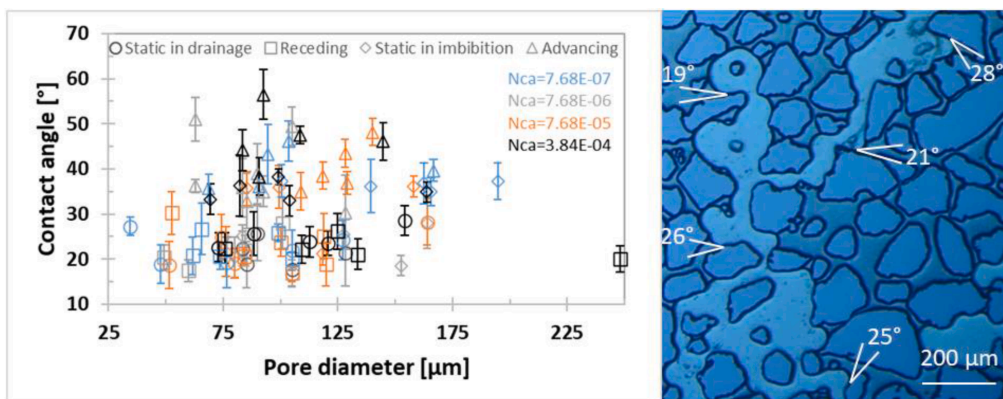| Capillary number, N_{Ca}	Drainage		Imbibition		Calculated Equilibrium angle, θ_E [deg]
	Static angle, $\theta_{S,DR}$ [deg]	Receding angle, θ_R [deg]	Static angle, $\theta_{S,IM}$ [deg]	Advancing angle, θ_A [deg]	
$7.68 \cdot 10^{-7}$	22 ± 5	23 ± 4	37 ± 4	40 ± 6	32
$7.68 \cdot 10^{-6}$	21 ± 6	21 ± 6	24 ± 5	39 ± 9	30
$7.68 \cdot 10^{-5}$	22 ± 6	24 ± 6	30 ± 8	40 ± 6	32
$3.84 \cdot 10^{-4}$	25 ± 4	22 ± 4	35 ± 4	47 ± 7	35

Fig. 10. Measured contact angles (left) and an example showing how static in imbibition angles were measured at N_{Ca}=7.68$\cdot$10^{-6} (right).
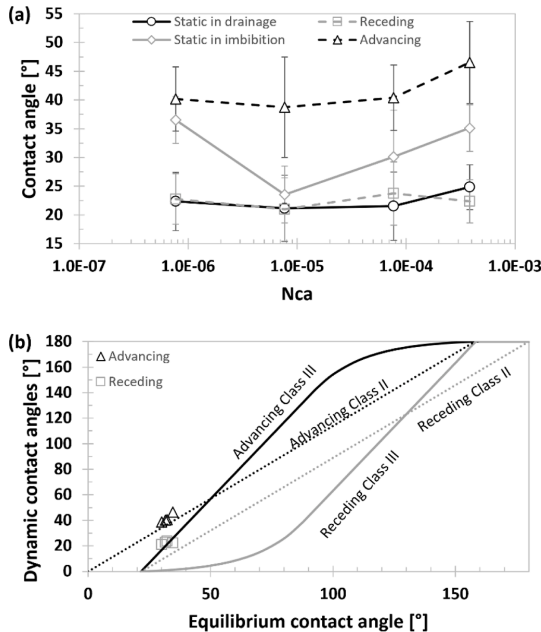
Fig. 11. (a) Average contact angles as a function of N_{Ca}. As expected, the advancing contact angles were higher compared with receding contact angles. (b) Dynamic (receding and advancing) contact angles as a function of calculated equilibrium angles. The solid and dashed curves represent the literature-based relationship (Morrow 1975) for Class III and Class II behaviour, respectively. Our results fit Class II behaviour.

$\left(\frac{\sin^3\theta_R}{2-3\cos\theta_R+\cos^3\theta_R}\right)^{\frac{1}{3}}$. The calculated θ_E were plotted together with the measured θ_A and θ_R (Fig. 11b), and compared with the original relationship based on the measurements through the capillary rise in polytetrafluoroethylene (PTFE) tubes (Morrow 1975). In the seminal work of Morrow, three different classes were defined, depending on the degree of surface roughness where the contact angles were measured: Class I – on smooth surfaces ($\theta_A = \theta_R$); Class II – on slightly roughened surfaces; and Class III – on well roughened surfaces. Our results showed that hydrogen-water fluid pair in a natural sandstone-based micromodel fit Class II behaviour, although the θ_R were slightly overestimated. This overestimation could be attributed to the difference in the measurement procedures. In our work, the θ_E were calculated based on the equation and the measured θ_A and θ_R in the heterogeneous micromodel with realistic pore geometries, whereas in Morrow (1975) both θ_E and θ_A/θ_R were experimentally measured in PTFE tubes which cannot account for the effect of the pore geometries.

The relationship between θ_E and θ_A/θ_R is essential for pore-scaling modelling, where Class III behaviour is widely implemented generally (Valvatne and Blunt 2004) and for hydrogen in particular (Hashemi et al., 2021). With known contact angles, relative permeability and capillary pressure functions can be predicted using pore-scale modelling and then upscaled for field-scale applications. Discrepancies between the pore-scale modelling approaches, which use Class III behaviour (well roughened surfaces), and our results showing Class II behaviour (slightly roughened surfaces) has a direct impact on understanding hydrogen pore-scale flow physics. Although the micromodel, used in this study, was reproduced with 100 nm surface roughness (Buchgraber et al., 2012), the micromodel may not be sufficiently rough to accurately reproduce the experimental results with pore-scale modelling. Mismatch

between the experimental and simulated data may be expected when using Class III behaviour as the modelling input.

3.4.2. Contact angle hysteresis

Hysteresis was estimated for dynamic, $\Delta\theta_D = \theta_A - \theta_R$, and static contact angles, $\Delta\theta_S = \theta_{S,IM} - \theta_{S,DR}$ (Fig. 12a). As expected, static contact angle hysteresis ($\Delta\theta_S$) was lower than the dynamic one ($\Delta\theta_D$). No clear relationship was noted between $\Delta\theta_S$ and N_{Ca}, likely due to lower θ_S reproducibility in the micromodels as discussed earlier. On the other hand, $\Delta\theta_D$ seemed to depend on N_{Ca}, with nearly constant value until a slight increase at $N_{Ca} > 7.68 \cdot 10^{-5}$. The $\Delta\theta_D$ is expected to increase with increasing N_{Ca}, due to increasing θ_A and decreasing θ_R (Eral et al., 2013). A theoretical model for liquid-gas systems (Hoffman 1983) showed that the increase in θ_A becomes more pronounced at $N_{Ca} \geq 10^{-4}$–10^{-3}, comparable with our threshold $N_{Ca} > 7.68 \cdot 10^{-5}$. The $\Delta\theta_S$ is mainly attributed to surface roughness/heterogeneity (Joanny and Degennes 1984) or disjoining/conjoining pressure isotherm in the three-phase contact line (Kuchin and Starov 2016), whereas the $\Delta\theta_D$ is due to local surface blemishes which pin the three-phase contact line (Tadmor 2004). The $\Delta\theta_D$ dependency on N_{Ca} originates from competition between capillary and viscous forces (Friedman 1999).

Hysteresis may also be described by comparing the static and dynamic contact angles in each injection process, where drainage hysteresis describes the difference between $\theta_{S,DR}$ and θ_R and imbibition hysteresis refers to $\theta_{S,IM}$ and θ_A. Several models have been proposed to characterize imbibition hysteresis through the following equation (Jiang et al., 1979; Seebergh and Berg 1992; Li et al., 2013): $\frac{\cos\theta_{S,IM} - \cos\theta_A}{\cos\theta_{S,IM} + 1} =$
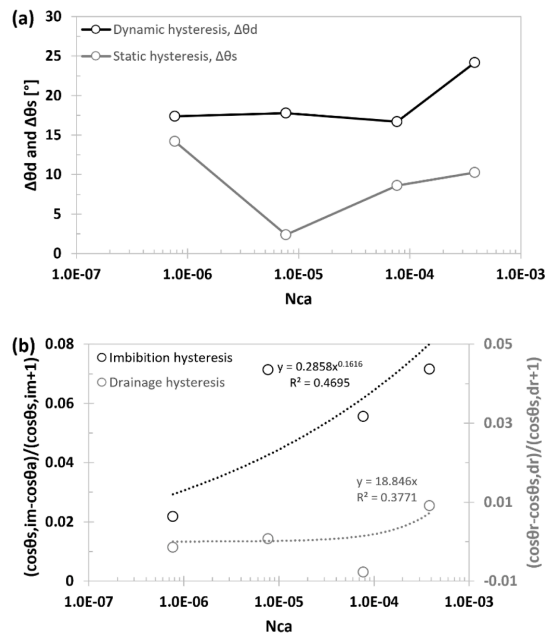

Fig. 12. Contact angle hysteresis. (a) Dynamic contact angle hysteresis, $\Delta\theta_D$, defined as the difference between advancing and receding contact angles, and static contact angle hysteresis, $\Delta\theta_S$, defined as the difference between static angles in imbibition and drainage. Dynamic contact angle hysteresis increased at $N_{Ca} > 7.68 \cdot 10^{-5}$, whereas no clear trend was observed for static angle hysteresis. (b) Drainage/imbibition contact angle hysteresis, which represent the difference between static and dynamic angles in each injection process. The data points were fitted with literature models (Jiang et al., 1979; Shi et al., 2018).

$B_1 \cdot N_{Ca}^{B_2}$. This model was recently adapted for drainage hysteresis in liquid bridges as follows (Shi et al., 2018): $\frac{cos\theta_R - cos\theta_{S,\ DR}}{cos\theta_{S,\ DR}+1} = B_1 \cdot N_{Ca}^{B_2}$. We applied these models to estimate drainage and imbibition hysteresis (Fig. 12b). Our contact angles were fitted with B_1=18.8 and B_2=1.0 for drainage and B_1=0.29 and B_2=0.16 for imbibition, but the correlation was poor with R^2=0.38 and R^2=0.47, respectively. Note, however, that for field-scale implications drainage/imbibition hysteresis is less important than the dynamic one ($\Delta\theta_D$) as discussed above. The $\Delta\theta_D$ can be used to estimate drainage/imbibition hydrogen-water relative permeability curves.

3.4.3. Discussion on measurement techniques

Literature data on hydrogen contact angles is scare, despite being highly relevant for wettability and relative permeability estimations. Our contact angle measurements matched well with θ_S reported for hydrogen in Berea sandstone (Hashemi et al., 2021) and with θ_R in Vosges sandstone (Yekta et al., 2018), but were higher than θ_E in basaltic (Al-Yaseri and Jha 2021) and θ_D in quartz (Iglauer et al., 2021) rocks. Inconsistency between literature results may be related to different experimental conditions, measurement techniques, and cleaning procedures (Iglauer et al., 2015). Contact angle dependency on pressure and temperature was showed with tilted plate method (Al-Yaseri and Jha 2021; Iglauer et al., 2021) and core-scale steady-state drainage (Yekta et al., 2018), whereas the captive-bubble method did not identify any pressure, temperature and salinity effects (Hashemi et al., 2021). Micromodel-based measurement technique used in this study is unconventional and relatively novel, previously applied by a few CO$_2$ studies only (Hu et al., 2017; Jafari and Jung 2017; Chang et al., 2020). However, this measurement method is valuable as it provides direct static and dynamic contact angle measurements in micromodel pores, thus representing multiphase flow in porous media more accurately than indirect measurements. Our results can enhance understanding of wettability as well as relative permeability and capillary pressure hysteresis, which are well-recognized in natural gas storage (Colonna et al., 1972) but not appropriately studied for hydrogen.

Despite being valuable for wettability and hysteresis determination in real pore structures, our measurement technique possessed several sources of uncertainties. The first source was related to the identification of the hydrogen-grain contact line, caused by non-planar grain surfaces and shadows due to non-vertical pore walls. To minimize this error, sufficiently long contact lines were selected on nearly flat grains. The second source of uncertainties was linked to the tangent line drawn along the hydrogen-water curvature. The third source was caused by random hydrogen distribution, which did not allow to measure all four contact angle types in the same pore, enhancing local effect on the measurements. To suppress the effect of uncertainties, the contact angles measurements were repeated five times in each measurement and average values were reported together with uncertainties, thus adding reliability to our measurements.

3.5. Discussion on implications and methodologies

Our results have several field scale implications. Hydrogen saturation after drainage increased with increasing injection rate, suggesting the storage site development is the most efficient at high injection rates. Nevertheless, the Roof snap-off was observed at the highest injection rate (N_{Ca} = 3.84•10^{-4}). This resulted in hydrogen disconnection and trapping, potentially leading to lower storage efficiencies. The observations of the drainage snap-off show that current pore-scale modelling approaches, based on invasion percolation and static snap-off criteria, should be revisited (Roman et al., 2017; Herring et al., 2018). Note that UHS field scale projects will use intermittent hydrogen injections with various frequencies and loads, potentially resulting in reconnection of the residually trapped hydrogen.

If the drainage snap-off occurs at N_{Ca} = 3.84•10^{-4}, the corresponding field-scale injection rate would be approximately 1.7 million Sm^3/d (standard cubic metre per day), based on the perforation length of 30 m and experimental injection velocity. Lower hydrogen injection rates (< 1.7 million Sm^3/d) may therefore be preferred to avoid the hydrogen disconnection. Note, however, that the laboratory N_{Ca} should be applied for field-scale implications with caution because they do not account for important reservoir parameters such as gravity, heterogeneity, and wettability.

Despite low solubility in water, direct pore-scale hydrogen dissolution was observed in our work. Hydrogen dissolution is undesired in storage projects due to loss of recoverable hydrogen (Carden and Paterson 1979). The observed dissolution emphasizes the importance of the cushion gas composition, where other-than-hydrogen cushion gases with low solubility in water are preferred. Moreover, hydrogen dissolution may be enhanced by water encroachment during withdrawal, as well as the buoyancy-driven hydrogen injection from the reservoir bottom. Non-equilibrium dissolution, if valid at the reservoir-scale, is in turn more favourable compared with the equilibrium one, leading to slower hydrogen dissolution. Under subsurface conditions, hydrogen dissolution kinetics is expected to change according to the literature solubility data: hydrogen solubility increases with increasing pressure and decreases with increasing salinity (Chabab et al., 2020).

The numerical approach dominates the UHS literature, relying on the parameter approximations without exact knowledge. Since the UHS is an emerging field, the models need to be validated with hydrogen laboratory data. Microfluidics offers systematic investigation of the parameter space to collaborate model development. However, upscaling of microfluidic experiments to field scale should be implemented with caution, due to their 2D nature with lack of gravitational effects and heterogeneity. Furthermore, the interactions between viscous/capillary and gravitational forces become more pronounced at field scale. The most suitable way to upscale the microfluidic experiments is through pore-scale modelling. For future work, we recommend coupling microfluidic experiments and pore-scale modelling to support the proposed models of hydrogen behaviour in porous media.

4. Conclusions

Microfluidic drainage and imbibition experiments were performed to examine the hydrogen-water flow in a natural sandstone geometry. In situ live camera monitoring provided qualitative data describing hydrogen displacement and trapping mechanisms. Hydrogen dissolution kinetics and contact angles were quantified using image processing. We summarize our main findings as follows:

- Hydrogen saturation after drainage increased with increasing capillary number (N_{Ca}). Hydrogen phase connectivity was generally high except for high-N_{Ca} (3.84•10^{-4}) drainage, where disconnected hydrogen phase established due to Roof snap-off.
- Hydrogen displacement during imbibition was mainly governed by I1 imbibition mechanism, whereas hydrogen disconnection with subsequent residual trapping was generally triggered by I2 imbibition mechanism. Hydrogen dissolution occurred at one end of the bubble mainly.
- Hydrogen dissolution kinetics was quantified showing that average depletion rate of individual hydrogen bubbles ranged between 2.3•10^{-12} to 22•10^{-12} g/sec and appeared to depend on N_{Ca} and initial bubble size. The average global hydrogen depletion rate varied between 3.6•10^{-10} to 277•10^{-10} g/sec. The average dissolved hydrogen concentration in injected water mass was within the range of 6.4•10^{-4} to 11•10^{-4} mol/kg, which was only 16.0–28.3% of the literature solubility, demonstrating the non-equilibrium dissolution.
- Static and dynamic contact angles ranged from 17 to 56°, confirming the non-wetting hydrogen nature. The equilibrium angle calculations fit Class II behaviour. Hysteresis was quantified showing that dynamic contact angle hysteresis was higher than the static.

CRediT authorship contribution statement

Maksim Lysyy: Conceptualization, Methodology, Formal analysis, Investigation, Writing – original draft, Visualization. **Geir Ersland:** Conceptualization, Formal analysis, Writing – review & editing, Supervision, Project administration. **Martin Fernø:** Conceptualization, Formal analysis, Writing – review & editing, Visualization, Supervision, Project administration.

Declaration of Competing Interest

None.

Supplementary materials

Supplementary material associated with this article can be found, in the online version, at doi:10.1016/j.advwatres.2022.104167.

References

Akbarabadi, M., Piri, M., 2013. Relative permeability hysteresis and capillary trapping characteristics of supercritical CO2/brine systems: an experimental study at reservoir conditions. Adv. Water Resour. 52, 190–206.

Al-Yaseri, A., Jha, N.K., 2021. On hydrogen wettability of basaltic rock. J. Pet. Sci. Eng. 200.

al, N.S.M.e, 2022. A review on underground hydrogen storage: insight into geological sites, influencing factors and future outlook. Energy Reports.

Alcorn, Z.P., Foyen, T., Gauteplass, J., Benali, B., Soyke, A., Ferno, M., 2020. Pore- and core-scale insights of nanoparticle-stabilized foam for co2-enhanced oil recovery. Nanomaterials 10 (10).

Andrew, M., Menke, H., Blunt, M.J., Bijeljic, B., 2015. The imaging of dynamic multiphase fluid flow using synchrotron-based x-ray microtomography at reservoir conditions. Transp. Porous Media 110 (1), 1–24.

Armstrong, R.T., Berg, S., 2013. Interfacial velocities and capillary pressure gradients during Haines jumps. Phys. Rev. E 88 (4).

Beckingham, L.E., Winningham, L., 2020. Critical knowledge gaps for understanding water-rock-working phase interactions for compressed energy storage in porous formations. ACS Sustain. Chem. Eng. 8 (1), 2–11.

Berta, M., Dethlefsen, F., Ebert, M., Schafer, D., Dahmke, A., 2018. Geochemical effects of millimolar hydrogen concentrations in groundwater: an experimental study in the context of subsurface hydrogen storage. Environ. Sci. Technol. 52 (8), 4937–4949.

Bo, Z., Zeng, L., Chen, Y., Xie, Q., 2021. Geochemical reactions-induced hydrogen loss during underground hydrogen storage in sandstone reservoirs. Int. J. Hydrogen Energy.

Buchgraber, M., Al-Dossary, M., Ross, C.M., Kovscek, A.R., 2012a. Creation of a dual-porosity micromodel for pore-level visualization of multiphase flow. J. Pet. Sci. Eng. 86-87, 27–38.

Buchgraber, M., Kovscek, A.R., Castanier, L.M., 2012b. A study of microscale gas trapping using etched silicon micromodels. Transp. Porous Media 95 (3), 647–668.

Cao, S.C., Dai, S., Jung, J., 2016. Supercritical CO2 and brine displacement in geological carbon sequestration: micromodel and pore network simulation studies. Int. J. Greenhouse Gas Control 44, 104–114.

Carden, P.O., Paterson, L., 1979. Physical, chemical and energy aspects of underground hydrogen storage. Int. J. Hydrogen Energy 4 (6), 559–569.

Chabab, S., Theveneau, P., Coquelet, C., Corvisier, J., Paricaud, P., 2020. Measurements and predictive models of high- pressure H-2 solubility in brine (H2O+NaCl) for underground hydrogen storage application. Int. J. Hydrogen Energy 45 (56), 32206–32220.

Chang, C., Kneafsey, T.J., Wan, J.M., Tokunaga, T.K., Nakagawa, S., 2020. Impacts of mixed-wettability on brine drainage and supercritical CO2 storage efficiency in a 2.5-D heterogeneous micromodel. Water Resour. Res. 56 (7).

Chang, C., Zhou, Q.L., Kneafsey, T.J., Oostrom, M., Ju, Y., 2019. Coupled supercritical CO2 dissolution and water flow in pore-scale micromodels. Adv. Water Resour. 123, 54–69.

Chang, C., Zhou, Q.L., Kneafsey, T.J., Oostrom, M., Wietsma, T.W., Yu, Q.C., 2016. Pore-scale supercritical CO2 dissolution and mass transfer under imbibition conditions. Adv. Water Resour. 92, 142–158.

Chang, C., Zhou, Q.L., Xia, L., Li, X.Y., Yu, Q.C., 2013. Dynamic displacement and non-equilibrium dissolution of supercritical CO2 in low-permeability sandstone: an experimental study. Int. J. Greenhouse Gas Control 14, 1–14.

Chatzis, I., Morrow, N.R., Lim, H.T., 1983. Magnitude and detailed structure of residual oil saturation. Soc. Pet. Eng. J. 23 (2), 311–326.

Chen, L., Wang, M.Y., Kang, Q.J., Tao, W.Q., 2018. Pore scale study of multiphase multicomponent reactive transport during CO2 dissolution trapping. Adv Water Resour 116, 208–218.

Colonna, J., Brissaud, F., Millet, J.L., 1972. Evolution of capillarity and relative permeability hysteresis. Soc. Pet. Eng. J. 12 (1), 28-&.

De Lucia, M., Pilz, P., Liebscher, A., Kühn, M., 2015. Measurements of H2 solubility in saline solutions under reservoir conditions: preliminary results from project H2STORE. Energy Procedia 76, 487–494.

Deng, W., Balhoff, M., Cardenas, M.B., 2015. Influence of dynamic factors on nonwetting fluid snap-off in pores. Water Resour. Res. 51 (11), 9182–9189.

Duchateau, C., Broseta, D., 2012. A simple method for determining brine-gas interfacial tensions. Adv. Water Resour. 42, 30–36.

Eral, H.B., 't Mannetje, D.J.C.M., Oh, J.M., 2013. Contact angle hysteresis: a review of fundamentals and applications. Colloid. Polym. Sci. 291 (2), 247–260.

Flesch, S., Pudlo, D., Albrecht, D., Jacob, A., Enzmann, F., 2018. Hydrogen underground storage-Petrographic and petrophysical variations in reservoir sandstones from laboratory experiments under simulated reservoir conditions. Int. J. Hydrogen Energy 43 (45), 20822–20835.

Friedman, S.P., 1999. Dynamic contact angle explanation of flow rate-dependent saturation-pressure relationships during transient liquid flow in unsaturated porous media. J. Adhes. Sci. Technol. 13 (12), 1495–1518.

Hashemi, L., Blunt, M., Hajibeygi, H., 2021a. Pore-scale modelling and sensitivity analyses of hydrogen-brine multiphase flow in geological porous media. Sci. Rep. 11 (1).

Hashemi, L., Glerum, W., Farajzadeh, R., Hajibeygi, H., 2021b. Contact angle measurement for hydrogen/brine/sandstone system using captive-bubble method relevant for underground hydrogen storage. Adv. Water Resour. 154.

Herring, A.L., Gilby, F.J., Li, Z., McClure, J.E., Turner, M., Veldkamp, J.P., Beeching, L., Sheppard, A.P., 2018. Observations of nonwetting phase snap-offduring drainage. Adv. Water Resour. 121, 32–43.

Hoffman, R.L., 1983. A study of the advancing interface .2. Theoretical prediction of the dynamic contact-angle in liquid gas systems. J. Colloid Interface Sci. 94 (2), 470–486.

Hornbrook, J.W., Castanier, L.M., Pettit, P.A., 1991. Observation of foam/oil interactions in a new, high-resolution micromodel. In: SPE Annual Technical Conference and Exhibition. Dallas, Texas, Society of Petroleum Engineers.

Hu, R., Wan, J.M., Kim, Y., Tokunaga, T.K., 2017. Wettability impact on supercritical CO2 capillary trapping: pore-scale visualization and quantification. Water Resour. Res. 53 (8), 6377–6394.

Iglauer, S., Ali, M., Keshavarz, A., 2021. Hydrogen wettability of sandstone reservoirs: implications for hydrogen geo-storage. Geophys. Res. Lett. 48 (3).

Iglauer, S., Pentland, C.H., Busch, A., 2015. CO2 wettability of seal and reservoir rocks and the implications for carbon geo-sequestration. Water Resour. Res. 51 (1), 729–774.

Jafari, M., Jung, J., 2017. Direct measurement of static and dynamic contact angles using a random micromodel considering geological CO2 sequestration. Sustainability 9 (12).

Jafari, M., Jung, J., 2019. Salinity effect on micro-scale contact angles using a 2D micromodel for geological carbon dioxide sequestration. J. Pet. Sci. Eng. 178, 152–161.

Jiang, T.S., Oh, S.G., Slattery, J.C., 1979. Correlation for dynamic contact-angle. J. Colloid Interface Sci. 69 (1), 74–77.

Joanny, J.F., Degennes, P.G., 1984. A model for contact-angle hysteresis. J. Chem. Phys. 81 (1), 552–562.

Johnson, R.E., Dettre, R.H., 1964. Contact angle hysteresis .3. Study of an idealized heterogeneous surface. J. Phys. Chem. 68 (7), 1744-&.

Kuchin, I.V., Starov, V.M., 2016. Hysteresis of the contact angle of a meniscus inside a capillary with smooth, homogeneous solid walls. LangmuirLangmuir 32 (21), 5333–5340.

Lenormand, R., Touboul, E., Zarcone, C., 1988. Numerical-models and experiments on immiscible displacements in porous-media. J. Fluid Mech. 189, 165–187.

Lenormand, R., Zarcone, C., Sarr, A., 1983. Mechanisms of the displacement of one fluid by another in a network of capillary ducts. J. Fluid Mech. 135 (Oct), 337–353.

Li, D.D., Beyer, C., Bauer, S., 2018. A unified phase equilibrium model for hydrogen solubility and solution density. Int. J. Hydrogen Energy 43 (1), 512–529.

Li, X.X., Fan, X.F., Askounis, A., Wu, K.J., Sefiane, K., Koutsos, V., 2013. An experimental study on dynamic pore wettability. Chem. Eng. Sci. 104, 988–997.

Lopez-Lazaro, C., Bachaud, P., Moretti, I., Ferrando, N., 2019. Predicting the phase behavior of hydrogen in NaCl brines by molecular simulation for geological applications. Bsgf-Earth Sci. Bull. 190.

Lord, A.S., Kobos, P.H., Borns, D.J., 2014. Geologic storage of hydrogen: scaling up to meet city transportation demands. Int. J. Hydrogen Energy 39 (28), 15570–15582.

Lubon, K., Tarkowski, R., 2021. Influence of capillary threshold pressure and injection well location on the dynamic CO2 and H-2 storage capacity for the deep geological structure. Int. J. Hydrogen Energy 46 (58), 30048–30060.

Lysyy, M., Ferno, M., Ersland, G., 2021. Seasonal hydrogen storage in a depleted oil and gas field. Int. J. Hydrogen Energy 46 (49), 25160–25174.

Kanaani, Mahdi, S, B., Asadian-Pakfar, Mojtaba, 2022. Role of cushion gas on underground hydrogen storage in depleted oil reservoirs. J. Energy Storage.

Massoudi, R., King, A.D., 1974. Effect of pressure on surface-tension of water - adsorption of low-molecular weight gases on water at 25 degrees. J. Phys. Chem. 78 (22), 2262–2266.

Moebius, F., Or, D., 2012. Interfacial jumps and pressure bursts during fluid displacement in interacting irregular capillaries. J. Colloid Interface Sci. 377, 406–415.

Mohanty, K.K., Davis, H.T., Scriven, L.E., 1987. Physics of oil entrapment in water-wet rock. SPE Reservoir Eng. 2 (01), 113–128.

Morrow, N.R., 1975. Effects of surface-roughness on contact angle with special reference to petroleum recovery. J. Can. Pet. Technol. 14 (4), 42–53.

Ozarslan, A., 2012. Large-scale hydrogen energy storage in salt caverns. Int. J. Hydrogen Energy 37 (19), 14265–14277.

Panfilov, M., 2010. Underground storage of hydrogen: in situ self-organisation and methane generation. Transp. Porous Media 85 (3), 841–865.

Panfilov, M., 2016. Underground and pipeline hydrogen storage. Compendium of Hydrogen Energy. Woodhead Publishing.

Paterson, L., 1983. The implications of fingering in underground hydrogen storage. Int. J. Hydrogen Energy 8 (1), 53–59.

Pérez, A., Pérez, E., Dupraz, S., Bolcich, J., 2016. In: Patagonia Wind - Hydrogen Project: Underground Storage and Methanation. *21st world hydrogen energy conference.* Zaragoza, Spain.

Pruess, K., Spycher, N., 2007. ECO2N - a fluid property module for the TOUGH2 code for studies of CO2 storage in saline aquifers. Energy Convers. Manage. 48 (6), 1761–1767.

Roman, S., Abu-Al-Saud, M.O., Tokunaga, T., Wan, J.M., Kovscek, A.R., Tchelepi, H.A., 2017. Measurements and simulation of liquid films during drainage displacements and snap-off in constricted capillary tubes. J. Colloid Interface Sci. 507, 279–289.

Roof, J.G., 1970. Snap-off of oil droplets in water-wet pores. Soc. Pet. Eng. J. 10 (1), 85-&.

Seebergh, J.E., Berg, J.C., 1992. Dynamic wetting in the low capillary number regime. Chem. Eng. Sci. 47 (17–18), 4455–4464.

Shi, Z., Zhang, Y., Liu, M.C., Hanaor, D.A.H., Gan, Y.X., 2018. Dynamic contact angle hysteresis in liquid bridges. Colloids Surfaces a-Physicochem. Eng. Aspects 555, 365–371.

Smigan, P., Greksak, M., Kozankova, J., Buzek, F., Onderka, V., Wolf, I., 1990. Methanogenic bacteria as a key factor involved in changes of town gas stored in an underground reservoir. FEMS Microbiol. Ecol. 73 (3), 221–224.

Tadmor, R., 2004. Line energy and the relation between advancing, receding, and young contact angles. LangmuirLangmuir 20 (18), 7659–7664.

Valvatne, P.H., Blunt, M.J., 2004. Predictive pore-scale modeling of two-phase flow in mixed wet media. Water Resour. Res. 40 (7).

Wu, D.S., Hu, R., Lan, T., Chen, Y.F., 2021. Role of pore-scale disorder in fluid displacement: experiments and theoretical model. Water Resour. Res. 57 (1).

Yekta, A.E., Manceau, J.C., Gaboreau, S., Pichavant, M., Audigane, P., 2018. Determination of hydrogen-water relative permeability and capillary pressure in sandstone: application to underground hydrogen injection in sedimentary formations. Transp. Porous Media 122 (2), 333–356.

Zhang, C.Y., Oostrom, M., Wietsma, T.W., Grate, J.W., Warner, M.G., 2011. Influence of viscous and capillary forces on immiscible fluid displacement: pore-scale experimental study in a water-wet micromodel demonstrating viscous and capillary fingering. Energy Fuels 25 (8), 3493–3505.

Paper 3

Microfluidic hydrogen storage capacity and residual trapping during cyclic injections: Implications for underground storage

Maksim Lysyy [*], *Na Liu, Celine M. Solstad, Martin A. Fernø, Geir Ersland*

Department of Physics and Technology, University of Bergen, Allegaten 55, 5007 Bergen, Norway

HIGHLIGHTS

- Microfluidics for examination of cyclic hydrogen injections.
- Microscopic hydrogen storage capacities up to 60% of the pore space.
- Reproducible residual hydrogen saturation between the injection cycles.
- Efficient reconnection of residually trapped hydrogen in the next drainage cycle.

GRAPHICAL ABSTRACT
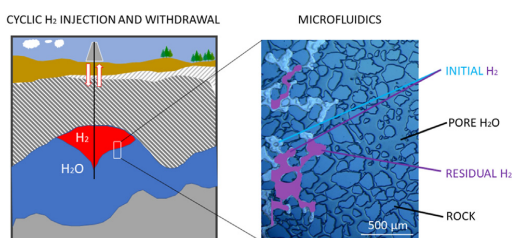
ABSTRACT

Long-term and large-scale H_2 storage is vital for a sustainable H_2 economy. Research in underground H_2 storage (UHS) in porous media is emerging, but the understanding of H_2 reconnection and recovery mechanisms under cyclic loading is not yet adequate. This paper reports a qualitative and quantitative investigation of H_2 reconnection and recovery mechanisms in repeated injection-withdrawal cycles. Here we use microfluidics to experimentally investigate up to 5 cycles of H_2 injection and withdrawal under a range of injection rates at shallow reservoir storage conditions. We find that H_2 storage capacities increase with increasing injection rate and range between ~10% and 60%. The residual H_2 saturation is in the same range between cycles (30–40%), but its distribution in the pore space visually appears to be hysteretic. In most cases, the residually trapped H_2 reconnects in the subsequent injection cycle, predominantly in proximity to the large pore clusters. Our results provide valuable experimental data to advance the understanding of multiple H_2 injection cycles in UHS schemes.

* *Corresponding author.* University of Bergen, Department of Physics and Technology, Allegaten 555007 Bergen Norway.
    E-mail address: maksim.lysyy@uib.no (M. Lysyy).

Introduction

Hydrogen (H_2) is an emission-free energy carrier and its wider use can contribute to climate change mitigation by decreasing the share of fossil fuels in the global energy mix. Full-scale industrial implementation in a global H_2 economy will require numerous storage sites and solutions [1]. Future H_2 storage demand in Europe is predicted to range between 63 and 180 billion standard m^3 in 2050, assuming H_2 total demand of 780—2251 TWh [2] and 24% storage capacity [3]. Underground H_2 storage (UHS) in depleted hydrocarbon fields and aquifers has been proposed as a reliable and safe storage technology due to the presence of an impermeable seal and large pore space [4,5]. The technicalities are similar to natural gas storage (UGS), where cushion gas remains in reservoir to maintain the target pressure and working gas is injected at peak supply (summer) and withdrawn at peak demand (winter). However, H_2 is a low density and low viscosity gas with high diffusivity and biogeochemical reactivity and therefore its behavior in porous media will differ from that of other gases. The experience with UHS in porous media is limited to: 1) two pilot tests in depleted gas fields [6,7] and 2) town gas storage in aquifers [8,9].

Scientific challenges relevant for the UHS arise from H2 physical properties as well as reactions with rock minerals and microorganisms, potentially reducing the storage efficiency [5,10]. H_2 injections are prone to unstable displacement and gravity override due to low viscosity and density. Moreover, a certain amount of H_2 may be permanently lost during storage operation by various physical, chemical and operating loss mechanisms [4]. Reservoir simulation and wettability studies are currently dominating the research literature in the field of UHS flow physics. Storage capacities and recovery factors have been estimated using conceptual reservoir models with extrapolated input parameters not specifically measured for H_2 [11,12].

Contact angle measurements indicated that H_2 is a non-wetting fluid on pure quartz surfaces and sandstones but shifts to intermediate-wet state in the presence of organic acids [13—16]. No clear difference in contact angles was reported between H_2, CH_4, H_2—CH_4 mixtures and N_2 using a captive-bubble method in sandstones and a borosilicate micromodel at pressures between 10 and 100 bar [17,18]. On the other hand, CO_2 was found to be more wetting, i.e. higher contact angles, compared to H_2 [13,16]. Note that the contact angle differences between various gases are expected to become more pronounced at pressures above 100 bar due to the increasing gas density differences, shown for basaltic rocks [19]. Moreover, rock-gas interfacial tension calculations indicated significant differences between H_2, CH_4 and CO_2 [20]. There are also discrepancies regarding the influence of pressure, temperature and salinity on H_2 wettability. H_2 contact angles increased with increasing pressure and temperature when using the tilted plate method [13,16], whereas no meaningful effect of pressure, temperature and salinity was reported using the captive bubble technique under a range of 7—207 bar, 20—50 °C and 1000—50000 ppm NaCl brine [14,15,17]. Neither reservoir simulations nor wettability studies can adequately describe pore scale influencing factors on UHS

such as interactions between H_2, reservoir rock and its native fluid as well as trapping mechanisms [21]. Residual trapping is recognized as one of the major H_2 loss mechanisms [4,22], which is expected to decrease with decreasing capillary forces and increasing H_2 wetting [23]. The UHS involves multiple cycles of H_2 injection (drainage) and withdrawal (imbibition), and residual trapping occurs during imbibition where water is available and mobile in the reservoir, e.g. in the H_2—H_2O transition zones. The residually trapped H_2 ganglia may reconnect during drainage due to hysteresis. Hysteresis was evident from relative permeability measurements [24,25] and microfluidic-based contact angle measurements [26], but it remains unaddressed for several injection-withdrawal cycles.

A few laboratory investigations of H_2 residual trapping used in-situ visualization of a single drainage-imbibition cycle in different sandstones. The initial and residual H_2 saturations in the pore space (values between 0 and 1) were measured to be 0.65 and 0.41, respectively [27]. H_2 recovery decreased from 43.1% when flooded with non-H_2-equilibrated brine to 31.6% for H_2-equilibrated brine [28]. The initial H_2 saturation was ~6 times lower compared to N_2 using the same injection rate [29]. No clear pressure impact on the initial H_2 saturation was evident, contrary to H_2 residual trapping which increased with increasing pressure and decreasing injection rate [30].

H_2 cyclic injections were only performed for two drainage-imbibition cycles and resulted in similar initial and residual H_2 saturations: 0.48 and 0.07, respectively [30]. In contrast, cyclic injections have been extensively investigated for CO_2 storage, where some studies indicated an increased residual trapping over the injection cycles [31—33], contradicting a classic trapping theory [34]. More systematic studies with the increased number of injection cycles are required to find out whether the multiple injection cycles can potentially result in hysteresis and increase H_2 residual trapping.

Microfluidics is a valuable tool for direct observations of pore space to corroborate core scale measurements. Small pore volumes are beneficial for the sake of time and safety when working with highly flammable H_2 gas at elevated pressures. In this work, we qualitatively describe hysteretic H_2 trapping and reconnection mechanisms during cyclic injections in a silicon-wafer micromodel with pore patterns resembling a natural sandstone. Up to 4—5 drainage-imbibition cycles were run under a wide range of injection rates at 40 bar and ambient temperature, representing the storage conditions of a shallow aquifer or a gas-water transition zone in a depleted gas field. An in-house MATLAB code was developed to quantify microscopic H_2 storage capacity, residual trapping and recovery factors. Our results add new experimental data, enhancing the understating of hysteretic H_2 behavior during multiple injection cycles.

Materials and methods

Porous material

We used a silicon micromodel capable of withstanding pressure up to 150 bar (Fig. 1). The irregular sandstone-based pore patterns (pure quartz) were etched and repeated 36 (4 × 9) times on the silicon wafer using deep reactive ioning etching
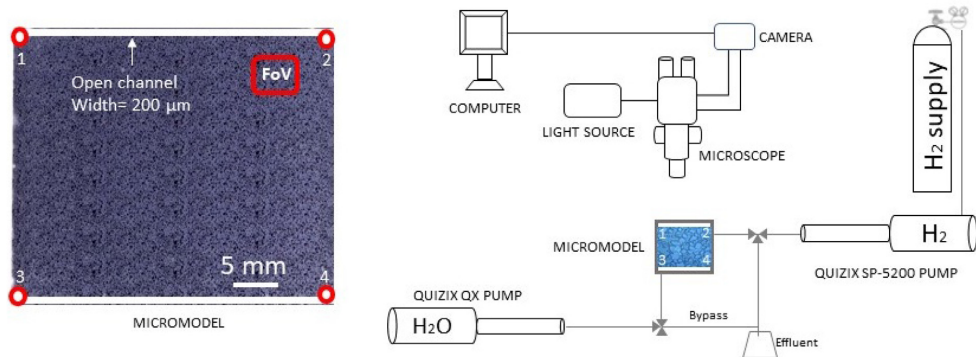
Fig. 1 — Left: Micromodel with irregular pore patterns replicating natural sandstone. The micromodel was built with four ports (1−4) and two open channels (from the ports 1 to 2 and from 3 to 4). The field of view (FoV) refers to the micromodel area observed by the microscope (not to scale). Right: Experimental setup consisting of the micromodel, two pumps for H_2 and H_2O injections and pressure control as well as the microscope equipped with the light source and the camera. H_2 and H_2O were injected diagonally from the opposite ports, i.e. from ports 2 and 3, respectively.

(DRIE) with an etching depth of 30 μm. The DRIE technique ensured a correct reproduction of morphological and topological features, preserving the sharp grain walls with a surface roughness of 100 nm and high aspect ratio and coordination number, which ensured a correct magnitude of the capillary forces. The micromodel top (transparent borosilicate glass) and bottom (silicon) surfaces were anodically bonded and produced with strongly hydrophilic surfaces, with measured H_2 contact angles ranging between 19° and 60°. The micromodel surfaces were not aged in organic acids, making them more hydrophilic than natural reservoirs [13,16]. The micromodel has two open channels (100% void space), connected from ports 1 to 2 and from 3 to 4. The pore network has a length of 27 mm and a width of 21.4 mm, with a total porosity of 61% (Table 1). The micromodel studied region is defined as the field of view (FoV) and represents approximately 1% of the entire area micromodel. A more detailed description of the micromodel construction procedure and its properties can be found elsewhere [35,36].

Experimental setup and procedures

The micromodel was assembled in the PEEK holder with four outlet ports connected to the 1/16″ PEEK tubing, where two tubes from the diagonally located ports (2 and 3) were connected to two Quizix pumps through 1/16" stainless-steel tubing (Fig. 1). Quizix QX pump was filled with filtered

deionized H_2O, whereas H_2 was accommodated by Quizix SP-5200 pump (cylinder C5000-10K-SS-AT). A microscope (Nikon SMZ1500) connected to a camera (Nikon D7100) and computer enabled us to directly observe the micromodel FoV, which was illuminated by a light source with spot lighting (Photonic LED F1 Cold light 5500K).

Two different groups of experiments were performed at pore pressure of 40 bar and ambient temperature (20 ± 1 °C): 1) Single-cycle of H_2 injection and withdrawal, i.e. primary drainage and imbibition only (experiments A1-A4) and 2) multiple cycles of H_2 injection and withdrawal (experiments B1−B4). An overview of experiments and key results are shown in Table 3. In the experiments A1-A4, the H_2O pump was used for H_2O withdrawal (drainage) and injection (imbibition), whereas the constant pressure in the micromodel was maintained by the H_2 pump. In total, single-cycle injection-withdrawal experiments were performed four times at different injection rates in the range of 0.1−50 mL/h.

In experiments B1−B4, the pump operation modes were different. During drainage, the H_2O pump was set to constant pressure and H_2 was injected from the H_2 pump at constant flow rate. After drainage, the tubing connection from the H_2O pump to the micromodel was cleaned with H_2O via the by-pass tubing to remove the remaining H_2, preventing the H_2−H_2O slug flow in the micromodel. During imbibition, both pumps were operated at constant flow rates where H_2O was injected in the micromodel while the piston in the H_2 pump retracted. Imbibition was terminated after the establishment of the residually trapped H_2 ganglia. Then the system was ready for a new drainage-imbibition cycle, which was repeated three-four times. Prior to a new cycle, H_2 was injected to the bypass line to remove the remaining H_2O. In total, four cyclic experiments were run at various injection rates in the range of 1−10 mL/h.

Dimensionless numbers describe the interplay between various forces acting on two-phase flow. In this work, the capillary number (the ratio of viscous to capillary forces) is defined as $N_{Ca} = U \bullet \mu / \sigma$, where U is the injection velocity [m/s], μ is the invading fluid viscosity [$\mu_{H2} = 8.8 \times 10^{-6}$ Pa s and

Table 1 − Micromodel properties.		
	Micromodel	Micromodel FoV
Length [mm]	27	3.5
Width [mm]	21.4	1.96
Depth [μm]	30	
Pore volume [μL]	11	0.09
Porosity [frac.]	0.61	0.44
Permeability [D]	2.97	
Pore throat length [μm]	10−300	

Table 2 – Flow conditions: Injection rate (Q) and injection velocity (U); and dimensionless numbers: Capillary (N_{Ca}), Reynolds (Re), Peclet (Pe), and Bond numbers (Bo).

Q [mL/h]	U [m/day]	N_{Ca}		Re		Pe	Bo
		Drainage	Imbibition	Drainage	Imbibition		
0.1	4.9	6.8×10^{-9}	7.7×10^{-7}	0.002	0.006	1.6	0.0017
1	48.6	6.8×10^{-8}	7.7×10^{-6}	0.02	0.06	15.9	
2.5	121.4	1.7×10^{-7}	1.9×10^{-5}	0.06	0.16	39.7	
5	242.9	3.4×10^{-7}	3.8×10^{-5}	0.12	0.32	79.3	
10	485.7	6.8×10^{-7}	7.7×10^{-5}	0.23	0.63	158.6	
50	2428.7	3.4×10^{-6}	3.4×10^{-4}	1.16	3.17	793.2	

Table 3 – Initial (S_{gi}) and residual (S_{gr}) H_2 saturations and recovery factors, defined as ($S_{gi} - S_{gr}$)/S_{gi}, during single-cycle (A1-A4) and multiple-cycles (B1–B4) injections.

Exp ID	Q [mL/h]	Cycle number	S_{gi} [fraction]	S_{gr} [fraction]	Recovery factor [fraction]
A1	0.1	1	0.09	0.04	0.53
A2	1	1	0.18	0.05	0.71
A3	10	1	0.61	0.33	0.45
A4	50	1	0.47	0.30	0.38
B1	1	1	0.14	0.03	0.44
		2	0.09	0.04	0.49
		3	0.13	0.07	0.48
		4	0.06	0.08	N/A
B2	2.5	1	0.36	0.35	0.02
		2	0.45	0.40	0.10
		3	0.50	0.42	0.16
		4	0.38	0.33	0.17
		5	0.73	0.48	0.34
B3	5	1	0.42	0.32	0.23
		2	0.60	0.31	0.48
		3	0.67	0.28	0.59
		4	0.53	0.32	0.40
		5	0.60	0.34	0.42
B4	10	1	0.50	0.29	0.42
		2	0.56	0.31	0.45
		3	0.42	0.29	0.32
		4	0.62	0.27	0.57
		5	0.58	0.28	0.51

$\mu_{H2O} = 1.0 \times 10^{-3}$ Pa s [37]], and σ is the H_2–H_2O interfacial tension [= 0.073 N/m [38]]. The injection velocity was calculated as follows: $U = Q/(L \cdot d \cdot \phi)$, where Q is the injection rate [m^3/s], ϕ is the micromodel porosity [faction], and L and d are the micromodel length and depth [m], respectively. The Reynolds number (the ratio of inertial to viscous forces) is defined as Re = $\rho \cdot U \cdot D_{50}/\mu$, where ρ is the invading fluid density [$\rho_{H2} = 3.2$ kg/m^3 and $\rho_{H2O} = 1000$ kg/m^3] and D_{50} = median grain diameter [= 1.1×10^{-4} m] – an approximation of the characteristic length scale [39]. The Peclet number correlates convection and diffusion transport and is defined as Pe = $U \cdot D_{50}/D$, where D is the H_2 diffusion coefficient through water equal to 4×10^{-9} m^2/s [40]. The Bond number (the ratio of gravitational to surface tension forces) is defined as Bo = $\Delta\rho \cdot g \cdot (D_{50})^2/\sigma$, where $\Delta\rho$ is the density difference between H_2 and H_2O, and g is the acceleration due to gravity. The range of various dimensionless numbers (Table 2) was estimated at experimental conditions and indicated that the H_2–H_2O flow occurred under the laminar flow regime, with the dominance of convection and surface tension (i.e., capillary forces) over diffusion and gravity. The interplay between viscous and capillary forces was non-trivial where both forces could compete because the experimental N_{Ca}-range belongs to the transition zone in the Log (N_{Ca})-flow diagram [26,41].

Image analysis

The raw images were processed and analyzed to calculate the FoV porosity and H_2 saturation using a combination of an open-source ImageJ software and in-house MATLAB code. The color gradients due to a spotlight required the image pre-processing with manual segmentation of the grains. The FoV porosity was therefore calculated for each image using color thresholding in ImageJ before further analysis in MATLAB. The H_2 saturations were calculated based on the in-house MATLAB code that used the background subtraction algorithm, with a background image of 100% H_2O-saturated FoV. The average relative uncertainty of H_2 saturation was estimated to be 9% and was related to the noise threshold, caused by inclusion of the H_2O droplets and small grains in the H_2 saturation. By adjusting a threshold value of several sequential images with equal quasi-steady-state H_2 saturation, the relative uncertainty was calculated as standard deviation.

Results and discussion

Displacement, trapping and re-connection mechanisms

Primary drainage injections at low rates (≤1 mL/h) resulted in the low H_2 saturation in the FoV (S_g < 0.20) due to high capillary entry pressures (Fig. 2, Table 3). At high injection rates (≥10 mL/h) the H_2 saturation increased by ~2–3 times and both connected and disconnected H_2 established due to Roof snap-off [42]. H_2 displacement and trapping during imbibition was governed by I1 imbibition and I2 imbibition mechanisms, respectively [43]. H_2 was displaced from several pores to a single pore (I1 imbibition), where H_2 was disconnected at the pore wall and residually trapped (I2 imbibition). Distribution of the residually trapped H_2 after imbibition (red + purple in Fig. 2) depended on the initial H_2 distribution after drainage (blue + purple in Fig. 2). In most cases, the residually trapped H_2 remained in the same pores (purple in Fig. 2c and d), but displacement to the neighboring pores was also observed (red in Fig. 2c and d). The observed displacement and trapping mechanisms corroborated our previous study in the same micromodel at 5 bar [26], suggesting that displacement
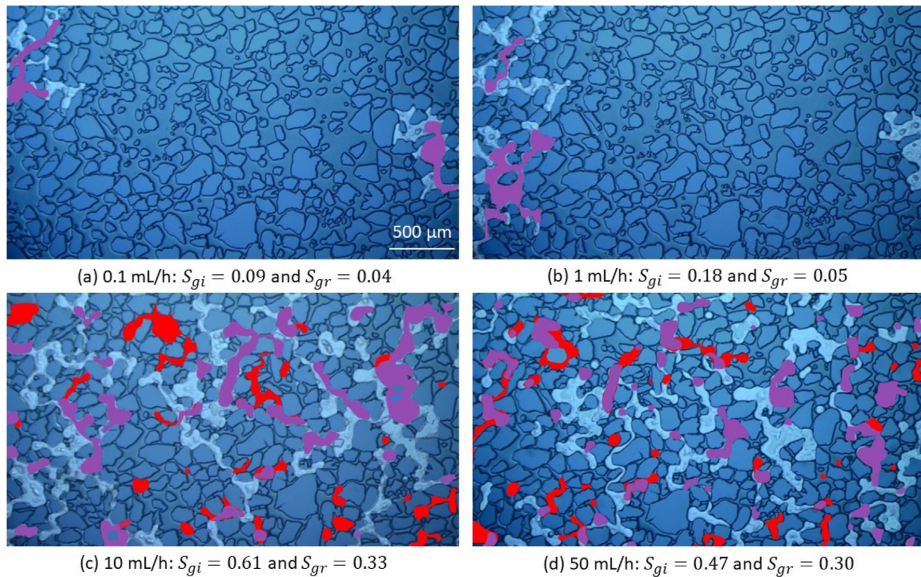
(a) 0.1 mL/h: $S_{gi} = 0.09$ and $S_{gr} = 0.04$

(b) 1 mL/h: $S_{gi} = 0.18$ and $S_{gr} = 0.05$

(c) 10 mL/h: $S_{gi} = 0.61$ and $S_{gr} = 0.33$

(d) 50 mL/h: $S_{gi} = 0.47$ and $S_{gr} = 0.30$

Fig. 2 – Combined images of H_2 saturation after primary drainage, S_{gi} (blue + purple), and after imbibition, S_{gr} (red + purple). Purple color highlights the intersection area of the H_2-filed pore space after drainage and after imbibition. The S_{gi} depended on the injection rate, with higher rates (≥10 mL/h) yielding higher S_{gi}. In most cases, the S_{gr} resided in the same pores as the S_{gi} (purple) but could also redistribute to the neighboring pores indicated with red color. (For interpretation of the references to color in this figure legend, the reader is referred to the Web version of this article.)

(a) Cycle 1: $S_{gi} = 0.42$ and $S_{gr} = 0.32$

(b) Cycle 2: $S_{gi} = 0.60$ and $S_{gr} = 0.31$

(c) Cycle 3: $S_{gi} = 0.67$ and $S_{gr} = 0.28$

(d) Cycle 4: $S_{gi} = 0.53$ and $S_{gr} = 0.32$

(e) Cycle 5: $S_{gi} = 0.60$ and $S_{gr} = 0.34$
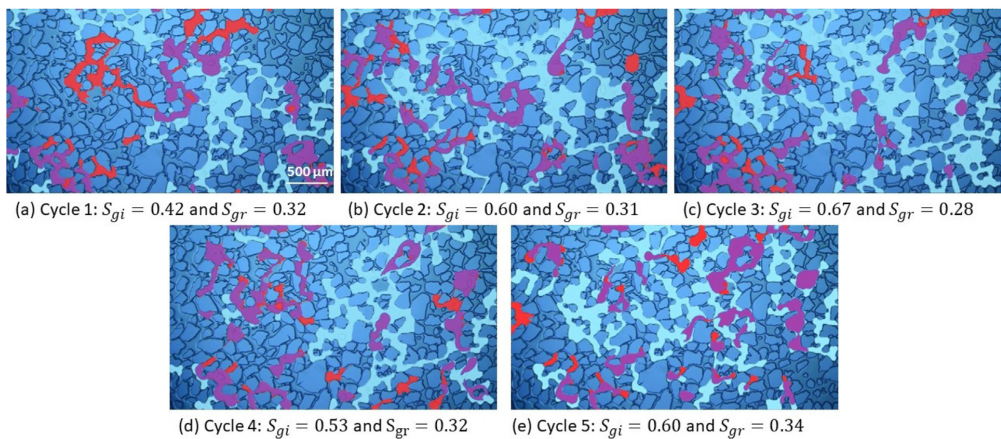
Fig. 3 – Cyclic H_2 injection and withdrawal at 5 mL/h (Exp B3), with the combined images of S_{gi} (blue + purple) and S_{gr} (red + purple). In general, the H_2 distribution varied between the cycles but was similar between cycles 2 and 3. The S_{gi} tended to distribute in the large, connected pore clusters (middle right area of the images), whereas the S_{gr} distribution changed over the cycles showing hysteresis despite having similar S_{gr} values of ~0.30. (For interpretation of the references to color in this figure legend, the reader is referred to the Web version of this article.)

mechanisms were independent of pressure in the 5–40 bar range.

Cyclic injections resulted in fluctuating H_2 saturation between 0.42 and 0.67 after drainage, due to the H_2 movement from outside the FoV (Fig. 3, Exp B3). H_2 preferentially occupied the large, connected pore clusters (middle, right region of the images in Fig. 3). The residual H_2 saturation after imbibition exhibited little variation over several cycles (average
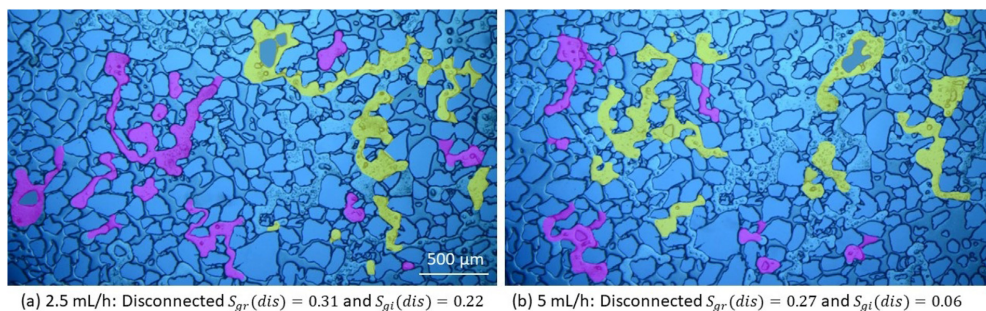
(a) 2.5 mL/h: Disconnected $S_{gr}(dis) = 0.31$ and $S_{gi}(dis) = 0.22$ (b) 5 mL/h: Disconnected $S_{gr}(dis) = 0.27$ and $S_{gi}(dis) = 0.06$

Fig. 4 – H$_2$ reconnection with the injected H$_2$ in the subsequent drainage cycle: (a) From cycle 3 to 4 at 2.5 mL/h (3 → 4), and (b) from cycle 4 to 5 at 5 mL/h (4 → 5). H$_2$ reconnection seemed somewhat stochastic locally but was favored in the large pore clusters with wide pore throats. A portion of the disconnected H$_2$ after imbibition, S_{gr} *(dis)* (yellow + purple) connected with the injected H$_2$ during the subsequent drainage (yellow) and the rest remained as disconnected, S_{gi} *(dis)* (purple). The injected H$_2$ is not manually segmented and appears in the image in its original light blue color. (For interpretation of the references to color in this figure legend, the reader is referred to the Web version of this article.)

$S_{gr} = 0.31 \pm 0.03$), however, its pore space distribution varied between cycles due to hysteresis. Variations in the residual H$_2$ distribution have also been reported during core flooding and μCT imaging, despite equal residual H$_2$ saturations [30]. In our case, the residually trapped H$_2$ was not necessarily immobile in the subsequent cycle and could reconnect with the injected H$_2$, described next.

The ability of H$_2$ ganglia to reconnect seemed stochastic locally between pores but the global distribution appeared to depend on the pore cluster morphology (Fig. 4). The H$_2$ ganglia in proximity to pore clusters with wide pore throats tended to reconnect during drainage (yellow in Fig. 4), whereas H$_2$ ganglia remained disconnected in the pores with narrow pore throats (purple in Fig. 4). In contrast, the core flooding experiments with μCT imaging showed that the residual CO$_2$ ganglia size gradually changed with increasing number of cycles, penetrating smaller pore throats [32,33]. Reconnection of H$_2$ ganglia during drainage was in general high, characterized by the amount reduction of H$_2$ ganglia in 9 out of 12 drainage injections relative to previous imbibition injections (Fig. 5). High H$_2$ ability to reconnect is favorable for real storage projects, reducing H$_2$ loss during cyclic injections.

Microscopic storage capacity

Microscopic H$_2$ storage capacity was evaluated based on capillary number correlation (CNC) and pore pressures (Fig. 6, Table 3). The initial H$_2$ saturation after drainage changed both monotonically (at 5 bar) and nonmonotonically (at 1, 30 and 40 bar) with increased capillary number. A monotonic increase after a plateau region was consistent with classic CNC at core scale [44] and some microfluidic studies [41,45]. Non-monotonic trends were also reported from micromodels [46–48], likely due to the crossover from capillary to viscous flow regimes and/or micromodel properties [44].

When averaged for a specific capillary number, the initial H$_2$ saturation exhibited a monotonic trend (Fig. 6). The critical drainage capillary number ranged between 3.4–6.8×10^{-7}, corresponding to maximum H$_2$ storage capacity of ~60% of the
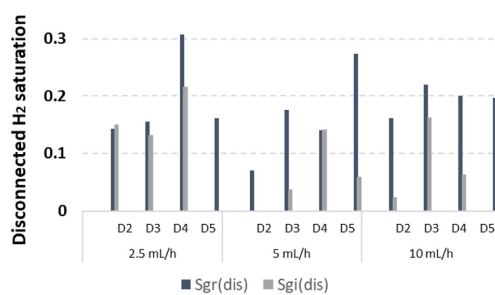

Fig. 5 – Quantification of the H$_2$ ganglia reconnection, by comparing the disconnected H$_2$ saturation after imbibition, S_{gr} *(dis)* (blue) and the subsequent drainage cycle, S_{gi} *(dis)* (gray) at the injection rates of 2.5, 5 and 10 mL/h. The horizontal axis compares the two subsequent cycles: The transition from the imbibition cycle 1 to the drainage cycle 2 is denoted as D2. In most cases, the disconnected H$_2$ saturation decreased in the subsequent drainage cycle, indicating high reconnection ability. (For interpretation of the references to color in this figure legend, the reader is referred to the Web version of this article.)

pore space. The optimal reservoir scale injection rate yielding the highest storage capacity would therefore be in the range of ~170–340 thousand standard m^3/day, assuming the injector perforation length of 30 m and the experimental injection velocity. Our storage capacity and injection rates were comparable with the reservoir simulations of aquifer storage assuming maximum H$_2$ saturations of 70% and injection rates of ~200–300 thousand standard m^3/day [11,12,49].

No clear pressure effect was observed on the initial H$_2$ saturation, contradicting classic threshold pressure phenomena [50]. The saturation independence from pressure was likely due to insignificant wettability and interfacial tension alterations in the H$_2$–H$_2$O systems under the studied pressure range of 1–40 bar. The H$_2$ contact angles (i.e. wettability)
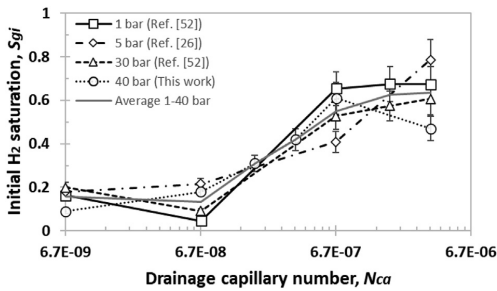
Fig. 6 — Microscopic H_2 storage capacity from the capillary number correlation (CNC) compared with the results from the same micromodel at 1, 5, and 30 bar [26,52]. The S_{gi} was independent of pressure. The maximum H_2 storage capacity was on average equal to ~60% of the pore space (gray curve). The error bars represent the image analysis relative uncertainty (9%).

showed no pressure dependence under the range of 20—100 bar in Berea and Bentheimer sandstones [14]. Insignificant contact angle changes of ~5° were reported for H_2 on the pure quartz surface for pore pressures ranging between 1 and 50 bar and room temperature [16]. The H_2—H_2O interfacial tension increases by less than 1% from 1 to 40 bar [38]. No correlation between initial gas saturation and pressure has been reported for CO_2, N_2, and H_2 at core scale [30,51], corroborating our results.

Residual trapping and microscopic recovery during cyclic injections

The initial and residual H_2 saturations were quantified for cyclic injections and the corresponding microscopic recovery factor was calculated for every cycle (Fig. 7, Table 3). The H_2 saturation range between the cycles depended on the injection rate, in accordance with the critical capillary number from the CNC (Fig. 6). The low injection rate (1 mL/h) resulted in a low saturation range between 0.03 and 0.14 (Fig. 7a), with an increase up to 0.27—0.73 at higher injection rates (≥2.5 mL/h) (Fig. 7b—d). The initial H_2 saturation varied between the cycles at higher injection rates, whereas the residual H_2 remained nearly constant and equal to ~0.43 at 2.5 mL/h, ~0.31 at 5 mL/h, and ~0.29 at 10 mL/h, explained next.

The reason for the fluctuations in the initial H_2 saturation could be twofold: 1) H_2 redistribution from outside the FoV, caused by random H_2 injection patterns, and/or 2) the presence of the disconnected H_2 ganglia. A further analysis (Fig. 8) revealed that both connected and disconnected H_2 saturation were stochastic without any clear trend, meaning that H_2 redistribution (reason 1) was the main cause for the fluctuating initial saturations. The opposite was observed for n-hexane (C_6H_{14}, used as a proxy for CO_2) cyclic injections in a micromodel, where the amount of the disconnected C_6H_{14} increased over the cycles due to the converged injection patterns through the most accessed pore channels [53]. The discrepancies with our study were likely caused by the differences in the micromodel design. In our case, two open
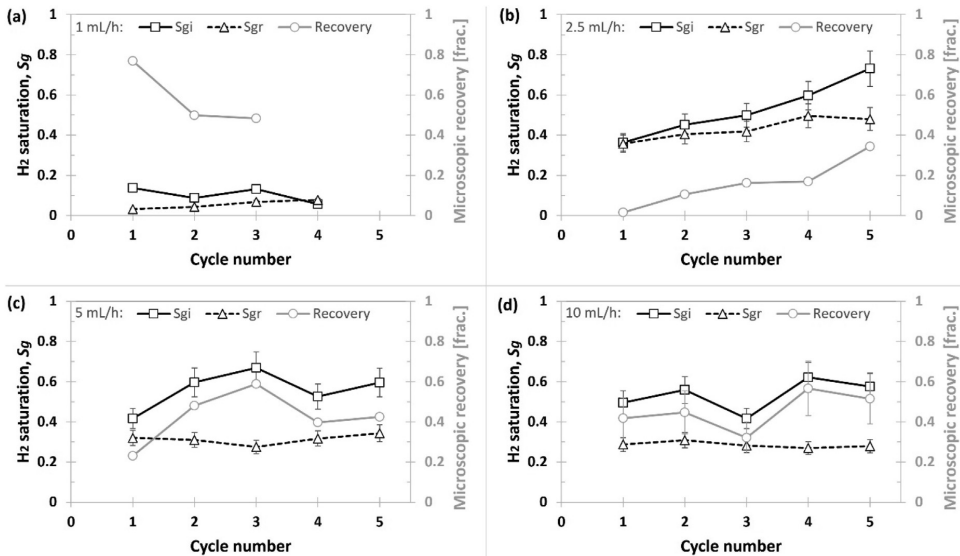

Fig. 7 — Initial (S_{gi}) and residual (S_{gr}) H_2 saturation and the resulting microscopic recovery factors during cyclic injections at the flow rate of: (a) 1 mL/h, (b) 2.5 mL/h, (c) 5 mL/h, (d) 10 mL/h. The S_{gi} fluctuated between the cycles due to H_2 redistribution from outside the FoV. In contrast, the S_{gr} showed better reproducibility, with nearly constant values throughout the cycles. The microscopic recovery factors reflected the fluctuations in the S_{gi}. The error bars represent the image analysis relative uncertainty (9%).
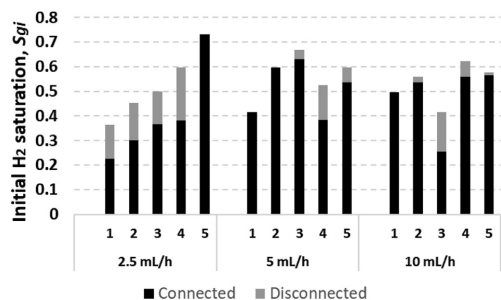
Fig. 8 – Share of the connected and disconnected initial H_2 saturation (S_{gi}) during cyclic injections (cycles 1–5) at the injection rate of 2.5, 5 and 10 mL/h. No clear trend was observed, meaning that the presence of the disconnected H_2 did not cause the fluctuations in the S_{gi} in Fig. 7.
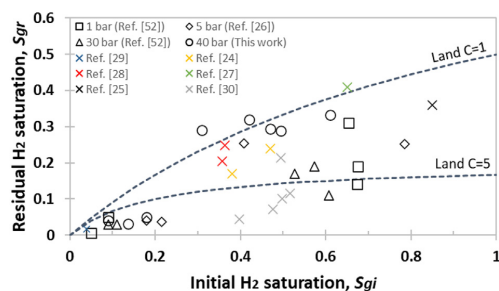

Fig. 9 – Trapping model based on H_2 saturations after primary drainage (S_{gi}) and imbibition (S_{gr}), combined with the results from the same micromodel at 1, 5 and 30 bar [26,52] and the literature H_2 data at core scale denoted by colored crosses [24,25,27–30]. Most of the measurements followed the Land trapping model with the trapping coefficients C = 1 and C = 5. The upper limit data points were comparable to CO_2 with the trapping coefficients between 0.2 and 2.1 in sandstones [56,57].

channels along the micromodel length (Fig. 1) resulted in crossflow, facilitating more random injection patterns in multiple directions. In the case of C_6H_{14} injections, the open channels were built in the opposite direction, that is along the micromodel widths, creating one-directional injection pattern.

Contrary to the initial H_2 saturation, the residual H_2 saturation was more reproducible because the H_2O injection was eased in a strongly hydrophilic system, with well-established injection patterns through the wetting H_2O films coating the grain surfaces. Note that natural reservoirs contain organic-rich material, making their rock surfaces more hydrophobic than our micromodel [13,16]. Greater reproducibility of the residual H_2 saturation throughout the cycles is beneficial from the storage perspective, permitting a better control of the H_2 loss due to residual trapping. The distribution of the residual H_2, however, visually changed over the cycles as mentioned in section 3.1 (Fig. 3). Such hysteretic behavior due to residual trapping can affect the imbibition relative permeability, and hysteresis in H_2–H_2O relative permeability has already been demonstrated at core scale [24,25].

The microscopic recovery factors, defined as $(S_{gi} - S_{gr})/S_{gi}$, fluctuated between the cycles, in alignment with the initial H_2 saturation (Fig. 7). The recovery factors ranged between 2% and 77% with an average of ~40%, comparable with the recovery factors from reservoir simulations of H_2 storage in the H_2O zone of a depleted hydrocarbon field: 49% [54] and aquifer storage: 36–59% [11,55]. Note that recovery factors from reservoir simulations are macroscopic and valid for the entire reservoir, contrary to microfluidics which deal with the microscopic phenomena. The highest H_2 saturation is expected in the near-well area, with gradually decreasing H_2 saturation when approaching the H_2–H_2O transition zone in the far-well area [11,12,49]. During cyclic injections, the H_2–H_2O transition boundary is constantly moving, resulting in increasing H_2O saturation during H_2 withdrawal with associated residual H_2 trapping. Hence, the reported microscopic recovery factors are mostly relevant for the H_2–H_2O transition zone.

Trapping model

We combine H_2 saturations after primary drainage and imbibition together with the results from the same micromodel at 1–30 bar and available H_2 data at core scale (Fig. 9), to construct H_2 trapping relationship based on an empirical Land model [34]. This model was derived from the measurements of the initial and residual gas saturations in sandstone core samples, defined as follows: $S_{gr} = S_{gi}/(1 + C \cdot S_{gi})$, where C is the trapping coefficient. The data points were greatly scattered and mostly fell within the trapping coefficient (C) range between 1 and 5. The upper boundary points matched the CO_2 trapping models in different sandstones, with the trapping coefficient range of 0.2–2.1 [56,57]. In contrast, the lower boundary points were outside the reported CO_2 data, indicating that less H_2 trapping may be expected compared to CO_2. The lower boundary points disagreed with the contact angle measurements which reported less H_2 wetting (more hydrophilic) compared to CO_2 [13,16], that in turn implies more H_2 trapping [23]. Greater scatter and disagreement of lower boundary H_2 data points with CO_2 data could be due to the differences in the porous materials and methodologies. The CO_2 measurements were obtained from conventional core flooding with the core length of 6–12 cm, whereas microfluidics and shorter core plugs of 1.5–5.7 cm were used for most H_2 saturation measurements.

The initial and residual H_2 saturations from cyclic injections (Fig. 10) showed no significant increase in residual trapping over the cycles for similar initial H_2 saturations, consistent with the Land model and corroborated by H_2 [30] and some CO_2 cyclic injection studies [58,59]. In contrast, some CO_2 measurements deviated from the Land model, with a sharp increase in residual saturations over the injection cycles [31–33]. The exact mechanism for this deviation is still poorly understood but could be attributed to pore throat blockage due to fines migration, CO_2 adhesion to the grain surfaces, and/or wettability alteration to a "patchy" mixed-
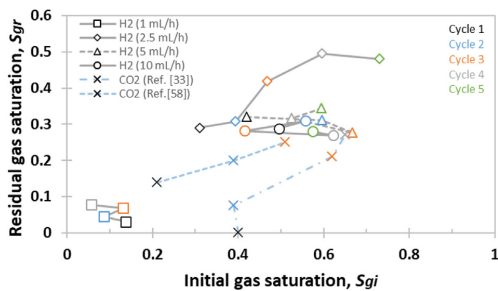
Fig. 10 − Initial (S_{gi}) and residual (S_{gr}) H_2 saturations during cyclic injections at the injection rates of 1, 2.5, 5 and 10 mL/h. The S_{gr} were nearly stable over the injection cycles for similar S_{gi}, consistent with the Land trapping model. Our results were compared with CO_2 studies (denoted by crosses), where there is currently a contradiction, with some studies following the Land model [58] and other studies deviating from it [33].

wet with discontinuous CO_2-wet areas [33,60]. Even though our results and one core scale H_2 study [30] did not indicate a significant increase in residual trapping, lack of H_2 studies and the disagreement in the CO_2 literature emphasizes the importance for further investigations of H_2 cyclic injections. A potential increase in residual H_2 trapping over the injection cycles is undesired as it will reduce H_2 storage efficiency.

Trapping models based on the 2D microfluidic experiments have a limited applicability for 3D reservoirs due to the small volume and the absence of gravity and heterogeneity. The same applies for the storage capacities and recovery factors quantified in sections 3.2 and 3.3. The 2D micromodels are suitable for qualitative description of the pore scale flow mechanisms, which can support core scale measurements. Extrapolation of the quantitative results to natural reservoirs requires caution and should be preferably done by pore scale modelling. However, our results followed classic CNC trends (Fig. 6) and the H_2 saturations were within the literature range at core scale (Fig. 9). Therefore, it is reasonable to claim that the quantified H_2 storage capacities and trapping model from microfluidics can temporarily substitute for missing measurements until a comprehensive core scale dataset is available.

Conclusions

We report a series of cyclic H_2− H_2O injections in a micromodel mimicking sandstone pore patterns and relevant for shallow H_2 storage in aquifers and depleted gas fields with an underlying water zone. We found that H_2 saturation after primary drainage increased with increasing capillary number, with maximum storage capacities up to ~60% of the pore scape. When combined with previous results from the same micromodel, the initial H_2 saturation was independent of pressure in the range of 1−40 bar. The distribution of initial and residual H_2 in the pore space were hysteretic over the injection cycles, with fluctuating initial but similar residual H_2

saturations. The residually trapped H_2 showed good reconnection ability, which was favored in proximity to the large pore clusters with wide pore throats. The H_2 trapping followed the Land model, with trapping coefficient between 1 and 5 where the upper limit values matched the CO_2 trapping models in sandstones. The microscopic H_2 recovery factors varied due to the fluctuating initial H_2 saturation and on average were equal to ~40%, relevant for the H_2−H_2O transition zone in the far-well area. Higher reconnection ability and reproducibility of residual H_2 saturation are beneficial for underground H_2 storage but this positive impact may be suppressed by its hysteretic distribution over the injection cycles. Future work should be focused on core scale cyclic injections and on pore scale modelling for upscaling to natural reservoirs.

Declaration of Competing Interest

The authors declare that they have no known competing financial interests or personal relationships that could have appeared to influence the work reported in this paper.

Acknowledgements

REFERENCES

[1] Navaid HB, Emadi H, Watson M. A comprehensive literature review on the challenges associated with underground hydrogen storage. Int J Hydrogen Energy 2023;48(28):10603−35.
[2] Undertaking HJ. Hydrogen roadmap Europe: a sustainable pathway for the European energy transition. 2019.
[3] Cihlar J, Mavins D, van der Leun K. Picturing the value of underground gas storage to the European hydrogen system. Guidehouse; 2021.
[4] Carden PO, Paterson L. Physical, chemical and energy aspects of underground hydrogen storage. Int J Hydrogen Energy 1979;4(6):559−69.
[5] Muhammed NS, et al. A review on underground hydrogen storage: insight into geological sites, influencing factors and future outlook. Energy Rep 2022;8:461−99.
[6] Pérez A, et al. Patagonia wind - hydrogen project: underground storage and methanation. In: 21st world hydrogen energy conference. Spain: Zaragoza; 2016.
[7] RAG, RAG Austria AG - Underground Sun Storage. Final report public13; 2020.
[8] Panfilov M. Underground and pipeline hydrogen storage. In: Compendium of hydrogen energy. Woodhead Publishing; 2016.
[9] Smigan P, et al. Methanogenic bacteria as a key factor involved in changes of town gas stored in an underground reservoir. FEMS Microbiol Ecol 1990;73(3):221−4.

[10] Dopffel N, Jansen S, Gerritse J. Microbial side effects of underground hydrogen storage - knowledge gaps, risks and opportunities for successful implementation. Int J Hydrogen Energy 2021;46(12):8594−606.

[11] Lubon K, Tarkowski R. Numerical simulation of hydrogen injection and withdrawal to and from a deep aquifer in NW Poland. Int J Hydrogen Energy 2020;45(3):2068−83.

[12] Sainz-Garcia A, et al. Assessment of feasible strategies for seasonal underground hydrogen storage in a saline aquifer. Int J Hydrogen Energy 2017;42(26):16657−66.

[13] Ali M, et al. Hydrogen wettability of quartz substrates exposed to organic acids; Implications for hydrogen geo-storage in sandstone reservoirs. J Petrol Sci Eng 2021;207.

[14] Hashemi L, et al. Contact angle measurement for hydrogen/brine/sandstone system using captive-bubble method relevant for underground hydrogen storage. Adv Water Resour 2021;154.

[15] Higgs S, et al. In-situ hydrogen wettability characterisation for underground hydrogen storage. Int J Hydrogen Energy 2022;47(26):13062−75.

[16] Iglauer S, Ali M, Keshavarz A. Hydrogen wettability of sandstone reservoirs: implications for hydrogen geo-storage. Geophys Res Lett 2021;48(3).

[17] Hashemi L, et al. A comparative study for H2−CH4 mixture wettability in sandstone porous rocks relevant to underground hydrogen storage. Adv Water Resour 2022;163.

[18] van Rooijen W, et al. Microfluidics-based analysis of dynamic contact angles relevant for underground hydrogen storage. Adv Water Resour 2022;164.

[19] Al-Yaseri A, Jha NK. On hydrogen wettability of basaltic rock. J Petrol Sci Eng 2021;200.

[20] Pan B, Yin X, Iglauer S. Rock-fluid interfacial tension at subsurface conditions: implications for H2, CO2 and natural gas geo-storage. Int J Hydrogen Energy 2021;46(50):25578−85.

[21] Pan B, et al. Underground hydrogen storage: influencing parameters and future outlook. Adv Colloid Interface Sci 2021:294.

[22] Raza A, et al. A holistic overview of underground hydrogen storage: influencing factors, current understanding, and outlook. Fuel 2022;330.

[23] Iglauer S, Pentland CH, Busch A. CO2 wettability of seal and reservoir rocks and the implications for carbon geo-sequestration. Water Resour Res 2015;51(1):729−74.

[24] Boon M, Hajibeygi H. Experimental characterization of H-2/water multiphase flow in heterogeneous sandstone rock at the core scale relevant for underground hydrogen storage (UHS). Sci Rep 2022;12(1).

[25] Lysyy M, et al. Hydrogen relative permeability hysteresis in underground storage. Geophys Res Lett 2022;49(17).

[26] Lysyy M, Ersland G, Ferno M. Pore-scale dynamics for underground porous media hydrogen storage. Adv Water Resour 2022;163.

[27] Jha NK, et al. Pore scale investigation of hydrogen injection in sandstone via X-ray micro-tomography. Int J Hydrogen Energy 2021;46(70):34822−9.

[28] Jangda Z, et al. Pore-scale visualization of hydrogen storage in a sandstone at subsurface pressure and temperature conditions: trapping, dissolution and wettability. J Colloid Interface Sci 2023;629:316−25.

[29] Al-Yaseri A, et al. Initial and residual trapping of hydrogen and nitrogen in Fontainebleau sandstone using nuclear magnetic resonance core flooding. Int J Hydrogen Energy 2022;47(53):22482−94.

[30] Thaysen, Eike M, et al. Pore-scale imaging of hydrogen displacement and trapping in porous media. Int J Hydrogen Energy 2023;48(8):3091−106.

[31] Edlmann K, et al. Cyclic CO2 - H2O injection and residual trapping: implications for CO2 injection efficiency and storage security. Int J Greenh Gas Control 2019;80:1−9.

[32] Herring AL, Andersson L, Wildenschild D. Enhancing residual trapping of supercritical CO2 via cyclic injections. Geophys Res Lett 2016;43(18):9677−85.

[33] Herring AL, et al. Evolution of bentheimer sandstone wettability during cyclic scCO(2)-brine injections. Water Resour Res 2021;57(11).

[34] Land CS. Calculation of imbibition relative permeability for two and three-phase flow from rock properties. Soc Petrol Eng J 1968;8(2):149−&.

[35] Benali B, et al. Pore-scale bubble population dynamics of CO2-foam at reservoir pressure. Int J Greenh Gas Control 2022;114.

[36] Buchgraber M, et al. Creation of a dual-porosity micromodel for pore-level visualization of multiphase flow. J Petrol Sci Eng 2012;86−87:27−38.

[37] Linstrom PJ, Mallard WG. The NIST Chemistry WebBook: a chemical data resource on the internet. J Chem Eng Data 2001;46(5):1059−63.

[38] Chow YTF, Maitland GC, Trusler JPM. Interfacial tensions of (H2O + H2) and (H2O + CO2 + H2) systems at temperatures of (298−448) K and pressures up to 45 MPa. Fluid Phase Equil 2018;475:37−44.

[39] Chomsurin C, Werth CJ. Analysis of pore-scale nonaqueous phase liquid dissolution in etched silicon pore networks. Water Resour Res 2003;39(9).

[40] Zhao X, Jin H. Investigation of hydrogen diffusion in supercritical water: a molecular dynamics simulation study. Int J Heat Mass Tran 2019;133:718−28.

[41] Zhang CY, et al. Influence of viscous and capillary forces on immiscible fluid displacement: pore-scale experimental study in a water-wet micromodel demonstrating viscous and capillary fingering. Energy Fuels 2011;25(8):3493−505.

[42] Roof JG. Snap-off of oil droplets in water-wet pores. Soc Petrol Eng J 1970;10(1):85. &.

[43] Lenormand R, Zarcone C, Sarr A. Mechanisms of the displacement of one fluid by another in a network of capillary ducts. J Fluid Mech 1983;135(Oct):337−53.

[44] Guo H, Song KP, Hilfer R. A brief review of capillary number and its use in capillary desaturation curves. Transport Porous Media 2022;144(1):3−31.

[45] Chang C, et al. Scaling the impacts of pore-scale characteristics on unstable supercritical CO2-water drainage using a complete capillary number. Int J Greenh Gas Control 2019;86:11−21.

[46] An SY, et al. Transition from viscous fingering to capillary fingering: application of GPU-based fully implicit dynamic pore network modeling. Water Resour Res 2020;56(12).

[47] Chang C, et al. Impacts of mixed-wettability on brine drainage and supercritical CO2 storage efficiency in a 2.5-D heterogeneous micromodel. Water Resour Res 2020;56(7).

[48] de Castro AR, et al. Experimental study on nonmonotonicity of Capillary Desaturation Curves in a 2-D pore network. Water Resour Res 2015;51(10):8517−28.

[49] Bai T, Tahmasebi P. Coupled hydro-mechanical analysis of seasonal underground hydrogen storage in a saline aquifer. J Energy Storage 2022;50.

[50] Thomas LK, Katz DL, Tek MR. Threshold pressure phenomena in porous media. Soc Petrol Eng J 1968;8(2):174. &.

[51] Niu B, Al-Menhali A, Krevor SC. The impact of reservoir conditions on the residual trapping of carbon dioxide in Berea sandstone. Water Resour Res 2015;51(4):2009−29.

[52] van der Hart PHK. A pore-scale study of underground hydrogen storage in porous media. The University of Bergen; 2021.

[53] Ahn H, et al. Migration and residual trapping of immiscible fluids during cyclic injection: pore-scale observation and quantitative analysis. Geofluids; 2020. p. 2020.

[54] Lysyy M, Ferno M, Ersland G. Seasonal hydrogen storage in a depleted oil and gas field. Int J Hydrogen Energy 2021;46(49):25160–74.

[55] Mahdi DS, et al. Hydrogen underground storage efficiency in a heterogeneous sandstone reservoir. Advances in Geo-Energy Research 2021;5(4):437–43.

[56] Krevor SCM, et al. Relative permeability and trapping of CO2 and water in sandstone rocks at reservoir conditions, vol.48. Water Resources Research; 2012.

[57] Ni H, et al. Predicting CO2 residual trapping ability based on experimental petrophysical properties for different sandstone types. Int J Greenh Gas Control 2019;86:158–76.

[58] Ruprecht C, et al. Hysteretic trapping and relative permeability of CO2 in sandstone at reservoir conditions. Int J Greenh Gas Control 2014;27:15–27.

[59] Saeedi A, et al. Multiphase flow behaviour during CO2 geo-sequestration: emphasis on the effect of cyclic CO2-brine flooding. J Petrol Sci Eng 2011;79(3–4):65–85.

[60] Ge JC, Zhang XZ, Le-Hussain F. Fines migration and mineral reactions as a mechanism for CO2 residual trapping during CO2 sequestration. Energy 2022:239.

Paper 4

Geophysical Research Letters®

Key Points:
- Steady state measurements of hydrogen-water relative permeability
- Numerical history matching needed for extrapolation
- Strong hysteresis observed between drainage and imbibition

Correspondence to:
M. Lysyy,
Maksim.Lysyy@uib.no

Hydrogen Relative Permeability Hysteresis in Underground Storage

Maksim Lysyy[1] , **Tore Føyen[2]** , **Else Birkeland Johannesen[1]**, **Martin Fernø[1]**, and **Geir Ersland[1]**

[1]Department of Physics and Technology, University of Bergen, Bergen, Norway, [2]SINTEF Industry, Trondheim, Norway

Abstract Implementation of the hydrogen economy for emission reduction will require storage facilities, and underground hydrogen storage (UHS) in porous media offers a readily available large-scale option. Lack of studies on multiphase hydrogen flow in porous media is one of the several barriers for accurate predictions of UHS. This paper reports, for the first time, measurements of hysteresis in hydrogen-water relative permeability in a sandstone core under shallow storage conditions. We use the steady state technique to measure primary drainage, imbibition and secondary drainage relative permeabilities, and extend laboratory measurements with numerical history matching and capillary pressure measurements to cover the whole mobile saturation range. We observe that gas and water relative permeabilities show strong hysteresis, and nitrogen as substitute for hydrogen in laboratory assessments should be used with care. Our results serve as calibrated input to field scale numerical modeling of hydrogen injection and withdrawal processes during porous media UHS.

Plain Language Summary Hydrogen storage facilities will need a ramp-up when the hydrogen share in the future energy mix increase. Large-scale hydrogen storage can be implemented in empty hydrocarbon fields or ground water reservoirs. Hydrogen storage in such media involve complex interactions with native rocks and fluids, and injection and withdrawal are typically described by flow functions. Relative permeability is one of the key flow functions that describe how easily hydrogen can flow through porous media in the presence of other fluids. In underground storage, hydrogen is cyclically injected and withdrawn multiple times, and its relative permeability may differ between these two processes, described as hysteresis. In this paper, we investigate hydrogen relative permeability in the laboratory and match with results from numerical simulations. We find that hydrogen relative permeability is different for injection and withdrawal and is also different from that of nitrogen. Our results are directly applicable in computer simulators that predict hydrogen storage efficiency.

1. Introduction

Hydrogen (H_2) will play a key role in low-carbon energy transitions, and it is vital to implement hydrogen storage technologies to enable its safe and economic use at industrial scale. Underground hydrogen storage (UHS) in porous media such as aquifers, depleted hydrocarbon fields, and coal seams has been proposed as widely available long-term and large-scale storage options (Iglauer et al., 2021; Muhammed et al., 2022). As for underground natural gas storage (UGS), UHS involves cyclic gas injection at peak supply (known as cushion gas) and withdrawal at peak demand (working gas). Despite the increasing attention to the topic worldwide, the fundamentals of multiphase hydrogen flow in porous media are still not well described. In particular, relative permeability hysteresis has not been addressed, although its impact has been previously assessed for UGS and CO_2 storage (Colonna et al., 1972; Juanes et al., 2006). The cyclic nature of the UHS suggests that distinct relative permeability functions must be implemented for hydrogen injection (drainage) and withdrawal (imbibition).

Relative permeability is a crucial input parameter for the UHS numerical modeling at field scale (Kanaani et al., 2022; Lysyy et al., 2021; Wang et al., 2022). Laboratory gas-water relative permeability curves often have low endpoint gas saturations (<65%) and relative permeabilities (<40%) due to the rock heterogeneity, capillary end effects, gravity segregation, and/or maximum experimental capillary pressure (Krevor et al., 2012; Muller, 2011). Numerical and/or analytical methods are therefore required to validate and extrapolate relative permeabilities in a wider saturation range.

Hydrogen-water relative permeability measurements are scarce in the open literature. Steady state drainage experiments resulted in low endpoint gas saturation (~60%) and relative permeability (~4%) (Yekta et al., 2018). The authors used experimental capillary pressure to analytically expand the relative permeability curves to higher

hydrogen saturations. However, their data set lacked numerical history matching. Unsteady state drainage measurements examined the effect of pressure, brine salinity, and rock type on hydrogen relative permeabilities (Rezaei et al., 2022). Their measurements were history matched but without extrapolation to higher gas saturations. None of the studies investigated relative permeability hysteresis. When used as input for field scale modeling studies, lack of numerical history matching and hysteresis may significantly impact the accuracy of modeling results.

We investigate hysteretic behavior in steady state hydrogen-water relative permeability during drainage, imbibition, and secondary drainage injections, aided by primary drainage capillary pressure measurements. The experimental measurements are numerically validated and history matched to derive relative permeabilities over the entire range of mobile gas saturations. Hydrogen primary drainage relative permeability is compared with nitrogen. Our results provide vital input with a direct impact on the USH modeling at field scale.

2. Materials and Methods

Steady state gas and water relative permeability (K_r) and porous plate capillary pressure (P_c) measurements were performed chronologically:

1. Primary drainage K_r with nitrogen (N_2),
2. Primary drainage K_r with hydrogen (H_2),
3. Primary drainage P_c and irreducible water saturation (S_{wirr}) establishment with N_2,
4. Imbibition K_r with H_2,
5. Secondary drainage K_r with H_2.

We used the same core sample for all experiments.

2.1. Materials

A Berea sandstone core sample was supplied by Kocurek Industries and analyzed for its key properties (Table S1 in Supporting Information S1). The porosity was measured by mass balance (brine) and $NaNO_3$ flooding, whereas the brine absolute permeability was determined based on the Darcy's law with four injection rates in the range of 0.15–0.60 ml/min. Brine was doped with cesium chloride CsCl (2.5 wt% NaCl/2.5 wt% CsCl) to enhance the brine *x*-ray adsorption, thereby improving the signal-to-noise ratio during in situ saturation monitoring.

A hydrophilic ceramic porous plate with 15 bar (gas-water) threshold pressure was provided by Soil Moisture and its properties were measured (Table S1 in Supporting Information S1). The porosity was determined by mass balance, whereas the absolute permeability was calculated based on induced water flux of 0.002 ml/min resulting from 1 bar differential pressure reported by the manufacturer.

2.2. Experimental Procedures

2.2.1. Relative Permeability Measurements

The K_r was measured by steady state method using eight injection steps with the total flow rate of 1 ml/min followed by a bump flood at 4 ml/min. The corresponding capillary numbers (N_{Ca}) were in the order of 10^{-8} (drainage) and 10^{-6} (imbibition), based on equations Equations S1, S2, and Table S4 in Supporting Information S1. Each injection step was terminated after differential pressure stabilization and injection of at least 15 pore volumes of total flow rate (Table S5 in Supporting Information S1). The experiments were run at 30 bar and 30°C, representing shallow storage conditions.

The experimental setup is a closed loop system where the fluids are fully recirculated (Figure S1 in Supporting Information S1). The core sample was wrapped in a 0.025 mm thick nickel foil to reduce hydrogen diffusion through the rubber sleeve in a vertically oriented biaxial core holder. Two Quizix pumps injected the gas and aqueous (brine) phases from the core holder top (drainage) or bottom (imbibition). A compensation pump maintained constant outlet pressure in the acoustic two-phase separator, where the effluent fluids were produced, measured, and circulated back to the injection pumps. The water saturation (S_w) profile was measured in situ using *x*-ray monitoring and calculated from the Beer-Lambert law (Equation S3 in Supporting Information S1), with the uncertainty ± 0.02 S_w units.

The closed loop setup enabled us to continuously monitor and detect potential hydrogen leaks. The volume changes of the compensation pump would indicate any impactful leakages in the system. The nickel foil proved to be a safe barrier between the core plug and the rubber sleeve. Hydrogen diffusion through the sleeve would easily be detected by the reduction in the confinement pressure that was continuously monitored. Small leakages are often inevitable when working with gases, but we accounted for any gas losses when interpreting the data from the two-phase separator. Overall, hydrogen can be safely used with conventional core flooding setup.

After primary drainage K_r experiments, the core sample was reestablished to $S_w = 1$, followed by P_c measurements toward S_{wirr}—an initial state prior to the imbibition K_r measurements. The secondary drainage K_r measurements started at the same core state established after the imbibition K_r measurements.

2.2.2. Capillary Pressure Measurements

Primary drainage P_c was measured with N_2 by porous plate method in a vertically oriented core holder and the core sample coupled in series with the porous plate. N_2 was injected from the top to the 100% brine-saturated core sample ($S_w = 1$), using four constant P_c steps in the range of 1.45–14 bar. The produced brine volume was recorded from a measuring cylinder, allowing to calculate the equilibrium S_w (i.e., termination of brine production) after each P_c step. The S_w after the final P_c step corresponded to S_{wirr} state, preparing the core sample for the imbibition K_r measurements.

2.3. Numerical History Matching

The commercial Sendra software was used to numerically verify the experimental performance and derive K_r and P_c (Prores, 2016). Sendra is a two-phase, one dimensional, black oil simulation tool for analysis of core scale experiments based on the Darcy's law and the continuity equation. The simulation model has 100 grid blocks in x-direction and hydrogen and water are immiscible. Hydrogen compressibility was neglected in the simulations because the compressibility factor is close to unity (<1.02) at experimental p-T conditions (Zhou & Zhou, 2001). Hydrogen thermodynamic properties (density and viscosity) were extracted from an open-source database (Linstrom & Mallard, 2001), which in turn used the equation of state and viscosity model derived specifically for hydrogen (Leachman et al., 2009; Muzny et al., 2013).

The initial solution was obtained through an automatic history matching of experimental measurements: Production data from two-phase separator, differential pressure, and S_w profiles from x-ray monitoring. The match quality was improved through a manual tuning of the LET model parameters for K_r and P_c (Lomeland et al., 2005, 2008):

Gas relative permeability:

$$K_{rg} = K_{rg}^* \cdot \frac{(1 - S_{wn})^{L_g}}{(1 - S_{wn})^{L_g} + E_g \cdot (S_{wn})^{T_g}} \tag{1}$$

Water relative permeability:

$$K_{rw} = K_{rw}^* \cdot \frac{(S_{wn})^{L_w}}{(S_{wn})^{L_w} + E_w \cdot (1 - S_{wn})^{T_w}} \tag{2}$$

where K_{rg}^* and K_{rw}^* are end points K_r at irreducible water saturation (S_{wirr}) and residual gas saturation (S_{gr}), respectively. L_g, E_g, T_g, L_w, E_w, and T_w are empirical fitting parameters. The normalized water saturation S_{wn} is defined as $S_{wn} = (S_w - S_{wirr})/(1 - S_{wirr} - S_{gr})$.

Primary drainage capillary pressure—simplified version for nonzero capillary threshold pressure:

$$P_c^{pd} = \frac{(P_{c,max} - P_{c,th}) \cdot (1 - S_{wx})^{L_s}}{(1 - S_{wx})^{L_s} + E_s \cdot (S_{wx})^{T_s}} + P_{c,th} \tag{3}$$

where $P_{c,max}$ and $P_{c,th}$ are maximum and threshold P_c, respectively, whereas L_s, E_s, and T_s are empirical fitting parameters. The normalized water saturation S_{wx} is defined as $S_{wx} = (S_w - S_{wirr})/(1 - S_{wirr})$.
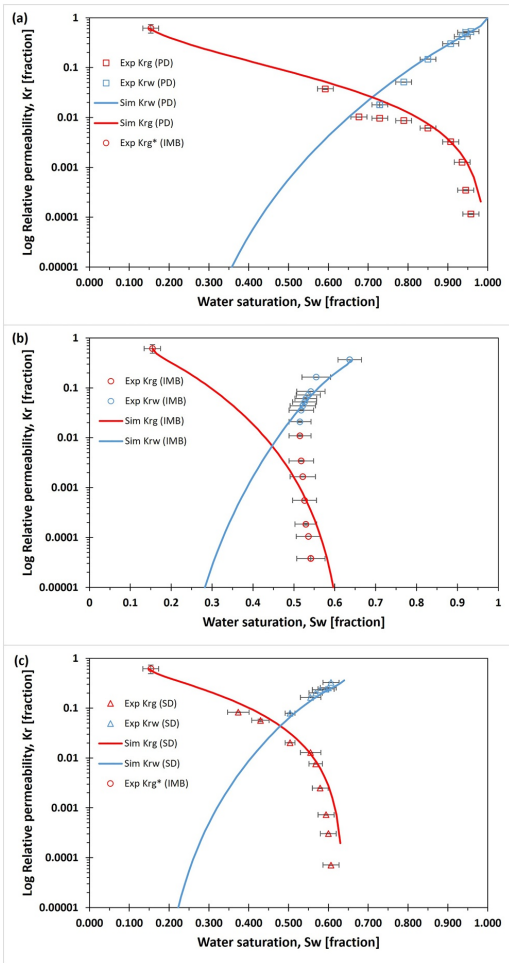
Figure 1. Experimental (Exp) and simulated (Sim) hydrogen-water relative permeabilities (K_r) on semilogarithmic scale for (a) primary drainage (PD), (b) imbibition (IMB), and (c) secondary drainage (SD). PD and SD K_r yield low endpoint values, and the endpoint $K_{rg}*$ at irreducible water saturation from IMB experiment is used to extrapolate K_r to low S_w region. The S_w values are calculated from x-ray scan for PD, whereas for IMB and SD the S_w are calculated as the average between x-ray scan and the two-phase separator production data. The K_r error bars represent the differential pressure uncertainty of ~2%, whereas the S_w error bars represent either the x-ray scan uncertainty of 0.02 S_w units (PD) or the uncertainty of the average S_w calculated from x-ray scan and two-phase separator (IMB and SD). Tabulated values are presented in Tables S6–S8, S10, and S11 in Supporting Information S1, respectively. A comparison between K_r is shown in Figure 2.

Imbibition and secondary drainage capillary pressure equations are presented in Equations S4 and S6 in Supporting Information S1.

3. Results and Discussion

3.1. Hydrogen-Water Relative Permeability

The hydrogen-water relative permeability was measured for primary drainage, imbibition, and secondary drainage injection processes (Figure 1). The endpoints were $K_{rg} = 0.04$ at $S_w = 0.59$ and $K_{rg} = 0.08$ at $S_w = 0.37$ after primary and secondary drainage, respectively. The low endpoints after primary and secondary drainage agreed with published K_r measurements in CO_2- and H_2-H_2O systems (Akbarabadi & Piri, 2013; Krevor et al., 2012; Yekta et al., 2018). The imbibition endpoints were $K_{rw} = 0.36$ at $S_w = 0.64$ (or $S_{gr} = 0.36$), within the expected range for Berea sandstones according to the Land trapping model with the trapping coefficients (C) between 1 and 1.407 and corresponding S_{gr} range of 0.35–0.42 (Krevor et al., 2012; Land, 1968; Ni et al., 2019).

The relative permeabilities curves were found directly from the stabilized differential pressure and saturation. Capillary end effects were evident (Figures S2c and S4c in Supporting Information S1), and the experimental measurements (Figures S2–S4 in Supporting Information S1) were history matched based on the LET model for relative permeability and capillary pressure (Tables 1 and 2). The primary and secondary drainage K_r were extrapolated for expected reservoir flows (lower S_w region), based on the $S_{wirr} = 0.15$ and history matched P_c from porous plate experiment and the endpoint $K_{rg}* = 0.61$ from imbibition experiment. A minor deviation between measured (points) and simulated (solid lines) K_r curves (Figure 1) arise from the underlying assumptions on P_c gradients: Measured K_r assumed homogenous rock properties and zero capillary pressure, whereas the simulation incorporates a more realistic nonzero capillary pressure. The quality of the history matching was lower in the imbibition experiment (Figure 1b). Most of the hydrogen was produced from the core after the first injection step, with very little production in subsequent injection steps until bump flood (Figure S3b in Supporting Information S1). This behavior resembled a typical unsteady state experiment, which affected the simulator performance in a steady state mode. In general, the simulated K_r will better represent reservoir flow and should therefore be used as input for field scale simulations.

3.2. Hysteresis in Hydrogen-Water Relative Permeability

The relative permeability curves K_{rg} and K_{rw} showed strong hysteresis and hydrophilic preference, with the following primary drainage cross point values: $K_{rg} = K_{rw} = 0.025$ at $S_w = 0.71$ (Figure 2). Berea sandstones are originally strongly hydrophilic (Iglauer et al., 2015), but hydrogen systems become less hydrophilic with increasing pressure and organic acid concentration and decreasing temperature (Ali et al., 2021). The K_{rg} was higher for primary drainage than imbibition, whereas the secondary drainage K_{rg} was positioned between these two K_{rg}. Hysteretic K_{rg} behavior was consistent with previous gas-water K_r measurements and arise from residual gas trapping during imbibition (Akbarabadi & Piri, 2013; Ge et al., 2022; Oak et al., 1990; Peng, 2020; Ruprecht et al., 2014). The K_{rw} was lower for primary drainage than imbibition, in agreement with most studies and explained by contact angle hysteresis (Akbarabadi & Piri, 2013; Ge et al., 2022;

Table 1
Relative Permeability LET Model Parameters

	S_{wirr}	S_{gr}	K_{rg}^*	K_{rw}^*	L_w	E_w	T_w	L_g	E_g	T_g
Primary drainage H_2	0.15	0	0.61	1	7.5	2.95	0.52	1.6	6.0	0.9
Primary drainage N_2	0.15	0	0.73	1	6.5	3.9	0.8	2.2	1.5	0.7
Imbibition H_2	0.15	0.36	0.61	0.36	7.5	2.0	0.6	4.2	2.5	0.6
Secondary drainage H_2	0.15	0.36	0.61	0.36	5.2	2.0	0.7	1.88	2.1	0.7

Peng, 2020). Nonhysteretic K_{rw} behavior has also been reported in literature and attributed to reproducibility of drainage and imbibition injections in strongly hydrophilic systems (Oak et al., 1990; Ruprecht et al., 2014). Discrepancies in reported K_{rw} hysteresis can have a significant impact on the UHS modeling at field scale and must therefore be targeted in future studies.

3.3. Effect of Gas Type on Primary Drainage Relative Permeability

The primary drainage K_r gas-water measurements were repeated with nitrogen (N_2) and resulted in endpoint $K_{rg} = 0.06$ at $S_w = 0.59$, similar to H_2-H_2O system (Figure 3). The K_{rg} and K_{rw} curves shifted upward in the N_2-H_2O system, reflecting the impact of increased gas-water viscosity ratio (Jeong et al., 2017): N_2 is two times more viscous than H_2 at experimental conditions (Table S4 in Supporting Information S1). Note that difference in K_{rg} and K_{rw} is asymmetric, with a significantly greater increase in K_{rg} (~100% higher than in H_2 experiment) compared to K_{rw} (~50% higher than in H_2 experiment). We attribute this phenomenon to the combined effect of increased viscosity ratio and uncertainties in N_2 experiment.

Uncertainties in K_r (N_2) curves were mainly related to (a) nonconstant S_w distribution prior to first injection step (Figure S5c in Supporting Information S1), (b) too low water injection rate (1/10 of planed rate) during the second injection step (Table S5 in Supporting Information S1), and (c) missing measurement of endpoint K_{rg}^* (N_2). The endpoint K_{rg}^* (N_2) was set to 0.73 equal to the upper uncertainty limit of K_{rg}^* (H_2) because a higher K_{rg} was necessary to history match the N_2-experimental data. Note that history matching can yield several nonunique solutions, depending on the input parameters and matching strategy. Hence, the observed increased K_{rg} for the N_2-H_2O system reflects the uncertainty span of gas-water K_r in a Berea sandstone and may not represent an actual difference between K_r curves using N_2 and H_2. Although the use of analog fluids has previously been justified for Berea sandstones (Krevor et al., 2012), caution should be taken when using N_2 as a substitute for H_2 experimental measurements.

3.4. Field Scale Implications

Low experimental endpoint S_g^{max} and K_{rg} demonstrated the importance of numerical history matching. Strong hysteresis was observed both for K_{rg} and K_{rw}, and a full cycle of drainage and imbibition relative permeabilities must be implemented in future modeling studies for more accurate prediction of H_2 injection and withdrawal in the UHS.

Table 2
Capillary Pressure LET Model Parameters

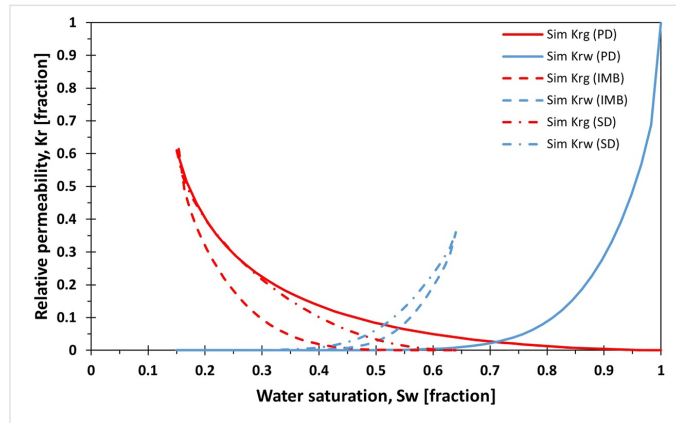|	$P_{c,max}$ (kPa)	$P_{c,min}$ (kPa)	$P_{c,th}$ (kPa)	S_{wsi}	L_s	E_s	T_s	L_f	E_f	T_f
Primary drainage H_2	1,400		5.0		1	130.0	1	1	0.002	1
Primary drainage N_2	1,400		12.35		1	129.6	1	1	0.007	1
Imbibition H_2	1,400	−1,400	−0.1	0.45	1		1	1	120.0	1
Secondary drainage H_2	1,400	−0.001	−0.05	0.19	1		1	1	156.3	1
Porous plate N_2	1,400		1		1	450.0	1	1	3.5	1

Figure 2. Hydrogen-water relative permeabilities show strong hysteresis both for hydrogen (K_{rg}) and water (K_{rw}).

Our K_r measurements are directly applicable for shallow sandstone aquifers with permeability in the order of ~100 mD but can be used for deeper aquifers too. It was previously shown that K_r measurements for H_2 were independent of pressure-temperature conditions (Yekta et al., 2018). If omitting hysteresis for the sake of computational efficiency, imbibition K_r is most suitable for the UHS in depleted gas fields with an underlying aquifer. Drainage K_r models would better represent H_2 storage in aquifers.

Differences between primary drainage K_r for H_2 and N_2 has major implication over the choice of cushion gas. Higher K_{rw} for N_2-H_2O system will result in a more efficient water removal during N_2 injection relative to H_2, making N_2 a suitable cushion gas. Our conclusion correlates with contact angle measurements that indicate stronger N_2 wetting and, hence, better injectivity relative to H_2 (Al-Yaseri & Jha, 2021). During gas withdrawal, on the other hand, higher K_{rg} for N_2 will result in a more rapid N_2 flow relative to H_2, leading to an earlier N_2 breakthrough in the producing well. From the economic perspective, earlier N_2 breakthrough is undesired due to reduced H_2 purity in the withdrawn gas mixture. Note that the actual K_{rg} difference between H_2 and N_2 may be less than observed in our work due to methodological uncertainties. Both H_2 and N_2 K_r can be used in the UHS simulation studies as a part of sensitivity analysis.

4. Conclusions

We measured steady state hydrogen-water relative permeabilities in a Berea sandstone under shallow reservoir storage conditions. Three different relative permeability measurements were performed: Primary drainage, imbibition, and secondary drainage and were supported with porous plate capillary pressure measurements. We observed low endpoints for drainage curves, with hydrogen relative permeabilities and saturations less than 0.08 and 0.63, respectively. Numerical history matching was performed to extrapolate relative permeabilities to lower water saturations. Relative permeability curves showed strong hysteresis, both for hydrogen and water. Primary drainage relative permeability measurements were repeated with nitrogen, and relative permeabilities were higher than that of hydrogen due to the combined effect of increased viscosity ratio and methodological uncertainties. Our results have a direct and immediate implication for the impact of hysteresis on field scale numerical modeling in underground hydrogen storage.
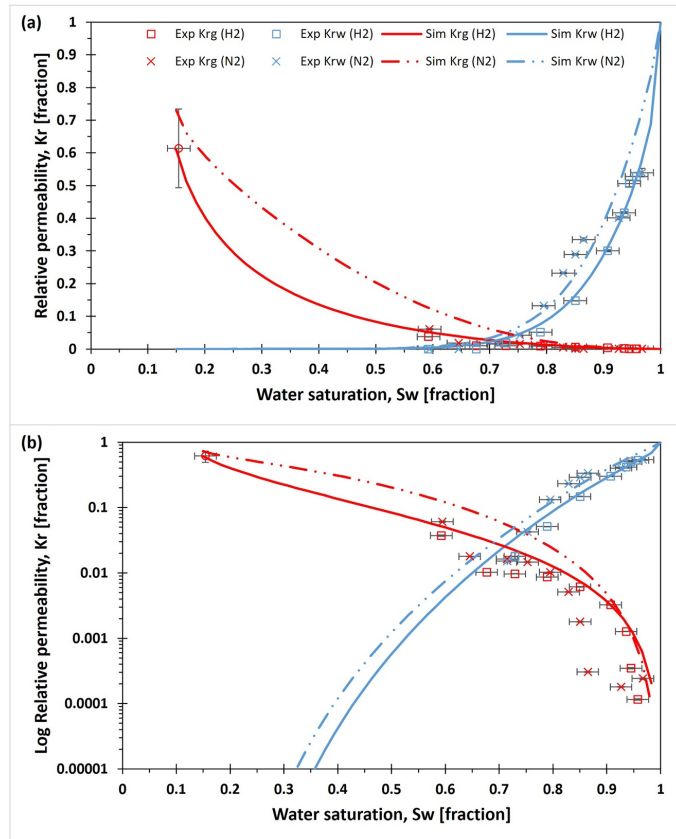
Figure 3. Hydrogen versus nitrogen primary drainage relative permeabilities, plotted in (a) linear and (b) semilogarithmic scales. Endpoint K_{rg} and S_w are similar for H_2 and N_2 measurements. K_{rg} and K_{rw} are higher for N_2, reflecting the combined effect of increased gas viscosity and methodological uncertainty. The endpoint K_{rg}^* at irreducible water saturation from H_2 imbibition experiment is used to extrapolate experimental K_{rg} (H_2) to low S_w region. The endpoint K_{rg}^* (N_2) at irreducible water saturation was not measured and is set to the upper uncertainty limit of the endpoint K_{rg}^* (H_2). Note that the K_{rg}^* from H_2 experiment represents a significant uncertainty (20%) due to small differential pressure (~4–8 mbar) caused by low hydrogen viscosity. Tabulated experimental and simulated values for N_2 experiment are presented in Tables S6 and S10 in Supporting Information S1, respectively.

Data Availability Statement

Data sets from relative permeability measurements are uploaded to http://dx.doi.org/10.17632/rfhf7wjydn.1, an open-source online data repository hosted by Mendeley Data. The core scale simulator Sendra developed by Prores AS is available at https://www.prores.no/solution/sendra.

References

Akbarabadi, M., & Piri, M. (2013). Relative permeability hysteresis and capillary trapping characteristics of supercritical CO_2/brine systems: An experimental study at reservoir conditions. *Advances in Water Resources*, *52*, 190–206. https://doi.org/10.1016/j.advwatres.2012.06.014

Ali, M., Yekeen, N., Pal, N., Keshavarz, A., Iglauer, S., & Hoteit, H. (2021). Influence of pressure, temperature and organic surface concentration on hydrogen wettability of caprock; implications for hydrogen geo-storage. *Energy Reports*, *7*, 5988–5996. https://doi.org/10.1016/j.egyr.2021.09.016

Al-Yaseri, A., & Jha, N. K. (2021). On hydrogen wettability of basaltic rock. *Journal of Petroleum Science and Engineering*, *200*, 108387. https://doi.org/10.1016/j.petrol.2021.108387

Colonna, J., Brissaud, F., & Millet, J. L. (1972). Evolution of capillarity and relative permeability hysteresis. *Society of Petroleum Engineers Journal*, *12*(1), 28–38. https://doi.org/10.2118/2941-Pa

Ge, J., Zhang, X., Liu, J., Almutairi, A., & Le-Hussain, F. (2022). Influence of capillary pressure boundary conditions and hysteresis on CO_2-water relative permeability. *Fuel*, *321*, 124132. https://doi.org/10.1016/j.fuel.2022.124132

Iglauer, S., Abid, H., Al-Yaseri, A., & Keshavarz, A. (2021). Hydrogen adsorption on sub-bituminous coal: Implications for hydrogen geo-storage. *Geophysical Research Letters*, *48*(10), e2021GL092976. https://doi.org/10.1029/2021GL092976

Iglauer, S., Pentland, C. H., & Busch, A. (2015). CO_2 wettability of seal and reservoir rocks and the implications for carbon geo-sequestration. *Water Resources Research*, *51*(1), 729–774. https://doi.org/10.1002/2014wr015553

Jeong, G. S., Lee, J., Ki, S., Huh, D. G., & Park, C. H. (2017). Effects of viscosity ratio, interfacial tension and flow rate on hysteric relative permeability of CO_2/brine systems. *Energy*, *133*, 62–69. https://doi.org/10.1016/j.energy.2017.05.138

Juanes, R., Spiteri, E. J., Orr, F. M., & Blunt, M. J. (2006). Impact of relative permeability hysteresis on geological CO_2 storage. *Water Resources Research*, *42*(12), W12418. https://doi.org/10.1029/2005wr004806

Kanaani, M., Sedaee, B., & Asadian-Pakfar, M. (2022). Role of cushion gas on underground hydrogen storage in depleted oil reservoirs. *Journal of Energy Storage*, *45*, 103783. https://doi.org/10.1016/j.est.2021.103783

Krevor, S. C. M., Pini, R., Zuo, L., & Benson, S. M. (2012). Relative permeability and trapping of CO_2 and water in sandstone rocks at reservoir conditions. *Water Resources Research*, *48*(2), W02532. https://doi.org/10.1029/2011wr010859

Land, C. S. (1968). Calculation of imbibition relative permeability for two and three-phase flow from rock properties. *Society of Petroleum Engineers Journal*, *8*(2), 149–156. https://doi.org/10.2118/1942-Pa

Leachman, J. W., Jacobsen, R. T., Penoncello, S. G., & Lemmon, E. W. (2009). Fundamental equations of state for parahydrogen, normal hydrogen, and orthohydrogen. *Journal of Physical and Chemical Reference Data*, *38*(3), 721–748. https://doi.org/10.1063/1.3160306

Linstrom, P. J., & Mallard, W. G. (2001). The NIST chemistry WebBook: A chemical data resource on the internet. *Journal of Chemical and Engineering Data*, *46*(5), 1059–1063. https://doi.org/10.1021/je000236i

Lomeland, F., Ebeltoft, E., & Thomas, W. H. (2005). A new versatile relative permeability correlation. In *The International Symposium of the Society of Core Analysts* (Vol. 112).

Lomeland, F., Ebeltoft, E., & Thomas, W. H. (2008). A new versatile capillary pressure correlation. In *The International Symposium of the Society of Core Analysts* (Vol. 29).

Lysyy, M., Ferno, M., & Ersland, G. (2021). Seasonal hydrogen storage in a depleted oil and gas field. *International Journal of Hydrogen Energy*, *46*(49), 25160–25174. https://doi.org/10.1016/j.ijhydene.2021.05.030

Muhammed, N. S., Haq, B., Al Shehri, D., Al-Ahmed, A., Rahman, M. M., & Zaman, E. (2022). A review on underground hydrogen storage: Insight into geological sites, influencing factors and future outlook. *Energy Reports*, *8*, 461–499. https://doi.org/10.1016/j.egyr.2021.12.002

Muller, N. (2011). Supercritical CO_2-brine relative permeability experiments in reservoir rocks-literature review and recommendations. *Transport in Porous Media*, *87*(2), 367–383. https://doi.org/10.1007/s11242-010-9689-2

Muzny, C. D., Huber, M. L., & Kazakov, A. F. (2013). Correlation for the viscosity of normal hydrogen obtained from symbolic regression. *Journal of Chemical and Engineering Data*, *58*(4), 969–979. https://doi.org/10.1021/je301273j

Ni, H., Boon, M., Garing, C., & Benson, S. M. (2019). Predicting CO_2 residual trapping ability based on experimental petrophysical properties for different sandstone types. *International Journal of Greenhouse Gas Control*, *86*, 158–176. https://doi.org/10.1016/j.ijggc.2019.04.024

Oak, M. J., Baker, L. E., & Thomas, D. C. (1990). Three-phase relative permeability of Berea sandstone. *Journal of Petroleum Technology*, *42*(8), 1054–1061. https://doi.org/10.2118/17370-PA

Peng, S. (2020). Gas-water relative permeability of unconventional reservoir rocks: Hysteresis and influence on production after shut-in. *Journal of Natural Gas Science and Engineering*, *82*, 103511. https://doi.org/10.1016/j.jngse.2020.103511

Prores. (2016). Sendra (Version 2016.2). Retrieved from https://www.prores.no/solution/sendra

Rezaei, A., Hassanpouryouzband, A., Molnar, I., Derikvand, Z., Haszeldine, R. S., & Edlmann, K. (2022). Relative permeability of hydrogen and aqueous brines in sandstones and carbonates at reservoir conditions. *Geophysical Research Letters*, *49*(12), e2022GL099433. https://doi.org/10.1029/2022GL099433

Ruprecht, C., Pini, R., Falta, R., Benson, S., & Murdoch, L. (2014). Hysteretic trapping and relative permeability of CO_2 in sandstone at reservoir conditions. *International Journal of Greenhouse Gas Control*, *27*, 15–27. https://doi.org/10.1016/j.ijggc.2014.05.003

Wang, G., Pickup, P., Sorbie, K., & Mackay, E. (2022). Scaling analysis of hydrogen flow with carbon dioxide cushion gas in subsurface heterogeneous porous media. *International Journal of Hydrogen Energy*, *47*(3), 1752–1764. https://doi.org/10.1016/j.ijhydene.2021.10.224

Yekta, A. E., Manceau, J. C., Gaboreau, S., Pichavant, M., & Audigane, P. (2018). Determination of hydrogen-water relative permeability and capillary pressure in sandstone: Application to underground hydrogen injection in sedimentary formations. *Transport in Porous Media*, *122*(2), 333–356. https://doi.org/10.1007/s11242-018-1004-7

Zhou, L., & Zhou, Y. P. (2001). Determination of compressibility factor and fugacity coefficient of hydrogen in studies of adsorptive storage. *International Journal of Hydrogen Energy*, *26*(6), 597–601. https://doi.org/10.1016/S0360-3199(00)00123-3
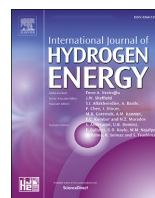
References From the Supporting Information

Foyen, T., Alcorn, Z. P., Ferno, M. A., Barrabino, A., & Holt, T. (2021). CO_2 mobility reduction using foam stabilized by CO_2- and water-soluble surfactants. *Journal of Petroleum Science and Engineering*, *196*, 107651. https://doi.org/10.1016/j.petrol.2020.107651

Massoudi, R., & King, A. D. (1974). Effect of pressure on surface-tension of water - adsorption of low-molecular weight gases on water at 25 degrees. *Journal of Physical Chemistry*, *78*(22), 2262–2266. https://doi.org/10.1021/j100615a017

Paper 5

# Seasonal hydrogen storage in a depleted oil and gas field

Maksim Lysyy[*], *Martin Fernø, Geir Ersland*

Department of Physics and Technology, University of Bergen, Allégaten 55, 5007, Bergen, Norway

HIGHLIGHTS

- Long-term and large-scale hydrogen storage is examined in a depleted oil and gas field.
- A real full-field simulation model with site-specific parameters was used.
- Preferred targets for seasonal hydrogen withdrawal were identified.
- Effect of the cushion gas nature, its composition and structural geometry were assessed.

GRAPHICAL ABSTRACT
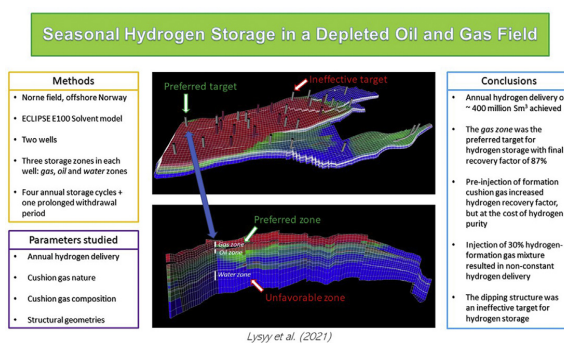
ABSTRACT

Hydrogen storage is essential in hydrogen value chains and subsurface storage may be the most suitable large-scale option. This paper reports numerical simulations of seasonal hydrogen storage in the Norne hydrocarbon field, offshore Norway. Three different storage schemes are examined by injecting pure hydrogen into the *gas-*, *oil-*, and *water* zones. Implementation of four annual withdrawal-injection cycles followed by one prolonged withdrawal period show that the thin *gas zone* is a preferred target with a final hydrogen recovery factor of 87%. The hydrogen distribution in the subsurface follow the geological structures and is restricted by fluid saturation and displacement efficiencies. Case studies show that the pre-injection of formation gas as a cushion gas efficiently increases the ultimate hydrogen recovery, but at the cost of hydrogen purity. The injection of 30% hydrogen-formation gas mixture results in a varying hydrogen fraction in the withdrawn gas. An alternative well placement down the dipping structure shows lower storage efficiency.

© 2021 Hydrogen Energy Publications LLC. Published by Elsevier Ltd. All rights reserved.

Introduction

Hydrogen storage in depleted oil and gas reservoirs is proposed as a strategy to increase flexibility for future supply and seasonal outtake. Large-scale hydrogen storage may become relevant for hydrogen value-chains in two ways: 1) integration of hydrogen storage into renewable energy systems and 2) accommodation of seasonal variations in hydrogen demand for power generation and supply in buildings. Hydrogen can aid renewable energy sources to equilibrate the imbalances between supply and demand. Using Power-to-Gas technology, excess electricity from the renewables is transformed into hydrogen through water electrolysis, and hydrogen is then temporarily stored for later withdrawal at peak demand [9]. Despite lower cost, duration of excess electricity is generally short, and the need for large-scale storage sites may not be decisive. The second application, if scaled-up, would require large-scale and long-term storage solutions.

Hydrogen technologies are of growing interest in Norway. With emerging offshore wind industry and existing petroleum infrastructure, the Norwegian Continental Shelf (NCS) can potentially become an attractive site for hydrogen value chains. Wind-based offshore hydrogen production offers a possible solution to the need for a power grid connection in the wind electricity systems [6]. On the other hand, many of hydrocarbon fields on the NCS are mature and are expected to be phased out in the middle-term future. Offshore hydrogen production can be an alternative to decommissioning of petroleum infrastructure by reusing existing platforms and pipeline networks [27]. The Netherlands and the UK are already evaluating possible opportunities for offshore hydrogen production from electrolysis (green hydrogen) and steam cracking of methane (blue hydrogen) using existing petroleum infrastructure [27,32]. Meier [18] performed a techno-economic evaluation of offshore hydrogen production from wind power on the NCS. They concluded that such projects would be technically feasible, but not profitable yet. The cost in operating and maintaining the offshore platform was pointed as the main uncertainty. However, their study did neither consider using existing infrastructure nor the underground storage sites into the value-chains. We speculate that the cost-effectiveness may be potentially improved by using existing offshore infrastructure. Dinh et al. [6] conducted a similar study by assessing hydrogen production from wind in the Irish Sea. They included underground hydrogen storage and estimated the profitable hydrogen price at €5/kg in 2030.

Natural gas can be stored in underground formations such as salt caverns, aquifers, and depleted hydrocarbon fields [14]. Storage site initialization involves injection of gases which will serve as cushion gas or working gas. Cushion gas will typically remain in the storage site to maintain the pressure required for stable withdrawal while the working gas may be produced at peak demand. Cushion and working gases may be identical or have different gas composition. In aquifers and depleted hydrocarbon fields, the fraction of cushion gas ranges from 50% to 80% of totally injected gas [2]. A typical storage site operates annually with one injection and one withdrawal period at peak demand (winter months). Injection period typically lasts from 200 to 250 days, and withdrawal period continues from 100 to 150 days. A similar strategy may be used for hydrogen storage [11]. Despite high potential for technical and operational knowledge transfer, there are important differences: hydrogen is much more mobile and prone to biogeochemical interactions in porous media [24]. Viscous fingering can occur during porous media hydrogen storage [26] due to large contrasts in viscosity and density between hydrogen and formation fluids. There are to date some experience with commercial storage of pure hydrogen in salt caverns [23], but not in aquifers or depleted hydrocarbon fields. Only town gas with hydrogen content up to 50–60% was stored in aquifers and salt caverns in Europe in the past centuries [25,31]. For future large-scale and long-term storage, depleted hydrocarbon fields appear to be a more cost-effective option, partially due to known characteristics and well-developed infrastructure [16].

Despite growing interest in hydrogen behavior in porous systems, the fundamentals of hydrogen flow properties are still not adequately investigated. Most research on underground hydrogen storage focuses on biogeochemical interactions. Rapid hydrogen consumption via sulphate reduction and acetate production was experimentally observed in aquifer hydrogen storage [3]. Permian and Triassic sandstones underwent major petrographic changes when saturated with pure hydrogen in static batch experiments, due to interactions with pore-filling anhydrite and carbonate cements [8]. Geochemical modelling showed that hydrogen storage in deep calcite-free formations minimized chemically induced hydrogen losses [4]. Measurements of hydrogen solubility showed significant deviations from theoretical values [5], whereas an analytically developed model for hydrogen solubility appeared to be consistent and accurate [15]. Multiphase hydrogen flow in porous media is only covered by one experimental [33] and several numerical studies [7,17,28,30]. Relative permeability and capillary pressure functions were measured for hydrogen-water system in sandstone [33]. Hydrogen contact angles, highly relevant for rock wettability determination, were derived for basaltic [1] and measured for quartz [13] rocks. Most of previous numerical studies were aimed at hydrogen storage in aquifers (Table 1). Only a single reported study examined hydrogen storage in depleted hydrocarbon (gas) field [7].

Seasonal hydrogen storage was examined in a depleted gas field using a small prismatic fragment of one of the largest onshore gas fields in Europe [7]. Viscous fingering and gravity override did not represent a major issue as opposed to hydrogen storage in aquifers. Hydrogen injection resulted in a highly saturated and homogenous hydrogen plume in the near-well area. Hydrogen purity in the extracted gas mixture increased with increasing number of withdrawal cycles. A

Table 1 – Summary of literature on numerical simulation of underground hydrogen storage.

Scientific paper	Software	Storage site	Location	Storage duration	Injected gas
Feldmann et al. [7]	DuMu^x	Depleted gas field	Part of one of the largest onshore gas fields in Europe	Long-term	Hydrogen
Lubon et al. [17]	PetraSim-TOUGH2	Aquifer	Geological structure in Poland	Long-term	Hydrogen
Pfeiffer et al. [28]	ECLIPSE E300	Aquifer	Existing anticlinal structure in Germany	Short-term	Hydrogen + nitrogen
Sainz-Garcia et al. [30]	COMSOL	Aquifer	Actual dome-shape structure in Spain	Long-term	Hydrogen

saline aquifer was evaluated for the seasonal storage of hydrogen generated from wind in Northern Spain [30]. The maximum hydrogen saturation emerged in the near-well area and in the top part of the reservoir. No viscous fingering was observed explained by the structure's deep slopes. Recovery rates up to 78% were achieved for single cycles. Upconing was the main issue affecting the storage efficiency. Implementation of different well placement strategies improved storage performance. Seasonal hydrogen storage in a deep aquifer was assessed using an existing anticlinal structure in NW Poland [17]. They focused on estimating the optimal conditions for hydrogen storage governed by water-coning and the capillary entry and fracturing pressure limits. When injected, hydrogen tended to rise upwards, leading to hydrogen accumulation along the top part of the reservoir. Hydrogen injection was favored in the highly permeable zones. Maximum hydrogen concentration occurred in the near-well area and in the top part of the reservoir. No viscous fingering was observed explained by steep reservoir boundary. Hydrogen recovery increased with increasing number of cycles, with maximum recovery rate of over 50%. Water-coning was pointed as the main limitation.

Short-term hydrogen storage was examined in aquifer in the North German Basin [28]. Nitrogen served as cushion gas, followed by initial filling with hydrogen. Hydrogen accumulated mainly in the near-well area whereas nitrogen migration was far-reaching. Gravitational effects were observed that resulted in hydrogen accumulation in the upper parts of the reservoir, with nitrogen being distributed in the lower part. Hydrogen recovery increased with increasing storage cycles. They concluded that changing the injection pattern of cushion gases could potentially improve the storage efficiency. An alternative storage strategy was suggested [10] to minimize hydrogen loss in aquifers due to viscous fingering. Using analytical methods and 2D numerical modelling, they proposed the "selective technology". This technology suggests placing the injector at the bottom of aquifer where horizontal overlying barriers exist. The injected gas will migrate upwards and decelerate at horizontal barriers. The injected gas is then withdrawn at the top of the structure before it spreads horizontally. The authors pointed out the complexity of this strategy. The "selective technology" has not been numerically investigated in 3D reservoir models.

With scarce literature on depleted hydrocarbon fields, there is a need for further studies in this topic. Previous numerical studies build their own models based on existing geological structures, with lack of site-specific data like relative permeability, residual saturations, capillary pressure etc. This work takes advantage of a real history-matched simulation model with site-specific parameters based on the Norne field offshore Norway. The field is a middle-size hydrocarbon field (oil with a thin gas cap) operated by Equinor Energy AS [21]. The field was put on stream in 1997 and was originally expected to be phased-out by 2014, but the lifetime was recently extended until 2026. The production strategy relies on water injection for pressure support. Gas injection terminated in 2005 and production from the gas cap started in 2019. The field is divided into four segments (C, D, E and G-segments) covering an area of 9 km × 3 km. The Jurassic sandstone-reservoir contained 25 m of gas and 110 m of oil initially. The reservoir porosity and permeability range between 25 and 30% and 20–2500 mD, respectively.
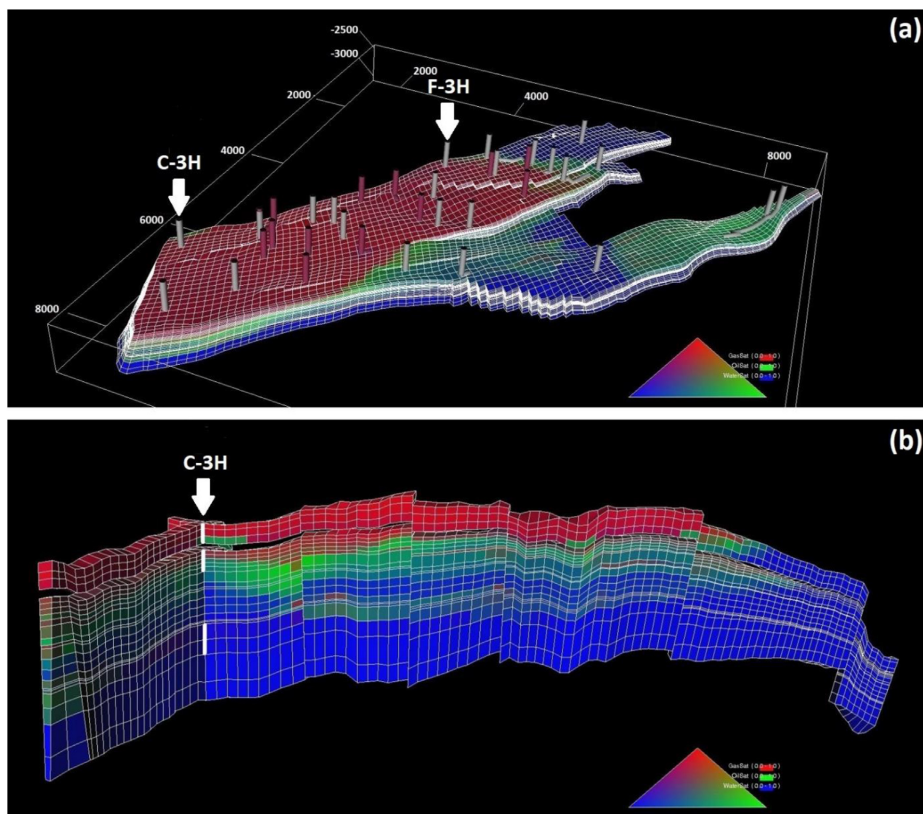
Fig. 1 – (a) Norne simulation grid with well locations denoted by vertical grey and red bars. The white downward arrows locate the wells C–3H and F–3H for hydrogen injection and withdrawal in this work. (b) Vertical xy-slice showing the perforation intervals (white bars) in C–3H which indicate three different storage zones (top to bottom): *gas*, *oil*, and *water*. Vertical distance is 5-times exaggerated. The ternary diagrams at the bottom of each figure represent a reservoir fluid system as follows: gas (red), oil (green), and water (blue).

Norne simulation model

The publicly available Norne simulation model (ECLIPSE E100 black-oil) enabled investigation on hydrogen storage under realistic reservoir geometry and properties [22]. The simulation model with faults, sloping pillars and 36 wells was history matched until December 2006 (Fig. 1a), with the following key features: end-point scaling for relative permeability and capillary pressure, multiple saturation regions, inter-region and fault transmissibility multipliers. The simulation model has 113,344 grid cells with the lateral individual grid resolution of 80–100 m and vertical resolution of 2–10 m.

The E100 Norne simulation model cannot directly be used to simulate hydrogen storage because a fourth fluid phase component must be included. Previous porous media hydrogen studies [28] use the compositional E300 version to accommodate the hydrogen phase, but E300 show poor performance in history matching hydrogen storage in a depleted gas reservoir [29]. Hence, we used the Solvent option in E100 to extend the Norne E100 model by introducing a new dry gas phase (hydrogen) distinguishable from the formation gas. The Solvent model, in contrast to full conversion to compositional models, may encourage the industrial actors to use existing black-oil models to easily adapt for planning hydrogen storage projects. The Solvent option in E100 offers two different modes – miscible and immiscible. Due to lack of appropriate miscibility data between hydrogen and oil, we use the immiscible mode with literature hydrogen properties [19]. We used original Norne relative permeability functions for gas, oil and water. The gas/hydrogen relative permeability was introduced, where the total relative permeability of the gas phase (formation gas + hydrogen) is a function of the total gas saturation, that is $Kr_{gt} = Kr_g (S_g + S_{H2})$. Default values for gas/hydrogen relative permeability were used, representing typical "straight-line" functions.

Model preparations

Hydrogen storage was studied using the history-matched Norne simulation model. To prepare the model for hydrogen studies, we continued oil and gas production until reaching a field oil production rate of 1500 Sm^3/d. The field was water-flooded with historical injection rates, with no gas injection. Formation gas was produced from the gas cap, consistent with the production strategy [21]. Hydrogen injection tests were run after reaching the 1500 Sm^3/d rate limit. Among the 36 wells, the well C−3H was chosen for hydrogen storage in all simulation runs, and one case study used well F−3H (Case study 3). The well C−3H was located on the edge of Norne C-segment, with the well F−3H drilled on the opposite side of the filed (Fig. 1a). Both wells were drilled vertically through gas, oil, and water zones.

The *gas zone* (*Garn* formation) in C−3H, mainly gas saturated (average Sg = 0.55) with irreducible water and some isolated oil pockets, was physically separated from underlying oil and water zones without vertical communication. Three perforations intervals with 27 m total depth (Fig. 1b) were used, where the lowest interval connected to an oil pocket (So = 0.70, Sg = 0), whereas the two upper perforations intervals connected to gas-saturated grid cells (Sg range between 0.84 and 0.90, So = 0). The *oil zone* (*Ile* formation) had four perforations over 24 m, where all perforations connected to grid cells with water (Sw range between 0.23 and 0.47). The two upper perforations connected to grid cells with liberated gas (Sg range between 0.48 and 0.62), whereas the lower two connected to oil-saturated grid cells (So range between 0.47 and 0.52). The oil zone communicated with underlying water saturated *Tofte* formation. The *water zone* (*Tilje 4/3* formation) was predominantly water-filled, with a small fraction of liberated gas (Sg < 0.1) in the near-injector area. Two perforations with total depth of 50 m were used. The water zone had poor vertical communication with the overlying Tofte and underlying Tilje 2/1 formations (transmissibility multipliers 0.001 and 0.00001, respectively).

All simulations were grouped into two packages. The first was defined as the *reference case* which examined the storage of 100% hydrogen into the well C−3H. The second, referred to as *case studies*, investigated the effect of various parameters — cushion gas, injected gas composition, and structural geometries. Both simulation packages studied the hydrogen storage in three different zones separately — *gas*, *oil*, and *water* zones. The perforation intervals in each storage zone are shown in Fig. 1b. Each simulation included three different stages — storage site *initialization*, *cyclic operation* and *prolonged withdrawal* period — described next.

Initialization

The average reservoir pressure was around 130 bar prior to hydrogen injection. We applied a bottom-hole-pressure (BHP) constrain of 270 bar, corresponding to initial reservoir pressure; when reached the mode of injection was switched to constant pressure. Hydrogen injection was terminated when the average reservoir pressure in the studied zone reached 250 bar; 20 bar below the initial reservoir pressure to avoid potential fracturing and leakages during storage operation.

The initialization stage used a constant volumetric injection rate of 3 million Sm^3/d, within the range of historically observed gas injection rates (2–4 million Sm^3/d) in the well C−3H. The initial injection rate was a compromise to achieve consistency of simulation conditions and a reasonable duration of initialization. For comparison, published simulation studies of underground hydrogen storage use injection rates between 0.2 and 0.8 million Sm^3/d [7,17,30].

Cyclic operation

Seasonal hydrogen storage operation consisted of four annual cycles with one 5-month withdrawal and one 7-month injection period in each cycle. The cyclic operation stage started immediately after initialization was completed, with a withdrawal/injection rate limit of 3 million Sm^3/d and BHP limits of 270 bar (upper) and 180 bar (lower). Prior to operation the average reservoir pressure in each zone was 250 bar. The choice of lower BHP limit ensured constant hydrogen deliverability during operation, and the withdrawal rate of 3 million Sm^3/d is within literature values [7,17,30].

Prolonged withdrawal

After the 4th withdrawal/injection cycle, a prolonged withdrawal period was simulated to estimate final hydrogen recovery factors. The withdrawal was controlled by a rate of 3 million Sm^3/d and a lower limit of 130 bar BHP to meet the average reservoir pressure prior to the initialization stage. Prolonged withdrawal period had an economic limit set to 1 million Sm^3/d of hydrogen. This critical rate was found based on the following data: 1) the total operating cost on the Norwegian Continental Shelf of NOK 60 billion/year for 87 fields [20]; 2) hydrogen production cost with CCUS in Europe of 2.32 USD/kgH$_2$ [12].

Results and discussion

This section presents and evaluates the simulation results and discuss their implications. The results are grouped into two main parts: 1) *Reference case* examining hydrogen storage into the well C−3H in gas, oil and water zones separately; 2) *Case studies* investigating the effect of three parameters on hydrogen storage: cushion gas and injected gas composition in the well C−3H, and structural geometries using the well F−3H.

Reference case

Initialization

Storage capacity. Prior to injection of hydrogen, the *gas zone* was predominantly saturated with formation gas (compressible fluid), whereas *oil* and *water* zones contained mixes of oil and water (incompressible fluids) with some liberated gas in top layers. The pressure-controlled injection of hydrogen determined the rate and total amount of hydrogen injected in each zone (Fig. 2; case *Ref* in Table 2). The *gas zone* did not reach the BHP limit and maintained constant injection during the entire period (1085 days). In contrast, the *water zone* BHP limit was reached upon initialization due to poor vertical
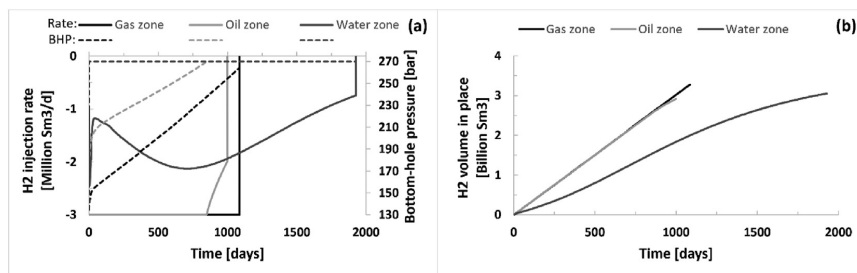
Fig. 2 – Results of the storage site initialization stage in the *gas*, *oil* and *water* zones for the reference case. (a) Hydrogen (H$_2$) injection rate (negative values reflect hydrogen from surface to reservoir, left y-axis) and the bottom-hole pressure (BHP, right y-axis) in C–3H: the injection in the *gas zone* was characterized by constant rate and gradual pressure development, whereas the *water zone* experienced variable injection rate due to an immediate achievement of the BHP upper limit. (b) Hydrogen volume injected: high storage capacity achieved in all storage zones, with *water zone* duration around two times longer than in the *gas* and *oil* zones.

Table 2 – Summary results of hydrogen storage in the reference case (Ref) and three case studies (Case 1A,B,C; Case 2; Case 3) in all storage zones – gas, oil and water. The results cover all three stages of hydrogen storage – initialization, cyclic operation and prolonged withdrawal.

Storage zone	Case	Initialization			Cyclic operation			Prolonged withdrawal	
		Duration [days]	Total H$_2$ injected [Billion Sm^3]	H$_2$ ratio in totally injected gas	H$_2$ withdrawn 1st cycle [Billion Sm^3]	H$_2$ recovery factor 1st cycle	Lowest H$_2$ fraction withdrawn 1st cycle	Total H$_2$ withdrawn [Billion Sm^3]	Final H$_2$ recovery factor
Gas	Ref	1085	3.26	100%	0.432	13%	100%	4.78	87%
	Case 1A	1219	0.75	20%	0.436	58%	81%	2.76	93%
	1B	1196	1.28	36%	0.456	36%	96%	3.28	94%
	1C	1124	2.32	60%	0.460	20%	99%	4.18	92%
	Case 2	1203	1.08	30%	0.137	13%	25%	1.58	91%
	Case 3	1193	3.37	100%	0.497	15%	100%	4.06	77%
Oil	Ref	999	2.91	100%	0.462	16%	100%	3.91	77%
	Case 1A	1079	0.84	26%	0.436	52%	82%	2.93	95%
	1B	1047	1.41	45%	0.452	32%	96%	3.39	92%
	1C	1007	2.38	80%	0.461	19%	99%	3.88	84%
	Case 2	1133	0.97	30%	0.126	13%	25%	1.32	82%
	Case 3	1347	3.09	100%	0.429	14%	100%	2.76	61%
Water	Ref	1928	3.05	100%	0.373	12%	100%	2.07	49%
	Case 1A	2309	0.69	20%	0.356	52%	72%	1.63	84%
	1B	2153	1.49	45%	0.384	26%	95%	1.90	70%
	1C	1967	2.58	82%	0.374	15%	99%	2.04	55%
	Case 2	2228	0.98	30%	0.085	9%	22%	0.62	47%
	Case 3	1047	3.14	100%	0.473	15%	100%	1.73	38%

communication and high water saturation. The lower hydrogen-water displacement efficiency, combined with water accumulations above and below the near-injector area, reduced the injection rate in the *water zone*. Hence, the duration of hydrogen injection was almost two times longer (1928 days) compared with the gas zone. The *oil zone* BHP development fell between the two other zones, with an initial sharp increase followed by a gradual increase until the injector reached the BHP limit 150 days before the initialization stage end (999 days).

The total hydrogen volumes injected varied with 13% for the three zones – oil zone: 2.91 billion Sm^3; *water zone* 3.05 billion Sm^3; *gas zone*: 3.26 billion Sm^3 (Fig. 2b; case *Ref* in Table

2). The lower storage capacities for *oil* and *water* zones relative to the *gas* zone were linked to the presence of immiscible fluids and reduced displacement efficiencies. For the *water zone* there was a clear disadvantage with injector perforations in regions with poor vertical communication, combined with high water saturations in the near-well area and in the neighboring overlying layers. For the *gas zone* the injected hydrogen volume was 5–35 times greater than reported seasonal hydrogen storage cases [7,17,30], demonstrating the high potential of hydrogen storage in middle-sized depleted hydrocarbon fields. Similar to results shown in [7]; the injected hydrogen efficiently displaced formation gas in the *gas zone*. The resulting residual gas saturation was equal to zero in cells entered by
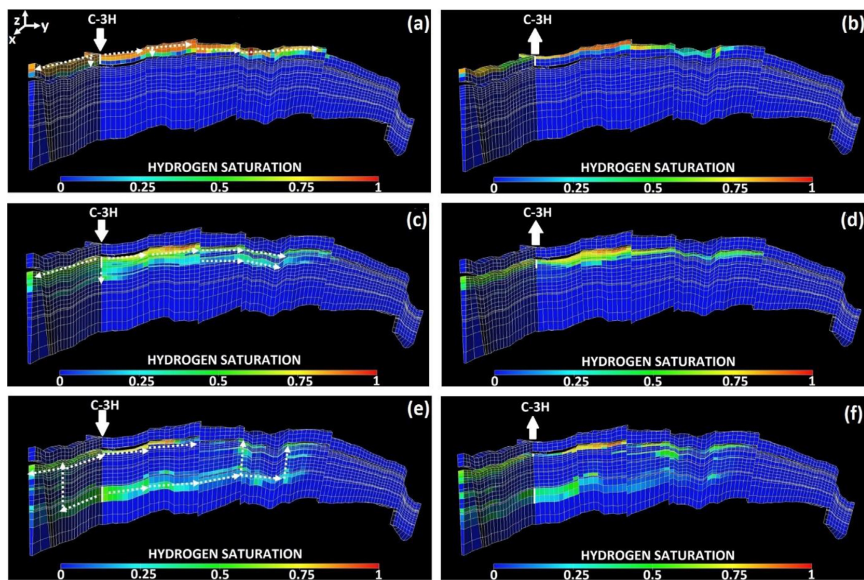
Fig. 3 — Vertical xy-slice of the simulation grid showing hydrogen saturation at the end of the storage site initialization (left) and of the prolonged withdrawal period (right) for the reference case. From top to bottom: hydrogen storage in *gas* (a, b), *oil* (c, d), and *water* zones (e, f) respectively. The white solid arrows show the location of the well C−3H and indicate injection or withdrawal, whereas the vertical bars denote the perforation intervals. Hydrogen propagation during injection is indicted by the dashed arrows (a,c,e). Downward hydrogen propagation was observed in the *gas* and *oil* zones (a,c). In the *water zone*, upward hydrogen propagation was hindered in the near-well area and occurred in the far-well area only (e). The fault blocks resulted in hydrogen bypassing along the discontinuous layers in the *oil zone* (c) but favored upward hydrogen propagation in the *water zone* (e). The hydrogen saturation upon completion of the initialization phase was the highest in the far-well area (a,c,e). The prolonged withdrawal period (b,d,f) resulted mainly in the vertical hydrogen plume shrinkage in the *gas* and *oil* zones (b,d) and some lateral shrinkage in the *gas zone* (b). In the *water zone*, hydrogen distribution was characterized as spotty and widely distributed (f). Upconing of liquids occurred in the *oil zone* (d) and in the *water zone* in the additionally opened perforation in the top of the reservoir (f).

hydrogen because the connate gas saturation was set zero in the simulation model.

Hydrogen propagation and final distribution. Hydrogen flow patterns (Fig. 3a,c,e) were largely determined by local permeability and presence of partially sealing fault blocks, where higher permeability regions favored hydrogen flow, corroborating previous work [17]. Minor viscous fingers developed in the *water zone*, consistent with the literature [17,30], whereas viscous fingers were completely absent in the *oil zone*. The previous studies explained the lack of fingers due to the structural geometries, stating that the steeply dipping structures limit the development of fingers. In our work, hydrogen was injected in the planar structure, without development of pronounced viscous fingers. We suggest that the absence of viscous fingers was caused by the modelling approach rather than the structural geometry. To adequately model field scale viscous fingers reservoir simulators require a very fine grid resolution or local grid refinement, and detailed studies aimed at improving the modelling of viscous fingers are required.

Vertical hydrogen flows were observed (Fig. 3a,c,e) despite lower permeability layers that hindered downwards (*gas zone* −

Fig. 3a) and upwards (*water zone* − Fig. 3e) hydrogen displacement from the onset of injection. Gravitational effects were less pronounced in the thin *gas zone*, corroborating earlier work [7]. Fault blocks resulted both in bypassing discontinuous, lower-permeable layers (*oil zone* − Fig. 3c) and enabling vertical hydrogen migration along the boundary between fault blocks (*water zone*). In the *oil zone*, simultaneous vertical and horizontal hydrogen migration in the near-well area occurred from a combination of two factors. First, the thicker *oil zone* provided access to the underlying high-permeable grid layers. Second, the hydrogen saturations were lower due to the presence of oil and water. Hence, the maximum hydrogen saturation and downward migration was achieved faster in *oil zone* compared to the *gas zone*. In the *water zone*, upwards hydrogen migration was delayed due to high water saturation (>0.80) in the overlying low-permeable layer and occurred in the far-well area where water saturation was significantly reduced (<0.60). While moving upwards, hydrogen accumulated below the low-permeable barriers and at the top of the reservoir where it spread laterally.

The final hydrogen distribution after storage site initialization was closely linked to the distribution of the initial water

saturation (*gas* and *water* zones) predefined in the simulation model or the total liquid saturation (*oil zone*). The highest hydrogen saturations were observed away from the near-well area, with a more heterogeneous distribution compared with previous hydrogen studies in depleted gas reservoirs [7]. This is explained by the variations in the initial water saturation. The high hydrogen saturation at the top of the reservoir was consistent with previous studies [17,30]. The high saturation of formation gas at the top of the reservoir favored hydrogen accumulation because displacement of formation gas by hydrogen was more efficient than displacement of oil and water. For the same reason, hydrogen did not penetrate the isolated oil-saturated grid cells surrounded by formation gas in the *gas zone*. Unlike the *gas zone*, hydrogen saturation in the *oil zone* was always higher in the uppermost grid layer than in underlying grid layers.

Cyclic operation

Hydrogen withdrawal (Fig. 4a,c) was maintained at maximum allowed rate (3 million Sm^3/d) for the *gas* and *oil* zones for all cycles, without reaching the lower BHP limit. In contrast, *water zone* withdrawal rates decreased for each cycle when reaching the lower BHP limit. Annual hydrogen delivery ranged between 292 and 480 million Sm^3, compared with 67–108 million Sm^3 reported in the literature [7,30]. Every withdrawal period was characterized by an initial sharp decline in BHP pressure, followed by a linear decrease for all zones, as previously observed for aquifer storage [28]. The

pressure declined most rapidly for the *water zone*, in part caused by higher saturation of incompressible water (relative to the *gas* and *oil* zones), exacerbated by poor vertical communication with over- and underlying formations. No formation gas was produced in the 5-month withdrawal periods for the three zones, but the *water zone* experienced water breakthrough (Fig. 4d). The hydrogen recovery factor for the first withdrawal period was low for all three zones — water: 12%; gas: 13%; oil: 16% (Case *Ref* in Table 2). Most of the injected hydrogen (>84%) during storage site initialization was trapped underground and served as pressure support for subsequently hydrogen withdrawal/injection cycles (Fig. 4b).

Hydrogen injection periods were characterized by reaching the upper BHP pressure limit for all zones with a corresponding injection rate reduction (Fig. 4a,c). The amount of hydrogen injected decreased for all zones over time because each injection period initiated at a higher BHP compared with the previous. Nevertheless, the total hydrogen amount increased over time for the *gas* and *oil* zones (Fig. 4b) because the hydrogen volume injected for each period was higher than hydrogen volume withdrawn (the injection periods were 7-months, whereas withdrawal periods were 5 months). This demonstrates the importance of planning the duration of the withdrawal/injection period when designing hydrogen storage projects. The total hydrogen amount in the *water zone* (Fig. 4b) decreased for each cycle because this zone experienced a deeper fall in injection rate, resulting in less amount of hydrogen injected after every cycle compared with *gas* and *oil* zones.
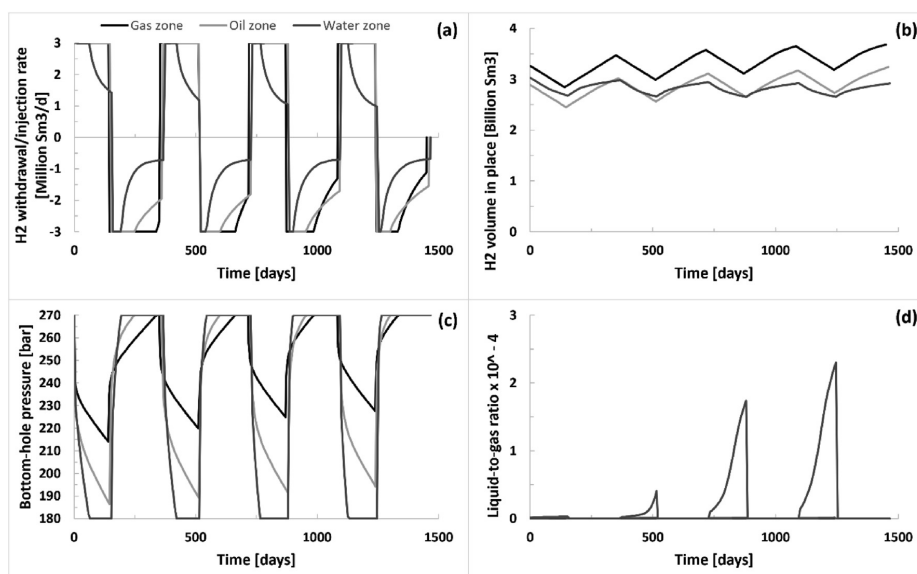

Fig. 4 – Results of the cyclic operation stage in the *gas*, *oil* and *water* zones for the reference case. (a) Hydrogen withdrawal (positive values reflect hydrogen from reservoir to surface) and injection rates (negative values reflect hydrogen from surface to reservoir): withdrawal was characterized by constant rate in the *gas* and *oil* zones, and declining rate in the *water zone*. Hydrogen injection rate declined for each cycle. (b) Hydrogen volume stored: most of the injected hydrogen during storage site initialization remained underground. (c) Bottom-hole pressure in C–3H. (d) Liquid (oil + water)-to-gas (hydrogen + formation gas) ratio: a water breakthrough occurred in the *water zone*.
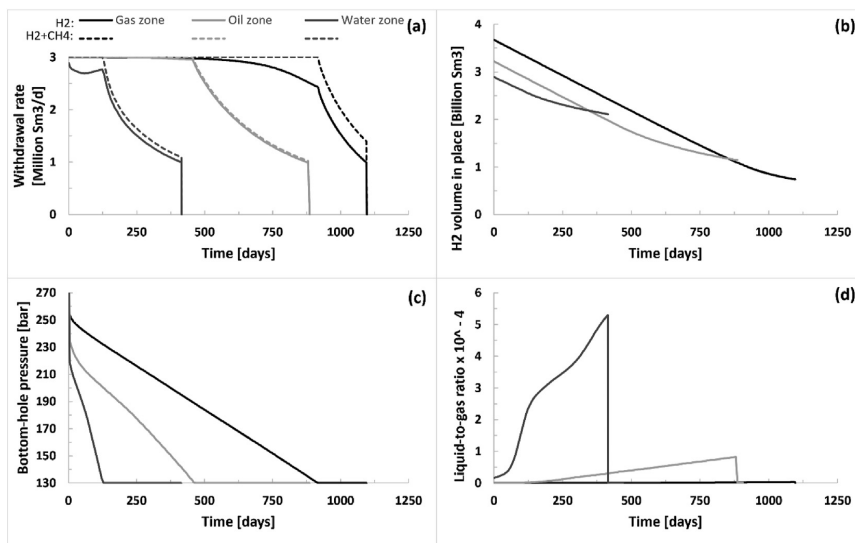
Fig. 5 — Results of the prolonged withdrawal period in the *gas*, *oil* and *water* zones for the reference case. (a) Withdrawal rate. The solid lines represent the hydrogen withdrawal rate, whereas the dashed lines denote the total withdrawal rate of hydrogen and formation gas: the initially constant withdrawal rate ($H_2 + CH_4$) was replaced by declining trend due to achievement of the BHP lower limit. The *gas zone* experienced the formation gas breakthrough. (b) Remaining hydrogen volume in the reservoir: the remaining hydrogen volume was low in the *gas* and *oil* zones, whereas the *water* zone showed poor hydrogen recovery. (c) Bottom-hole pressure in C−3H. (d) Liquid (oil + water)-to-gas (hydrogen + formation gas) ratio: a water breakthrough occurred in the *oil zone*, with both formation gas and water production in the *water zone*.

Prolonged withdrawal

The prolonged withdrawal period (Fig. 5) after the fourth cycle was characterized by a constant hydrogen withdrawal at maximum allowed rate (3 million Sm^3/d) for the *gas zone* (310 days) and *oil zone* (300 days). Subsequently, formation fluid breakthrough (formation gas in *gas zone* − Fig. 5a; mostly oil and water in *oil zone* − Fig. 5d) was observed, with decreasing ratios of withdrawn hydrogen. The prolonged withdrawal period ceased when the hydrogen withdrawal rate reached its lower economic limit (*gas zone*: 1094 days; *oil zone*: 880 days). This resulted in a final hydrogen recovery factor of 87% for the *gas zone*, 77% for the *oil zone* and 49% for the *water zone* (case *Ref* in Table 2). *Gas zone* recovery factor was comparable to the reported 82% recovery in an Austrian field pilot in depleted onshore gas field [29], suggesting that an isolated thin *gas zone* is a suitable target for hydrogen storage. The low hydrogen recovery in the *water zone* was influenced by the short duration (415 days) and pronounced water production (Fig. 5d), despite an additionally open well perforation in the uppermost layer (Fig. 3f) to test the "selective technology" [10]. Hydrogen accumulation in the uppermost perforation occurred due to horizontal hydrogen propagation and not vertical migration along the well. Hence, the upper well perforation did not have access to all hydrogen concentrated in the top part of the reservoir, resulting in lower hydrogen recovery, demonstrating the complexity of the "selective technology". *Water zone* hydrogen storage was therefore the least preferred option.

The final hydrogen distribution (Fig. 3b,d,f) demonstrated predominantly vertical with some horizontal hydrogen plume shrinkage for the *gas zone*, whereas the *oil zone* hydrogen plume contracted only in vertical direction. Generally, hydrogen saturations in the near-well area were lower (nominally 0.5) than on the flanks (nominally 0.8), partially influenced by the fault blocks. In the *oil zone*, upconing of liquids (oil and water) occurred in the near-well area, consistent with the reported observations [17,30]. This demonstrates the complexity of hydrogen withdrawal in the presence of multiple fluids (hydrogen, liberated gas, oil, and water) with varying mobility and displacement efficiencies. For both *gas* and *oil* zones, the unrecovered hydrogen predominantly accumulated at the top layers, and correlated with the maximum hydrogen saturations after storage site initialization. The remaining hydrogen in the *water zone* was characterized as spotty and widely distributed. The lowest hydrogen saturation was observed in the uppermost perforation (nominally 0.1), with the highest hydrogen saturation aligned with the site initialization. Water upconing did not occur in the lowermost perforations due to poor communication with underlying water-saturated formation. The water breakthrough occurred in lateral direction only. This illustrates that the well placement above the low-permeable layer is advantageous in water-saturated formations.

Case studies

Effect of cushion gas — case study 1

In real hydrogen storage projects, hydrogen migration far from the injection point may potentially lead to loss of hydrogen. From the perspective of maximum recoverable hydrogen volumes, we therefore evaluate the use of formation gas instead of hydrogen to increase initial reservoir pressure. We study three scenarios (A, B and C), where the storage site initialization in each scenario was performed in two steps: 1) 100% formation gas injection until a preset pressure value (A: 220 bar; B: 200 bar; C: 160 bar), followed by 2) 100% hydrogen injection until 250 bar. The injected hydrogen volumes (Case 1 in Table 2) were lower compared with reference case. The ratio between injected formation gas and hydrogen was similar for all zones in scenario A (nominally 20% hydrogen), whereas the *gas zone* received less hydrogen for the other scenarios (B: 36% and C: 60%) compared with the *oil zone* (B: 45% and C: 80%) and *water zone* (B: 45% and C: 82%). Hence, the *gas zone* required more formation gas to achieve the desired pressurization for each scenario, reducing the amount of injected hydrogen. This suggests that *gas zone* hydrogen storage was more favorable than in *oil* and *water* zones when using formation gas as cushion gas.

The hydrogen recovery factor for the first withdrawal period (Case 1 in Table 2) was *i*) higher for all zones compared with the reference case using pure hydrogen injection, and *ii*) increasing with increasing amount of formation gas injected. The highest hydrogen recovery factors for the first withdrawal period were observed in scenario A for all zones — gas: 58%; oil: 52% and water: 52%. However, scenario A showed the lowest hydrogen fraction in the withdrawn gas mixture (Case 1A in Table 2). Both hydrogen and formation gas were produced, starting with pure hydrogen with gradually increasing shares of formation gas (Fig. 6). The hydrogen fraction decreased more rapidly in the *water zone* (Fig. 6d), due to hydrogen losses caused by upward migration. In scenarios B and C, the hydrogen purity remained high and nearly constant for all withdrawal periods in all three storage zones. Hence, impurities in the withdrawn gas mixture can be avoided by injecting at least 60–80% of hydrogen in totally injected gas. The final hydrogen recovery factor decreased with increasing amount of hydrogen injected, being the lowest in scenario C — gas: 92%; oil: 84% and water: 55% (Case 1C in Table 2). Overall, the highest recovery factors were achieved at the cost of the hydrogen purity. When using cushion gases other than hydrogen, a detailed screening is needed to weigh between the hydrogen purity and recovery factors.

Effect of the injected gas composition — case study 2

Intermittent injection and withdrawal of pure hydrogen may perform differently compared with gas mixtures with lower hydrogen content. We investigate the effect of injecting a gas mixture with 70% formation gas and 30% hydrogen, highly relevant because current legal regulations limit the maximum allowed hydrogen fraction in gas mixtures [12]. We preset a lower economic withdrawal rate limit to 1 million Sm^3/d of the formation gas-hydrogen mixture.
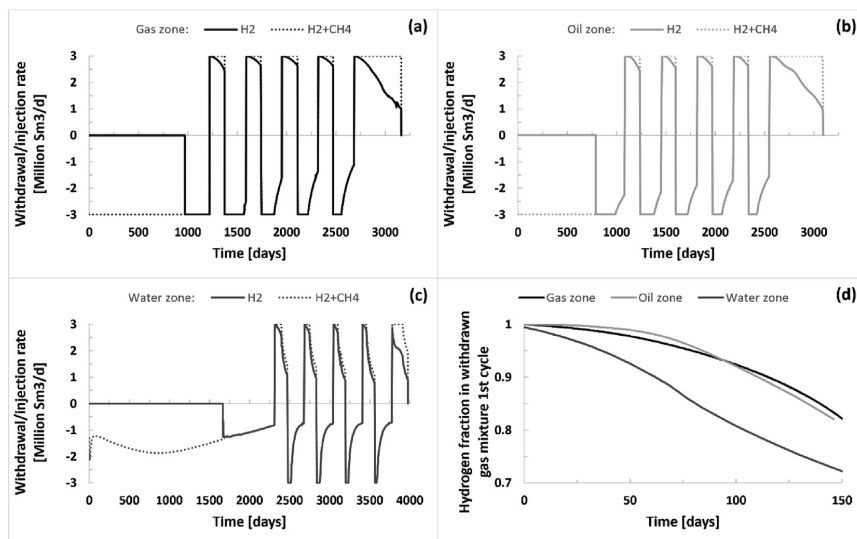

Fig. 6 — Case study 1 (scenario A) — the results of the initialization, cyclic operation and prolonged withdrawal stages. Withdrawal (positive values) and injection (negative values) rates in *gas* (a), *oil* (b), and *water* (c) zones, respectively. The solid lines represent the hydrogen rate (H_2), whereas the dashed lines denote the total rate of hydrogen and formation gas ($H_2 + CH_4$). The initialization stage started with 100% formation gas injection, followed by 100% hydrogen injection. Hydrogen withdrawal was characterized by declining hydrogen rate due to the formation gas break-through. (d) Hydrogen fraction in the withdrawn gas mixture during the 1st withdrawal period. Withdrawal periods started with pure hydrogen, with gradually decreasing hydrogen fraction in the withdrawn gas mixture.
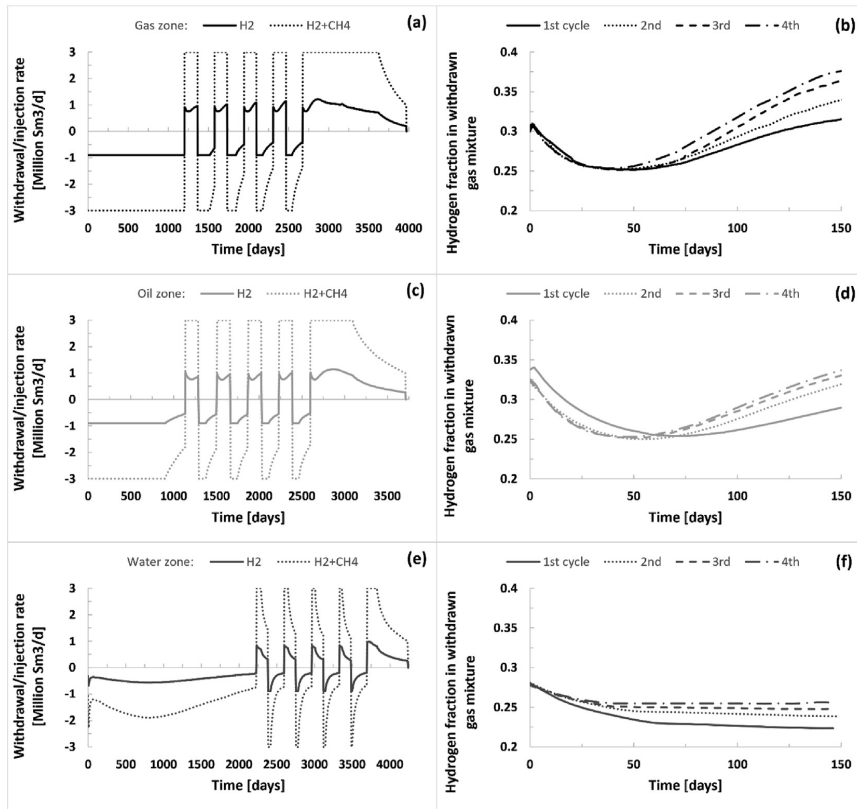
Fig. 7 — Case study 2 — the results of the initialization, cyclic operation and prolonged withdrawal stages. Withdrawal/injection (positive/negative values, respectively) rates (left) and hydrogen fraction in the withdrawn gas mixture (right). From top to bottom: hydrogen storage in *gas* (a, b), *oil* (c, d), and *water* zones (e, f), respectively. In (a, c, e) the solid lines represent the hydrogen rate (H_2), whereas the dashed lines denote the total rate of hydrogen and formation gas ($H_2 + CH_4$). The injected formation gas-hydrogen mixture consisted of 30% hydrogen during the storage site initialization and cyclic operation (a,c,e). The initial hydrogen fraction in withdrawn gas mixture varied for each zone (b,d,f), being the highest in the *oil zone* (d) and the lowest in the *water zone* (f). The hydrogen faction decreased for the first 50 days, before increasing in the *gas* and *oil* zones (b,d) and stabilizing in the *water zone* (f). The hydrogen fraction at the end increased with increasing number of cycles (b,d,f).

The average hydrogen recovery factor for the first withdrawal period (*Case 2* in Table 2) was equal to or lower than hydrogen injection cases with and without formation cushion gas (*Ref* and *Case 1*) for all three zones. The initial hydrogen fraction in withdrawn gas mixture varied for each zone. For the *gas zone* (Fig. 7b) it was equal to injected hydrogen fraction (30%) due to the small thickness and isolation from the other zones. The injected gas mixture did not migrate vertically, resulting in a homogenous hydrogen-formation gas concentration in the near-well area that flowed back into the well upon withdrawal. The initial hydrogen fraction in the withdrawn gas from the *oil zone* (Fig. 7d) was higher (34%) than the injected gas mixture because vertical communication allowed the injected gas mixture to gravitationally separate due to differences in density (hydrogen gas is around 9 times less dense than formation

gas at storage conditions). Hence, close to the well perforations (located towards the top of the *oil zone*) the hydrogen fraction was higher than the injected gas mixture. The initial hydrogen fraction in the withdrawn gas from the *water zone* (Fig. 7f) was lower (28%) than the injected fraction because the *water zone* was isolated from the neighboring underlying formations, with poor vertical communication with overlying formations. Hence, the injected gas mixture migrated upwards, away from the well and reduced withdrawn hydrogen fractions.

The hydrogen fraction was not constant during each withdrawal period, and decreased during the first 50 days, before increasing (*gas* and *oil* zones — Fig. 7a,b,c,d) or stabilizing (*water zone* — Fig. 7e and f) for the rest of withdrawal period. This behavior is related to gravity segregation. There was no shut-in period between injection and withdrawal, so

the gravity segregation occurred in the far-well area only. The injected gas mixture was therefore divided into two areas — a disperse accumulation with uniform hydrogen concentration in the near-well area, and a segregated accumulation with vertical gas separation in the far-well area. During withdrawal periods, the near-well dispersed gas accumulation flowed into the well first. When the segregated gas accumulation reached the well, the hydrogen fraction increased in the *gas* and *oil* zones due to higher permeability in hydrogen-saturated layers. In the *water zone*, the hydrogen fraction remained nearly constant after the first 50 days of withdrawal (Fig. 7e and f), because some of hydrogen escaped the storage zone due to vertical upward migration. For all storage zones, the hydrogen fraction in withdrawn gas mixtures increased with each withdrawal cycle (Fig. 7b,d,f), consistent with previous studies [7,28]. The observation of gravity segregation between hydrogen and formation gas suggests that it may be advantageous to include a shut-in period between injection and withdrawal, and/or to inject the gas mixture into the lower layers and to withdraw from the upper layers.

Effect of structural geometries — case study 3

The results reported so far are linked to the hydrogen storage in a nearly planar geometry using well C—3H. Scientific literature recommends storing hydrogen in steeply dipping structures to minimize the losses [17,26,28,30]. This section provides results from hydrogen storage in a steeply dipping geometry on the opposite side of the Norne field. Hydrogen storage was performed in *gas, oil* and *water* zones separately, using the well F—3H (Fig. 1a; Fig. 9), a vertical well previously served for water injection. The storage scenario and set of controlling parameters were unchanged from the reference case using well C—3H.

Initialization. Hydrogen injection in *gas zone* was similar to reference case and characterized by stable pressure development and injection rate (Fig. 8a). In contrast, injection in the *oil zone* resulted in an immediate achievement of BHP upper limit and variable injection rate (Fig. 8b). This behavior was linked to a horizontal low-permeable barrier below the lowermost perforation that limited hydrogen downward migration, resulting in high pressures in the near-well area. In the *water zone* (Fig. 8c), the injection was in turn more favorable compared with the reference case, with less pronounced near-well area pressure increase due to lower initial water saturation in the overlying grid layer. This allowed the injected hydrogen to escape the near-well area vertically more readily, leading to more stable pressure and injection rate development. As a result, the development time was reduced by around two times (from 1928 to 1047 days).

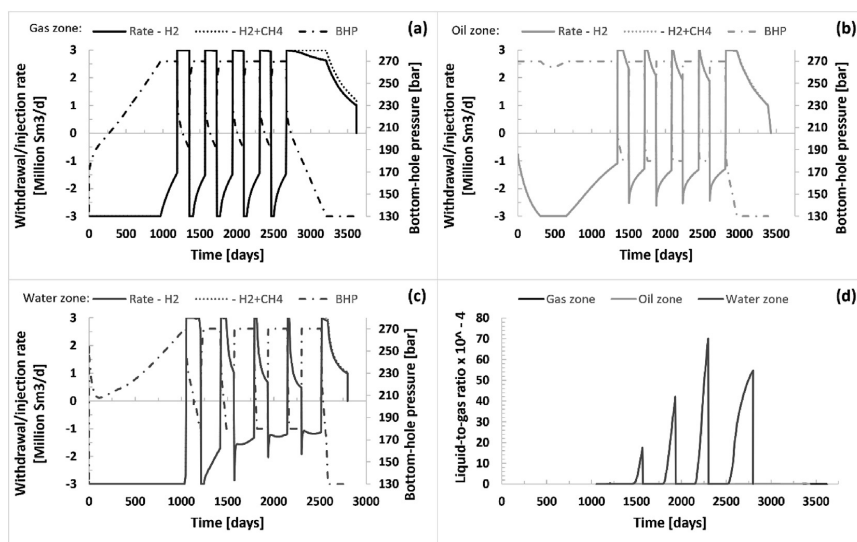Lateral hydrogen flows were greatly controlled by buoyancy, forcing hydrogen to move more in upslip direction

Fig. 8 — Case study 3 — the results of the initialization, cyclic operation and prolonged withdrawal stages. Withdrawal/injection rates (positive/negative values, respectively) and the bottom-hole pressure in F—3H in *gas* (a), *oil* (b), and *water* (c) zones, respectively. The solid lines represent the hydrogen rate (H_2), whereas the dashed lines denote the total rate of hydrogen and formation gas ($H_2 + CH_4$). The initialization stage was characterized by constant injection rate for most of time in the *gas* (a) and *water* (c) zones, whereas the varying injection rate was observed in the *oil zone* (b). During cyclic operation, the constant hydrogen withdrawal rates were observed in the *gas zone* (a), whereas the oil and *water* zones experienced decreasing hydrogen withdrawal rates (b,c). The prolonged withdrawal period in the *gas zone* was characterized by early formation gas breakthrough (a). (d) Liquid (oil + water)-to-gas (hydrogen + formation gas) ratio. The *water zone* withdrawal rate (c) reduction was caused by extensive water production (d).
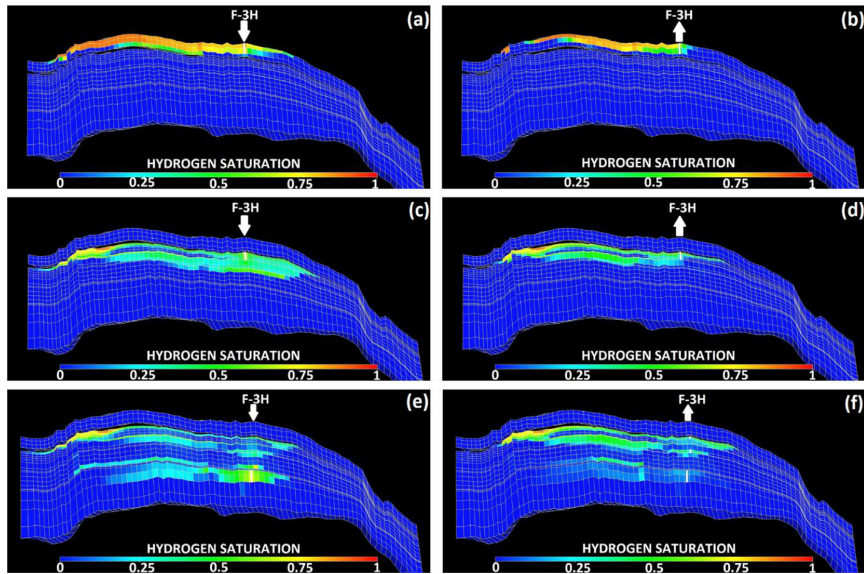
Fig. 9 — Case study 3 — vertical xy-slice of the simulation grid showing hydrogen saturation at the end of the storage site initialization (left) and of the prolonged withdrawal period (right) in F−3H. From top to bottom: hydrogen storage in *gas* (a, b), *oil* (c, d), and *water* zones (e, f) respectively. The white solid arrows show the location of the well F−3H, whereas the vertical bars denote the perforation intervals. Vertical distance is 5-times exaggerated. Lateral hydrogen propagation occurred more in upslip direction during the initialization stage (a,c,e). In the *water zone*, vertical hydrogen migration initiated in the near-well area (e). The remaining hydrogen at the end of the prolonged withdrawal accumulated mostly in upslip direction (b,d,f). In the *water zone*, two additional perforations were opened at the top of the reservoir during prolonged withdrawal (f).

(Fig. 9a,c,e). Vertical hydrogen flows were generally similar to reference case, except for the *water zone* where hydrogen upward migration occurred above the injector due to lower initial water saturation in the overlying grid cells. The final hydrogen distribution was similar to the reference case, characterized by heterogeneous hydrogen saturation with the maximum values in the far-well area.

Cyclic operation. Cyclic operation in *gas zone* performed similarly to the reference case, with constant withdrawal and declining injection rates (Fig. 8a), unlike *oil* and *water* zones. The *oil zone* exhibited declining withdrawal/injection rates due to a horizontal low-permeable barrier below the well perforations, leading to large pressure changes in the near-well area. The duration of constant withdrawal rates within each cycle decreased with increasing number of cycles, caused by increasing hydrogen concentration in the near-well area. In *water zone*, the first cycle was characterized by plateau withdrawal for the most of time due to better communication with overlying formation resulting in a slower pressure decline in the near-well area. However, constant withdrawal/injection rates were not maintained in the next cycles due to strong water production (Fig. 8d). Stronger and earlier water breakthrough occurred because hydrogen-water boundary

established closer to the well, caused by less hydrogen accumulation in downslip direction (Fig. 9e). Hydrogen recovery factor for the first withdrawal period was comparable with the reference case (Table 2).

Prolonged withdrawal. The prolonged withdrawal period initiated with constant hydrogen rate (Fig. 8a,b,c), similar to the reference case. Compared to the 4th withdrawal period, the increased duration of constant withdrawal was observed in the *oil* and *water* zones, as a result of lower BHP limit (*oil zone*) and two additionally opened perforations at the top of the reservoir (*water zone*). However, earlier and more pronounced breakthrough of formation fluids (in *gas* and *water* zones — Fig. 8a,d), coupled with a rapid decline in BHP (in *oil zone*), reduced the duration of constant hydrogen withdrawal. The final hydrogen recovery factors were lower compared with the reference case — 77% for the *gas zone*, 61% for the *oil zone* and 38% for the *water zone* (Case 3 in Table 2). The uncovered hydrogen resided mostly in upslip direction (Fig. 9b,d,f). Overall, our results suggest that dipping structures may be less preferred for hydrogen storage when placing the operating well down the structure because this leads to uneven hydrogen distribution in up- and downslip directions due to buoyancy.

Conclusions

- Reservoir simulations suggest high hydrogen storage capacity in a middle-sized offshore hydrocarbon field: ~3 billion Sm^3 during storage site initialization.
- Hydrogen delivery of ~400 million Sm^3 was achieved for each 5-month withdrawal period.
- Most of the injected hydrogen (>84%) remained underground as cushion gas, when injecting pure hydrogen only.
- The thin *gas zone* was the most preferred target for pure hydrogen storage with final recovery factor of 87%. Hydrogen storage was not recommended in the *water zone*, due to lower final recovery factor of 49%.
- Formation fluids were not produced in the *gas* and *oil* zones during cyclic operation, but their break-through decreased the efficiency of the prolonged withdrawal period.
- The underground hydrogen distribution was determined by structural effects (vertical communication and fault blocks), modelling approaches (initial water and connate gas saturations) and type of displacement process. Minor development of viscous fingers was observed in the *water zone*, in contrast to the *oil zone*. Unrecovered hydrogen accumulated in topmost layers.
- Injection of formation gas as cushion gas resulted in higher hydrogen recovery factor (both 1st withdrawal period and final), but at the cost of hydrogen purity in the withdrawn gas mixture. Impurities could be avoided by injecting at least 60–80% of hydrogen of the totally injected gas mixture.
- When injecting a 30% hydrogen-70% formation gas mixture, the hydrogen fraction in the withdrawn gas mixture varied during cyclic operation and was controlled by gravity segregation.
- Well placement down the dipping structure showed poor performance (recovery factor range between 77% and 38%), due to earlier and stronger break-through of formation fluids.

Future work

Subsurface hydrogen storage is an emerging field in scientific communities and improved understanding of processes across scientific disciplines needs to be addressed to confirm its feasibility. For improved modelling of hydrogen storage, the following aspects should be addressed:

- Detailed research on injection of gas mixtures with lower hydrogen content.
- Studies aimed at improving the modelling of viscous fingers, using simulation grid with very fine grid resolution, local grid refinement, and different structural geometries.
- Experimental studies of key hydrogen porous media parameters and functions as input for modelling – miscibility with oil, diffusivity and dispersion, residual saturations, capillary pressure, and relative permeability.

Declaration of competing interest

The authors declare that they have no known competing financial interests or personal relationships that could have appeared to influence the work reported in this paper.

Acknowledgments

REFERENCES

[1] Al-Yaseri A, Jha NK. On hydrogen wettability of basaltic rock. J Petrol Sci Eng 2021;200.
[2] Beckingham LE, Winningham L. Critical knowledge gaps for understanding water-rock-working phase interactions for compressed energy storage in porous formations. ACS Sustainable Chem Eng 2020;8(1):2–11.
[3] Berta M, Dethlefsen F, Ebert M, Schafer D, Dahmke A. Geochemical effects of millimolar hydrogen concentrations in groundwater: an experimental study in the context of subsurface hydrogen storage. Environ Sci Technol 2018;52(8):4937–49.
[4] Bo Z, Zeng L, Chen Y, Xie Q. Geochemical reactions-induced hydrogen loss during underground hydrogen storage in sandstone reservoirs. Int J Hydrogen Energy 2021;46(38):19998–20009.
[5] De Lucia M, Pilz P, Liebscher A, Kühn M. Measurements of H2 solubility in saline solutions under reservoir conditions: preliminary results from project H2STORE. Energy Procedia 2015;76:487–94.
[6] Dinh VNL, P, McKeogh E, Murphy J, Cummins V. Development of a viability assessment model for hydrogen production from dedicated offshore wind farms. Int J Hydrogen Energy 2020. https://doi.org/10.1016/j.ijhydene.2020.04.232 (in press).
[7] Feldmann F, Hagemann B, Ganzer L, Panfilov M. Numerical simulation of hydrodynamic and gas mixing processes in underground hydrogen storages. Environ Earth Sci 2016;75(16).
[8] Flesch S, Pudlo D, Albrecht D, Jacob A, Enzmann F. Hydrogen underground storage-Petrographic and petrophysical variations in reservoir sandstones from laboratory experiments under simulated reservoir conditions. Int J Hydrogen Energy 2018;43(45):20822–35.
[9] Gahleitner G. Hydrogen from renewable electricity: an international review of power-to-gas pilot plants for stationary applications. Int J Hydrogen Energy 2013;38(5):2039–61.
[10] Hagemann B, Rasoulzadeh M, Panfilov M, Ganzer L, Reitenbach V. Mathematical modeling of unstable transport in underground hydrogen storage. Environ Earth Sci 2015;73(11):6891–8.
[11] HyUnder. Assessment of the potential, the actors and relevant business cases for large scale and long term storage of renewable electricity by hydrogen underground storage in Europe (executive summary). 2014.
[12] IEA. The future of hydrogen. 2019.
[13] Iglauer S, Ali M, Keshavarz A. Hydrogen wettability of sandstone reservoirs: implications for hydrogen geo-storage. Geophys Res Lett 2021;48(3).

[14] Katz DL, Tek MR. Overview on underground-storage of natural-gas. J Petrol Technol 1981;33(6):943–51.

[15] Li DD, Beyer C, Bauer S. A unified phase equilibrium model for hydrogen solubility and solution density. Int J Hydrogen Energy 2018;43(1):512–29.

[16] Lord AS, Kobos PH, Borns DJ. Geologic storage of hydrogen: scaling up to meet city transportation demands. Int J Hydrogen Energy 2014;39(28):15570–82.

[17] Lubon K, Tarkowski R. Numerical simulation of hydrogen injection and withdrawal to and from a deep aquifer in NW Poland. Int J Hydrogen Energy 2020;45(3):2068–83.

[18] Meier K. Hydrogen production with sea water electrolysis using Norwegian offshore wind energy potentials. Int J Energy Environ Eng 2014;5.

[19] NIST. Chemistry WebBook - thermophysical properties of fluid systems. 2018.

[20] NP. Norwegian petroleum - investments and operating costs. 2020, https://www.norskpetroleum.no/en/economy/investments-operating-costs/; 2020.

[21] NPD. Norwegian petroleum directorate factpages - Norne. 2021, https://factpages.npd.no/en/field/pageview/all/43778; 2021.

[22] Opm. Open porous media - open datasets. https://opm-project.org/?page_id=559; 2021.

[23] Ozarslan A. Large-scale hydrogen energy storage in salt caverns. Int J Hydrogen Energy 2012;37(19):14265–77.

[24] Panfilov M. Underground storage of hydrogen: in situ self-organisation and methane generation. Transport Porous Media 2010;85(3):841–65.

[25] Panfilov M. Underground and pipeline hydrogen storage. In: Compendium of hydrogen energy. Woodhead Publishing; 2016.

[26] Paterson L. The implications of fingering in underground hydrogen storage. Int J Hydrogen Energy 1983;8(1):53–9.

[27] Pearson HP, C , Corradi L, Almeida A. Offshore infrastructure reuse contribution to decarbonisation. SPE offshore Europe conference and exhibition. Aberdeen, UK: Society of Petroleum Engineers; 2019.

[28] Pfeiffer WT, Beyer C, Bauer S. Hydrogen storage in a heterogeneous sandstone formation: dimensioning and induced hydraulic effects. Petrol Geosci 2017;23(3):315–26.

[29] RAG. RAG Austria AG - underground sun storage. 2020. Final Report Public 13.

[30] Sainz-Garcia A, Abarca E, Rubi V, Grandia F. Assessment of feasible strategies for seasonal underground hydrogen storage in a saline aquifer. Int J Hydrogen Energy 2017;42(26):16657–66.

[31] Smigan P, Greksak M, Kozankova J, Buzek F, Onderka V, Wolf I. Methanogenic bacteria as a key factor involved in changes of town gas stored in an underground reservoir. FEMS Microbiol Ecol 1990;73(3):221–4.

[32] Wind TOG, T. N. North Sea Energy D3. 6 towards sustainable energy production on the North Sea-Green hydrogen production and CO2 storage: onshore or offshore?. 2018.

[33] Yekta AE, Manceau JC, Gaboreau S, Pichavant M, Audigane P. Determination of hydrogen-water relative permeability and capillary pressure in sandstone: application to underground hydrogen injection in sedimentary formations. Transport Porous Media 2018;122(2):333–56.

Paper 6
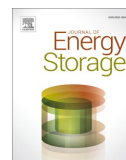
Research papers

Effect of relative permeability hysteresis on reservoir simulation of underground hydrogen storage in an offshore aquifer

Maksim Lysyy [*], Martin A. Fernø, Geir Ersland

Department of Physics and Technology, University of Bergen, Allegaten 55, 5007 Bergen, Norway

A B S T R A C T

Underground hydrogen storage (UHS) in porous media is proposed to balance seasonal fluctuations between demand and supply in an emerging hydrogen economy. Despite increasing focus on the topic worldwide, the understanding of hydrogen flow in porous media is still not adequate. In particular, relative permeability hysteresis and its impact on the storage performance require detailed investigations due to the cyclic nature of H_2 injection and withdrawal. We focus our analysis on reservoir simulation of an offshore aquifer setting, where we use history matched relative permeability to study the effect of hysteresis and gas type on the storage efficiency. We find that omission of relative permeability hysteresis overestimates the annual working gas capacity by 34 % and the recovered hydrogen volume by 85 %. The UHS performance is similar to natural gas storage when using hysteretic hydrogen relative permeability. Nitrogen relative permeability can be used to model the UHS when hysteresis is ignored, but at the cost of the accuracy of the bottom-hole pressure predictions. Our results advance the understanding of the UHS reservoir modeling approaches.

1. Introduction

Hydrogen (H_2) will play a vital role in the future net-zero energy mix and its industrial scale-up will require a range of storage solutions in all dimensions and time scales. Underground H_2 storage (UHS) has been proposed as one storage option which can account for seasonal and regional variations in demand and supply [1]. The H_2 storage demand in Europe in 2050 is expected to be in the range of 63–180 billion Sm³ (standard cubic meter) under the assumption of 780–2251 TWh total demand [2] and 24 % storage capacity [3]. Relevant underground storage formations include salt caverns, depleted hydrocarbon fields and aquifers [4] as well as more unconventional storage sites such as coal seams and basaltic rocks [5,6]. Salt caverns can accommodate smaller H_2 volumes to meet short-term storage needs, whereas porous reservoirs (i.e. depleted fields and aquifers) can be suitable for larger H_2 volumes in the long-term. Most potential storage sites are considered onshore, but offshore H_2 storage in the North Sea is attractive with regards to existing infrastructure and a growing offshore wind industry [7]. Water electrolysis can use wind-based excess electricity to produce H_2 that can be stored underground for later use.

Technically, the UHS is similar to natural gas storage (UGS) with gas injection at peak supply, followed by gas withdrawal at peak demand in repeatable annual cycles. To maintain a stable pressure support during withdrawal, cushion gas is required to remain in the reservoir while working gas is cyclically injected and withdrawn [1]. The cushion and working gases can be the same or differ in its type. Pure H_2 has never been stored in porous reservoirs at commercial scale, with town gas storage in aquifers in the 1970s [8,9] and two recent pilot tests of H_2 blends in depleted gas fields [10,11].

Despite technical similarities, low H_2 density and viscosity coupled with high biogeochemical activity hampers direct knowledge transfer [4,12]. H_2 wettability, biogeochemical interactions and reservoir simulations are currently dominating the research literature. It was found out that H_2 is a non-wetting phase in sandstones with pure quartz surfaces and is less wetting than CO_2 [13–16]. An empirical equation of H_2-brine interfacial tension was derived from experimental measurements under a range of pressure, temperature and brine salinity conditions [17]. Evaluation of caprock interfacial tension and wettability for H_2 storage showed that caprock integrity decreased with increasing pressure, temperature, organic acid concentration and total organic content [18,19]. H_2 geochemical reactivity was suppressed in calcite- and anhydrite-free sandstones [20–22]. Reservoir simulations showed that the UHS performed differently than CH_4 and CO_2 storage when comparing gas containment and working capacity [23].
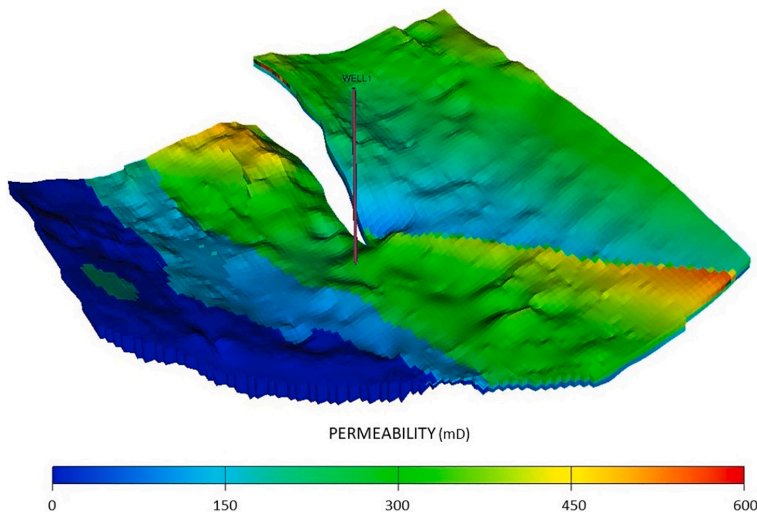
Fig. 1. A sector model of the Johansen formation with the well location and horizontal permeability distribution. The lateral extent of the sector model is around 50 km × 50 km, with the average grid size of 500 m × 500 m × 20 m. Shale layers above the Johansen formation are not shown. The vertical distance is 10 times exaggerated.

Reservoir simulation is a valuable and time efficient tool for decision making and predicting future storage performance under different reservoir management strategies. The UHS reservoir simulation studies mostly focused on feasible strategies to estimate the ultimate H_2 recovery and the impact of cushion gas. The maximum recovery factor of 78 % was achieved for single cycles in a saline aquifer, with the highest H_2 saturation in the near-well area and the reservoir top [24]. H_2 storage in a depleted oil and gas field showed that the gas zone was the most suitable target with a final recovery factor of 87 %, that was reduced to 49 % in the water zone [25]. The cushion-to-working gas ratio varied between 0.15 and 1.5 in a saline aquifer, being the lowest in deeper reservoirs with higher permeability [26]. Among different types of cushion gases: CH_4, N_2 and CO_2, the highest H_2 recovery factor (90 %) was achieved with CH_4 in a depleted oil reservoir [27], whereas N_2 was the most effective cushion gas in a partially depleted gas condensate reservoir with the H_2 recovery factor of 98 % [28]. Screening criteria for site selection were proposed based on the reservoir pressure, dipping angle, storage depth, geothermal gradient and permeability and porosity range [29].

Most UHS studies implemented nonhysteretic relative permeability in reservoir models, not specifically measured for H_2. Despite being more reliable than analytical methods, the reservoir models require real field and/or experimental data for more accurate predictions. It is still debated whether a proxy gas can be used to accurately model H_2 behavior. The gas-water injection experiments in sandstone core samples showed that N_2 is a poor proxy gas for H_2 [30,31], or it should be used with care [32]. In contrast, the opposite conclusion was drawn from another study stating that N_2 can be used as a proxy gas [33]. On the other hand, cyclic H_2 injection and withdrawal will result in reversable drainage and imbibition processes in the reservoir, indicating that relative permeability hysteresis must be considered in reservoir simulations. Measurements of H_2-H_2O drainage and imbibition relative permeability confirmed strong hysteresis both for H_2 and H_2O [32,34].

Reservoir simulation studies on the impact of H_2-H_2O relative permeability hysteresis are scarce. Hysteresis was considered in an aquifer H_2 storage study [35] where relative permeability and capillary pressure were derived from an analytical van Genuchten–Mualem model aimed to represent a typical gas-H_2O system in a sandstone. The relative

permeability model resulted in a pronounced gas hysteresis, whereas H_2O showed a minor difference between drainage and imbibition. The impact of hysteresis on H_2 storage efficiency was not evaluated as the model did not include a nonhysteretic case for comparison. One of the first attempts to study the impact of hysteresis on H_2 storage was performed in a synthetic aquifer reservoir [36]. The authors used the experimentally measured drainage H_2-H_2O relative permeability [37] and the Killough model [38] to construct imbibition H_2 relative permeability, but hysteresis in H_2O relative permeability and capillary pressure was neglected. Another study of aquifer storage implemented both H_2 and H_2O relative permeability hysteresis [39], derived from pore scale modeling without experimental support [40]. A more recent study [41] implemented the measured hysteretic H_2-H_2O relative permeability [34], and performed an analytical extrapolation beyond experimental endpoints. No history matching of experimental pressure and production data was performed to confirm the analytical extrapolation and capillary pressure hysteresis. For imbibition H_2O relative permeability, they could not find a reliable analytical model and used tabulated experimental data instead.

The abovementioned studies agreed that the absence of relative permeability hysteresis overestimated the H_2 recovery factor but disagreed in terms of H_2O production. The performance of H_2 and CO_2 storage were significantly different [39], and CO_2 relative permeability cannot be used as a proxy to model the UHS [41]. Note that impact of hysteresis has been extensively investigated for CO_2 storage, indicating that hysteresis is necessary for more accurate modeling approaches [42–45]. Experiences from CO_2 hysteresis studies are not directly applicable for H_2 storage due to the absence of CO_2 withdrawal stage.

In this paper, we use reservoir simulation to study the UHS in an offshore aquifer. We implement the measured hysteretic H_2-H_2O relative permeability and capillary pressure with numerical extrapolation from history matching of experimental production and pressure data [32], thus being a more accurate input for reservoir simulations. The Johansen sandstone formation was selected as a storage site with a real geological model built for CO_2 storage studies on the Norwegian continental shelf [46]. We examine the impact of hysteresis and a proxy gas relative permeability on the UHS and compare the results with CH_4 storage. Our findings emphasize the importance of relative permeability
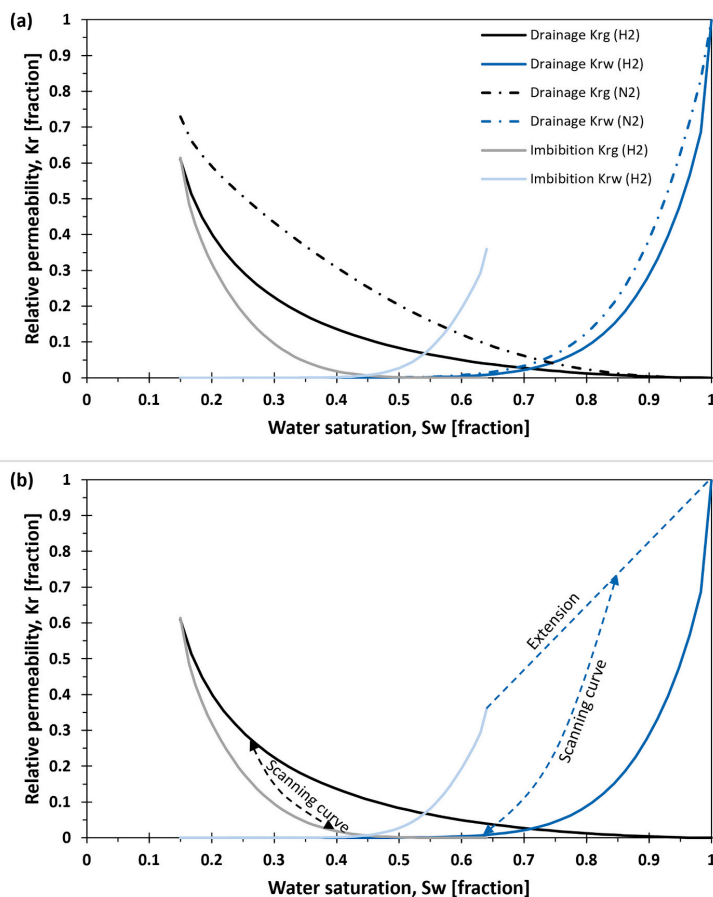
Fig. 2. Input relative permeability curves and hysteresis model used in the simulations. (a) H_2-H_2O (solid curves) and N_2-H_2O (dashed curves) relative permeabilities were directly taken from the literature dataset, derived from experimental measurements and numerical history matching [32]. The drainage H_2 (K_{rg}) and H_2O (K_{rw}) curves are represented by black and dark blue colour, respectively; whereas the imbibition K_{rg} and K_{rw} are denoted by grey and light blue, respectively. For drainage, the endpoint K_{rg}^* at irreducible H_2O saturation of 0.15 are equal to 0.61 and 0.73 for H_2 and N_2, respectively. For imbibition, the endpoint K_{rw}^* at residual H_2 saturation of 0.36 is equal to 0.36. (b) Killough hysteresis model applied to input H_2-H_2O relative permeability. The dashed curves with arrows represent typical scanning curves starting at arbitrary points. (For interpretation of the references to colour in this figure legend, the reader is referred to the web version of this article.)

hysteresis for accurate modeling of underground H_2 storage in reservoirs.

2. Numerical methods

2.1. The Johansen simulation model

The Johansen formation on the Norwegian continental shelf was selected as a storage site in our study. We used an open-license geological sector model with heterogenous porosity and horizontal permeability distribution of 0.1–0.29 (average 0.15) and 0.01–875 (average 97) mD, respectively [46]. The vertical permeability was set to 10 % of the horizontal one. The sector model was discretized into 100 × 100 × 11 grid cells with an average grid size of 500 m × 500 m × 20 m (Fig. 1). The sandstone reservoir was represented by five grid layers, vertically connected to five shale layers above and one shale layer below the reservoir. The model was constructed with a non-zero dipping angle and five faults with the transmissibility multipliers of 0.1. A more detailed description of the Johansen formation and its geological model can be found elsewhere [47].

We used a commercial black-oil ECLIPSE reservoir simulator to construct a dynamic model of the Johansen formation. The model was

governed by Darcy's law and mass conservation and contained two components: gas and water. Diffusion, dissolution and biogeochemical reactions were not included to focus on the UHS hydrodynamics. The model was initiated with no-flow boundary conditions and pressure of 313.1 bar at 3100 m true vertical depth. The gas and water densities and viscosities were extracted from an open-source database for a pressure range of 50–500 bar and reservoir temperature of 94 °C [48]. Relative permeability and capillary pressure were directly taken from the literature H_2 dataset, derived from history matched experimental measurements in a sandstone with permeability of 107 mD [32]. The rock type and its permeability are comparable to the Johansen sandstone reservoir with the average model permeability of 97 mD, making the literature dataset reliable for our H_2 storage study. Both nonhysteretic and hysteretic relative permeabilities and capillary pressures were considered, described next.

2.2. Relative permeability hysteresis model

Drainage relative permeability and capillary pressure functions were implemented in a nonhysteretic case, where two different sets of relative permeabilities were tested: H_2-H_2O and N_2-H_2O (Fig. 2a). In a hysteretic case, drainage and imbibition relative permeability and capillary

Table 1
Summary results of H_2 and CH_4 storage schemes with different relative permeability (K_r) input.

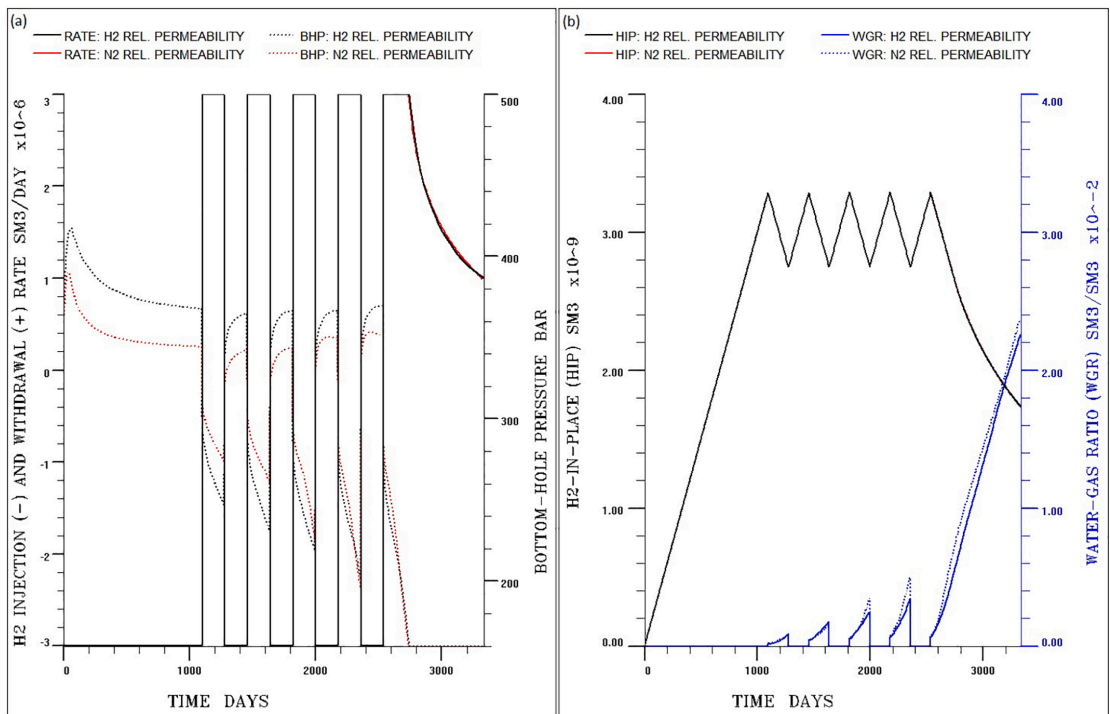| Gas type	Input K_r	Gas withdrawn [Million Sm^3]					Gas recovery factor	
		1st cycle	2nd cycle	3rd cycle	4th cycle	5th cycle	1st cycle	Final
H_2	Drainage H_2-H_2O	540	540	540	540	1560	16 %	68 %
H_2	Drainage N_2-H_2O	540	540	540	540	1550	16 %	68 %
H_2	Hysteretic H_2-H_2O	451	390	388	393	391	14 %	37 %
CH_4	Hysteretic H_2-H_2O	436	378	376	380	380	13 %	37 %

Fig. 3. Nonhysteretic case of H_2 storage with two different simulation inputs: H_2 and N_2 relative permeabilities. (a) H_2 injection (negative values) and withdrawal (positive values, solid curves on the primary x-axis) rates and the bottom-hole pressure (BHP, dashed curves on the secondary x-axis). The first injection period lasted for 1095 days, and the prolonged fifth withdrawal period began after 2538 days. The constant injection/withdrawal rates of 3 million Sm^3/d were maintained until the prolonged fifth withdrawal period, characterized by a rate reduction due to a BHP limit of 180 bar. (b) H_2 volume in place (HIP, black and red curves on the primary x-axis) and water-gas ratio (WGR, blue curves on the secondary x-axis). The HIP remained in the same range during the cyclic injection and withdrawal, whereas the WGR increased with the increasing number of cycles. The H_2 and N_2 relative permeabilities showed similar results, except for the BHP development. (For interpretation of the references to colour in this figure legend, the reader is referred to the web version of this article.)

pressure were applied for both gas and water using the Killough hysteresis model [38]. The hysteresis model implies that relative permeability functions follow a scanning curve when drainage or imbibition processes are reversed (Fig. 2b). The same scanning curve is applied for both drainage and imbibition when the injection process is reversed at any point on the scanning curve. Non-wetting phase (H_2) scanning curves are calculated based on an interpolative method that requires Land trapping model [49] and bounding drainage and imbibition curves as input. In the absence of experimental bounding data, the scanning curves can be estimated using a parametric interpolation method, which requires an input free parameter. In our case, the ECLIPSE simulator generated scanning curves from experimental drainage and imbibition data [32]. Wetting phase (H_2O) scanning curves additionally require a free parameter (set to 1 in our model), even if experimental bounding

curves are given. The H_2O scanning curve may deviate beyond a region enclosed by the drainage and imbibition curves if the imbibition curve initial gradient is small. To keep H_2O scanning curve inside the region of drainage and imbibition curves, the ECLIPSE simulator runs a correction scheme based on the reduced portion of the imbibition curve.

2.3. Storage scenarios

We evaluated four storage scenarios with both nonhysteretic and hysteretic relative permeability curves (Table 1). In the nonhysteretic cases, we examined the effect of relative permeability on the H_2 storage performance by comparing two different inputs: drainage H_2-H_2O and N_2-H_2O relative permeabilities. In the hysteretic cases, the same set of drainage and imbibition H_2-H_2O relative permeabilities was
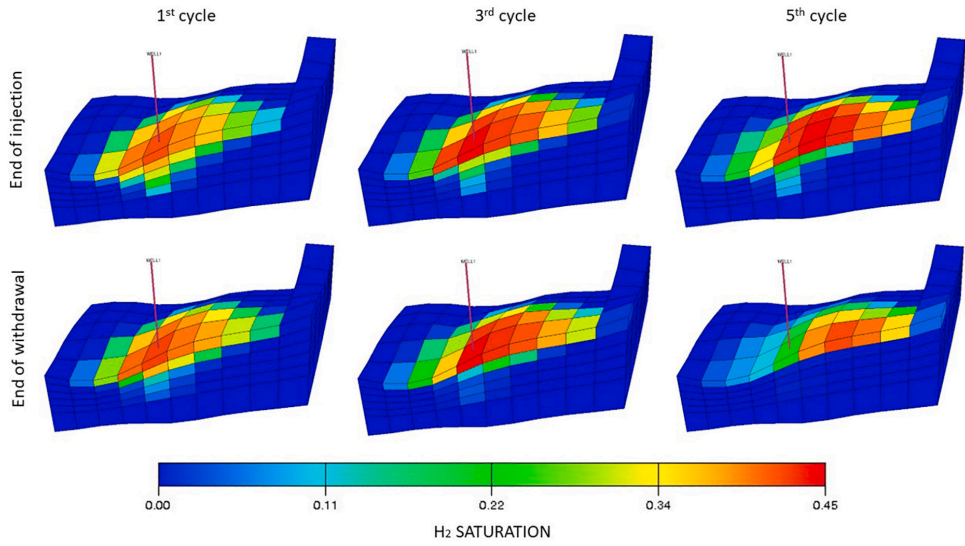
Fig. 4. Vertical slice of the 3D simulation grid part showing H_2 distribution by the end of injection (top) and by the end of withdrawal (bottom) after the 1st, 3rd and 5th cycles in the nonhysteretic case. The H_2 plume formed a cone-like shape with a stable lateral extent which contracted vertically during withdrawal, with the highest H_2 saturation at the top well perforation. Vertical distance is 10-times exaggerated.
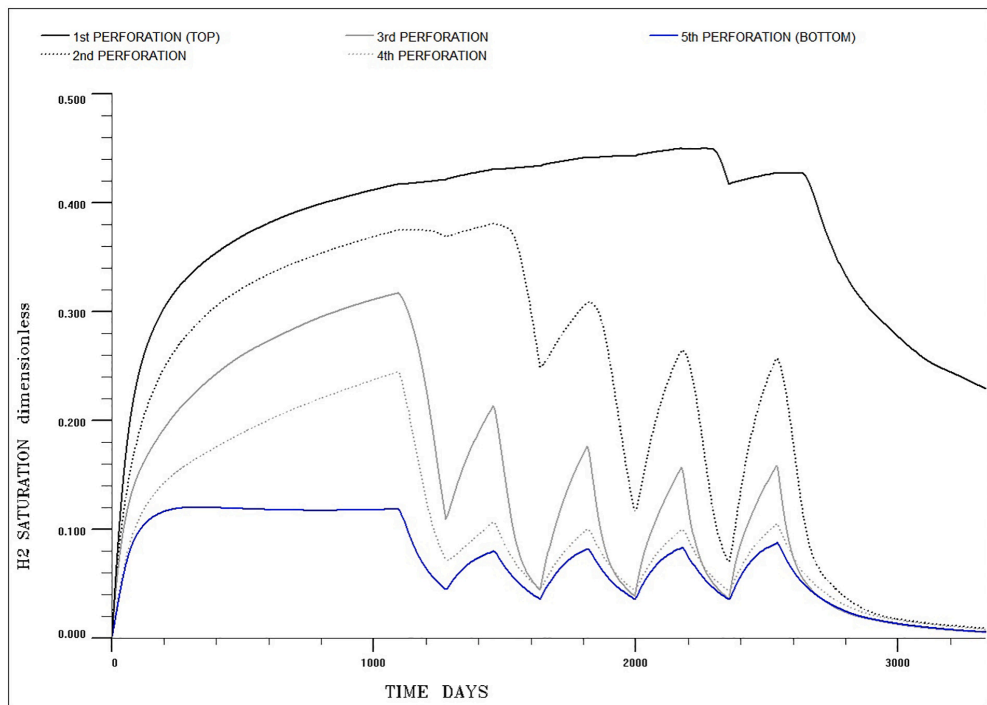

Fig. 5. H_2 saturation in the well perforations, numbered from top (1st) to bottom (5th). The H_2 saturation increased with increasing number of cycles in the 1st perforation but decreased in the 2nd and 3rd perforations due to water upconing.
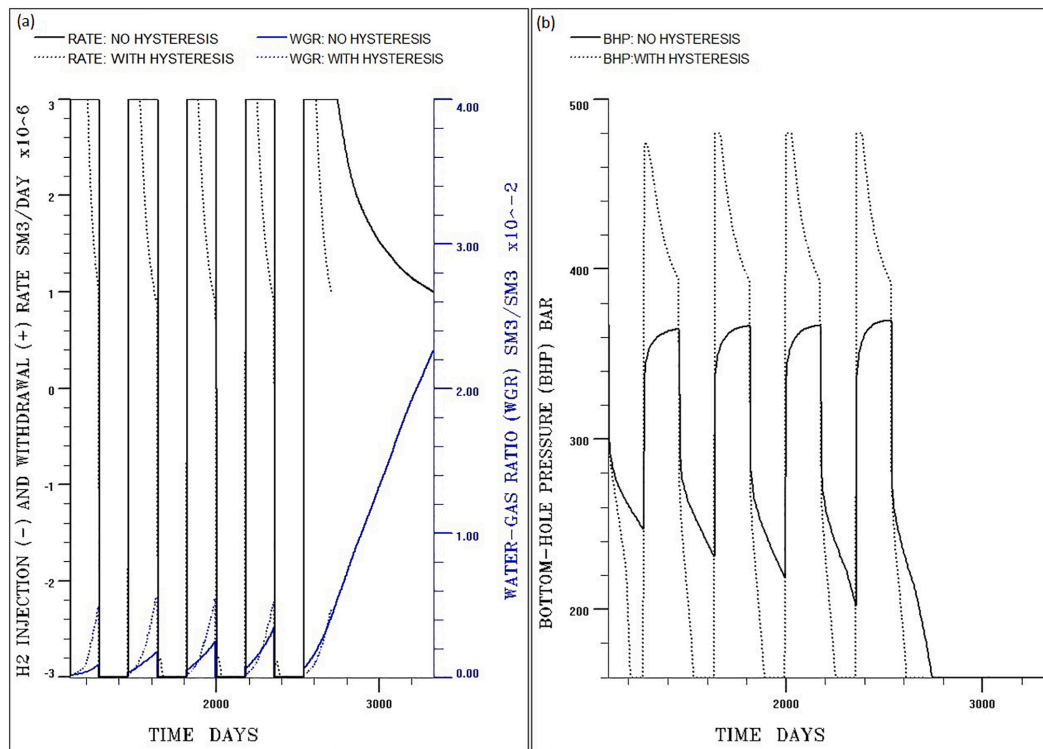
Fig. 6. Effect of relative permeability hysteresis on the storage performance. (a) H_2 injection (negative values) and withdrawal (positive values, black curves on the primary x-axis) rates and water-gas ratio (WGR, blue curves on the secondary x-axis). (b) Bottom-hole pressure (BHP). The hysteresis resulted in lower withdrawal and injection rates caused by the lower and upper BHP limits, respectively. The WGR increased and remained nearly constant in the hysteretic case. (For interpretation of the references to colour in this figure legend, the reader is referred to the web version of this article.)

implemented to compare the H_2 and CH_4 storage.

All storage scenarios followed the same operation scheme: Five injection-withdrawal cycles at the rate of 3 million Sm^3/d, with H_2 acting as both cushion and working gas. The first cycle started with a 36-month long initial filling with gas, followed by a six-month withdrawal period. The three subsequent cycles were repeated annually, with equally long injection and withdrawal periods of six months. The fifth cycle consisted of a six-month injection period, followed by a prolonged withdrawal period until the economic limit of 1 million Sm^3/d was reached [25]. A single vertical well for injection and withdrawal was placed in the center of the reservoir model through the five grid blocks where the permeability and porosity ranged between 74 and 278 mD and 0.17–0.21, respectively. The well operation was controlled by the bottom-hole pressure (BHP), constrained to 480 and 160 bar during injection and withdrawal, respectively. The BHP constrains were equal to ±50 % of the initial reservoir pressure where the upper BHP limit was below the typical fracture pressure on the Norwegian continental shelf [50]. When the BHP limits were reached, the injection/withdrawal rates were reduced to maintain constant BHP.

3. Results and discussion

3.1. Maximum working gas capacity and recovery factor

The first injection period maintained a pre-defined H_2 injection rate of 3 million Sm^3/d, but with a nonmonotonic BHP (Fig. 3a). An initial

sharp increase in BHP by 110 bar from the initial reservoir pressure reversed to a gradually declining trend as the H_2 plume expanded away from the injector. The withdrawal periods were characterized by an initial sharp decrease in BHP, followed by a more gradual trend. The endpoint BHP decreased with an increasing number of cycles, due to increasing water production with a resulting increase in the bottom-hole saturation of incompressible water (Fig. 3b).

The maximum working gas capacity was 540 million Sm^3 (~1.6 TWh) in all six-month withdrawal periods, achieved with nonhysteretic H_2-H_2O relative permeability (Table 1). The working gas capacity was equivalent to 16 % of the total H_2 volume injected during the first injection period and corresponded to 0.9 % of the predicted lower-end H_2 storage demand in Europe in 2050 [3]. The working-to-total gas volume ratio was consistent with the reported literature range of ~15–30 % when using H_2 cushion gas in aquifer storage [23–25,36]. Note that the working gas capacity increases if H_2 is replaced by other cushion gases, albeit with a decrease in H_2 fraction in the withdrawn gas mixture [25,27,36].

The maximum final H_2 recovery factor was 68 % by the end of the prolonged fifth withdrawal period which lasted for 795 days until an economic limit of 1 million Sm^3/d was reached (Table 1, Fig. 3a). Constant withdrawal rate of 3 million Sm^3/d was maintained for 207 days, followed by a declining rate due to the lower BHP limit. Comparable recovery factors (69–75 %) were reported for aquifer storage where the BHP upper limit was set to ≥50 % of the initial reservoir pressure [36,51]. In contrast, a significantly lower recovery factor (49
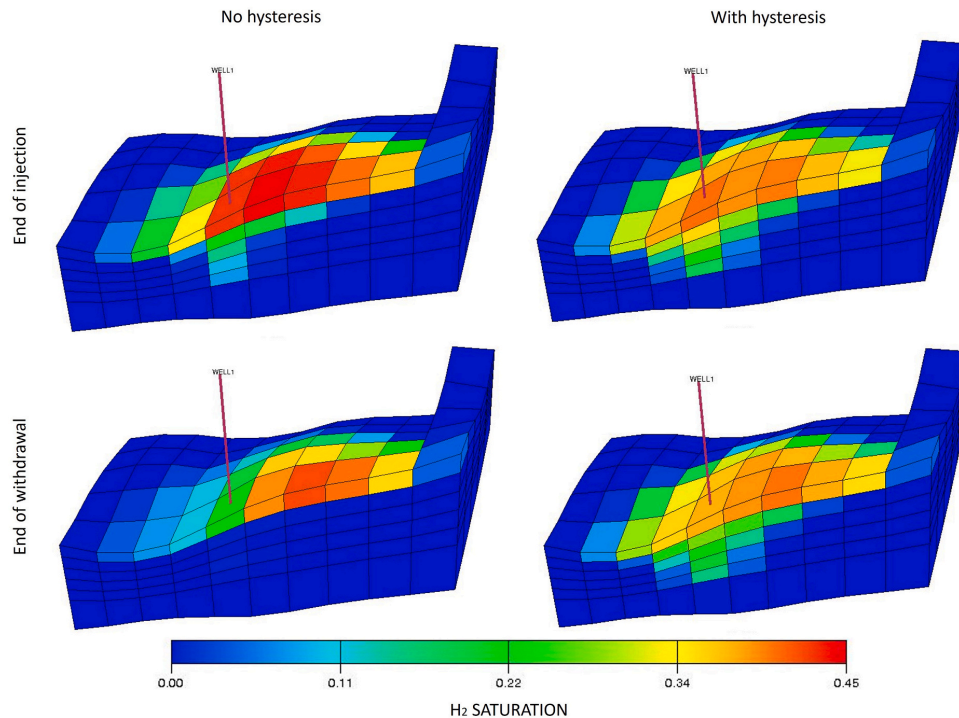
Fig. 7. Effect of relative permeability hysteresis on the H_2 distribution by the end of injection (top) and by the end of withdrawal (bottom) after the 5th cycle in the nonhysteretic (left) and hysteretic cases (right). After injection, the H_2 saturation was more concentrated in the near-well area in the nonhysteretic case due to decreased residual trapping. After withdrawal, the H_2 saturation accumulated in all perforated layers in the hysteretic case due to less H_2 volume withdrawn.

%) was estimated for the isolated water zone in a depleted hydrocarbon field because the upper BHP limit was set to the initial reservoir pressure [25]. Discrepancies in the recovery factors show that the BHP constraints are among the crucial parameters affecting the H_2 storage efficiency.

3.1.1. Effect of proxy gas relative permeability

N_2 relative permeability was evaluated as the simulation input and showed no significant impact on working gas capacity and recovery (Table 1, Fig. 3). An initial 10 % decrease in BHP during the first injection period diminished with an increasing number of cycles to a 5 % difference by the end of the fifth injection period. The results suggest that N_2 relative permeability can be used as proxy in reservoir simulations in the absence of H_2 relative permeability data. However, a mismatch between the measured and simulated BHP may be expected during real storage projects. For comparison, CO_2 relative permeability failed to accurately model the UHS [41].

3.1.2. Hydrogen plume dynamics

The H_2 plume developed a cone-like shape in vertical direction, governed by gravitational effects (Fig. 4). The maximum H_2 saturation was established in the top perforation ($S_g = 0.42$), with a gradually decreasing H_2 saturation toward the plume boundaries (minimum $S_g = 0.06$). The withdrawal periods were characterized by an upward shrinking of the H_2 plume, leading to water upconing in the well. No lateral movement of the H_2 plume was observed because the injected and withdrawn H_2 volumes were equal for all six-month periods. A stable lateral distribution is beneficial for H_2 storage because it minimizes the risk of leakage at the reservoir boundaries. The observed H_2

plume dynamics was consistent with the literature [24,35,36,51].

The H_2 saturation in the top perforation increased with an increasing number of cycles, from 0.42 to 0.45 by the end of the first and fifth injection periods, respectively (Fig. 5). In contrast, the H_2 saturation decreased in the second and third perforations, whereas this effect was suppressed in the lower perforations. This demonstrates that water upconing is more pronounced in the middle part of the well. The final H_2 distribution by the end of the prolonged fifth withdrawal period accumulated at the reservoir top.

3.2. Effect of relative permeability hysteresis

Implementation of relative permeability hysteresis reduced the working gas capacity and final recovery factor, compared with the nonhysteretic case (Table 1). The working gas capacity after the first cycle decreased from 540 to 451 million Sm^3, with a further reduction to 393 million Sm^3 after the fifth cycle. The duration of the prolonged fifth withdrawal period was shortened by 627 days, yielding a significant reduction in the final H_2 recovery factor from 68 % to 37 % (Table 1). The reduction in the working gas capacity and recovery factor was attributed to reaching the lower BHP during withdrawal, leading to a reduction in the withdrawal rates to maintain constant pressure (Fig. 6). The BHP decrease was governed by the inflow performance relationship in Eclipse reservoir simulator: $Q_g = T_w \bullet M_g \bullet (p_{grid} - p_{BHP} - p_{head})$, where Q_g is the H_2 withdrawal rate, T_w is the grid connection transmissibility factor, M_g is the H_2 mobility, p_{grid} is the grid connection pressure, p_{BHP} is the BHP, and p_{head} is the pressure head between the grid connection and bottom hole. The BHP must reduce to maintain a constant H_2 withdrawal rate at the reduced H_2 mobility caused by lower H_2 relative
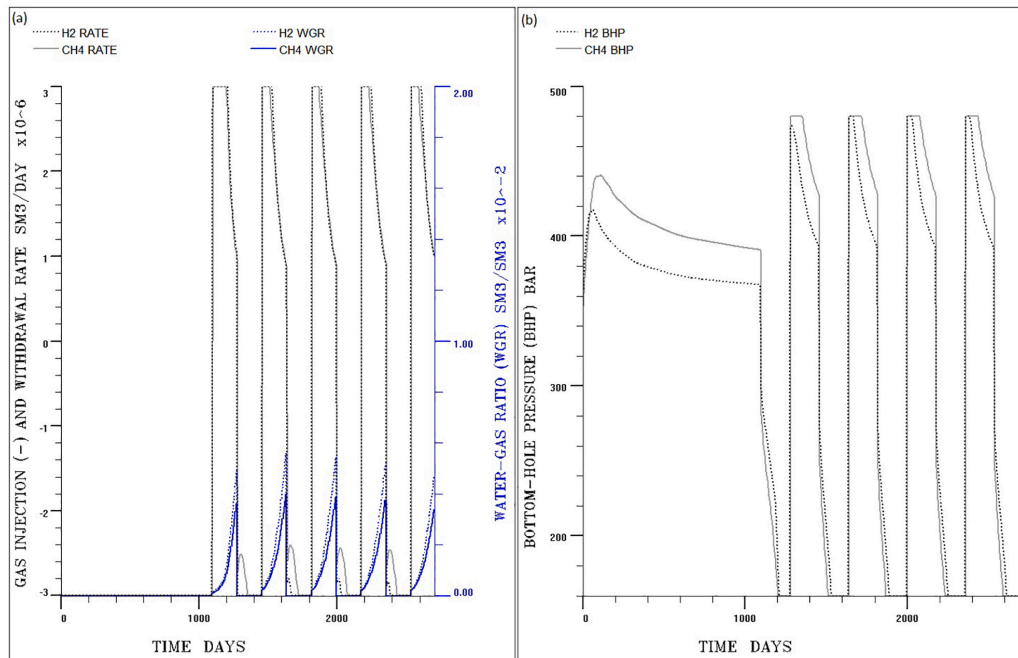
Fig. 8. Effect of gas type on the storage performance using the hysteretic relative permeability. (a) Gas injection (negative values) and withdrawal rates (positive values, black curves on the primary x-axis) and water-gas ratio (WGR, blue curves on the secondary x-axis). (b) Bottom-hole pressure (BHP). The injection and withdrawal rates were similar, whereas CH_4 storage resulted in lower WGR and higher injection BHP. (For interpretation of the references to colour in this figure legend, the reader is referred to the web version of this article.)

permeability.

A higher BHP during injection (Fig. 6b) was due to the reduced H_2 mobility, requiring higher pressure to maintain the same injection rate as in the nonhysteretic case. The upper BHP limit was reached in the third-fifth injection periods, reducing the H_2 injection rates to 2.8 million Sm^3/day before gradually returning to 3 million Sm^3/day after the first 25 days. The water-gas ratio (Fig. 6a) was nearly constant by the end of withdrawal periods, but about six times higher than in the non-hysteretic case in the first cycle, diminishing to a 1.5 times difference in the fourth cycle.

Reduction in the working gas capacity and recovery factor due to hysteresis agreed with other reservoir simulation studies of H_2 storage in aquifers [36,39]. The authors reported a 15 % reduction in the working gas capacity after the first cycle, but the difference with the nonhysteretic case decreased with increasing number of cycles. The final recovery factor was reduced by 5 percentage points after the fifth cycle, from 69.1 % to 64.1 % [36] and from 31 % to 26 % [39]. The reduction in storage efficiency in the hysteretic case was explained by the increased residual trapping, making the disconnected H_2 phase more difficult to mobilize. A higher reduction in the H_2 recovery factor was reported after the 10th cycle, from 98 % to 82–84 % depending on the hysteresis model [41]. Low recovery factors between 7 % and 36 % and their dependency on the injection rate were reported for a one-cycle storage scheme with a caprock present [35]. This was likely caused by a short duration of the withdrawal stage (one year) compared to the injection stage (three years) and hysteresis, but a direct comparison with the nonhysteretic case was missing.

The increased water-gas ratio due to hysteresis was consistent with one study [41]. In contrast, two other studies reported a decreased water-gas ratio [36,39], likely caused by lower water relative

permeability and/or inclusion of a shut-in period. Lower imbibition water relative permeability at the endpoint (<0.20) than in our study (0.36) led to lower water mobility, whereas a shut-in period contributed to a higher H_2 concentration in the near-well area prior to withdrawal. Discrepancies between different studies imply that there is no universal rule regarding the water production handling, which seems to depend on input parameters and operational conditions. Detailed pre-screening with reservoir simulations is therefore required when planning real storage projects.

The H_2 plume dynamics was comparable to the nonhysteretic case, with a vertical contraction during withdrawal and a stable lateral extent (Fig. 7). However, in the nonhysteretic case the vertical H_2 distribution was more concentrated in the well perforations, with 0.03 higher H_2 saturation in the top perforation after the fifth injection period, compared to the hysteretic case. This was because of the decreased residual trapping, enabling more H_2 to mobilize and accumulate in the near-well area. In the hysteretic case, the unrecovered H_2 after the prolonged fifth withdrawal period accumulated not only in the top layer, but also in the lower layers in a cone-like shape.

3.3. Effect of gas type: H_2 vs CH_4 storage

We used the hysteretic H_2 relative permeability to compare H_2 and CH_4 storage schemes. The working gas capacity and final recovery factors were comparable (Table 1), but with differences in the BHP and water-gas ratio (Fig. 8). The CH_4 injection resulted in higher BHP and longer injection duration at the BHP upper limit (Fig. 8b), leading to smaller injected CH_4 volumes (Fig. 8a). Higher BHP raises the operating costs, and is therefore disadvantageous from an economic perspective [44]. The water-gas ratio by the end of every cycle was on average 28 %
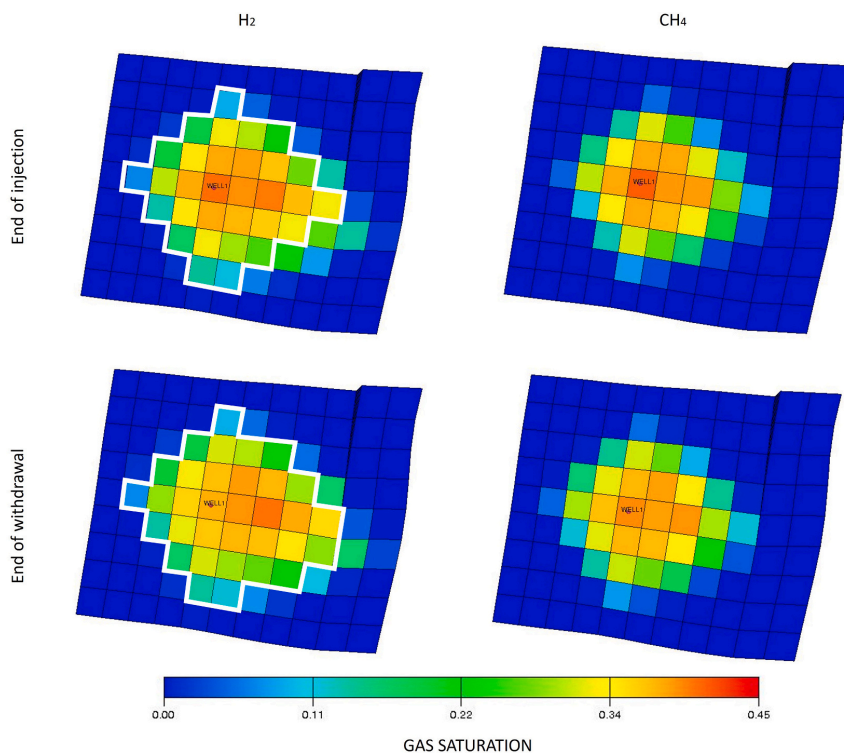
Fig. 9. Effect of gas type on its top-view distribution by the end of injection (top) and by the end of withdrawal (bottom) after the 5th cycle for H_2 (left) and CH_4 (right). The CH_4 plume contours are drawn in white on the left images to compare with the H_2 plume. The CH_4 plume shape appeared to be more uniform, with a less lateral spreading on the right boundary.

lower for CH_4 storage, due to a reduced water-gas mobility ratio. The CH_4 plume lateral spreading was ~500 m shorter than the H_2 plume on the right boundary due to the minor reservoir dipping (Fig. 9). CH_4 is less buoyant, thus less subjected to upslip migration.

Our results indicated that H_2 and CH_4 exhibited a similar performance under the examined conditions, contrary to a single available comparison study [23]. The authors reported a 39 % reduction in the maximum working gas capacity for H_2 storage, caused by a higher wellhead pressure and explained by the difference in the gas physical properties. The discrepancies with our results could be due to the presence of reservoir oil in their study. CH_4 developed a partial miscibility with the reservoir oil, resulting in a higher oil production during CH_4 withdrawal compared with H_2. Moreover, the authors observed a significantly larger lateral extent of the H_2 plume compared to CH_4, due to reservoir heterogeneity and an increasing amount of unrecovered H_2 with the increasing number of cycles.

4. Conclusions

We investigated the impact of the measured and history matched relative permeability hysteresis on H_2 storage in an actual aquifer using a black-oil reservoir simulator. Nonhysteretic relative permeability overestimated the working gas capacity and final recovery factor. Implementation of hysteresis reduced the working gas capacity from 540 million Sm^3 (~1.6 TWh) to 388–451 million Sm^3 and final recovery factor from 68 % to 37 %. The H_2 and CH_4 storage showed comparable working gas capacities and recovery factors when using hysteresis, but CH_4 storage yielded lower water production and higher bottom-hole

pressure. Drainage N_2 relative permeability can substitute for missing H_2 data, albeit at the decreased reliability of the bottom-hole pressure predictions. Our results imply that relative permeability hysteresis must be considered to avoid an overestimation of the storage performance and that knowledge transfer from CH_4 to H_2 storage is feasible from a hydrodynamic perspective.

CRediT authorship contribution statement

Maksim Lysyy: Conceptualization, Methodology, Investigation, Formal analysis, Writing – original draft. **Martin A. Fernø:** Writing – review & editing, Supervision, Funding acquisition. **Geir Ersland:** Writing – review & editing, Supervision, Funding acquisition.

Declaration of competing interest

The authors declare that they have no known competing financial interests or personal relationships that could have appeared to influence the work reported in this paper.

Data availability

Data will be made available on request.

Acknowledgements

project *Hydrogen Storage in Subsurface Porous Media—Enabling Transition to Net-Zero Society* (project number 325457) – a part of the Centre for Sustainable Subsurface Resources (project number 331841).

References

[1] P.O. Carden, L. Paterson, Physical, chemical and energy aspects of underground hydrogen storage, Int. J. Hydrog. Energy 4 (6) (1979) 559–569.

[2] H.J. Undertaking, Hydrogen Roadmap Europe: A Sustainable Pathway for the European Energy Transition, 2019.

[3] J. Cihlar, D. Mavins, K. van der Leun, in: Guidehouse (Ed.), Picturing the Value of Underground Gas Storage to the European Hydrogen System, 2021.

[4] N.S. Muhammed, et al., A review on underground hydrogen storage: insight into geological sites, influencing factors and future outlook, Energy Rep. 8 (2022) 461–499.

[5] M. Hosseini, et al., Basalt-H2-brine wettability at geo-storage conditions: implication for hydrogen storage in basaltic formations, J.Energy Storage (2022) 52.

[6] S. Iglauer, et al., Hydrogen adsorption on sub-bituminous coal: implications for hydrogen geo-storage, Geophys. Res. Lett. 48 (10) (2021).

[7] A. Hassanpouryouzband, et al., Offshore geological storage of hydrogen: is this our best option to achieve net-zero? ACS Energy Lett. 6 (6) (2021) 2181–2186.

[8] M. Panfilov, Underground and pipeline hydrogen storage, in: Compendium of Hydrogen Energy, Woodhead Publishing, 2016.

[9] P. Smigan, et al., Methanogenic bacteria as a key factor involved in changes of town gas stored in an underground reservoir, FEMS Microbiol. Ecol. 73 (3) (1990) 221–224.

[10] A. Pérez, et al., Patagonia wind - hydrogen project: underground storage and methanation, in: 21st World Hydrogen Energy Conference, 2016. Zaragoza, Spain.

[11] RAG, RAG Austria AG - Underground Sun Storage: Final Report Public 13, 2020.

[12] N. Dopffel, S. Jansen, J. Gerritse, Microbial side effects of underground hydrogen storage - knowledge gaps, risks and opportunities for successful implementation, Int. J. Hydrog. Energy 46 (12) (2021) 8594–8606.

[13] M. Ali, et al., Hydrogen wettability of quartz substrates exposed to organic acids; implications for hydrogen geo-storage in sandstone reservoirs, J. Pet. Sci. Eng. 207 (2021).

[14] L. Hashemi, et al., Contact angle measurement for hydrogen/brine/sandstone system using captive-bubble method relevant for underground hydrogen storage, Adv. Water Resour. 154 (2021).

[15] S. Higgs, et al., In-situ hydrogen wettability characterisation for underground hydrogen storage, Int. J. Hydrog. Energy 47 (26) (2022) 13062–13075.

[16] S. Iglauer, M. Ali, A. Keshavarz, Hydrogen wettability of sandstone reservoirs: implications for hydrogen geo-storage, Geophys. Res. Lett. 48 (3) (2021).

[17] M. Hosseini, et al., H-2-brine interfacial tension as a function of salinity, temperature, and pressure; implications for hydrogen geo-storage, J. Pet. Sci. Eng. 213 (2022).

[18] M. Hosseini, et al., Assessment of rock-hydrogen and rock-water interfacial tension in shale, evaporite and basaltic rocks, J.Nat.Gas Sci.Eng. 106 (2022).

[19] M. Hosseini, et al., Capillary sealing efficiency analysis of caprocks: implication for hydrogen geological storage, Energy Fuel 36 (7) (2022) 4065–4075.

[20] Z. Bo, L. Zeng, Y. Chen, Q. Xie, Geochemical reactions-induced hydrogen loss during underground hydrogen storage in sandstone reservoirs, Int. J. Hydrog. Energy 46 (38) (2021) 19998–20009.

[21] S. Flesch, et al., Hydrogen underground storage-petrographic and petrophysical variations in reservoir sandstones from laboratory experiments under simulated reservoir conditions, Int. J. Hydrog. Energy 43 (45) (2018) 20822–20835.

[22] A.E. Yekta, M. Pichavant, P. Audigane, Evaluation of geochemical reactivity of hydrogen in sandstone: application to geological storage, Appl. Geochem. 95 (2018) 182–194.

[23] M. Delshad, et al., Hydrogen storage assessment in depleted oil reservoir and saline aquifer, Energies 15 (21) (2022).

[24] A. Sainz-Garcia, et al., Assessment of feasible strategies for seasonal underground hydrogen storage in a saline aquifer, Int. J. Hydrog. Energy 42 (26) (2017) 16657–16666.

[25] M. Lysyy, M. Ferno, G. Ersland, Seasonal hydrogen storage in a depleted oil and gas field, Int. J. Hydrog. Energy 46 (49) (2021) 25160–25174.

[26] N. Heinemann, et al., Hydrogen storage in saline aquifers: the role of cushion gas for injection and production, Int. J. Hydrog. Energy 46 (79) (2021) 39284–39296.

[27] M. Kanaani, B. Sedaee, M. Asadian-Pakfar, Role of cushion gas on underground hydrogen storage in depleted oil reservoirs, J.Energy Storage (2022) 45.

[28] M. Zamehrian, B. Sedaee, Underground hydrogen storage in a partially depleted gas condensate reservoir: influence of cushion gas, J. Pet. Sci. Eng. (2022) 212.

[29] E.R. Okoroafor, S.D. Saltzer, A.R. Kovscek, Toward underground hydrogen storage in porous media: reservoir engineering insights, Int. J. Hydrog. Energy 47 (79) (2022) 33781–33802.

[30] A. Al-Yaseri, et al., Initial and residual trapping of hydrogen and nitrogen in Fontainebleau sandstone using nuclear magnetic resonance core flooding, Int. J. Hydrog. Energy 47 (53) (2022) 22482–22494.

[31] E.M. Thaysen, et al., Pore-scale imaging of hydrogen displacement and trapping in porous media, Int. J. Hydrog. Energy 48 (8) (2022) 3091–3106.

[32] M. Lysyy, et al., Hydrogen relative permeability hysteresis in underground storage, Geophys. Res. Lett. 49 (17) (2022).

[33] A. Rezaei, et al., Relative permeability of hydrogen and aqueous brines in sandstones and carbonates at reservoir conditions, Geophys. Res. Lett. 49 (12) (2022).

[34] M. Boon, H. Hajibeygi, Experimental characterization of H-2/water multiphase flow in heterogeneous sandstone rock at the core scale relevant for underground hydrogen storage (UHS), Sci. Rep. 12 (1) (2022).

[35] D.S. Mahdi, et al., Hydrogen underground storage efficiency in a heterogeneous sandstone reservoir, Adv.Geo-Energy Res. 5 (4) (2021) 437–443.

[36] R. Ershadnia, et al., Impact of geological and operational conditions on underground hydrogen storage, Int. J. Hydrog. Energy 48 (4) (2022) 1450–1471.

[37] A.E. Yekta, et al., Determination of hydrogen-water relative permeability and capillary pressure in sandstone: application to underground hydrogen injection in sedimentary formations, Transp. Porous Media 122 (2) (2018) 333–356.

[38] J.E. Killough, Reservoir simulation with history-dependent saturation functions, Soc. Pet. Eng. J. 16 (1) (1976) 37–48.

[39] B. Pan, et al., Impacts of relative permeability hysteresis, wettability, and injection/withdrawal schemes on underground hydrogen storage in saline aquifers, Fuel 333 (2023).

[40] L. Hashemi, M. Blunt, H. Hajibeygi, Pore-scale modelling and sensitivity analyses of hydrogen-brine multiphase flow in geological porous media, Sci. Rep. 11 (1) (2021).

[41] Z. Bo, et al., Impact of experimentally measured relative permeability hysteresis on reservoir-scale performance of underground hydrogen storage (UHS), Int. J. Hydrog. Energy (2023), https://doi.org/10.1016/j.ijhydene.2022.12.270.

[42] E.A. A-Khdheeawi, et al., Influence of injection well configuration and rock wettability on CO2 plume behaviour and CO2 trapping capacity in heterogeneous reservoirs, J.Nat.Gas Sci.Eng. 43 (2017) 190–206.

[43] E.A. Al-Khdheeawi, et al., Impact of reservoir wettability and heterogeneity on CO2-plume migration and trapping capacity, Int.J.Greenhouse Gas Control 58 (2017) 142–158.

[44] R. Juanes, et al., Impact of relative permeability hysteresis on geological CO2 storage, Water Resour. Res. 42 (12) (2006).

[45] S. Krevor, et al., Capillary trapping for geologic carbon dioxide storage - from pore scale physics to field scale implications, Int.J.Greenhouse Gas Control 40 (2015) 221–237.

[46] G.T. Eigestad, et al., The Johansen Data Set. https://co2datashare.org/dataset/the-johansen-dataset, 2009.

[47] G.T. Eigestad, et al., Geological modeling and simulation of CO2 injection in the Johansen formation, Comput. Geosci. 13 (4) (2009) 435–450.

[48] P.J. Linstrom, W.G. Mallard, The NIST Chemistry WebBook: a chemical data resource on the internet, J.Chem.Eng.Data 46 (5) (2001) 1059–1063.

[49] C.S. Land, Calculation of imbibition relative permeability for two and three-phase flow from rock properties, Soc. Pet. Eng. J. 8 (2) (1968) 149. &

[50] F. Riis, E. Halland, CO2 storage atlas of the Norwegian continental shelf: methods used to evaluate capacity and maturity of the CO2 storage potential, Energy Procedia 63 (2014) 5258–5265.

[51] T. Bai, P. Tahmasebi, Coupled hydro-mechanical analysis of seasonal underground hydrogen storage in a saline aquifer, J.Energy Storage (2022) 50.

uib.no